Thermal Runaway of Li-ion Batteries: Triggering, Emission, and Mitigation

A Dissertation Presented for the

Doctor of Philosophy

Degree

The University of Tennessee, Knoxville

Liwen Zhang

May 2024

DEDICATION

To my parents, elder sister, and nephew

Your support, guidance, and belief in my abilities have been the foundation of my strength.

This dissertation is dedicated to you as an expression of gratitude for your endless encouragement, which has fueled my academic journey.

ACKNOWLEDGEMENTS

I would like to express my deepest gratitude to my research advisor, Dr. Peng Zhao, for his invaluable support, patient guidance, and expert advice throughout my Ph.D. career. I am grateful for the opportunity to have been a part of the Lab of Advanced Mobility and Power (LAMP), where my research into Li-ion battery thermal runaway, one of the most challenging safety issues, was conducted.

Special thanks go to Dr. Xia Wang, Dr. Feng-Yuan Zhang, and Dr. Hsin Wang, who served on my doctoral advisory committee. Their constructive feedback and valuable suggestions significantly contributed to the depth of my research.

I am also grateful to Dr. Kwo Young for his mentorship and the numerous opportunities he provided during my academic journey. His guidance and positive impact have been instrumental in shaping my academic career.

My colleagues in the LAMP group: Ahmad Hadi Bakir, Dr. Mohammad Ahmadian Elmi, Virendra Deepak Talele, Keisuke Akita, and my colleagues from Oakland University, Meng Xu, Mingyuan Tao, Qi Yang, Han Lin, Zhibang Xu, have been companions in my study and a source of joy throughout my entire Ph.D. program.

I must also acknowledge the UTSI staff, Dr. Lu Liu, Dr. Brian K. Canfield, Douglas Warnberg, Alexander Terekhov, Joel Davenport, Jenell Burt, Charlene Hane, Jessie Tipton, Pamela Ledford and Courtney Maricle-Frazier, for their countless assistance with my research.

Deep appreciation is extended to Camel Energy Inc, General Motors, and Tesla Inc. for the invaluable internship that played a crucial role in my research and professional

development. Each organization has significantly contributed to my skills and understanding in the field.

I would like to extend heartfelt thanks to my two cats, Fatty and Rocky, for their indispensable companionship throughout this journey. Their comforting presence has been a source of joy and support.

Last but not least, I owe immense thanks to my family and all my friends for their steadfast support throughout my doctoral studies. A special appreciation goes to my parents, elder sister, and nephew—Jiyun Zhang, Cuiying Yu, Lifang Zhang, and Bingyan Song—and to my best friend, Wenwen Zhang, for their tremendous, unconditional love and belief, which empowered me to pursue my dreams and stay focused on my goals.

ABSTRACT

In the contemporary landscape, lithium-ion batteries (LIBs) are key components powering a wide array of electronic devices and electric vehicles (EVs). As society increasingly relies on these batteries for their efficiency and functionality, understanding and mitigating potential risks, such as thermal runaway (TR) events, become imperative. The objective of this dissertation is to comprehensively understand TR characteristics of LIBs through a combination of experiments and numerical simulation, thereby enhancing battery safety, refining design standards, and providing insights and guidelines for the prevention and management of TR events.

Firstly, this dissertation explores the safety regime of LIBs TR through a computational approach, identifying critical heat source intensity and duration time that determine the boundaries between TR and safe operational zones. Additionally, it studies heat release during an internal short circuit (ISC) event, combining thermal-electrochemical and thermal runaway models.

Secondly, this dissertation presents an in-depth investigation into the effects of radiative heat transfer on TR propagation. It employs a theoretical model to assess the nonlinear and non-monotonic nature of radiative effects between cylindrical Li-ion cells and examines the blocking effect in various cell arrangements.

Thirdly, this dissertation investigates cell-to-cell variability in TR characteristics among LIBs with lithium cobalt oxide (LCO), highlighting the challenges in accurately predicting TR events. It also explores the utility of statistical analysis and uncertainty quantification in TR kinetic models.

Fourthly, this dissertation analyzes the impact of aging on the TR behavior of lithium nickel cobalt manganese oxide (NCM) and lithium iron phosphate (LFP) batteries. It reveals significant effects of aging on battery safety, including variations in onset temperatures for exothermic reactions, TR delay time, and cell voltage drops.

Lastly, this dissertation introduces a novel approach to suspend TR, focusing on preserving the electrochemical performance retention of LFP cells. It emphasizes the importance of a temperature threshold for preventing further damage. Furthermore, size and time dependence of particle emission from TR has been investigated for its environmental and health concerns.

This dissertation adopts a comprehensive approach involving experimental research, statistical analysis, and modeling. It provides valuable insights for enhancing battery safety and mitigating potential hazards.

TABLE OF CONTENTS

LIST OF TABLES

LIST OF FIGURES

LIST OF ABBREVIATIONS

2D	Two-dimensional
3D	Three-dimensional
ARC	Accelerating Rate Calorimeter
BDF	Backward Differentiation Formula
BEV	Battery Electric Vehicle
BMS	Battery Management Systems
BOL	Beginning of Life
CCCV	Constant Current Constant Voltage
CFD	Computational Fluid Dynamics
DSC	Differential Scanning Calorimetry
ECM	Equivalent Circuit Models
ED	Electrolyte Decomposition
EDS	Energy Dispersive Spectroscopy
EIA	Energy Information Administration
EIS	Electrochemical Impedance Spectroscopy
EOL	End of Life
EVs	Electric Vehicles
HEV	Hybrid Electric Vehicle
HWS	Heat-Wait-Seek
ISC	Internal short circuit
LAM	Loss of Active Material

LCO	Lithium Cobalt Oxide
LFP	Lithium Iron Phosphate
LIBs	Lithium-ion Batteries
LLI	Loss of Lithium Inventory
MUMPS	Multifrontal Massively Parallel Sparse
NCM	Nickel Cobalt Manganese Oxide
NE	Negative Electrode-Electrolyte Reaction
ODE	Ordinary Differential Equation
PE	Positive Electrode-Electrolyte Reaction
PHEV	Plug-in Hybrid Electric Vehicle
SEI	Solid-Electrolyte-Interphase
SEI-D	SEI decomposition
SEM	Scanning Electron Microscopy
SOC	State of Charge
SOH	State of Health
THT	Thermal Hazard Technology
TR	Thermal Runaway
TRP	Thermal Runaway Propagation

INTRODUCTION

Overview

In the expanding landscape of energy storage, lithium-ion batteries (LIBs) power a diverse range of applications, from portable electronic devices to electric vehicles (EVs). They play a crucial role in renewable energy storage and vehicle electrification, thus becoming an integral part of modern energy solutions. As their utilization grows, ensuring the safety of LIBs, particularly in preventing thermal runaway (TR) events, becomes a critical concern. Thermal runaway events in LIBs can result in severe consequences, including fire, explosion, and damage to battery integrity. In the pursuit of a cleaner and more sustainable energy future, addressing the safety challenges associated with LIBs, particularly thermal runaway, emerges as a key priority. Understanding and mitigating the risks of thermal runaway in LIBs is essential not only for enhancing the safety of electronic devices and EVs but also for promoting sustainable energy practices. This dissertation embarks on a multifaceted exploration of thermal runaway characteristics in LIBs, integrating experimental methodologies and numerical simulations. Its aim is to reveal the complexities of thermal runaway phenomena, enhance safety protocols, influence battery design, and increase public confidence in the reliability of LIBs. Through these efforts, it provides valuable insights and makes a significant contribution to research and safety considerations of LIBs.

Background

Overview of Li-ion batteries

Li-ion batteries (LIBs) have become integral to modern technology, powering everything from small electronic devices to EVs [1–3]. Their attributes, including high energy density, high specific power, rechargeability, and high efficiency, make them ideal for a wide range of applications [4–7]. As the world progresses towards sustainable energy solutions, the role of LIBs in energy storage and conversion systems becomes increasingly critical, contributing significantly to decarbonization and energy electrification [8–14].

Li-ion batteries offer numerous advantages and have demonstrated great potential for commercialization, yet they still present certain safety concerns due to inherent drawbacks. Over time, Li-ion batteries can degrade, leading to reduced capacity and efficiency, and thus resulting in unstable performance [15–18]. Moreover, they are sensitive to temperatures, which can exacerbate degradation and increase the risk of fire or explosion [19–21]. Additionally, environmental concerns arise from the production and disposal of these batteries, due to the extraction of rare materials and difficulties in recycling [22–25]. Another critical issue is the potential risks of thermal runaway, a dangerous condition in which the battery can overheat and potentially lead to fires or explosions [26–30]. This can be triggered by factors such as short circuits [31–33], overcharging [34–38], physical damage [39–43], or exposure to high temperatures [44–46].

Despite their extensive use in numerous fields, ranging from powering portable electronic devices to EVs, Li-ion batteries still present potential safety hazards. Among

these challenges, thermal runaway is a prominent issue that can cause hazardous damage to a cell as well as its environment, making it the focus of this dissertation.

Working principle and configuration of Li-ion batteries

Li-ion batteries, recognized for their high energy density and efficiency, operate on a set of complex electrochemical reactions. These batteries are primarily composed of two key electrodes — the negative electrode and the positive electrode, both made from lithium intercalation compounds, along with an electrolyte and a separator. The typical negative electrode materials include natural graphite or hard carbons, while common materials for the cathode are metal oxides. These oxides can have a layered structure like Lithium Cobalt Oxide ($LiCoO_2$), a spinel structure such as Lithium Manganese Oxide ($LiMn_2O_4$), or an olivine structure like Lithium Iron Phosphate ($LiFePO_4$), as shown in Figure 1 [47].

During charging, the positive electrode undergoes oxidation, and the negative electrode experiences reduction. Conversely, during discharge, these reactions are reversed. The schematic for the reaction of charging and discharging is shown in Equation (1.) - Equation (3.) (where M is Co, Ni, Mn, etc. and MO refers to metal oxide) [48]. Throughout these processes, lithium ions intercalate or are extracted from the interstitial spaces in the atomic layers of the active materials, effectively shuttling back and forth between the negative and positive electrodes. This movement, driven by potential and concentration gradients, includes both migration and diffusion. The electrolyte, a mixture of organic carbonates, facilitates the transfer of lithium ions. Meanwhile, the separator, a microporous material, ensures ion conductivity while preventing electronic conduction and

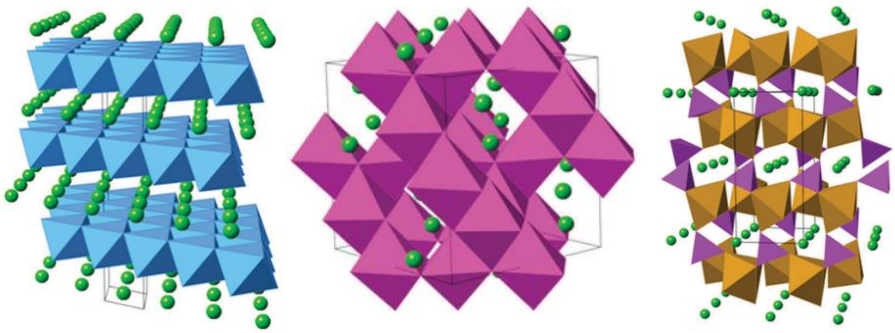

(a) (b) (c)

Figure 1. Representative crystal structure of cathode materials for Li-ion batteries (a) layered α-$LiCoO_2$; (b) cubic $LiMn_2O_4$ spinel; (c) olivine-structured $LiFePO_4$.

direct contact between the electrodes, thus avoiding short circuits. Figure 2 illustrates the structure and working principle of Li-ion battery.

Positive electrode:

$$LiMO_z \underset{Discharge}{\overset{Charge}{\rightleftarrows}} Li_{1-x}MO_z + xLi^+ + xe^- \quad (1.)$$

Negative electrode:

$$yC + xLi^+ + xe^- \underset{Discharge}{\overset{Charge}{\rightleftarrows}} Li_xC_y \quad (2.)$$

Overall:

$$LiMO_z + yC \underset{Discharge}{\overset{Charge}{\rightleftarrows}} Li_{1-x}MO_z + Li_xC_y \quad (3.)$$

Moreover, the structure of a battery is designed to support these reactions efficiently. Both the negative electrode and positive electrode include current collectors, typically made of copper foil for the negative electrode and aluminum foil for the positive electrode, which facilitate the conduction of electrons from the active materials to the external circuit. The separator also plays multiple roles — it prevents the direct short circuit between the electrodes, acts as a reservoir for the electrolyte, accommodates electrode expansion, and serves as a safety layer against Li-dendrite formation.

In summary, the charging and discharging of a lithium-ion battery are characterized by the reversible intercalation and extraction of lithium ions between the negative electrode and positive electrode, accompanied by a corresponding flow of electron through the

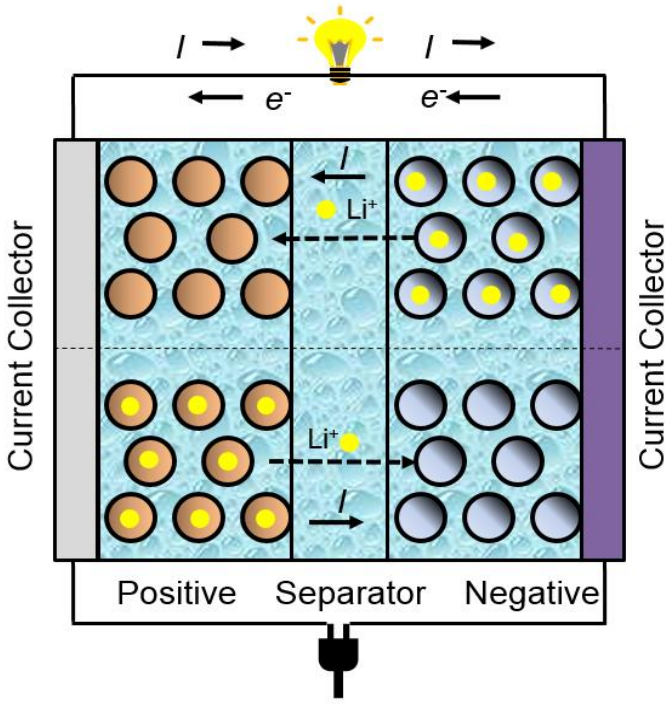

Figure 2. Schematic of a Li-ion battery during charge and discharge.

external circuit. This process is governed by redox reactions at the electrodes, facilitated by the movement of ions through the electrolyte, and controlled by the separators and current collectors.

The emergence of lithium-ion batteries has significantly contributed to the advancement of energy storage and human society, making a key technological breakthrough that powers everything from small electronics to EVs. This innovation has developed into several types, including cylindrical cells, prismatic cells, pouch cells, each with unique characteristics and applications that have profoundly impacted industry and driven forward the sustainable energy revolution.

Among the various lithium-ion battery types, as shown in Figure 3, cylindrical cells have been a staple in the industry, especially in consumer electronics and early electric vehicle models [49]. Known for their high mechanical stability and efficient heat dissipation, these batteries have been foundational for companies like Tesla. However, the cylindrical design, while mature in its manufacturing process, faces limitations in space utilization and complexity in module design. Tesla's progression from the 18650 cells to the more advanced 2170 and recently developed 4680 cells illustrates the efforts to overcome these limitations [49]. This evolution has been driven by the need for higher energy density and reduced costs, leading to significant improvements in EV range and battery performance.

In contrast to cylindrical cells, prismatic and pouch cells offer distinct advantages, primarily in terms of design flexibility and space efficiency. Prismatic cells, with their flat,

(a)

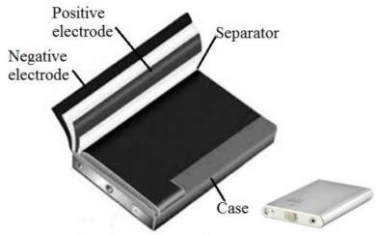

(b)

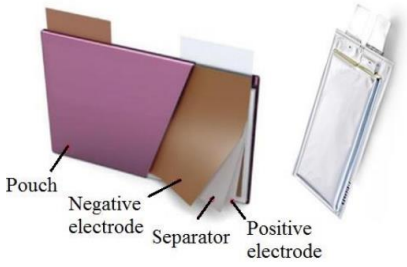

(c)

Figure 3. Configuration of different types of Li-ion batteries (a) cylindrical cell; (b) prismatic cell; (c) pouch cell.

rectangular shapes are widely used in various applications, including consumer electronics and EVs. Their compact battery design allows for improved space utilization, making them a popular choice for devices and vehicles where efficient use of space is crucial [50]. However, these cells present manufacturing challenges in terms of sealing and ensuring safety. On the other hand, pouch cells, which are enclosed in flexible pouches, allow for a variety of shapes and sizes, making them ideal for space-constrained applications [51]. They offer high energy density and efficient space usage but require complex protective structures due to their susceptibility to physical damage.

The advancements in lithium-ion battery technology, from Tesla's pioneering work with cylindrical cells to the broad adoption of prismatic and pouch cells, demonstrate the industry's relentless pursuit of innovation. These developments have far-reaching implications, enabling EVs to achieve longer ranges, enhanced reliability, and addressing critical challenges such as safety and environmental sustainability. The continuous evolution of battery technology underscores its key role in shaping a sustainable energy future and marks it as a cornerstone of the ongoing energy revolution.

Thermal runaway of Li-ion batteries

Lithium-ion batteries (LIBs) pose significant safety risks due to the potential for thermal runaway, a condition where internal battery temperatures escalate uncontrollably, leading to fires and explosions. This phenomenon results from a complex interplay of chemical and physical processes within the battery. Thermal runaway can be likened to a combustion process, where the battery contains both "fuel" and "oxidizer." It begins with an increase in internal temperature, which can trigger the decomposition of solid-

electrolyte-interphase (SEI) layer. This layer is thermally unstable and can decompose under high temperatures, leading to a series of exothermic reactions in the electrodes or electrolyte of batteries [52–54].

These reactions often involve the direct contact of lithium with the electrolyte, generating flammable substances like lithium carbonate and ethylene. As these reactions release heat, materials inside the battery, such as the electrolyte or separator, may start to break down, further exacerbating heat generation and releasing flammable gases. This creates a self-sustained chain of highly exothermic reactions [55,56]. If the resulting increase in temperature and pressure is not adequately dissipated, it can lead to structural damage to the battery, potentially causing the cell casing to rupture and the flammable electrolyte to ignite. This rapid and uncontrollable escalation can result in battery fires or explosions, posing a major concern for electronic devices and electric vehicles (EVs). Uncontrolled thermal runaway can have catastrophic consequences.

Overall, the factors that can initiate thermal runaway in lithium-ion batteries can be summarized into three main categories: mechanical abuse, electrical abuse, and thermal abuse [57]. Mechanical abuse [58] refers to physical damage that can compromise the structural integrity of batteries. This includes impacts, punctures, crushing, or any form of deformation. When a lithium-ion battery undergoes mechanical stress, it can lead to the breakdown of internal components, creating conditions that promote internal short circuits. Such shorts can rapidly increase the temperature within the cell, potentially triggering thermal runaway. For example, if a battery is dropped or punctured, the physical force can breach the separator between the anode and cathode, leading to direct contact and

subsequent heat generation. Mechanical abuse is particularly concerning in scenarios where batteries are used in harsh environments, highlighting the need for robust battery designs and protective casings.

Electrical abuse occurs when a battery is subjected to conditions outside its specified electrical operating range [58]. This includes overcharging (charging the battery beyond its maximum voltage), deep discharging (discharging the battery below its cut-off voltage), and exposure to currents exceeding its safe limits. Such conditions chemically stress the battery, leading to excessive heat generation. For instance, overcharging can cause lithium plating on the anode, creating an unstable buildup that can trigger internal shorts. Similarly, charging or discharging a battery at extreme current rates can overwhelm the battery's thermal management capabilities, rapidly elevating its temperature and risking thermal runaway. Electrical abuse underscores the importance of precise battery management systems (BMS) that monitor and control the charging and discharging processes to ensure safety.

Thermal abuse involves exposing a battery to temperatures beyond its safe operational limits [58]. At the high operating temperature, excessive heat can accelerate the degradation of battery components, disrupt the electrochemical balance, and increase the risk of thermal runaway. For instance, if a battery is situated near a heat source, the elevated ambient temperature can initiate a series of internal exothermic reactions, leading to runaway conditions. Conversely, exposure to extreme cold can also be harmful. It increases internal resistance, which can lead to localized heating during charging or discharging, creating hot spots within the battery that could trigger thermal runaway. These

events can release heat and flammable gases, leading to larger-scale thermal runaway propagation and posing direct threats to life and property.

Figure 4 [30] illustrates the interrelated nature of various abuse conditions in LIBs, highlighting how mechanical abuse can often lead to electrical abuse, and both can subsequently lead to thermal abuse. This correlation suggests that mechanical and electrical stresses can compromise the integrity of the separator of battery. Once the separator is damaged, it frequently results in an internal short circuit, triggering a series of chain reactions characterized by the rapid release of large amounts of heat, ultimately leading to thermal runaway. The susceptibility of LIBs to thermal runaway under these varied abuse conditions has become a significant concern, emphasizing the importance of addressing these safety challenges. Improving the safety of LIBs against such abusive conditions remains a priority and a key obstacle to further advancements in the technology of LIBs.

Motivation and objective

Thermal runaway in LIBs typically begins with thermal initiation at a hot spot, followed by undesired exothermic chemical reactions triggered at elevated temperatures, fundamentally positioning it as an ignition issue. Our goal is (1) to establish the safety regime of LIBs against thermal runaway through a computational approach, identifying critical heat source intensity and duration times that determine the boundary between thermal runaway and safe operational zones, (2) evaluate key kinetic features and the effects of electrode material properties on thermal runaway to understand the threshold conditions that lead to TR, and (3) quantify the heat release rate in internal short circuit (ISC) scenarios to assess its potential in triggering thermal runaway, thereby enhancing

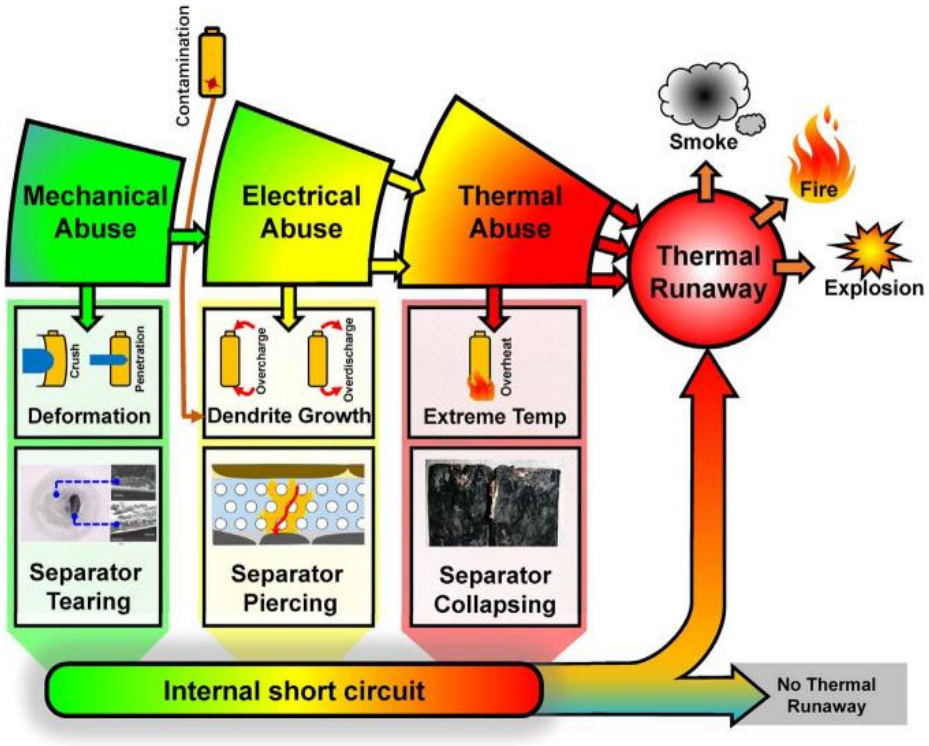

Figure 4. Abuse conditions leading to thermal runaway.

our understanding of LIBs safety and focusing on identifying the critical conditions under which thermal runaway can occur.

After investigating the initiation of thermal runaway, our focus shifted to another challenge in battery safety: thermal runaway propagation within a battery pack. This aspect is crucial for understanding how a thermal event in one hot cell can affect neighboring cells and potentially the entire battery system. A key factor in this process is radiative heat transfer, which significantly influences thermal runaway propagation within a Li-ion battery pack. We aim to develop a theoretical model based on view factor theory to predict how radiative heat impacts thermal runaway propagation. This model will consider non-linear and non-monotonic effects to thoroughly explore the impact of radiative heat on thermal runaway propagation in Li-ion battery packs, especially when exposed to adjacent heat or fire sources.

In addition, a significant challenge in understanding thermal runaway in LIBs is the cell-to-cell variability observed even among new cells with similar initial conditions. This variability, observed in thermal runaway key features such as onset temperature, heat release rate, delay time, and maximum temperature, poses challenges for accurately modeling and predicting thermal runaway behavior. Addressing this variability is crucial for cell-level safety evaluation and for understanding thermal runaway propagation in battery modules and packs.

Another crucial aspect to consider is cell degradation and its varied patterns, which significantly influence thermal runaway. Research indicates that the degradation patterns in LIBs are complex and diverse, significantly affecting the tendency towards thermal

runaway. The mechanisms of degradation include processes such as lithium plating, electrolyte decomposition, and breakdown of cathode materials. These processes significantly impact the internal resistance, thermal stability, and heat generation characteristics of the cells. For example, lithium plating can lead to dendrite formation, which may puncture the separator and induce internal short circuits, a direct cause to thermal runaway. The complexity of battery degradation, coupled with cell variability, complicates the task of accurately predicting and simulating thermal runaway in LIBs. Consequently, a comprehensive understanding of the impact of aging on Li-ion battery thermal runaway becomes essential.

Furthermore, it is important to study vent gas and aerosol emissions during thermal runaway. Understanding the type and amounts of hazardous substances released is critical for assessing health and environmental risks.

After gaining a comprehensive understanding of thermal runaway in LIBs through experiments and simulation, a critical question arises how to suspend thermal runaway while maintaining battery functionality. Our research aims to identify a based criterion as the last waring sign to stop thermal runaway and meanwhile to retain the functionality of the battery.

The primary objectives and contributions of the current work are to provide a comprehensive understanding of the thermal runaway characteristics in LIBs, emphasizing the complexity of cell variability, degradation patterns, thermal behavior, and heat transfer mechanisms. The dissertation includes experimental testing, statistical analysis, kinetic modeling, and numerical simulations to investigate these aspects in detail.

CHAPTER I

COMPUTATIONAL IDENTIFICATION OF THE SAFETY REGIME OF LI-ION BATTERY THERMAL RUNAWAY

A version of this chapter was originally published by Liwen Zhang, Peng Zhao, Meng Xu, Xia Wang:

L. Zhang, P. Zhao, M. Xu, X. Wang, "Computational identification of the safety regime of Li-ion battery thermal runaway." *Applied Energy* 261 (2020): 114440.

CRediT authorship contribution statement.

Liwen Zhang: Methodology, Software, Validation, Investigation, Data Curation, Visualization.; Peng Zhao: Conceptualization, Methodology, Formal Analysis, Visualization, Resources, Writing - Original Draft, Writing - Review & Editing, Supervision, Project Administration. Meng Xu: Methodology, Software. Xia Wang: Methodology, Resources, Writing - Review & Editing.

Abstract

Internal short circuit (ISC) and the subsequent electrochemical heat release is frequently a direct cause to trigger Li-ion battery thermal runaway. In this work, a decouple-recombine modeling approach is adopted to reveal the feature of thermal runaway induced by a typical ISC event. The thermal response and chemical kinetic feature of thermal runaway is computationally investigated in a three-dimensional configuration with assigned heat source intensity and duration. The threshold runaway state and the safety regime diagram are identified, corresponding to a pair of critical heat source intensity and critical duration time. Consequently, a safety regime diagram is computationally identified to distinguish the thermal runaway zone and safety zone. Simulation and analysis have been conducted to evaluate the dominant physical-chemical parameters, and the dependence of cathode material during thermal runaway. Meanwhile, the power dissipation during a representative

ISC scenario is analyzed, where the local current could be an order of magnitude higher than that for a regular 1 C discharge, and the maximum heat release rate is around 10^{12} W/m^3. This heat release is input as source in the thermal runaway simulation, to demonstrate the coupling of the ISC and thermal abuse models. This work provides useful guidance to the fundamental understanding and prediction of thermal runaway phenomena induced by internal short circuit in Li-ion batteries.

1. Introduction

According to a recent projection made by the US Energy Information Administration (EIA), the combined share of sales attributable to gasoline and flex-fuel vehicles declines from 93 % in 2018 to 75 % in 2050 due to the growth in battery electric vehicle (BEV), plug-in hybrid electric vehicle (PHEV), and hybrid electric vehicle (HEV) scales [59]. As an advanced power storage medium, the development of Li-ion battery has attracted extensive research interest, as reviewed in [12,60,61]. Most previous research efforts target three major fundamental challenges of Li-ion battery, i.e., low energy density, undesired irreversible change and strong dependence on temperature. Specifically, the first fundamental challenge in Li-ion battery development and implementation is its relatively low energy density compared to conventional energy sources, such as petroleum-based fuels. The specific energy of gasoline is approximately 45 MJ/Kg, while the value for the state of art Li-ion battery is around 250 Wh/Kg [61], leading to a specific energy density ratio of 50 between gasoline and battery. This partly leads to the large size of battery packs in vehicles and slow charging issue, and has become a primary driving force for the development of new battery materials and chemistry. The second challenge is induced by

the irreversible physical-chemical change such as degradation and aging [62]. The formed internal fracture or other unwanted physical structure change, e.g., Lithium-dendrite, during multiple charge-discharge cycling adds to more resistance for Li ion transfer and aggravates cycle-to-cycle and cell-to-cell variations [63] and may even cause failure and thermal runaway [64]. The third primary challenge is induced by the temperature sensitivities of Li-ion batteries. At relatively low temperatures, Li-ion batteries suffer from slow ion and charge transfer rate as well as slow electrochemistry, exhibiting high internal resistance and meanwhile aggravating the formation and growth of Li dendrite [64]. This feature intrinsically limits the cold performance of Li-ion batteries, however, it could be still improved by designing various heating protocols [65]. Under high temperature abuse or accidental conditions [66–72], undesired reactions such as Solid-Electrolyte-Interphase (SEI) decomposition, reaction between electrodes and electrolyte, and electrolyte decomposition, etc., can occur inside of the battery, leading to thermal runaway and subsequent explosion hazard [73–76]. In addition to these major challenges, the development of low-cobalt cathode material and battery recycling technology has attracted extensive interest, due to the environmental concerns from battery manufacturing and disposal.

Among these fundamental challenges and opportunities, the most urgent one is the monitor and prediction of thermal runaway, since it directly threatens properties and human lives. The mechanisms of thermal runaway are classified into mechanical abuse, electrical abuse and thermal abuse, and have been systematically reviewed in [30]. According to the survey conducted in [30], almost all reported EV accidents are associated with fire caused

by thermal runaway, mostly likely, triggered by short circuit. The first and mostly adopted thermal runaway model of Li-ion batteries was developed by Hatchard et al. [73], where kinetic parameters of chemical reactions between electrodes and electrolyte were measured and calibrated from accelerating rate calorimetry (ARC) and differential scanning calorimeter (DSC), and the model results fit well with the oven exposure test for 18650 $LiCoO_2$/graphite cell. Later, Spotnitz et al. [74] did a more systematic review of thermal behavior of components in Lithium-ion battery and a more complete set of exothermic reactions including the reaction of electrolyte decomposition. Based on these understanding, Kim et al. [75] developed a thermal abuse model and applied it to a 3D Li-ion battery configuration, further accounting for cell geometry and anisotropy of material thermal properties and successfully demonstrated the multidimensional behaviors of Li-ion battery thermal runaway. Since then, this thermal abuse model and simulation approach has been adopted in various studies related to Li-ion battery thermal runaway [38,77–84]. These studies, for instance, include the influence of different material properties [77], the effectiveness of cooling system on runaway and propagation prevention [78] as well as thermal runaway under different experimental conditions such as constant-power heating test [79], overcharge [38], nail penetration [80] and internal short circuit [81]. Submodels including battery aging and other factors have also been developed [85] and combined with this thermal abuse model. Although Li-ion battery thermal runaway is largely cell and material dependent, there are intrinsic common features rooted in this class of phenomena, in that it is always thermally initiated by a hot spot, followed by undesired exothermic chemical reactions triggered at elevated temperatures. Therefore, Li-ion battery thermal

runaway is intrinsically an ignition problem. With the widely adopted and validated models for thermal runaway and the electrochemistry, the goal of the current work is to answer three of the most critical questions regarding thermal runaway and ISC of Li-ion batteries: (1) What is the threshold condition, i.e., power density (in W/m^3) and duration, for a hot spot to trigger Li-ion thermal runaway? (2) What are the chemical kinetic features and key parameters during thermal runaway? (3) For a typical ISC scenario, how large is the heat release rate, and will it be sufficient to trigger thermal runaway?

2. Configuration and modeling methodology

2.1 Configuration

As shown in Figure 5(a), a 3D box configuration with a cylinder region is adopted to represent a prismatic battery with nail penetration for the thermal runaway modeling part. The dimensions of the domain are 180 mm (height) × 130 mm (width) × 50 mm (depth) [78]. A cylindrical region of 1.5 mm (radius) × 40 mm (length) is placed perpendicular to the left surface. In this configuration, thermal runaway is triggered by two dominants physical–chemical processes: heat transfer from the cylindrical region with an artificially assigned uniform heat source intensity Q (W/m^3) and duration time dt (s), and the runaway chemical kinetics involving the electrodes and electrolyte that contribute to heat generation within the bulk of battery.

The energy conservation equation of the computational domain is shown in the following:

$$\frac{\partial\left(\rho c_p T\right)}{\partial t} = \nabla \cdot (k \nabla T) + S \qquad (4.)$$

where ρ is the density, c_p is the heat capacity, k is the thermal conductivity, T is temperature. In the main computational domain within the cell, $S = S_{sei} + S_{ne} + S_{pe} + S_e$, the meaning of these heat source terms related to thermal runaway is explained in Sec. 2.2. Given the much larger size of the battery compared to a single layer of cathode-separator-anode, the thermal runaway reactions are assumed to be uniformly distributed within the cell. While in the cylindrical region, we have $S = \begin{cases} Q & if\ t < dt \\ 0 & if\ t \geq dt \end{cases}$, representing a uniform heat source lasting a certain duration time. Due to the multi-layered structure of the Li-ion battery, the anisotropic thermal conductivity of the battery (through-plane and in-plane) is considered. The values of thermal properties of a typical $LiCoO_2$/graphite battery are listed in Appendix Table 1 [78].

To understand the actual heat generation rate (in W/m^3) from a typical internal short circuit (ISC) event, a 2D unit cell model is developed for thermal-electrochemical modeling, including copper negative current collector, a porous negative electrode (typically made of graphite), an ion-conductive but electron-insulating separator, a porous positive electrode made of Li and transition metal oxide, aluminum positive current collector and a piece of Aluminum metal directly connecting two electrodes. The structure and thickness of each layer is shown in Figure 5(b). A liquid electrolyte permeates the electrodes and separator region. The solid-phase in electrodes is described by a lattice of spherical particles with uniform size, representing the intercalation center for metallic Li diffusion. During a typical discharging process, metallic Li is deintercalated out of the anode. An equal amount of Li ion and electrons are generated at the electrode-electrolyte interface of each spherical particle. These Li ions are transferred through the electrolyte,

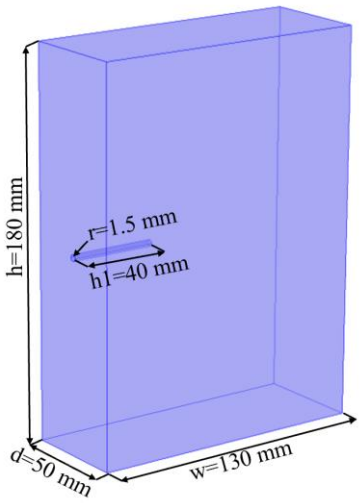

(a)

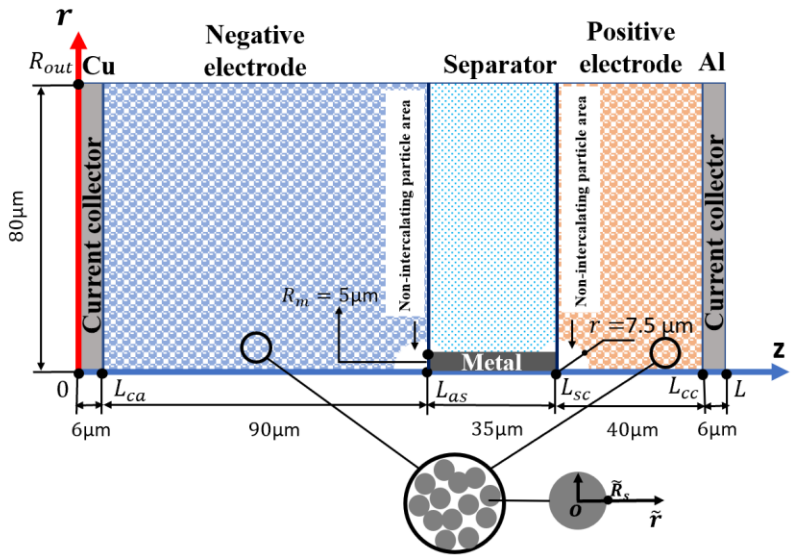

(b)

Figure 5. (a) a 3D configuration of a prismatic cell for the simulation of thermal runaway, including a cylindrical region representing nail penetration; (b) a 2D unit cell model with metal penetrating the separator for internal short circuit modeling.

across the separator, to the cathode; while the electrons migrate through the external circuit and back to the positive current collector, and eventually recombine with these Li ions. Consequently, these metallic Li atoms eventually intercalate into each solid spherical particle. By design, electrons are not allowed to penetrate the separator and are forced to go through the external circuit under this normal discharging condition. For simplicity, ISC in the current work is triggered by a piece of Aluminum that directly connects the positive and negative electrodes, which creates an alternative path for the migration of electrons within the battery.

The mass and charge conservation equations, energy conservation and the electrochemical kinetics given by Bulter-Volmer equation are solved together following the configuration in Figure 5 (b), subject to properly given boundary conditions. More details on ISC thermal electrochemical modeling are provided in Sec. 2.3. The power dissipation density (in W/m^3) is then calculated to measure rate of energy dissipation and heat release from the electrochemical system to the thermal system.

2.2 Thermal runaway modeling

The thermal runaway models demonstrated in [73–76] are briefly reviewed and adopted in the current study. Solid electrolyte interface (SEI) formed during the first cycle in Li-ion batteries plays a vital role in preventing the side reaction between the electrodes and electrolyte. This layer is metastable and can decompose exothermically at elevated temperature. The corresponding reaction can be expressed in the following equations:

$$S_{sei}(T, c_{sei}) = -H_{sei} W_c \frac{dc_{sei}}{dt} \tag{5.}$$

$$\frac{dc_{sei}}{dt} = -A_{sei} exp\left[-\frac{E_{a,sei}}{RT}\right] c_{sei}^{m_{sei}} \quad (6.)$$

where $S_{sei}(T, c_{sei})$ is the heat release rate from the SEI decomposition, which depends on the dimensionless amount of lithium-containing meta-stable species (c_{sei}) in the SEI, the temperature of the battery (T) and the battery material.

Once the SEI layer starts to decompose, it cannot protect the negative electrode from contacting with the electrolyte such that the exothermic reaction between the intercalated lithium and electrolyte can occur:

$$S_{ne}(T,\ c_{ne},\ t_{sei}) = -H_{ne} W_c \frac{dc_{ne}}{dt} \quad (7.)$$

$$\frac{dc_{ne}}{dt} = -A_{ne} exp\left[-\frac{t_{sei}}{t_{sei,ref}}\right] c_{ne}^{m_{ne,n}} exp\left[-\frac{E_{a,ne}}{RT}\right] \quad (8.)$$

$$\frac{dt_{sei}}{dt} = A_{ne} exp\left[-\frac{t_{sei}}{t_{sei,ref}}\right] c_{neg}^{m_{ne,n}} exp\left[-\frac{E_{a,ne}}{RT}\right] \quad (9.)$$

where $S_{ne}(T, c_{ne}, t_{sei})$ is the heat release rate from the negative-electrolyte reaction. It depends on the dimensionless amount of lithium intercalated within the carbon (c_{ne}), the dimensionless measure of SEI layer thickness (t_{sei}), the temperature of the battery (T) and other material properties.

At oxidized state, the positive material reacts directly with the electrolyte. The chemical reduction of the positive active material with the electrolyte is highly exothermic:

$$S_{pe}(T,\ \alpha) = H_{pe} W_p \frac{d\alpha}{dt} \quad (10.)$$

$$\frac{d\alpha}{dt} = A_{pe} \alpha^{m_{pe,p1}} (1-\alpha)^{m_{pe,p2}} exp\left[-\frac{E_{a,pe}}{RT}\right] \quad (11.)$$

where $S_{pe}(T, \alpha)$ is the heat release rate from the positive electrode-electrolyte reaction. It

depends on the degree of conversion (α), the temperature of the battery (T) and the material properties of the battery.

Eventually, the electrolyte can also decompose exothermically at elevated temperatures:

$$S_e(T,\ c_e) = -H_e W_e \frac{dc_e}{dt} \tag{12.}$$

$$\frac{dc_e}{dt} = -A_e c_e^{m_e} exp\left[-\frac{E_{a,e}}{RT}\right] \tag{13.}$$

where $S_e(T, c_e)$ is the heat release rate from the electrolyte decomposition, depending on the dimensionless concentration of electrolyte (c_e), the temperature of the battery (T), and the materials properties of the battery.

Depending on the battery materials, parameters involved in this thermal runaway model could be calibrated using ARC, DSC and TGA analysis, such that the model exhibits satisfactory predictability for thermal runaway behavior. A detailed nomenclature including parameter values for a typical $LiCoO_2$/graphite battery is listed in Appendix Table 2 [73,75,76,78]. It is also worth noting that since we are interested in very fast runaway process (with delay time around 10 s), during which the cooling design on the surface of a battery can hardly be effective, the thermal boundary conditions are hence intentionally set as adiabatic. Such simplification can also help to rule out the uncertainty of threshold ignition energy induced by the ambiguity in boundary conditions, as shown in the following sections.

2.3 A 2D Thermal-electrochemical model of internal short circuit

The thermal-electrochemical model adopted in the current ISC simulation is based on previous studies [86–98]. Five conservation equations are solved together, linked by the constitution relation of the electrochemistry Bulter-Volmer equation. These equations include: (1) Metallic Li mass conservation in the solid phase; (2) Li ion mass conservation in the liquid phase; (3) the electron charge conservation in the solid phase; (4) the Li ion charge conservation in the liquid phase; (5) Energy conservation equation describing temperature evolution. Based on the current 2D cylindrical configuration for ISC with metal penetration as in Figure 5(b), a detailed introduction to the thermal-electrochemical model and its boundary conditions is given below.

2.3.1 Mass conservation of lithium in the solid phase

The solid phase in the electrodes is modeled as a lattice of spherical particles with uniform size. Within each particle, the intercalation and deintercalation of Li atom follows Fick's law of diffusion in polar coordinates:

$$\frac{\partial c_s}{\partial t} = \frac{D_s}{\tilde{r}^2}\frac{\partial}{\partial \tilde{r}}\left(\tilde{r}^2 \frac{\partial c_s}{\partial \tilde{r}}\right) \tag{14.}$$

where c_s is the concentration of lithium in the active material particles of electrode, $\tilde{r}$ is the radial coordinate, D_s is the solid phase diffusivity of Li atom.

At the center of the particle, zero flux is specified from symmetry, while the species flux in and out the particle surface is related to the local current density:

$$\frac{\partial c_s}{\partial \tilde{r}}|_{\tilde{r}=0} = 0 \tag{15.}$$

$$-D_s \frac{\partial c_s}{\partial \tilde{r}}|_{\tilde{r}=\tilde{R}_s} = \frac{i_{loc}}{F} \tag{16.}$$

2.3.2 Mass conservation of lithium ions in the electrolyte phase

The transport of lithium ions in the electrolyte phase follows Fick's diffusion law and the electromigration:

$$\frac{\partial c_l \varepsilon_l}{\partial t} = \nabla \cdot (D_{l,eff} \nabla c_l) + a_s \frac{(1 - t_+)}{F} i_{loc} \quad (17.)$$

where c_l is the lithium ion concentration in the electrolyte, ε_l is the volume fraction of the electrolyte phase, a_s is the specific interfacial area, i_{loc} is the electrode current density, t_+ is the transference number of lithium ions, $D_{l,eff}$ is the effective diffusion coefficient given by the Bruggeman relation:

$$D_{l,eff} = D_l {\varepsilon_l}^{1.5} \quad (18.)$$

Zero flux boundary conditions are set at the interface with current collectors, metal surface and the outer radial surface due to no ion penetration [90,92]. Zero flux boundary conditions are also given along the axis with r = 0 from symmetry. These boundary conditions are listed below:

$$\frac{\partial c_l}{\partial r}|_{r=0} = 0 \quad (19.)$$

$$\frac{\partial c_l}{\partial r}|_{r=R_{out}} = 0 \ \ (L_{ca} < z < L_{cc}) \quad (20.)$$

$$\frac{\partial c_l}{\partial z}|_{z=L_{as}} = \frac{\partial c_l}{\partial z}|_{z=L_{sc}} = 0 \ \ (0 < r < R_m) \quad (21.)$$

$$\frac{\partial c_l}{\partial z}|_{z=L_{ca}} = \frac{\partial c_l}{\partial z}|_{z=L_{cc}} = 0 \quad (22.)$$

$$\frac{\partial c_l}{\partial r}|_{r=R_m} = 0 \ \ (L_{as} < z < L_{sc}) \quad (23.)$$

2.3.3 Charge conservation in the solid phase of electrodes

Charge in the solid phase is contributed by electrons. The governing equation for the electrical charge balance in the electrodes is described by:

$$\nabla \cdot i_s = -a_s i_{loc} \tag{24.}$$

where a_s is the specific interfacial area which characterizes electrode performance:

$$a_s = \frac{3\varepsilon_s}{\tilde{R}_s} \tag{25.}$$

i_s is the electrical current density in the solid phase as described by ohm's law:

$$i_s = -\sigma_{s,eff} \nabla \phi_s \tag{26.}$$

where ϕ_s is the solid phase potential, $\sigma_{s,eff}$ is the effective solid-phase electrical conductivity, depending on the electrical conductivity of the bulk material and the porosity, following the Bruggeman relation:

$$\sigma_{s,eff} = \sigma_s {\varepsilon_s}^{1.5} \tag{27.}$$

At the solid-electrolyte interface (SEI) (excluding interface with the metal), zero electrical current boundary condition is specified:

$$\frac{\partial \phi_s}{\partial z}|_{z=L_{as}} = \frac{\partial \phi_s}{\partial z}|_{z=L_{sc}} = 0 \ (R_m < r < R_{out}) \tag{28.}$$

Symmetry boundary is applied for solid-phase potential along the axis of $r = 0$, and insulation boundary condition is applied on the outer radial surface of solid-phase in the electrodes:

$$\frac{\partial \phi_s}{\partial r}|_{r=0} = 0 \tag{29.}$$

$$\frac{\partial \phi_s}{\partial r}|_{r=R_{out}} = 0 \ (L_{ca} < z < L_{cc}) \tag{30.}$$

2.3.4 Charge conservation in the electrolyte

Current in the electrolyte is contributed by the migration and diffusion of Li ions. Transport of lithium ions in the electrolyte can be described by the balance equation for ionic current density i_l:

$$\nabla \cdot i_l = a_s i_{loc} \tag{31.}$$

$$i_l = -\kappa_{l,eff} \nabla \phi_l + \left(\frac{2\kappa_{l,eff} RT}{F}\right)\left(1 + \frac{\partial ln f_{\pm}}{\partial ln c_l}\right)(1 - t_+)\nabla ln c_l \tag{32.}$$

where ϕ_l is the potential in the liquid phase, $f_{\pm}$ is the average molar activity coefficient, $\kappa_{l,eff}$ is the effective ionic conductivity in the electrolyte:

$$\kappa_{l,eff} = \kappa_l {\varepsilon_l}^{1.5} \tag{33.}$$

Along the axis $r = 0$, symmetric boundary condition is again assigned for ϕ_l. At the interface of current collector and electrode and the outer axial surface of the electrodes and separator, zero flux boundary condition for ionic current is specified due to non-ion penetration:

$$\frac{\partial \phi_l}{\partial r}|_{r=0} = 0 \tag{34.}$$

$$\frac{\partial \phi_l}{\partial z}|_{z=L_{ca}} = \frac{\partial \phi_l}{\partial z}|_{z=L_{cc}} = 0 \tag{35.}$$

$$\frac{\partial \phi_l}{\partial r}|_{r=R_{out}} = 0 \ (L_{ca} < z < L_{cc}) \tag{36.}$$

2.3.5 Electrochemical kinetics

To bring a closure to this model, a constitution relation that correlates the current density with overpotential is needed. The electrode current density is given by Butler-Volmer equation:

$$i_{loc} = i_0 \left\{ exp\left(\frac{\alpha_a F\eta}{RT}\right) - exp\left(\frac{-\alpha_c F\eta}{RT}\right) \right\} \quad (37.)$$

where i_0 is the exchange current density, α_c denotes the cathodic charge transfer coefficient and α_a denotes the anodic charge transfer coefficient. These two coefficients are equal to each other [99]. η is the activation over potential, *F* is the Faraday constant, *R* is the universal gas constant.

The exchange current density is calculated by:

$$i_0 = F k_0 (c_l)^{\alpha_a} \left(c_{s,max} - c_s\right)^{\alpha_a} (c_s)^{\alpha_c} \quad (38.)$$

where k_0 is a rate constant, $c_{s,max}$ is the maximum solid-phase Li concentration, the activation over potential η is defined as the potential difference between the operating voltage and the thermodynamic equilibrium potential U_{eq}:

$$\eta = \phi_s - \phi_l - U_{eq} \quad (39.)$$

where the equilibrium potential U_{eq} is a function of both the state of charge and temperature:

$$U_{eq} = U_{eq,i} + \frac{\partial U_{eq,i}}{\partial T}\left(T - T_{ref}\right) \quad (40.)$$

The state of charge could be determined by the relative portion of Li in the electrodes. For example, in a LCO battery with positive electrode Li_xCoO_2 and negative electrode Li_yC_6, $U_{eq,i}$ and $\frac{\partial U_{eq,i}}{\partial T}$ for both electrodes can be provided as functions of Li stoichiometric ratios *x* or *y*, as discussed in[100,101].

2.3.6 Energy conservation

In general, ignoring the internal contact resistance, internal heat generation of a Li ion battery comes from three sources: (1) heat generation due to entropy changes in the

material structure during charging and discharging, which is frequently referred to as the reversible entropic heat $q_{rev} = a_s i_{loc} T \frac{\partial U_{eq}}{\partial T}$; (2) heat generation from irreversible electrochemical reactions, as manifested by the reaction current and overpotential $q_{irr} = a_s i_{loc} \eta$; (3) heat generation from electron conduction in the solid phase, and the migration and diffusion of Li ion in the electrolyte, which is referred to as ohmic heat q_{ohm}. Here, accounting for the heat generation from reversible entropic heat q_{rev}, irreversible reaction heat q_{irr} and ohmic heat q_{ohm}, the energy conservation is:

$$\rho C_p \frac{\partial T}{\partial t} = \lambda \nabla^2 T + q_{rev} + q_{irr} + q_{ohm} \quad (41.)$$

The ohmic heat consists of three terms: electrical ohmic heat $q_{ohm,s}$, ionic ohmic heat $q_{ohm,l}$ and internal short circuit heat $q_{ohm,m}$ in the metal or current collector, that gives:

$$\begin{aligned} q_{ohm} &= q_{ohm,s} + q_{ohm,l} + q_{ohm,m} \\ &= -i_s \cdot \nabla \phi_s - i_l \cdot \nabla \phi_l - i_m \cdot \nabla \phi_m \end{aligned} \quad (42.)$$

Adiabatic boundary conditions are applied to all the boundaries in Figure 5(b).

2.3.7 Governing equations in metal, current collector and non-intercalating particle area

The governing equation for the electrical charge balance in the metal or current collector is described by:

$$\nabla \cdot i_m = 0 \quad (43.)$$

where i_m is the electrical current density in the solid metal phase. The electron transfer in the solid metal phase is described by ohm's law:

$$i_m = -\sigma_m \nabla \phi_m \quad (44.)$$

where σ_m is the metal electrical conductivity, and ϕ_m is the potential in the metal.

At the interfaces of current collector-electrode, metal-electrode and metal-separator, due to the electron-conduction and ion-insulation feature, zero flux of ionic current conditions are satisfied to ensure the consistency in the electronic charge flux. It is worth noting that a quarter-circle non-intercalating particle region is assigned at each end of the metal to ensure the consistency of non-ion penetration condition approaching the metal surface. Compared to regular solid-phase, the only difference in this non-intercalating particle region is that while the solid phase is still electron conductive, Li ions are not allowed to enter this region. Therefore, this non-intercalating region is considered similar to metal or current collector as an electron conductor, such that the only governing equation is electron charge conservation.

The boundary conditions at the current collectors are related to the flux of charge in and out of the electrode. At the current collector, insulation is specified for electrical current in solid phase [86,88,92]:

$$\frac{\partial \phi_s}{\partial z}|_{z=0} = \frac{\partial \phi_s}{\partial z}|_{z=L} = 0 \qquad (45.)$$

The negative electrode terminal is grounded, the positive electrode terminal is the cell voltage corresponding to SOC = 100 % and the rest of the outer axial boundaries are set to be electrically insulated:

$$\phi_s|_{r=R_{out}} = 0V, if\ 0 < z < L_{ca} \qquad (46.)$$

$$\phi_s|_{r=R_{out}} = 4.3V, if\ L_{cc} < z < L \qquad (47.)$$

2.4 Numerical methods

Both thermal runaway and ISC cases are solved by commercial software COMSOL Multiphysics 5.3. In the thermal runaway simulation, a domain Ordinary differential equation (ODE) model is used to account for the heat generation due to the chemical reactions. The fastness of the chemical reactions could place substantial difficulty on the usage of explicit Computational fluid dynamics (CFD) solvers and requires tiny integration time step, which is frequently referred as the chemical stiffness [102]. Therefore, we choose the backward differentiation formula (BDF) method to set as the time stepping method, one of the available implicit time-dependent solvers, with the maximum BDF order of 5 and minimum BDF order of 2. The relative tolerance and absolute error tolerance are set as 1E-6 and 1E-8 respectively. In the ISC simulation, we choose time-dependent solver using BDF for time marching, with the maximum BDF order of 2 and minimum BDF order of 1.

Grid independence study has been conducted for both scenarios by using three different mesh specifications, varying from sparse to dense. As shown in Appendix Figure 13 and Figure 14, the maximum temperature evolution during thermal runaway, and the average power dissipation during ISC event using meshes with different levels of refinement exhibits negligible difference, we have hence demonstrated the meshes adopted are sufficient for simulation.

2.5 Model validation

Both the thermal runaway and thermal-electrochemical models are extensively validated against literature reported experimental data, and all the comparisons are further

supplied as Figure 15 to Figure 19 in Appendix. Specifically, the thermal runaway model is validated against experimental targets acquired in oven exposure tests under iso-thermal [78], constant heating rate [70] , and near adiabatic conditions [70]. The thermal-electrochemical model is validated against experimental data including surface temperature under constant discharging rate [103], temperature and battery voltage measurement at different discharging rates [100,104]. These data also cover all different battery materials and chemistry involved in the current work, and all comparisons show very good quantitative agreement as such provide great confidence in the simulation results. It is also noted that although more detailed thermal runaway models have been developed recently based on thermal calorimetry measurement [70], the model we adopted is so far the most widely-used one and is being applied in battery research until very recently [76]. To make sure the conclusion is not affected by the difference in the thermal runaway models, we have used our model and parameters to simulate the same two sets of oven tests in [70] and compared with their simulation. As shown in Appendix Figure 16(a) and Figure 16(b), the current model has quantitative agreement with the detailed simulation and the oven test data. This adds to great confidence to the current model for the prediction of thermal runaway onset condition, and confirms that the concepts and conclusions will not change with changes in cell chemistry.

3. Results and discussion

3.1 Critical state and safety regime of thermal runaway

Thermal runaway of Li-ion battery has become a major concern of societal safety. Fundamentally, it is also a problem featured by reaction-transport coupling, similar to the

combustion process. One of the key combustion concepts is the minimum ignition energy [105], which characterizes the critical amount of energy needed to successfully trigger a flame in a reactive mixture by an ignition kernel. Made of explosive materials, Li-ion batteries tend to ignite and explode when an internal heat source is beyond a certain threshold. Hence, to understand and predict the safety regime of a Li-ion battery, we ask the same question on Li-ion batteries based on the concept of minimum ignition energy: What is the critical power needed to trigger thermal runaway by a hot spot? To capture the critical condition that can trigger thermal runaway in the delay time of interest, different combinations for heat source intensity (Q) and duration time (dt) in the cylindrical region have been applied in the configuration shown in Figure 5(a). Figure 6(a) compares the maximum temperatures for four different heat source intensities and durations, to demonstrate the phenomena of thermal runaway. For the base Case 1 with Q = 1.18E9 W/m^3 and duration time dt = 14 s, the maximum temperature gradually increases in the initial period and then sharply rises and achieves ignition right before 14 s. The substantial heat release rate and fast temperature rise indicates thermal runaway. Starting from this benchmark Case 1, by reducing either the duration time of heat source to dt = 13 s (Case 2) or the heat source intensity to Q = 1.17E9 W/m^3 (Case 3), the maximum temperature reaches a local maximum and decays due to heat conduction. Consequently, no thermal runaway phenomenon has been observed for these two cases. The sensitive dependence of runaway events on the heat source intensity and duration time has allowed us to identify the critical runaway state. Such a critical state corresponds to a pair of critical heat source intensity and duration time, below which thermal runaway cannot occur. Typically, a

combined thermal-chemical mechanism is adopted to explain phenomena of ignition and explosion nature [106], where positive feedback exists between the temperature rise and the rate of major exothermic reactions in a system. The next question is then: what are the thermal and chemical effects from the runaway reactions during a typical runway event? We have therefore conducted simulation with another Case 4, with the same heat source intensity and duration time as Case 1, yet without the thermal runaway chemical source terms. Clearly, deviation between Case 1 and Case 4 does not appear until about 6 s, indicating the negligible role of heat release from thermal runaway chemistry during this period. By combining the information shown later in Figure 8, the negligible thermal effect from SEI decomposition in this period is hence identified. After that, the maximum temperature of Case 1 starts to build up, as induced by runaway exothermic reactions.

By calculating the critical runaway states with different combinations of threshold heat source intensity and duration time, we have successfully identified a safety regime diagram for Li-ion batteries, as shown in Figure 6(b). Below this curve, a hot spot either does not contain sufficient power or does not last for sufficient residence time, thermal runaway cannot be triggered; while above the curve, ignition occurs due to elevated hot spot intensity and/or extended duration. This curve is fitted to a power law form as Q = 6E9 $dt^{-0.758}$ W/m^{3}dt (Q in W/m3 and dt in s). With shorter duration, the critical Q is more sensitive to dt; while for longer duration time, such dependence becomes less and less sensitive. This formula can provide useful guidance for battery safety prediction and control. As shall be discussed later, this safety regime depends on battery materials, the hot spot size and potentially cooling conditions for sufficiently long ignition delays. The

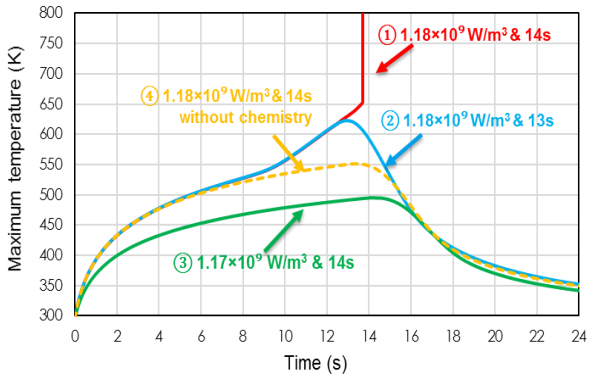

(a)

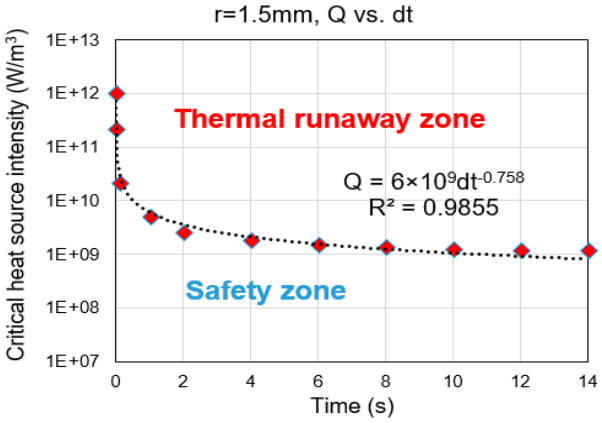

(b)

Figure 6. (a) comparison of maximum temperature history of runaway and non-runway cases, demonstrating the concept of critical runaway state. (b) Safety regime of a $LiCoO_2$/Graphite battery shown by critical heat source intensity and duration, with heat source radius 1.5 mm.

concept of critical runaway state and the computational methodology we have developed is however general, and could be extended to arbitrary Li-ion batteries.

To further understand the geometric effect of the heat source, simulations have been conducted for different heat source radius with fixed heat source intensity (Q = 1.18E9 W/m^3) and duration (dt = 14 s) as Case 1 in Figure 6(a). As seen in Figure 7, compared to the base case with radius of 1.5 mm, the delay time of thermal runaway is substantially decreased to about 4 s, a 71.4 % relative change, when the hot spot radius is increased to 2 mm by 33.3 %. On the other hand, with a sufficiently small radius of the heat source, thermal runaway does not occur at all, as in the case of radius 1 mm in Figure 7(a). The results are reasonable because the interface of the heat source plays a crucial role in heat transfer, and a larger radius indicates a larger surface area which can create a broader high temperature region for thermal runaway reactions to occur. With fixed dt = 14 s, the critical heat source intensity needed to trigger thermal runaway is shown in Figure 7(b). A monotonic decreasing trend is observed, where the threshold heat source intensity is less and less sensitive to hot spot size with increasing radius. A power law fitting formula has been obtained for the current $LiCoO_2$/graphite battery, showing $Q = 2E5r^{-1.32}$.

3.2 Chemical kinetic feature and key parameters during thermal runaway

To gain insights into the chemical reaction most relevant to thermal runaway, we have compared the evolution of the dimensionless concentrations and other parameters for two cases with the same heat source Q = 1.18E9 W/m^3, but different duration time dt. Consequently, the case with dt = 14 s is the same as Case 1 in Figure 6(a), and thermal runaway is triggered; while the other case with dt = 12 s belongs to the safe regime below

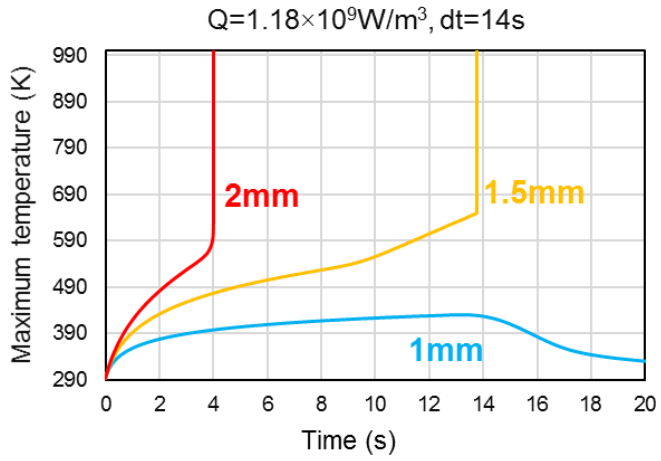

(a)

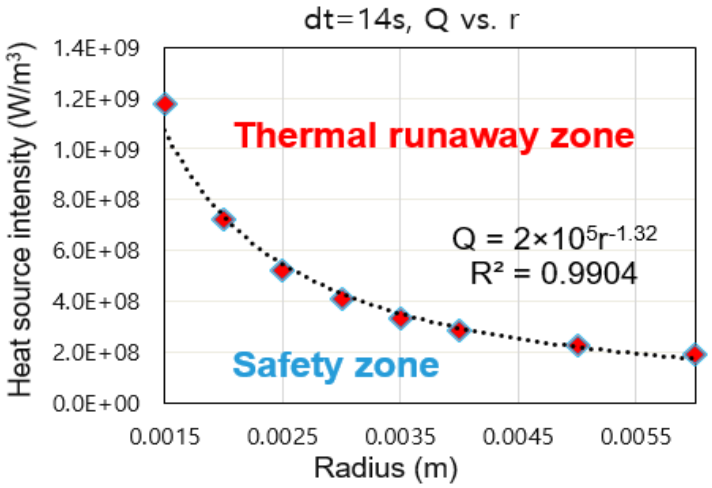

(b)

Figure 7. (a) evolution of maximum temperature for the heat source with same intensities and durations but different radius; (b) safety regime of a $LiCoO_2$/Graphite battery shown by critical heat source intensity and heat source radius, with fixed heat source duration 14 s.

the threshold limit, and hence does not trigger thermal runaway. As shown in Figure 8(a), the only kinetic difference between the runaway and non-runaway cases appears in the profiles of the dimensionless amount of lithium intercalated in the negative electrode (c_{ne}) and the dimensionless measure of SEI layer thickness (t_{sei}), while the evolution of the rest dimensionless parameters overlaps. According to Equation. (7.) - Equation. (9.), these differences will directly affect the heat release term S_{ne}, the reaction between the electrolyte and negative electrode, as shown in Figure 8(b). Different from the other three reactions with a single peak, the heat release profile of negative electrode – electrolyte reaction has a broad, plateau-shape evolution profile and can last very long. The occurrence of thermal runaway is directly induced by the larger heat release from negative electrode-electrolyte reaction right before runaway occurs. It is also seen that the sequence of the four runaway reactions follow the order of SEI decomposition (SEI-D), negative electrode-electrolyte reaction (NE), positive electrode-electrolyte reaction (PE) and eventually electrolyte decomposition (ED). This order is also consistent with the understanding of battery stability and aging. It is generally considered that the SEI on the anode is more unstable due to the evident reduction reactions and the larger volume expansion of anode materials, compared to the SEI on the cathode [107,108].

To further identify the key thermal-chemical-physical parameter in affecting thermal runaway, we have conducted sensitivity analysis and calculated the dimensionless sensitivity, as defined by: $\frac{\partial ln\tau}{\partial ln\chi}$, where τ is the ignition delay time for thermal runaway, defined as the duration from the starting point to the instant when the maximum temperature rise rate occurs, χ is any parameter of interest in the thermal runaway model,

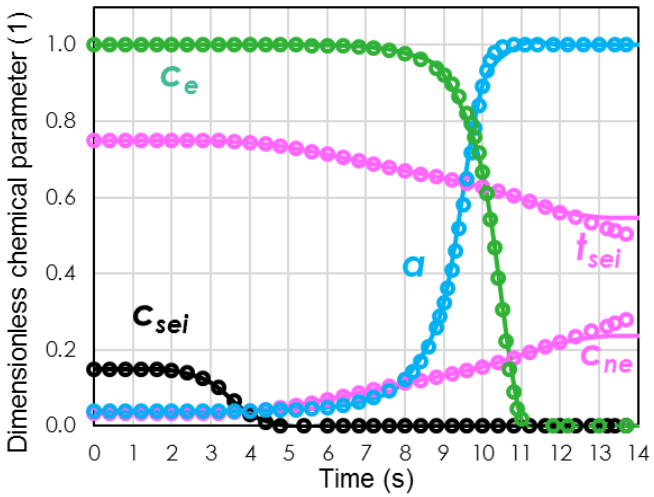

(a)

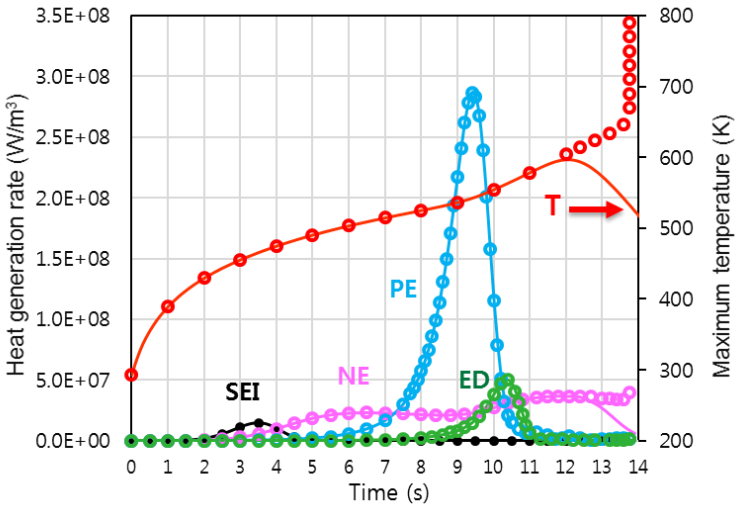

(b)

Figure 8. Comparison of chemical kinetic feature of runway (symbol) and non-runway (solid line) cases (a) evolution of the dimensionless concentrations in different thermal runaway reactions for a randomly selected point close to the interface; (b) evolution of heat generation rate from each chemical reaction.

such as the reaction rate, density, and conductivity. This normalized sensitivity is defined in such a way that it does not have a dimension, and hence it helps to equally evaluate the significance of all the parameters involved in the model. When calculating the sensitivity, the same computation is repeated by only perturbing the parameter of interest by 5 % while holding the values fixed for the other parameters. Consequently, this method is also referred to as the trial-and-error approach. For example, a normalized sensitivity of −3 means −15 % of change in τ is expected if the target parameter is increased by 5 %. The normalized sensitivity has been conducted for the frequency factors and activation energies in Equations. (5.), (7.), (10.), (12.), cell density, heat capacity, heat conductivity in and through plane, as shown in Figure 9(a) and Figure 9(b). For the chemical reactions, the rate of positive electrode-electrolyte reaction plays the most important role in affecting the delay time for thermal runaway. Regarding thermal physical parameters, the selected parameters exhibit similar value of normalized sensitivity and hence play similar roles in affecting the delay time. These calculations provide useful guidance on the usage and optimization of the thermal runaway model for validation purposes.

3.3 Material effects of thermal runaway

Extensive research has been conducted looking for high density, stable, cheap and environment benign Li-ion battery materials. The thermal runaway model adopted in the current study has been validated against battery experiments of different electrode materials. Three batteries with unique thermal-chemical parameters are selected from the literature. As shown in Table 3 in Appendix, Battery 1 and 3 are both $LiCoO_2$/Graphite, while Battery 2 is NMC based. The runaway kinetic parameters of 1 and 3 are the same (as

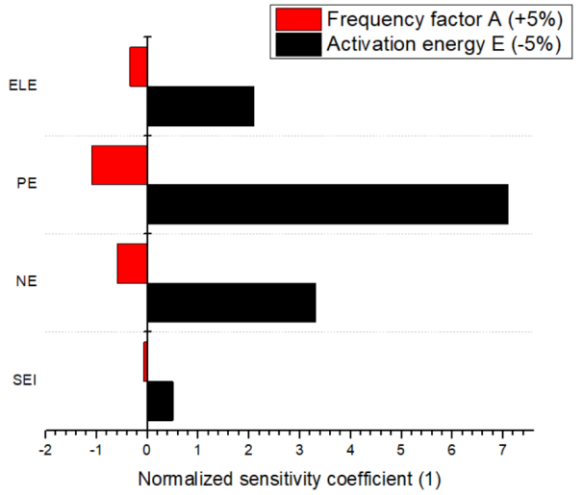

(a)

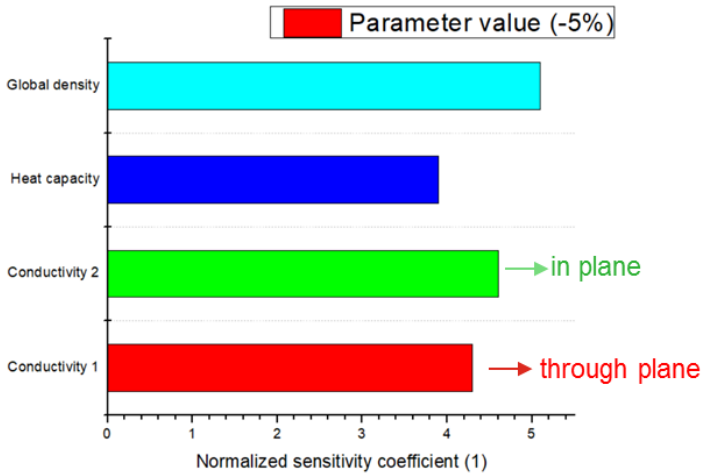

(b)

Figure 9. Identification of key thermal runaway parameters using the model (a) normalized sensitivity coefficients of chemical kinetic parameters including reaction rate constant and activation energy; (b) normalized sensitivity coefficients of thermal physical parameters including density, specific heat capacity and conductivity.

shown in Appendix Table 2), however, their thermal conductivities are very different, according to measured data. As in Table 3, compared to Battery 1, thermal conductivity in and through plane is higher by 36.8 % and 228.5 % for Battery 3, respectively. This leads to a much broader safety region of Battery 3, as shown in Figure 10. For the NMC Battery 2 (detailed runaway data provided in Appendix Table 4), whose activation energy of anode-electrolyte is higher by 10.3 %, a broader safety region is also observed from Figure 10. Although conductivity in plane for Battery 2 is lower by 15.5 % compared to LCO Battery 1, which is expected to narrow its safety regime, such an effect is however reversed by that from the elevated activation energy. The results have demonstrated the feasibility of predicting and comparing the safety region of different Li ion batteries. Concerns on accurate measure of battery thermal properties are also raised, which can substantially affect the safety evaluation of different battery materials.

3.4 Heat release during an open-circuit internal short event

So far, the concepts of critical states and the regime of thermal runaway of different Li-ion batteries have been demonstrated, using artificially assigned heat source intensity and duration. In reality, an initial hot spot is most likely to be caused by heat release from electrochemical reactions in an ISC event. The question to be raised is therefore: how large is the heat release rate in a typical ISC scenario, and will it be sufficient to trigger thermal runaway? Based on the ISC configuration in Figure 5(b) and the thermal-electrochemical model as described in Sec. 2, distribution and evolution of potential, current and temperature are calculated, based on which the heat release rate in a single-layer battery structure for three different batteries LCO, NMC and LFP can be evaluated. Parameters

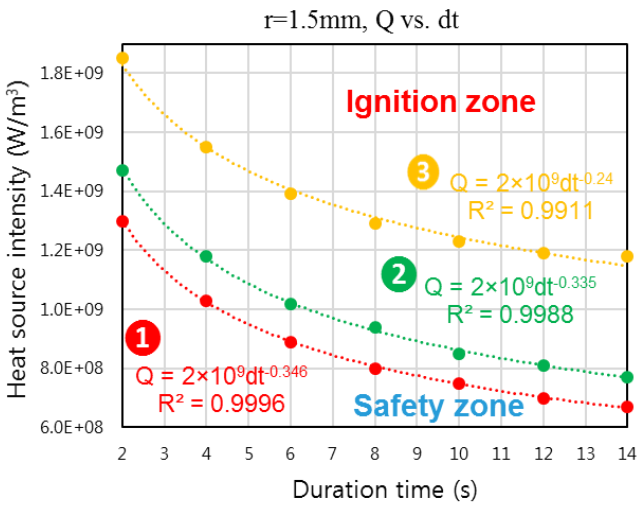

Figure 10. Comparison of the thermal runaway regime of three different Li-ion batteries.

involved in the electrochemical models for these materials are taken from the literature [77,89,94,96–98,100,101,104,109–115] as detailed in Table 5 to Table 7. Electrochemical parameters for $LiFePO_4$/graphite battery. in Appendix, and their performance validation is shown in Figure 17 to Figure 19 in Appendix.

As shown in Figure 11(a), in the initial period of the electrical field development, the maximum heat release rate occurs in the metal region, due to the high potential drop and the high current. As the electrical field approaches equilibrium, the potential drop on the metal decreases for its low resistance, and the heat release rate in the metal region therefore starts to drop. In the meantime, heat release rate in the non-intercalating particles area on both sides of the metal gradually increases and becomes dominant, eventually forming a plateau. Depending on the material, the maximum heat release can appear on either side of the non-intercalating particle area. For example, maximum heat release rate occurs on the positive side of metal for LCO and LFP batteries, while it occurs on the negative side for NMC, as shown in the zoom-in subplot in Figure 11(a). Regardless of the battery material, relaxation time for the field to achieve equilibrium is around 1 ms, and the maximum local heat release rate in the whole field can be as high as 1E12 W/m^3. The evolution of heat release shows both qualitative and quantitative agreement among the three battery materials, exhibiting negligible difference. This implies that the dominant effect in ISC heat release is largely electrical. The maximum temperature in these batteries can increase by 30 °C within 2 ms for this ISC event, equivalent to a temperature rise rate of 15000 °C/s. The LFP battery, however, exhibits the modest temperature increment, due to its slightly lower heat release rate and higher heat capacity.

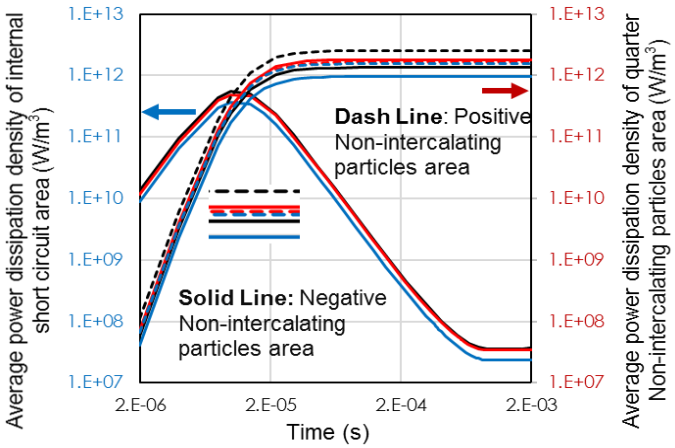

(a)

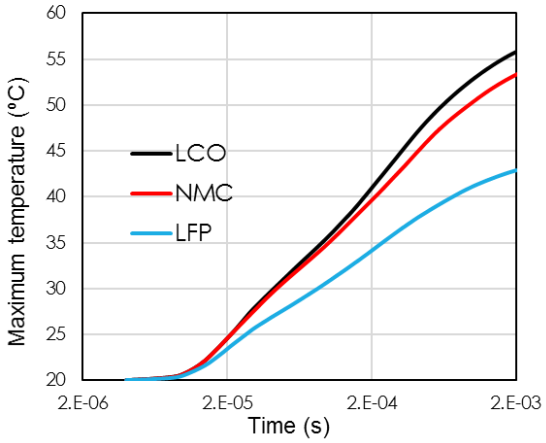

(b)

Figure 11. Identification heat release and thermal response during a typical ISC event (a) average heat release rate evolution in the ISC and the non-intercalating particle areas; (b) Maximum temperature rise of different battery materials during the current ISC event.

3.5 Combined analysis of ISC and thermal runway

In the real situation, electrochemical reactions quickly heat up the battery structure which further triggers the thermal runaway chemistry. Such simulation is achieved in a decouple-recombine manner in the current work. With the heat release rate separately evaluated from the electrochemistry, it becomes feasible to combine the results from the ISC modeling and the thermal runaway modeling, and to eventually answer the question if the ISC event is able to trigger thermal runaway or not. Specifically, the peak heat release rate history shown in Figure 11(a) could be assigned as the intensity of the hot spot in thermal runaway modeling. As shown in Figure 12, runaway occurs right before 1 ms as shown by the instantaneous sharp temperature rise, which is very close to the relaxation time of the electrical field equilibrium in Figure 11(a). Such consistency not only shows that thermal runaway will occur in this typical ISC scenario, but also adds to great confidence in the usage of both models, given that they are separately developed and validated against different types of measurement. Recent findings have shown that internal short circuits are responsible for very little (~10 %) of the total heat generated during thermal runaway, although they contribute to triggering the redox reactions after the separator collapses [71,72]. Without comparing the ISC heat release and the total heat release during thermal runaway, our work focuses on the evaluation of the local heat release rate from the electrochemical reactions during ISC, and its relevance to the critical heat source intensity needed to trigger thermal runway. Obviously, the total heat release during the entire process of thermal runaway is a much larger value and substantially depends on the enthalpy of formation of battery materials. It is noted that while complex interaction

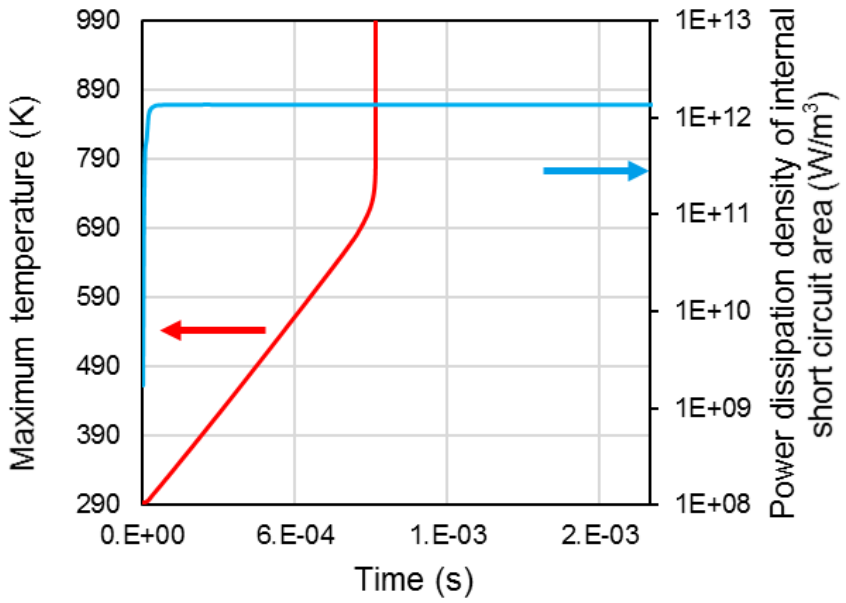

Figure 12. Evolution of local maximum heat release rate during ISC, and the battery temperature evolution using the thermal runaway model, demonstrating the combined effect of the ISC model and the thermal runaway model.

between electrochemistry and thermal runaway can exist in a typical event of ISC induced thermal runaway, our results help to bridge the two and to develop physics-based models for this important phenomenon.

4. Conclusion

This work is a comprehensive computational study to identify the safety regime of Li-ion batteries. The concept of critical thermal runaway state is demonstrated, which is characterized by the critical heat source intensity and duration time. Below the critical state, thermal runaway cannot occur either due to insufficient heat source intensity or residence time. By exploring different critical states and connecting them, a safety regime diagram is identified and extended to further incorporate the effect of heat source size and material dependence. The chemical kinetic feature during thermal runaway is identified through detailed comparison of runaway and non-runaway cases. It is found that the negative electrode – electrolyte reaction has a unique heat release profile, and directly correlates to thermal runaway. Normalized sensitivity analysis has been conducted to evaluate the key thermal-physical-chemical parameters for thermal runaway delay time, and the results show the delay time is more sensitive to the positive electrode-electrolyte reaction, in terms of its activation energy and frequency factor. The results here provide useful insights into the key factors, as well as direct guidance on how to validate thermal runaway models. To evaluate the potential of thermal runaway induced by ISC, a comprehensive thermal-electrochemical model is used to simulate the heat release rate from a typical ISC event. It is seen that in the initial period, the maximum heat release rate occurs in the metal region; as the electrical field approaches equilibrium, dominant heat release comes from the non-

intercalating particle region, which could be as high as 1E12 W/m^3. This heat release rate profile is assigned as the intensity of the hot spot in thermal runaway modeling, which shows that thermal runaway is successfully triggered. The consistency in thermal runaway time and the electrical relaxation time suggests the consistency and validity of both models. Our results help to bridge the electrochemistry and thermal runaway in the event of ISC induced thermal runaway and to develop physics-based models for this important yet complex phenomena.

Appendix

Table 1. Global thermal material properties of the $LiCoO_2$/graphite battery.

Parameter	Battery	Cylinder
k (W/ (m·K))	3.4 (through-plane) 34 (in-plane)	44.5
c_p (J/ (kg·K))	830	475
ρ (kg/m^3)	1700	7850

Table 2. Physical and kinetic parameters adopted in the thermal runaway model of $LiCoO_2$/graphite battery.

Symbol	Value	Physical description
A_{sei}	1.667×10^{15} (1/s)	SEI-decomposition frequency factor
A_{ne}	2.5×10^{13} (1/s)	Negative-electrolyte frequency factor
A_{pe}	6.667×10^{13} (1/s)	Positive-electrolyte frequency factor
A_e	5.14×10^{25} (1/s)	Electrolyte decomposition frequency
$E_{a,sei}$	1.3508×10^{5} (J/mol)	SEI-decomposition activation energy
$E_{a,ne}$	1.3508×10^{5} (J/mol)	Negative-electrolyte activation energy
$E_{a,pe}$	1.396×10^{5} (J/mol)	Positive-electrolyte activation energy
$E_{a,e}$	2.74×10^{5} (J/mol)	Electrolyte decomposition activation
c_{sei0}	0.15	Initial value of c_{sei}
c_{ne0}	0.75	Initial value of c_{ne}
α_0	0.04	Initial value of α
c_{e0}	1	Initial value of c_e
t_{sei0}	0.033	Initial value of t_{sei}
m_{sei}	1	Reaction order for c_{sei}
$m_{ne,n}$	1	Reaction order for c_{ne}
$m_{pe,p1}$	1	Reaction order for α
$m_{pe,p2}$	1	Reaction order for $(1-\alpha)$
m_e	1	Reaction order for c_e
H_{sei}	2.57×10^{5} (J/kg)	SEI-decomposition heat release

Table 2 continued

Symbol	Value	Physical description
H_{ne}	1.174×10^{6} (J/kg)	Negative-electrolyte heat release
H_{pe}	3.14×10^{5} (J/kg)	Positive-electrolyte heat release
H_e	1.55×10^{5} (J/kg)	Electrolyte decomposition heat release
W_c	6.104×10^{2} (kg/m^3)	Specific carbon content in jellyroll
W_p	1.221×10^{3} (kg/m^3)	Specific positive active content in jellyroll
W_e	4.069×10^{2} (kg/m^3)	Specific electrolyte content in jellyroll
R	8.314(J/mol/K)	Universal gas constant

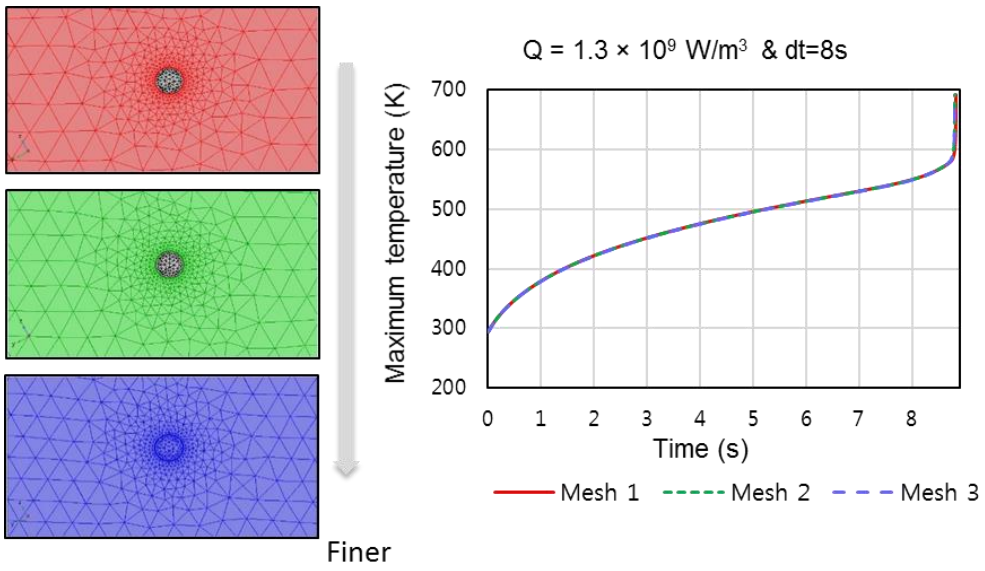

Figure 13. Mesh independence checking for thermal runaway simulation.

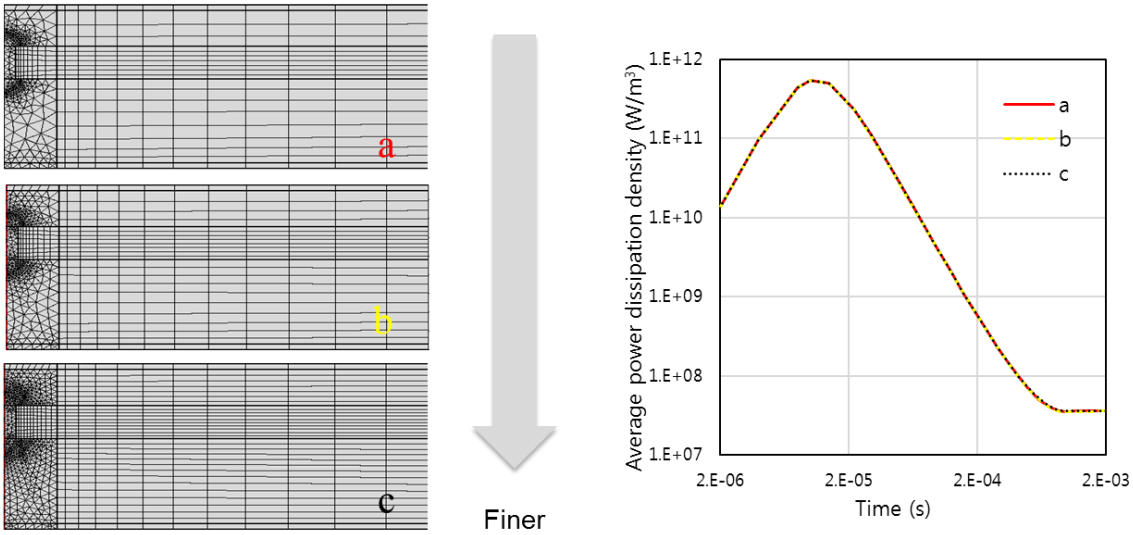

Figure 14. Mesh independence checking for electrochemical ISC event simulation.

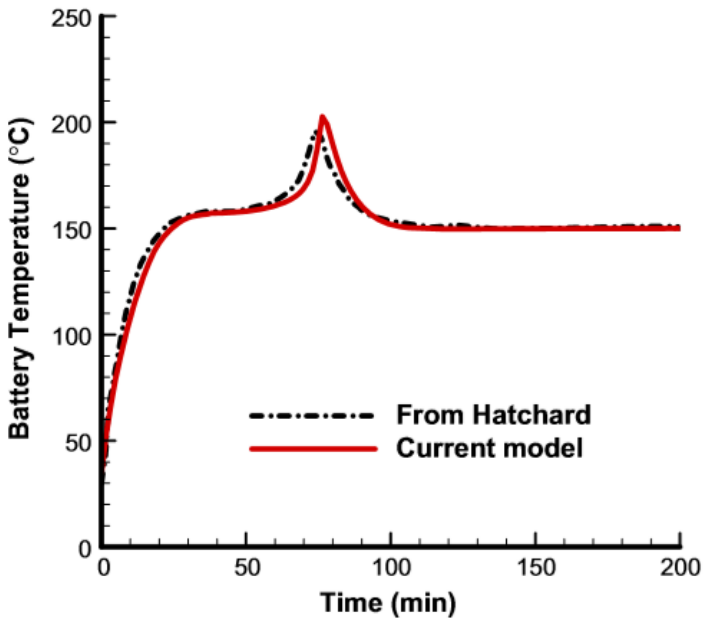

Figure 15. Validation of the current thermal runaway model and parameters against the oven test. In this experiment, a standard 18650 $LiCoO_2$/graphite cylindrical cell with an initial temperature of 27 °C was placed in the oven with a constant temperature at 150 °C [78]**.**

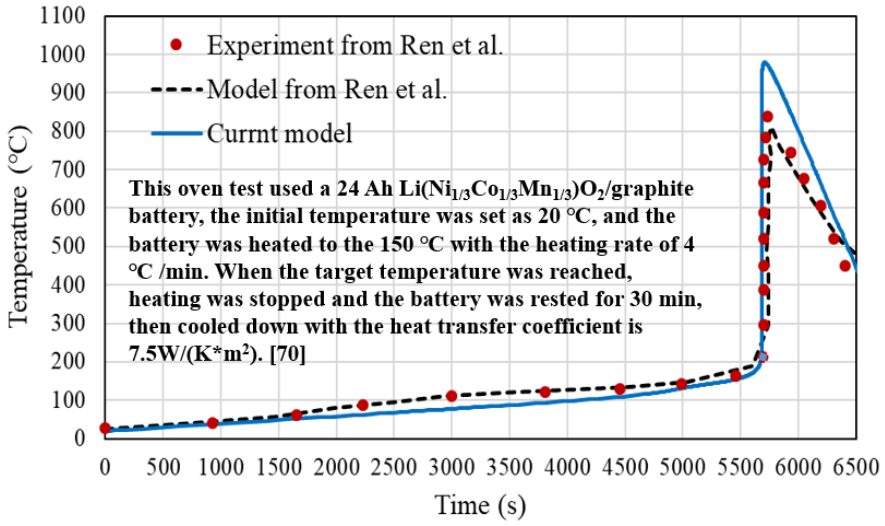

(a)

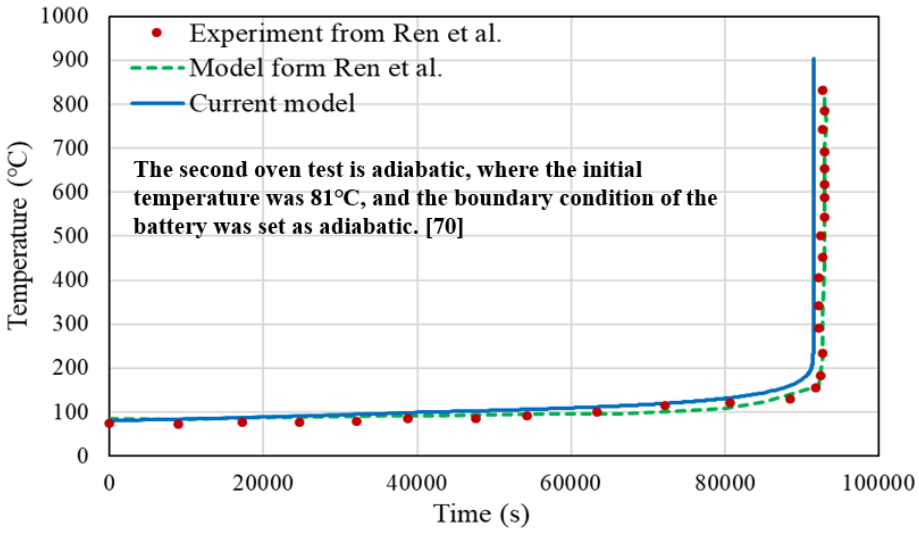

(b)

Figure 16. (a) prediction of battery thermal runaway behavior under 150 °C in oven heating test; (b) Prediction of battery thermal runaway behaviors in an adiabatic oven test.

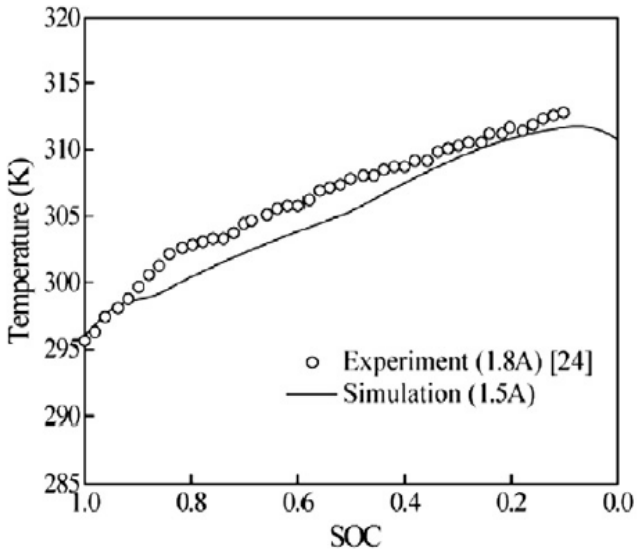

Figure 17. Comparison between simulation and experiment at a discharge rate of 1C. A SONY-18650 $LiCO_2$/graphite cell was discharged at 1C rate at the constant temperature of 300K and natural convection heat transfer coefficient of 7.17 W/(K*m^2) [103]**.**

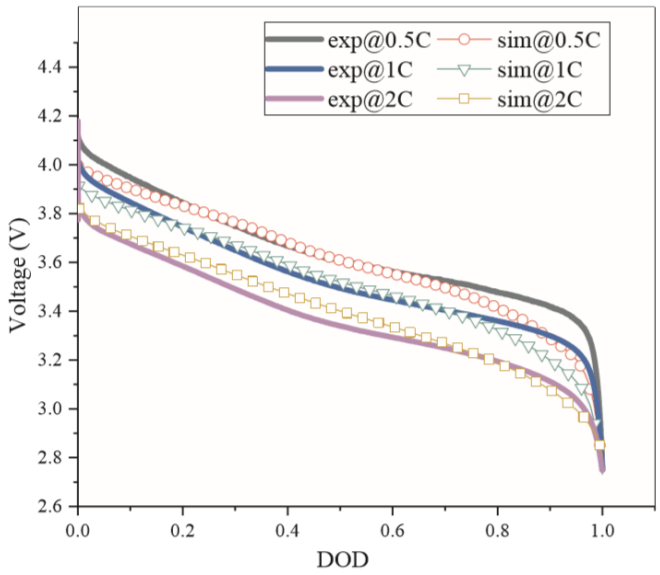

Figure 18. Comparison of simulation results of discharge curve with experimental data during 0.5 C, 1 C and 2 C discharge rates for an NMC111 battery with ambient temperature 298K [97].

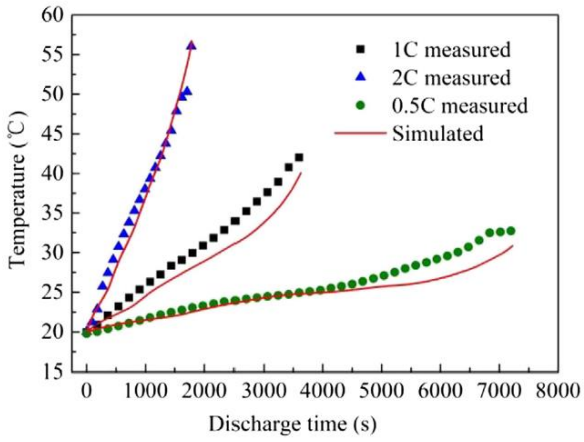

(a)

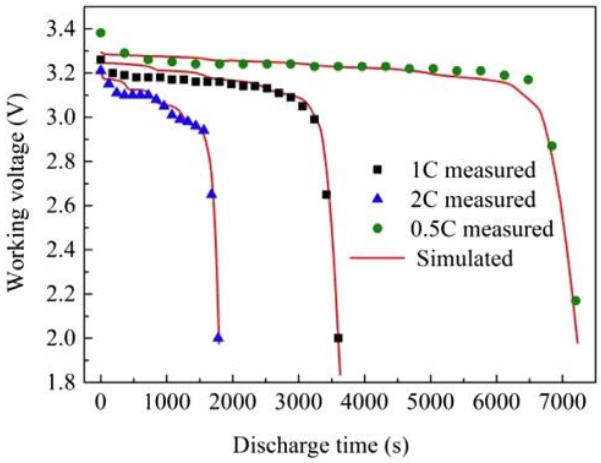

(b)

Figure 19. (a) Comparison of simulated surface temperatures with experimental data during galvanostatic discharge (0.5 C, 1 C, 2 C); (b) Comparison of simulated working voltage with experimental data during galvanostatic discharge (0.5 C, 1 C, 2 C). An LP2770120 $LiFePO_4$/graphite prismatic battery was discharged under different discharge rates (0.5 C, 1 C, 2 C) at ambient temperature of 20 °C.

Table 3. The properties of three difference Li-ion batteries.

Battery	E_{pe} ($J \cdot mol^{-1}$) [77]	Conductivity in plane (W/(m·k))	Conductivity through plane (W/(m·k))
LCO-1	1.396×10^5	24.84 [109]	1.035 [109]
NMC	1.54×10^5	21 [110]	1.1 [110]
LCO-2	1.396×10^5	34 [78]	3.4 [78,111]

Table 4. Physical and kinetic parameters adopted in the thermal runaway model of $LiNi_{1/3}Mn_{1/3}Co_{1/3}O_2$/graphite battery.

Symbol	Value [77]	Physical description
A_{sei}	1.667×10^{15} (1/s)	SEI-decomposition frequency factor
A_{ne}	2.5×10^{13} (1/s)	Negative-electrolyte frequency factor
A_{pe}	2.25×10^{14} (1/s)	Positive-electrolyte frequency factor
A_e	5.14×10^{25} (1/s)	Electrolyte decomposition frequency
$E_{a,sei}$	1.3508×10^{5} (J/mol)	SEI-decomposition activation energy
$E_{a,ne}$	1.3508×10^{5} (J/mol)	Negative-electrolyte activation energy
$E_{a,pe}$	1.54×10^{5} (J/mol)	Positive-electrolyte activation energy
$E_{a,e}$	2.74×10^{5} (J/mol)	Electrolyte decomposition activation
c_{sei0}	0.15	Initial value of c_{sei}
c_{ne0}	0.75	Initial value of c_{ne}
α_0	0.04	Initial value of α
c_{e0}	1	Initial value of c_e
t_{sei0}	0.033	Initial value of t_{sei}
m_{sei}	1	Reaction order for c_{sei}
$m_{ne,n}$	1	Reaction order for c_{ne}
$m_{pe,p1}$	1	Reaction order for α
$m_{pe,p2}$	1	Reaction order for $(1-\alpha)$
m_e	1	Reaction order for c_e
H_{sei}	2.57×10^{5} (J/kg)	SEI-decomposition heat release
H_{ne}	1.174×10^{6} (J/kg)	Negative-electrolyte heat release
H_{pe}	7.9×10^{5} (J/kg)	Positive-electrolyte heat release
H_e	1.55×10^{5} (J/kg)	Electrolyte decomposition heat release

Table 4 continued

Symbol	Value [77]	Physical description
W_c	6.104×10^2 (kg/m^3)	Specific carbon content in jellyroll
W_p	1.293×10^3 (kg/m^3)	Specific positive active content in jellyroll
W_e	4.069×10^2 (kg/m^3)	Specific electrolyte content in jellyroll
R	8.314(J/mol/K)	Universal gas constant

Table 5. Electrochemical parameters for $LiCoO_2$/graphite battery.

Parameter	Symbol	Unit	Negative current collector	Negative Electrode	Separator	Positive Electrode	Positive current collector
Electrode thickness	δ	μm	6[a]	90[a]	35[a]	40[a]	6[a]
Particle radius	$\widetilde{R}_s$	μm	—	2[a]	—	2[a]	—
Volume fraction of solid phase	ε_s	—	—	0.49[113]	—	0.59[113]	—
Volume fraction of electrolyte (Porosity)	ε_l	—	—	0.485[112, 113]	0.724[112, 113]	0.365[113]	—
Reaction rate constant	k_0	$m^{2.5}$ ·$mol^{-0.5}$/s	—	1.764×10^{-14} [104]	—	3.626×10^{-11} [104]	—

Table 5 continued

Parameter	Symbol	Unit	Negative current collector	Negative Electrode	Separator	Positive Electrode	Positive current collector
Initial Li concentration in solid	$c_{s,0}$	$mol \cdot m^{-3}$	—	25971[a]	—	2577[a]	—
Maximum *Li* concentration in solid	$c_{s,max}$	$mol \cdot m^{-3}$	—	30555[112, 113]	—	51554[112, 113]	—
Initial *Li* concentration in electrolyte	$c_{l,0}$	$mol \cdot m^{-3}$	—		1000[112]		—
Reference temperature	T_{ref}	K			298.15		

Table 5 continued

Parameter	Symbol	Unit	Negative current collector	Negative Electrode	Separator	Positive Electrode	Positive current collector
Li_xCoO_2 equilibrium potential	$U_{eq,p}$	V	$4.0459+exp(-42.30027x+16.56714)-0.04880arctan(50.01833x-26.48897)$ $-0.05447arctan(18.99678x-12.32362)-exp(78.24095x-78.68074)$ [101]				
Li_yC_6 equilibrium potential	$U_{eq,n}$	V	$0.13966+0.68920exp(-49.20361y)+0.41903$ $exp(-254.40067y)-exp(49.97886y-43.37888)-0.028221$ $arctan(22.52300y-3.65328)-0.01308arctan(28.34801y-13.439)$ [101]				
Li_xCoO_2 entropy coefficient	$\frac{\partial U_{eq,p}}{\partial T}$	$V\cdot K^{-1}$	$(-0.19952+0.92837x-1.36455x^2+0.61154x^3)/$ $1-5.66148x+11.47636x^2-9.82431x^3+3.04876x^4$ [101]				
Li_yC_6 entropy coefficient	$\frac{\partial U_{eq,n}}{\partial T}$	$V\cdot K^{-1}$	$(0.00527+3.29927y-91.79326y^2+1004.91101y^3-5812.27813y^4+19329.7549y^5-$ $37147.8947y^6+38379.18127y^7-16515.05308y^8/(1-48.09287y+1017.23480y^2-10481.80419y^3$ $+59431.30001y^4-195881.64880y^5+374577.3152y^6-385821.1607y^7+165705.85970y^8)$ [101]				

Table 5 continued

Parameter	Symbol	Unit	Negative current collector	Negative Electrode	Separator	Positive Electrode	Positive current collector
Li diffusion coefficient in solid	D_s	$m^2 \cdot s^{-1}$	—	3.9×10^{-14}[112]	—	1×10^{-13}[112]	—
Li diffusion coefficient in electrolyte	D_l	$m^2 \cdot s^{-1}$	—		7.5×10^{-10}[112]		—
Ionic conductivity	κ_l	$S \cdot m^{-1}$	$4.1253\times10^{-4}+5.007\times10^{-3}c_l-4.7212\times10^{-3}\,c_l{}^2+1.5094\times10^{-3}\,c_l{}^3-1.6018\times10^{-4}\,c_l{}^4$[96]				
Electronic conductivity in solid	σ_s	$S \cdot m^{-1}$	6×10^7[113]	100[114]	—	10[114]	3.8×10^7[113]
Transference number	t_+	—	—	—	0.38[113]	—	—

Table 5 continued

Parameter	Symbol	Unit	Negative current collector	Negative Electrode	Separator	Positive Electrode	Positive current collector
Charge-transfer coefficient	α_a, α_c	—	—	0.5[114]	—	0.5[114]	—
Faraday constant	F	$C \cdot mol^{-1}$			96485		
Gas constant	R	$J \cdot mol^{-1}K^{-1}$			8.314		
Heat capacity	c_p	$J \cdot Kg^{-1}K^{-1}$	385[77]	1437.4[77]	1978[77]	700[77]	903[77]
Thermal conductivity	λ	$W \cdot m^{-1}K^{-1}$	398[77]	1.04[77]	0.334[77]	1.48[77]	238[77]
Cell density	ρ	$Kg \cdot m^{-3}$	8900[77]	2660[77]	492[77]	2500[77]	1500[77]

Note: Superscript “a” implies assigned values.

Table 6. Electrochemical parameters for $LiNi_{1/3}Mn_{1/3}Co_{1/3}O_2$/graphite battery.

Parameter	Symbol	Unit	Negative current collector	Negative Electrode	Separator	Positive Electrode	Positive current collector
Electrode thickness	δ	μm	6[a]	90[a]	35[a]	40[a]	6[a]
Particle radius	$\widetilde{R}_s$	μm	–	2[a]	–	2[a]	–
Volume fraction of solid phase	ε_s	—	–	0.65[97]	–	0.43[97]	–
Volume fraction of electrolyte (Porosity)	ε_l	—	–	0.59[115]	0.42[115]	0.54[115]	–
Reaction rate constant	k_0	$m^{2.5}$ ·$mol^{-0.5}$/s	—	1.764×10^{-14} [104]	—	3.626×10^{-11} [104]	—

Table 6 continued

Parameter	Symbol	Unit	Negative current collector	Negative Electrode	Separator	Positive Electrode	Positive current collector
Initial Li concentration in solid	$c_{s,0}$	$mol \cdot m^{-3}$	–	26265[a]	–	2475[a]	–
Maximum *Li* concentration in solid	$c_{s,max}$	$mol \cdot m^{-3}$	–	30900[115]	–	49500[115]	–
Initial *Li* concentration in electrolyte	$c_{l,0}$	$mol \cdot m^{-3}$	–		1200[115]		–
Reference temperature	T_{ref}	K			298.15		

Table 6 continued

Parameter	Symbol	Unit	Negative current collector	Negative Electrode	Separator	Positive Electrode	Positive current collector
$Li_xNi_{1/3}Co_{1/3}Mn_{1/3}O_2$ equilibrium potential	$U_{eq,p}$	V	$44.563+2.595x-16.77x^2+23.88x^3-10.27x^4$ [100]				
Li_yC_6 equilibrium potential	$U_{eq,n}$	V	$0.1493+0.8439\ exp(-61.79y)+0.3824\ exp(-665.8y)-exp(39.42y-41.92)-0.0313arctan(25.59-4.099)-0.009434arctan(32.49y-15.74)$ [100]				
$Li_xNi_{1/3}Co_{1/3}Mn_{1/3}O_2$ entropy coefficient	$\frac{\partial U_{eq,p}}{\partial T}$	$V\cdot K^{-1}$	$-0.64816+4.34612x-8.05595x^2+4.44722x^3$ [100]				
Li_yC_6 entropy coefficient	$\frac{\partial U_{eq,n}}{\partial T}$	$V\cdot K^{-1}$	$-1.25571e^{-4}+4.66239e^{-5}/(\sqrt{2\pi}\times0.98567y)\times exp(-(\ln(y/0.08017))^2/(2\times0.98567^2))$ [100]				
Li diffusion coefficient in solid	D_s	$m^2\cdot s^{-1}$	—	3.2×10^{-14} [94]	—	2.2×10^{-13} [94]	—

Table 6 continued

Parameter	Symbol	Unit	Negative current collector	Negative Electrode	Separator	Positive Electrode	Positive current collector
Li diffusion coefficient in electrolyte	D_l	$m^2 \cdot s^{-1}$	—		2.6×10^{-10}[94]		—
Ionic conductivity	κ_l	$S \cdot m^{-1}$	$4.1253\times10^{-4}+5.007\times10^{-3}c_l-4.7212\times10^{-3}\,c_l{}^2+1.5094\times10^{-3}\,c_l{}^3-1.6018\times10^{-4}\,c_l{}^4$[96]				
Electronic conductivity in solid	σ_s	$S \cdot m^{-1}$	6×10^7[104]	100[97]	—	10[97]	3.8×10^7[89]
Transference number	t_+	—	—	—	0.363[97]	—	—
Charge-transfer coefficient	α_a, α_c	—	—	0.5[97]	—	0.5[97]	—

Table 6 continued

Parameter	Symbol	Unit	Negative current collector	Negative Electrode	Separator	Positive Electrode	Positive current collector
Faraday constant	F	$C \cdot mol^{-1}$			96485		
Gas constant	R	$J \cdot mol^{-1}K^{-1}$			8.314		
Heat capacity	c_p	$J \cdot Kg^{-1}K^{-1}$	385[97]	1437.4[97]	2050[97]	1150[97]	897[97]
Thermal conductivity	λ	$W \cdot m^{-1}K^{-1}$	395[97]	0.4[97]	0.5[97]	1.50[77]	240[97]
Cell density	ρ	$Kg \cdot m^{-3}$	8960[97]	1200[97]	525[97]	2860[97]	2700[97]

Note: Superscript “a” implies assigned values.

Table 7. Electrochemical parameters for $LiFePO_4$/graphite battery.

Parameter	Symbol	Unit	Negative current collector	Negative Electrode	Separator	Positive Electrode	Positive current collector
Electrode thickness	δ	μm	6[a]	90[a]	35[a]	40[a]	6[a]
Particle radius	$\widetilde{R}_s$	μm	–	2[a]	–	2[a]	–
Volume fraction of solid phase	ε_s	—	–	0.56[104]	–	0.435[104]	–
Volume fraction of electrolyte (Porosity)	ε_l	—	–	0.3[104]	0.4[104]	0.28[104]	–
Reaction rate constant	k_0	$m^{2.5}$ ·$mol^{-0.5}$/s	—	1.764×10^{-14} [104]	—	3.626×10^{-11} [104]	—

Table 7 continued

Parameter	Symbol	Unit	Negative current collector	Negative Electrode	Separator	Positive Electrode	Positive current collector
Initial Li concentration in solid	$c_{s,0}$	$mol \cdot m^{-3}$	–	26809[a]	–	1319[a]	–
Maximum *Li* concentration in solid	$c_{s,max}$	$mol \cdot m^{-3}$	–	31540[104]	–	26390[104]	–
Initial *Li* concentration in electrolyte	$c_{l,0}$	$mol \cdot m^{-3}$	–		1200[98]		–
Reference temperature	T_{ref}	K			298.15		

Table 7 continued

Parameter	Symbol	Unit	Negative current collector	Negative Electrode	Separator	Positive Electrode	Positive current collector
Li_xFePO_4 **equilibrium potential**	$U_{eq,p}$	V	$3.4323-0.4828\ exp(-80.2493(1-x)^{1.3198}) -3.2474\times10^{-6}exp(20.2645(1-x)^{3.8003})+3.2482\times10^{-6}exp(20.2646(1-x)^{3.7995})$ [98]				
Li_yC_6 **equilibrium potential**	$U_{eq,n}$	V	$0.6379+0.5416exp(-305.5309y) +0.044tanh(-(y-0.1958)/0.1088) -0.1978\ tanh((y-1.0571)/0.0854) -0.6875\ tanh((y+0.0117)/0.0529) -0.0175tanh((y-0.5692)/0.0875)$ [98]				
Li_xFePO_4 **entropy coefficient**	$\frac{\partial U_{eq,p}}{\partial T}$	$V\cdot K^{-1}$	$-0.35376x^8+1.3902x^7-2.2585x^6+1.9635x5-0.98716x4+0.28857x^3-0.046272x^2+0.003215x-1.9186\times10^{-5}$ [98]				
Li_yC_6 **entropy coefficient**	$\frac{\partial U_{eq,n}}{\partial T}$	$V\cdot K^{-1}$	$344.1347148\times (exp(-32.9633287y+8.316711484)/(1+749.0756003exp(-34.79099646y+8.887143624))-0.8520278805y+0.362299229y^2+0.2698001697$ [98]				

Table 7 continued

Parameter	Symbol	Unit	Negative current collector	Negative Electrode	Separator	Positive Electrode	Positive current collector
Li diffusion coefficient in solid	D_s	$m^2 \cdot s^{-1}$	—	3.2×10^{-14}[94]	—	1.3×10^{-13}[94]	—
Li diffusion coefficient in electrolyte	D_l	$m^2 \cdot s^{-1}$	—		2.6×10^{-10}[94]		—
Ionic conductivity	κ_l	$S \cdot m^{-1}$	$4.1253\times10^{-4}+5.007\times10^{-3}c_l-4.7212\times10^{-3}\,c_l{}^2+1.5094\times10^{-3}\,c_l{}^3-1.6018\times10^{-4}\,c_l{}^4$[96]				
Electronic conductivity in solid	σ_s	$S \cdot m^{-1}$	6×10^7[104]	100[98]	—	0.5[98]	3.8×10^7[104]
Transference number	t_+	—	—	—	0.363[104]	—	—

Table 7 continued

Parameter	Symbol	Unit	Negative current collector	Negative Electrode	Separator	Positive Electrode	Positive current collector
Charge-transfer coefficient	α_a, α_c	—	—	0.5[104]	—	0.5[104]	—
Faraday constant	F	$C \cdot mol^{-1}$			96485		
Gas constant	R	$J \cdot mol^{-1}K^{-1}$			8.314		
Heat capacity	c_p	$J \cdot Kg^{-1}K^{-1}$	385[104]	1437.4[104]	1978[104]	1260[104]	903[104]
Thermal conductivity	λ	$W \cdot m^{-1}K^{-1}$	400[104]	1.04[104]	0.334[104]	1.48[104]	160[104]
Cell density	ρ	$Kg \cdot m^{-3}$	8900[104]	2660[104]	492[104]	1500[104]	2700[104]

Note: Superscript “a” implies assigned values.

CHAPTER II

RADIATION INDUCED THERMAL RUNAWAY PROPAGATION A CYLINDRICAL LI-ION BATTERY PACK: NON-MONOTONICITY, CHEMICAL KINETICS, AND GEOMETRIC CONSIDERATIONS

A version of this chapter was originally published by Liwen Zhang, Yi Chen, Haiwen Ge, Ankur Jain, Peng Zhao:

L. Zhang, Y. Chen, H. Ge, A. Jain, P. Zhao, " Radiation induced thermal runaway propagation in a cylindrical Li-ion battery pack: Non-monotonicity, chemical kinetics, and geometric considerations." *Applied Sciences* 13.14 (2023): 8229.

CRediT authorship contribution statement

Liwen Zhang: Investigation, Methodology, Software, Resources, Data Curation Formal Analysis, Writing - Original Draft Preparation, Visualization; Yi Chen: Investigation, Data Curation, Writing - Review and Editing; Haiwen Ge: Methodology, Validation, Writing - Review and Editing; Ankur Jain: Conceptualization, Validation, Writing - Review and Editing; Peng Zhao, Conceptualization, Methodology, Validation, Formal Analysis, Investigation, Resources, Writing - Original Draft Preparation, Visualization, Supervision, Project Administration, Funding Acquisition

Abstract

Li-ion batteries play a key role in energy storage and conversion in engineering systems such as electric vehicles and grid energy storage, with critical impact on electrification and storage of renewable energy. A key unresolved technological challenge in Li-ion batteries pertains to thermal runaway initiation and propagation in a battery pack, which can lead to subsequent fire and explosion. Despite significant past work, there remains a critical need to understand how thermal runaway propagates in a pack. This work presents a comprehensive investigation of the effect of radiative heat transfer on thermal runaway propagation. Radiation can be important when a battery is exposed to adjacent heat and fire

sources, as well as in thermal runaway propagation from one hot cell to another. A theoretical radiative heat transfer model based on view factor theory is developed. Calculations based on this model for a simple 2D cylinder-to-cylinder geometry are found to be in very good agreement with analytical expressions. Radiation-induced thermal runaway propagation between two cylindrical 18650 batteries is evaluated. It is shown that radiation may play a key role in thermal runaway propagation, depending strongly on the triggering temperature. It is found that radiative effects in thermal runaway propagation exhibit both nonlinear and non-monotonic characteristics. At high temperatures, thermal runaway is triggered rapidly in the region close to the battery surface, where the chemical reactions are strongly coupled, and radiation plays a dominant role. In contrast, at lower temperatures, thermal runaway is triggered much more slowly and towards the core of the cell, where some chemical reactions may be decoupled, and pre-runaway chemical heat release plays an increasingly important role. The results presented here suggest that radiation can either facilitate or mitigate thermal runaway. The net radiation heat flux has a cross-over instant, beyond which radiation starts to retard thermal runaway. Additionally, the blocking effect in radiative heat transfer between cells arranged in equal-spacing homogenous or orthogonal arrangements in a battery pack is investigated, along with the effect of the hot spot size. Results from this work help understand the role of radiation in thermal runaway propagation and provide useful insights into the thermal runaway control and design of safe Li-ion battery packs.

1. Introduction

Li-ion battery (LIB) technology has attracted extensive research interest, as it offers an efficient mechanism for energy conversion and storage, thus contributing towards decarbonization and energy electrification [116]. LIBs offer very high conversion efficiency between chemical and electrical energy. If the electricity comes from clean and renewable energy resources, LIB technology with sufficiently long cycle life will not further increase the carbon footprint from electricity generation and utilization. Moreover, LIBs can be seamlessly integrated with existing infrastructure and ongoing efforts in the energy sector, for example, the electricity grid, centralized carbon capture and sequestration, etc. Li-ion battery-based energy storage systems include large-scale Li-ion battery packs with additional control and thermal management modules, which enable load-shifting, frequency regulation, long-term storage, and decentralized deployment. In addition, LIB based energy storage systems facilitate synergistic integration of other technologies toward decarbonization, such as battery regeneration and material recycling. Through the combination of existing grid infrastructure, diversified power generation, centralized carbon capture and sequestration, increased renewable energy, and efficient battery regeneration, a clean and sustainable energy sector can be expected in the future with LIB-based energy storage systems.

However, the operation of LIBs is extremely sensitive to temperature. Thermal runaway and subsequent fires can be triggered when LIBs are exposed to abuse conditions such as overheating [117,118], internal short circuit [32,119], collision and nail penetration [120,121]. Thermal runaway of LIBs has attracted extensive research interest in the recent

past. These research efforts include characterization of the thermal stability of battery materials [70,122], battery and pack-level thermal runaway testing [123,124], development of kinetic models of thermal runaway [73,125], optimized cooling system design to mitigate thermal runaway and its propagation [78,126–129], modelling and simulation of thermal runaway using detailed and reduced-order models [38,130], venting gas generation and subsequent fires [131–133].

Figure 20 shows the thermal runaway mechanism in a typical LIB with $LiCoO_2$ cathode, electrolyte of ethylene carbonate ($C_3H_4O_3$) and Lithium hexafluorophosphate ($LiPF_6$), and a graphite anode. The solid electrolyte interphase (SEI) layer is thermally unstable and can decompose when subjected to high temperature or other abuse. Lithium in the anode will then directly contact the electrolyte and form lithium carbonate and ethylene. In addition, the cathode and electrolyte can directly react through the oxygen generated from cathode decomposition. Finally, the electrolyte material carbonate and salt can decompose under elevated temperatures. These reactions are largely exothermic and accompanied by the formation of gases such as ethylene and oxygen, thereby creating a self-sustained, destructive chain of highly exothermic reactions.

Understanding the factors that impact the propagation of thermal runaway in a large battery pack remains an important research challenge. Past work has shown that multiple factors including cell-to-cell gap, thermal properties of the interstitial material, and kinetics of the decomposition reactions all play a key role in determining whether thermal runaway propagation occurs or not [134]. However, the role of radiative heat transfer in thermal runaway propagation has remained poorly understood, primarily due to the strong

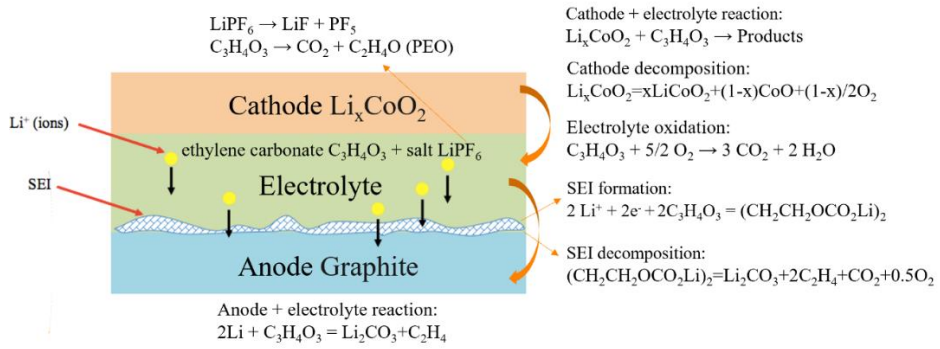

Figure 20. Configuration and thermal runaway reactions for a typical LCO LIB.

nonlinearity of radiation and its coupling with thermal runaway chemistry. Radiative heat transfer is usually dominant in high-temperature processes, such as combustion, which are, in principle, similar to thermal runaway. In the context of Li-ion cells, radiation is known to play a critical role in increasing the battery temperature and activating thermal runaway reactions [135–140]. The role of radiation in thermal runaway propagation in a pack of cylindrical cells has been investigated computationally [141]. These results have shown that neglecting radiation leads to a prediction of onset in the trigger battery but an erroneous prediction of no thermal runaway propagation. In addition, thermal radiation has often been combined with the effects of conduction and convection in studying the triggering of thermal runaway [110,140], leading to ambiguity on the specific role of radiative heat transfer. A radiative shielding method to minimize thermal runaway propagation has been presented, where the fraction of heat flux due to radiation in a battery pack during thermal runaway is also evaluated [142]. More recently, our experiments have demonstrated battery-to-battery variability in thermal runaway [143], even among batteries with the same chemistry and near-identical initial conditions. It is hence expected that variation from radiation in the triggering cell can lead to different modes and paths for thermal runaway propagation in a pack, which necessitates study on the specific role of radiative heat transfer.

The literature cited above clearly highlights the importance of radiative heat transfer and the need for a comprehensive investigation of how radiative heat transfer impacts thermal runaway propagation. This work presents an investigation of the role of radiative heat transfer in thermal runaway propagation when a LIB is exposed to fire and

other heat sources. A limiting condition for triggering thermal runaway by radiative heat transfer between two closely-packed cylindrical cells is computationally investigated. Results indicate the existence of complex nonlinear coupling between chemical reactions and thermal radiation. A key novelty of the work is that we have identified the non-monotonic impact of radiation on thermal runaway triggering and have mapped out the regime diagram under both low and high-temperature limits. We have shown that depending on conditions, radiation can either facilitate or mitigate thermal runaway. When the triggering cell is at relatively low temperature, we have further shown that pre-runaway chemistry plays an increasingly significant role. We extend our investigation to battery packs and practical conditions where radiative blocking effects and localized hot spots may be important. Results presented here highlight the importance of radiative heat transfer in thermal runaway propagation and can help guide future efforts towards mitigation of thermal runaway in safe electrochemical energy storage systems.

2. Materials and methods

In this study, a 2D model is developed in COMSOL Multiphysics 5.5, where the heat transfer module is used to implement surface-to-surface radiation. Figure 21(a) shows a schematic of a typical pack of multiple, orthogonally arranged Li-ion cells with equal spacing. In general, the interest here is to understand how radiative heat transfer may facilitate the propagation of thermal runaway from one cell to the other. While the general problem comprising a number of cells is considerably complicated, for simplicity, the radiative exchange between a cell and one of its neighbors is considered first. The problem

of radiation-induced thermal runaway between two neighboring cells may be treated as a 2D radiation heat transfer problem between two equal cylinders, as shown in Figure 21(b).

In order to understand how these two cells exchange heat radiatively, the general energy conservation equation is first written. Thermal conduction in the axial direction is ignored, since a typical cylindrical cell has high aspect ratio. The transient differential equation that balances heat conduction in the axial and azimuthal directions as well as thermal runaway chemical heat release is given by:

$$\rho c_p \frac{\partial T}{\partial t} = \frac{1}{r}\frac{\partial}{\partial r}\left(k_r r \frac{\partial T}{\partial r}\right) + \frac{1}{r^2}\frac{\partial}{\partial \theta}\left(k_\theta \frac{\partial T}{\partial \theta}\right) + Q \qquad (48.)$$

where $t, r, \theta, \rho, c_p, T, k$ and Q are time, radial coordinate, polar coordinate, battery density, heat capacity, thermal conductivity, and heat generation within the battery, respectively. Based on previous work [143], values of thermophysical properties of a typical Li-ion cell are provided in Table 8. Considering the jellyroll layered structure of a cylindrical cell, the azimuthal in-plane thermal conductivity is much higher compared to the out-of-plane radial thermal conductivity. As such, the limiting heat conduction that is essential for thermal runaway initiation is in the radial direction. For these considerations, the problem is simplified as a 2D limiting condition with both k_r and k_θ having equal out-of-plane thermal conductivity.

The heat generation term Q originates from four well-known semi-global thermal runaway chemical reactions [73]. These exothermic reactions include the solid-electrolyte-interface decomposition reaction, the anode-electrolyte reaction, the cathode-electrolyte reaction, and the electrolyte decomposition. The rates of these reactions depend on the battery material properties, thermal chemical parameters, and the battery temperature. The

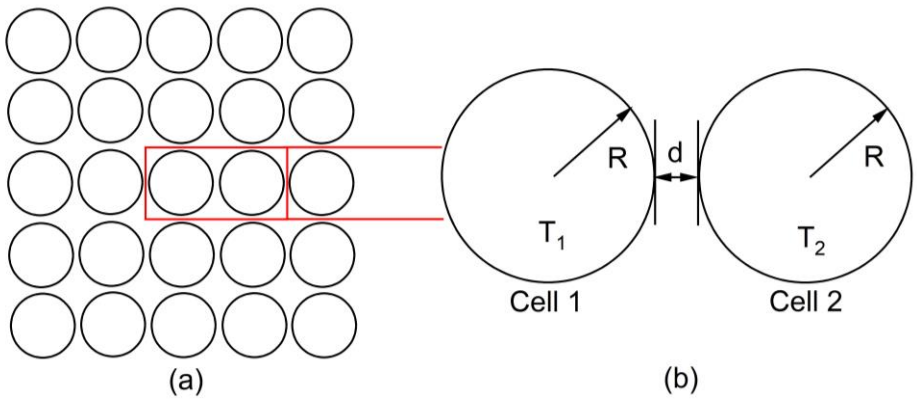

Figure 21. Schematic of simulation geometry of two equal cylinders with radius *R* and separation *d*.

Table 8. Model parameters in the thermal radiation model.

Parameter (unit)	Value
Battery radius, $R(mm)$	9
Battery density, $\rho(kg/m^3)$	2060
Heat capacity, $c_p(J/kg \cdot K)$	1000
Thermal conductivity, $k(W/m \cdot K)$	0.8

reaction model, frequency factor, and activation energy that describe the kinetics between the electrolyte and electrode materials have been previously obtained by fitting the experimental measurements from accelerating rate calorimetry (ARC) and differential scanning calorimetry (DSC) tests. Expressions for the chemical reaction rates and heat generation rates for these reactions are shown in Table 9 and Table 10, with symbols and parameter values used here as our previous work [144,145]. The present model for LCO thermal runaway chemistry is capable of accounting for more complicated reaction models and other cathode chemistry.

At the surface, thermal radiation is considered exclusively, and convective effects are ignored. This corresponds to the practical condition in a pack where there is no forced convective flow and the radiation heat transfer dominants. A schematic diagram of radiative heat exchange between the two cells is shown in Figure 22. The radiation heat flux emitted from Cell 1 is the irradiation *G*:

$$G = \varepsilon\sigma {T_1}^4 \tag{49.}$$

For Cell 2, we can define the radiosity *J*, the radiation heat flux leaving its surface:

$$J = \varepsilon\sigma {T_2}^4 + (1-\varepsilon)F_{12}G \tag{50.}$$

where the radiosity has been expressed as the sum of diffusively reflected and emitted radiation from Cell 2. Consequently, the net radiation heat flux on Cell 2 can be written as:

$$q = F_{12}G - J \tag{51.}$$

In these equations, ε is the emissivity, σ is the Stefan-Boltzmann constant, T_1 is the temperature of Cell 1, T_2 is the temperature of Cell 2, T_{amb} is ambient temperature, and F_{12} is the view factor from Cell 1 to Cell 2.

Table 9. Heat generation from side chemical reactions equations of thermal abuse model.

Reaction term	Equations	
SEI decomposition	$\frac{dc_{sei}}{dt} = -A_{sei} exp\left[-\frac{E_{a,sei}}{RT}\right] c_{sei}^{m_{sei}}$	$Q_{sei} = -H_{sei} W_c \frac{dc_{sei}}{dt}$
Anode-electrolyte reaction	$\frac{dc_{ne}}{dt} = -A_{ne} exp\left[-\frac{t_{sei}}{t_{sei0}}\right] c_{ne}^{m_{ne,n}} exp\left[-\frac{E_{a,ne}}{RT}\right]$	$Q_{ne} = -H_{ne} W_c \frac{dc_{ne}}{dt}$
	$\frac{dt_{sei}}{dt} = A_{ne} exp\left[-\frac{t_{sei}}{t_{sei0}}\right] c_{ne}^{m_{ne,n}} exp\left[-\frac{E_{a,ne}}{RT}\right]$	
Cathode-electrolyte reaction	$\frac{d\alpha}{dt} = A_{pe} \alpha^{m_{pe,p1}} (1-\alpha)^{m_{pe,p2}} exp\left[-\frac{E_{a,pe}}{RT}\right]$	$Q_{pe} = -H_{pe} W_p \frac{d\alpha}{dt}$
Electrolyte decomposition	$\frac{dc_e}{dt} = -A_e exp\left[-\frac{E_{a,e}}{RT}\right] c_e^{m_e}$	$Q_e = -H_e W_e \frac{dc_e}{dt}$
Overall heat generation	$Q = Q_{sei} + Q_{ne} + Q_{pe} + Q_e$	

Table 10. Thermochemical parameters adopted in the thermal runaway model of $LiCoO_2$/graphite battery.

Symbol	Value [35,36]	Physical description
A_{sei}	1.667×10^{15} (1/s)	SEI-decomposition frequency factor
A_{ne}	2.5×10^{13} (1/s)	Anode-electrolyte frequency factor
A_{pe}	6.667×10^{13} (1/s)	Cathode-electrolyte frequency factor
A_e	5.14×10^{25} (1/s)	Electrolyte decomposition frequency factor
$E_{a,sei}$	1.3508×10^{5} (J/mol)	SEI-decomposition activation energy
$E_{a,ne}$	1.3508×10^{5} (J/mol)	Anode-electrolyte activation energy
$E_{a,pe}$	1.396×10^{5} (J/mol)	Cathode-electrolyte activation energy
$E_{a,e}$	2.74×10^{5} (J/mol)	Electrolyte decomposition activation energy
c_{sei0}	0.15	Initial value of c_{sei}
c_{ne0}	0.75	Initial value of c_{ne}
α_0	0.04	Initial value of α
c_{e0}	1	Initial value of c_e
t_{sei0}	0.033	Initial value of t_{sei}
m_{sei}	1	Reaction order for c_{sei}
m_{ne}	1	Reaction order for c_{ne}
m_{pe1}	1	Reaction order for α
m_{pe2}	1	Reaction order for $1-\alpha$
m_e	1	Reaction order for c_e
H_{sei}	2.57×10^{5} (J/kg)	Reaction heat of SEI-decomposition
H_{ne}	1.714×10^{6} (J/kg)	Reaction heat of anode-electrolyte
H_{pe}	3.14×10^{5} (J/kg)	Reaction heat of cathode-electrolyte
H_e	1.55×10^{5} (J/kg)	Reaction heat of electrolyte decomposition

Table 10 continued

Symbol	Value [35,36]	Physical description
W_c	6.104×10^2 (kg/m^3)	Specific carbon content in jellyroll
W_p	1.221×10^3 (kg/m^3)	Specific positive active content in jellyroll
W_e	4.069×10^2 (kg/m^3)	Specific electrolyte content in jellyroll
$\bar{R}$	8.314 (J/mol/K)	Universal gas constant

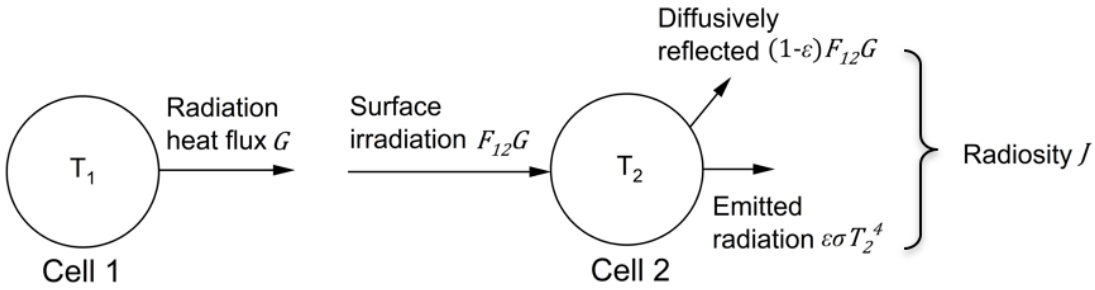

Figure 22. Schematic of thermal radiation between two equal external cylindrical cells.

In order to validate the thermal radiation modelling, a quasi-steady state radiative heat transfer problem between two equal cylinders of radius R = 9 mm is considered. With given separation distance and cylinder temperatures, we can numerically simulate the radiation heat flux received by Cell 2 among the total radiation emitted from Cell 1, that is, GF_{12}. Meanwhile, in classical heat transfer theory, the radiation heat flux between two cylinders is analytically available with a known view factor, which can be used to validate the simulation results. The view factor between two equal cylinders has been derived from the view factor for general parallel cylinders as follows [146]:

$$F_{12} = \frac{\sqrt{\left(\frac{2R+d}{R}\right)^2 - 4} - \frac{2R+d}{R} + 2\arcsin\left(\frac{2R}{2R+d}\right)}{2\pi} \quad (52.)$$

As shown in Figure 23(a) and (b), the numerical radiation heat flux is compared with the analytical theory between two equal blackbody cylinders (i) with fixed temperature but varying distance, and (ii) with fixed distance but varying temperature of the Cell 1. The results suggest that as the distance of two cells increases, the radiation heat flux decreases. Also, as the temperature of Cell 1 increases, the radiation heat flux received by Cell 2 increases. The numerical calculation of the radiation heat flux is in excellent agreement with analytical results, further substantiating the simulation tool.

In the thermal runaway simulation, we fix the temperature T_1 of Cell 1 and the ambient temperature (293 K) in each case. The initial temperature of Cell 2 is also taken to be 293 K. The evolution of T_2 is numerically solved by accounting for radiation, conduction, and thermal runaway chemical heat release based on Equation (48.). The surface-to-surface radiation is simulated using the Hemicube method. A time-dependent

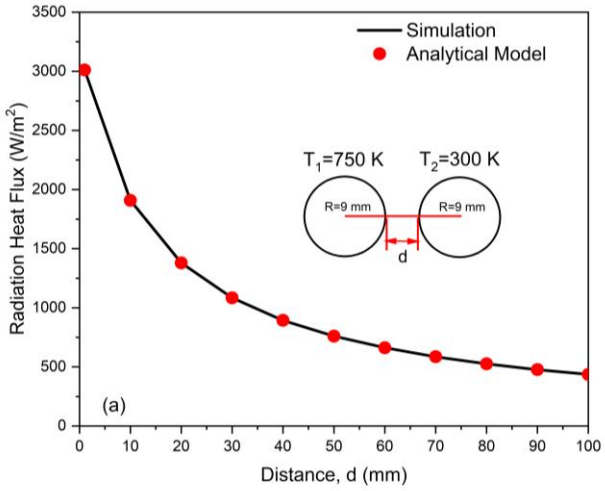

(a)

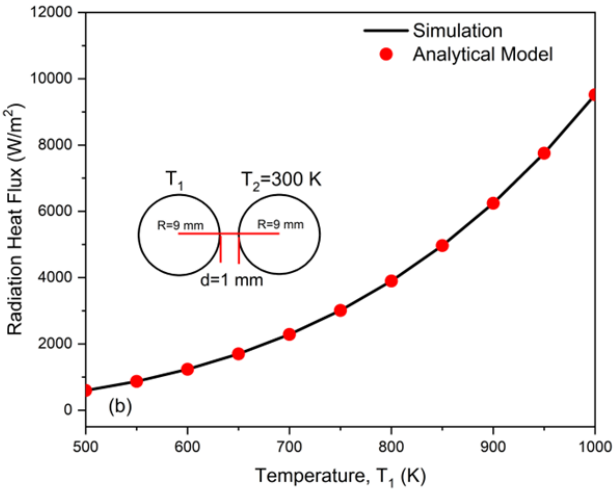

(b)

Figure 23. Validation of simulation results against analytical model for surface-to-surface radiation modeling (a) radiation heat flux vs. distance *d* between two cells with fixed cell temperatures; (b) radiation heat flux vs. Temperature T_1 of Cell 1 with fixed distance *d* and temperature T_2 of Cell 2.

Multifrontal Massively Parallel Sparse (MUMPS) solver is used to solve for the thermal energy conservation equation. Backward Differentiation Formula (BDF) method is used for time stepping. The relative tolerance for the solution is 10^{-3}. Based on this general methodology, a number of investigations are carried out to understand the nature of radiation induced thermal runaway, as well as the coupling between radiation and chemical heat generation. These results are discussed in the next section.

In the following (Sec. 3.1-3.3), we have adopted a cell spacing *d* of 1 mm to investigate the feature of radiation induced thermal runaway. There are two primary considerations behind the choice of d: energy density and safety. For energy considerations, the larger the cell spacing, the fewer number of cells can be accommodated in a given space, hence reducing the energy density of the pack. For safety, however, larger spacing is preferred, as thermal runaway propagation less likely. As such, there is eventually a trade-off effect between these two considerations. Cell spacing of 1 mm in a battery pack has been adopted previously in [147–149]. Note that concepts and techniques developed in this work can also easily be applied to investigate radiative heat transfer for other cell spacing configurations.

3. Results and discussions

3.1 General features of radiation induced thermal runaway

Figure 24(a) shows the evolution of maximum temperature of Cell 2 with different temperature of Cell 1, T_1. The results show that for $T_1 > 602$ K, thermal runaway occurs in Cell 2, as indicated by the sharp increase in T_2. For all these cases, the higher the T_1, the

earlier is the thermal runaway triggered in Cell 2, as expected. When T_1 is increased to 900K, the thermal runaway delay time is reduced to around 1 min. There is a sharp change in the nature of curves in Figure 24(a) when T_1 is below a threshold value of 602 K, wherein it is found that thermal runaway is not triggered in Cell 2, even at much longer times. The maximum temperature of Cell 2 in such cases is found to eventually reduce to around 450 K where a quasi-thermal equilibrium is reached due to the balance between the net radiation heat flux and chemical heat generation.

Figure 24(b) presents plots of T_2 as well as various dimensionless concentrations for two cases very close to the threshold found in Figure 24(a) T_1 = 601 K and T_1 = 602 K. As shown in Figure 24(b), the dimensionless SEI concentration is completely consumed around 2000 s for both T_1 = 602 K and 601 K cases, much earlier than the complete consumptions of other species, which occur at the instant of thermal runaway. Results suggest that the four chemical reactions may occur at different stages of thermal runaway, and their occurrence can be decoupled depending on the thermal runaway time scale. Evolution of the other dimensionless concentrations shows distinct behaviors, with much stronger consumption under thermal runaway conditions, as expected.

By defining the onset of thermal runaway as the instant with the maximum rate of temperature rise, Figure 25(a) and (b) plot spatial distributions of temperature and net heat generation rate, respectively, within Cell 2 at the onset of thermal runaway. It can be seen that the maximum temperature and peak heat release occurs in the vicinity of the surface of Cell 2 for high triggering temperature T_1, due to the large radiation heat flux from Cell 1. For extremely high T_1, the surface temperature of Cell 2 will rise so rapidly that thermal

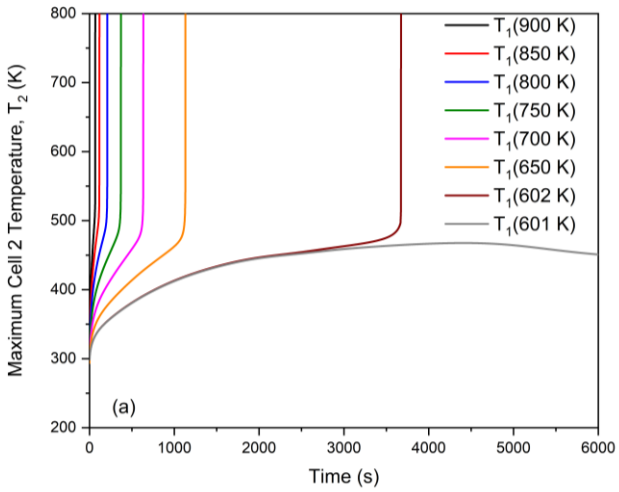

(a)

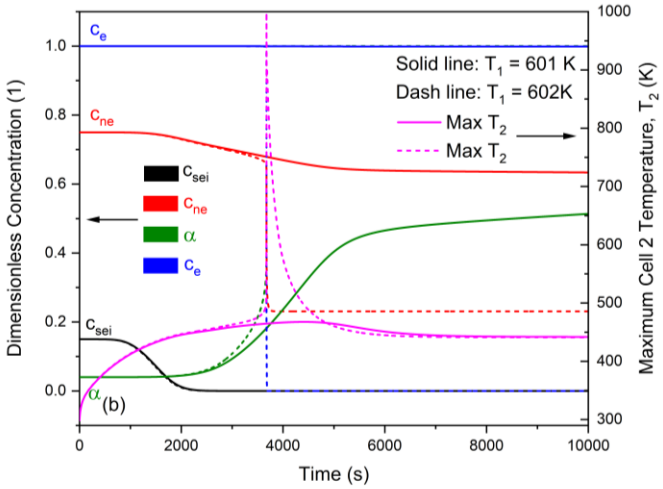

(b)

Figure 24. (a) maximum temperature of Cell 2 as a function of time for different T_1; (b) comparison of evolution of average dimensionless concentration and temperature for two cases close to the thermal runaway threshold T_1 = 601 K (solid lines) and T_1 = 602 K (dashed lines).

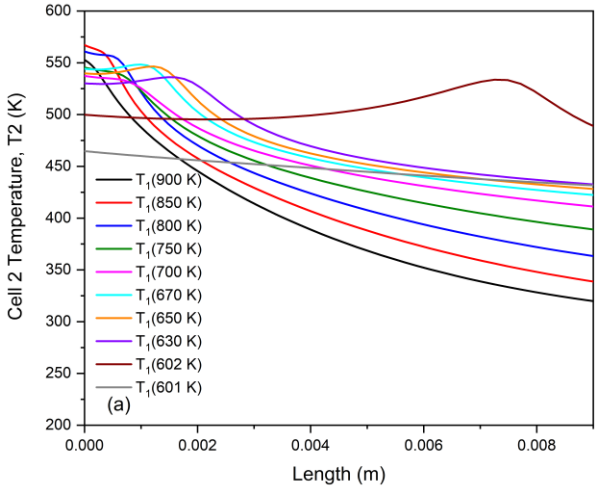

(a)

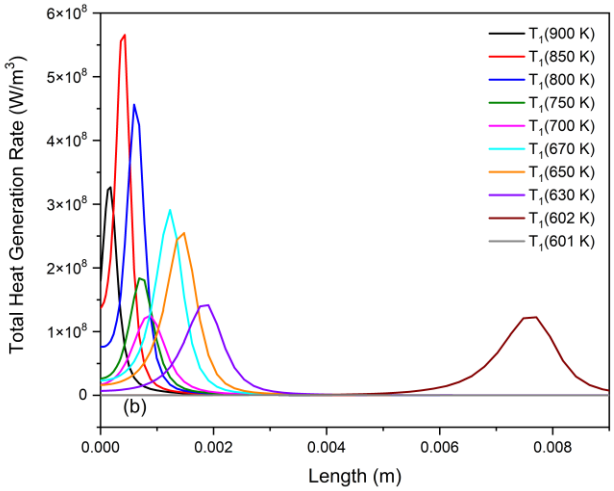

(b)

Figure 25. (a) temperature distribution; (b) heat generation rate distributions within Cell 2 at the time of onset of thermal runaway for different values of T_1.

runaway will occur at or very close to the surface. Given that thermal runaway for high T_1 occurs so rapidly, as shown in Figure 24(a), it is expected that radiation plays the sole dominant role for temperature rise during thermal runaway. At lower values of T_1, the location corresponding to the maximum temperature and peak heat release gradually moves to the internal region of the battery, indicating increased influence of heat conduction and heat generation from the chemical reactions during the much longer thermal runaway. For the threshold case with T_1 = 602 K, the peak heat release occurs very close to the center of Cell 2. The distinction between high T_1 and low T_1 behavior shown in Figure 25 can be explained on the increase of radiation time scales at reduced temperatures, where thermal conduction, as much slower, diffusive process, tends to play increasingly significant role.

To further characterize the different thermal chemical processes for thermal runaway triggered by high and low temperature radiation, Figure 26 shows the evolution of dimensionless concentration and temperature in Cell 2 for a relatively high triggering temperature T_1 = 900 K. Compared to the low triggering temperature case with T_1 = 602 K shown in Figure 24(b), the thermal runaway is triggered much quicker. More interestingly, the mean dimensionless concentrations in the high temperature 900 K scenario do not exhibit obvious change before thermal runaway is triggered. The reactions are not separated in either spatial or time domain, and tend to be activated simultaneously in the vicinity of the battery surface due to rapid radiative heating.

In summary, results so far demonstrate that radiation induced onset of thermal runaway exhibits intrinsic differences depending on the triggering temperature: when $T_1$is high, the thermal runaway is triggered very fast in the vicinity of the battery surface, and

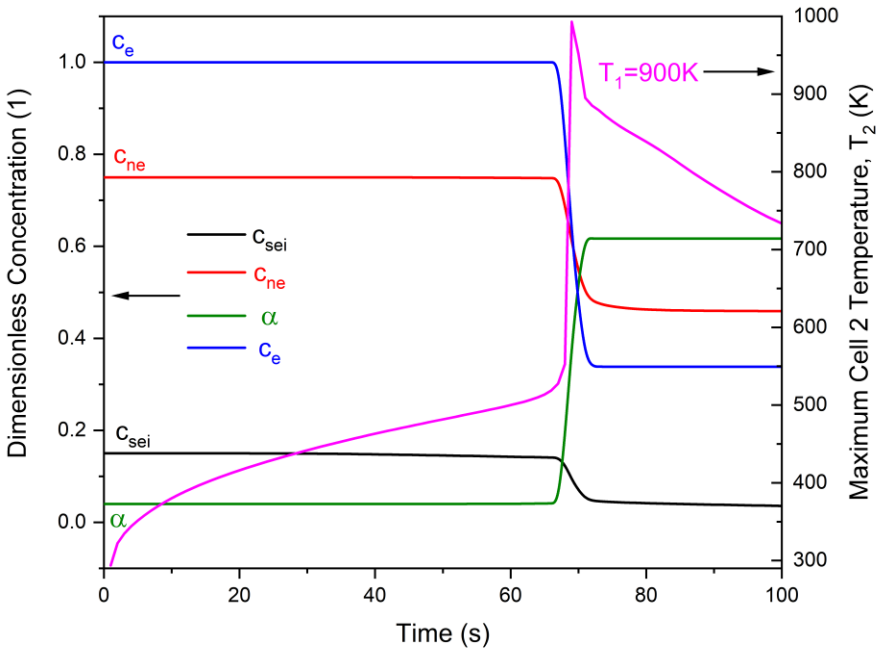

Figure 26. Evolution of average dimensionless concentration and temperature with thermal runaway triggering temperature T_1 = 900 K.

the thermal runaway reactions occur simultaneously in spatial and time. In such a case, radiation plays a solely dominant and direct role. In contrast, for low T_1, thermal runaway is triggered much slowly in the internal region of the battery, and the thermal runaway reactions can separate in spatial and time domains due to the depletion of certain species. In this case, radiation plays a less significant role.

3.2 Non-monotonicity in radiation induced thermal runaway

It should be noted that although Cell 2 receives radiation heat flux from Cell 1, it also emits radiation to the ambient. Therefore, at a certain state, the net radiation heat flux may become zero, even before thermal runaway occurs. In this scenario, the net radiation heat flux on Cell 2 can actually be negative, which may counteract the occurrence of thermal runaway. Figure 27 shows the evolution of net radiation heat flux q over the surface of Cell 2. It can be seen that for cases with T_1 = 602 K, q transitions to a negative value much earlier than the onset of thermal runaway, defined as the instant with maximum temperature rise rate. Therefore, in this case, radiation facilitates thermal runaway in the early stage before net radiation flux vanishes, and it actually mitigates thermal runaway in the later stage when net radiation flux becomes negative. With elevated temperature – when T_1 reaches close to 650 K, the cross over state of q occurs very close to the onset of thermal runaway, indicating the constant promotion effects of radiation during thermal runaway at higher triggering temperatures.

To further characterize the role of radiative heat transfer at different triggering temperatures, a time integrated radiative heat flux is calculated by integrating the net radiation flux q over the surface of Cell 2 from the initial condition to the instant of when

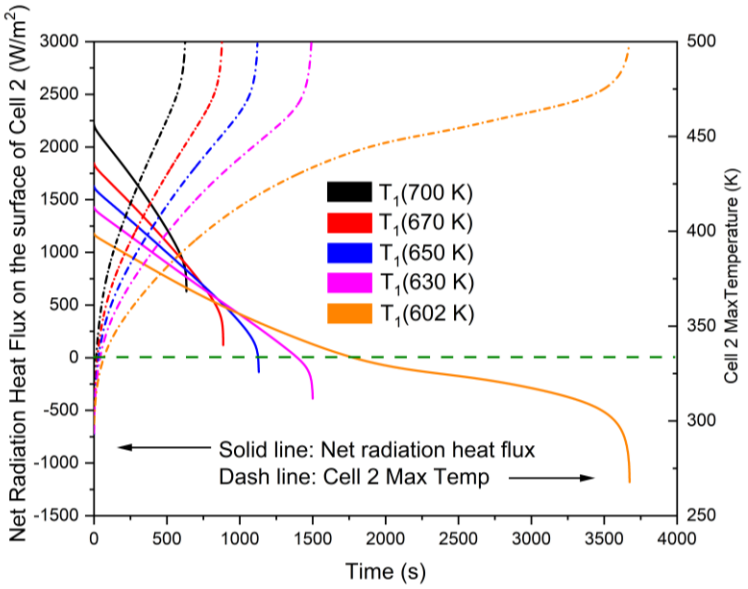

Figure 27. Evolution of net radiation heat flux *q* during thermal runaway with different T_1.

the net radiation heat flux in Cell 2 vanishes. This provides a basis to evaluate the maximum facilitation effect of radiation on the triggering of thermal runaway. Interestingly, as shown in Figure 28, the time-integrated radiative heat flux so defined exhibits a counter-intuitive non-monotonic dependence on temperature. On the high temperature branch, the integrated radiative heat flux decreases with increase in the triggering temperature, as expected. However, the peak integrated radiative heat flux does not occur at the lowest temperature, as one might expect. Instead, it occurs at an intermediate temperature, around 700 K in this case. One possible explanation of such a non-monotonic trend may be offered by considering the time duration for the integral: higher triggering temperature T_1 leads to higher radiative heat flux, which nevertheless leads to a much shorter time scale to cancel out net radiation flux q. On the other hand, lower triggering temperature T_1 leads to lower radiative heat flux, which, however, elongates the time scale to cancel out net radiation. This nevertheless only partially explains the role of radiation with varying triggering temperature, in that heat release from the exothermic thermal runaway reactions will also facilitate the temperature increment. With longer thermal runaway delay time at low temperatures, it allows longer residence time for the chemical reaction progress and heat release to accumulate internally within the cell.

3.3 Role of pre-runaway chemical heat release in radiation induced thermal runaway

To isolate the effect of chemical heat release before thermal runaway, Figure 29 compares the maximum temperature evolution of Cell 2 with and without the chemical heat source term included in the calculations. Results without chemical heat release

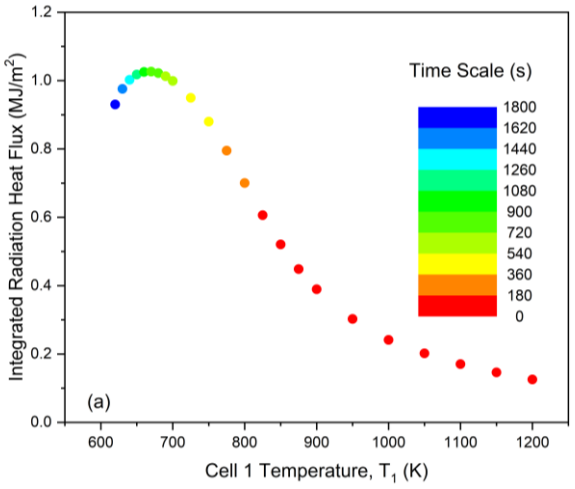

(a)

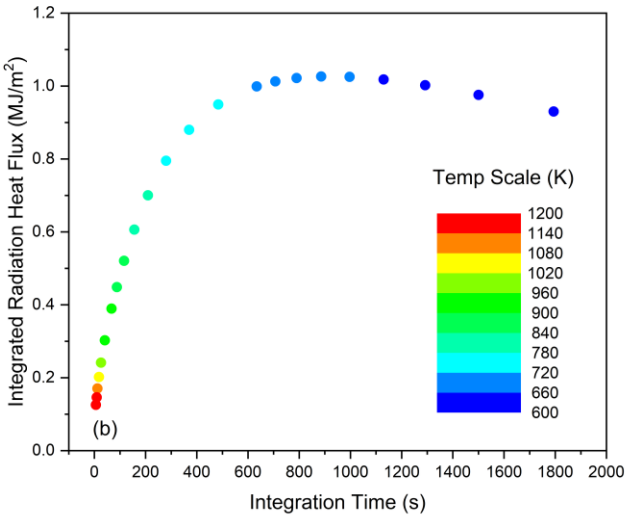

(b)

Figure 28. (a) time integrated net radiation heat flux at different triggering temperature, color indicates the time with zero net radiation flux; (b) time integrated net radiation heat flux versus integration time, color indicates thermal runaway triggering temperature.

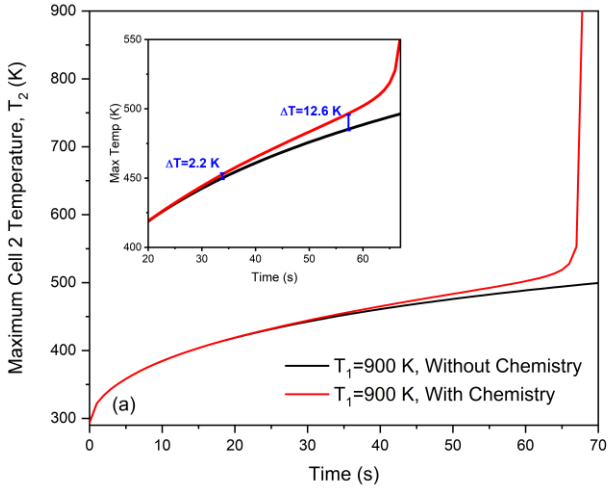

(a)

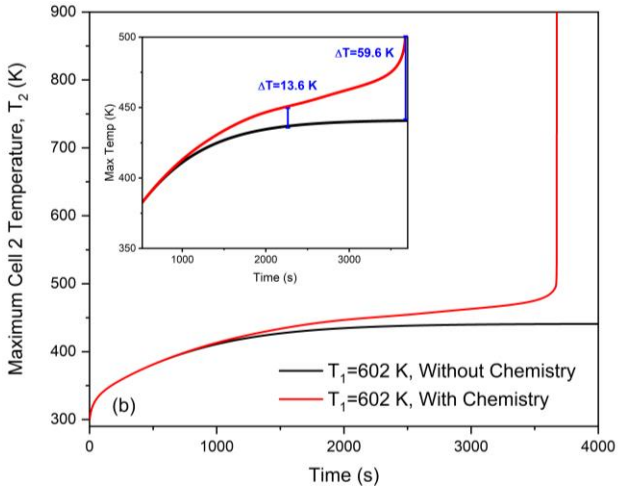

(b)

Figure 29. Temperature evolution with and without chemistry (a) in high triggering temperature T_1 = 900 K; (b) in low triggering temperature T_1 = 602 K, showing the role of heat release from pre-runaway chemistry.

represent contributions solely from radiation, while the difference between the cases with and without chemistry effectively represents the contribution from chemical heat release. We can select a temperature as the onset temperature of thermal runaway during the temperature rise, for example 450 K or 500 K, and evaluate the temperature differences at these selected reference points. Figure 29(a) plots the temperature evolution with and without chemistry in high triggering temperature case T_1 = 900 K. At reference onset temperature T_{ref} = 450 K, the temperature difference ΔT between the cases with and without chemistry is around 2.2 K, indicating the role of pre-runaway chemistry. Considering the total temperature rise at the reference $T_{\mathrm{ref}} - T_{\mathrm{ini}} = 450 - 293 = 157$ K includes the combined effects of radiation and pre-runaway chemistry, the contribution of chemistry can therefore be reasonably isolated. Similarly, in the lower triggering temperature case as shown in Figure 29(b), the contribution of pre-runaway chemistry increases the battery temperature by 13.6 K, much higher compared to the higher triggering temperature case in Figure 29(a).

The ratio of temperature rise from pre-runaway chemistry to the total temperature rise is evaluated at different triggering temperatures. It is shown in Figure 30 that at high triggering temperatures, the contribution of pre-runaway chemistry is very small, below 1 % for T_{ref} = 450 K, and below 5 % for T_{ref} = 500 K. This indicates the sole dominant role of radiation for high temperature radiation induced thermal runaway. While for the low triggering temperature conditions, the contribution of pre-runaway chemistry increases to around 10 % for reference temperature 450 K and nearly 30 % for onset reference

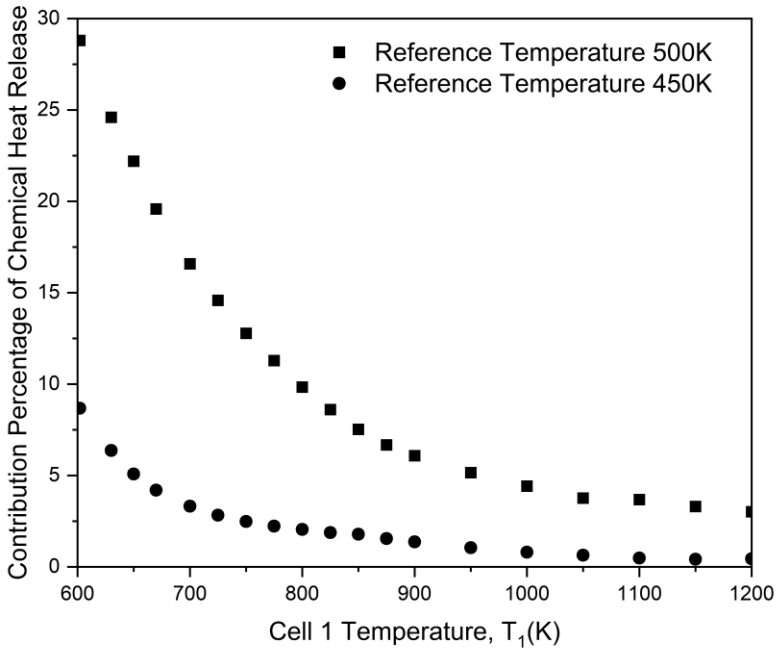

Figure 30. The contribution of chemical heat release during radiation induced thermal runaway with different T_1.

temperature 500 K. The impact of pre-runaway chemistry becomes comparable to radiation and hence cannot be neglected.

3.4 Effects from blockage on radiation heat flux in practical battery packs

In practical battery packs, depending on the separation distance d, thermal radiation from a trigger cell to another cell in the pack may be blocked by adjacent cells. For example, as shown by the schematic plot in Figure 31, radiation flux from *O1* to *O2* is blocked by the presence of *O3*, in that any photon emitted beyond point A on the surface of *O1* is unable to directly reach the surface of *O2*. In general, the interest is in determining the extent of radiative exchange that will occur between any pair of cells in a battery pack, how this is influenced by the presence of other cells and how the cells are arranged in the pack. Here, we considered two specific packing arrangements - equal-spacing homogenous or orthogonal.

Following Hotel's classical cross string theory [146], the view factor for arbitrary 2D geometry can be evaluated as:

$$F_{12} = \frac{\sum crossed\ strings - \sum uncrossed\ strings}{2 * source\ string} \tag{53.}$$

For the case of homogeneous arrangement of cells, we can express the view factor between cells 1 and 2, F_{12} as:

$$F_{12} = \frac{2 * \left(\widehat{AB} + BC + \widehat{CD}\right) - 2 * \left(AE + \widehat{EF} + FG\right)}{2 * 2\pi R} \tag{54.}$$

$$= \frac{\left(\frac{2\pi R}{3} + 2Rtan\theta\right) - \left(4Rtan\theta + R\left(\frac{\pi}{3} - 2\theta\right)\right)}{2\pi R}$$

$$= \frac{1}{6} - \frac{tan\theta}{\pi} + \frac{\theta}{\pi} = \frac{1}{6} - \frac{\sqrt{h^2-4}}{2\pi} + \frac{1}{\pi} arccos\frac{2}{h}$$

Equation (52.) and (54.) can then be compared to understand the effect of blockage on radiation effect in a homogenously arranged battery pack, as demonstrated in Figure 32. As $h = H/R$ approaches 2, the gap between each pair of cells approaches 0. This is the limit where the effect of blocking is most substantial, and it is shown that the difference of view factor and hence the radiation heat flux is as large as 8.2 % with and without blockage. In the other limit with gradually increased cell separations, the effect from blockage gradually vanishes as expected, and hence Equation (52.) and (54.) reduce to the same results.

Instead of being homogenously arranged, a more widely adopted practical real geometry of battery pack is the orthogonal configuration, as shown in Figure 33. Compared to the homogeneous arrangement, this configuration has reduced energy density for a given packing volume but provides more convenience for sequential and parallel electrical interconnection, as well as provisioning of cooling. In this configuration, assuming the hot radiation source is the center Cell 5. The radiation heat flux from Cell 5 to any one of its immediate neighbors 2, 4, 6 and 8 is free of blockage, and, using Equation (52.), the view factor may be written as

$$F_{52} = F_{54} = F_{56} = F_{58} = \frac{\sqrt{h^2-4} - h + 2\arcsin\left(\frac{2}{h}\right)}{2\pi} \qquad (55.)$$

Radiative heat flux from the center cell 5 to any one of the other cells 1, 3, 7, and 9 can potentially be blocked, depending on the average separation among the cells. Due to symmetry, one can easily recognize that these view factors are equal:

$$F_{51} = F_{53} = F_{57} = F_{59} \qquad (56.)$$

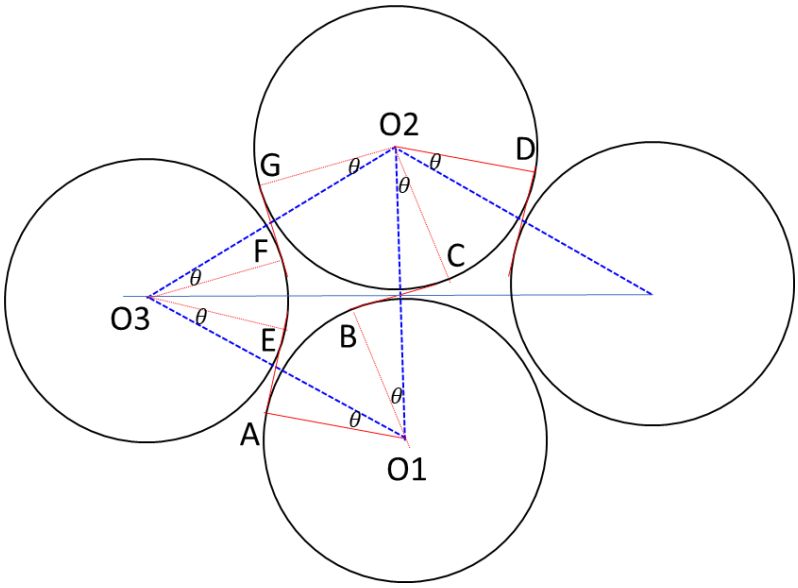

Figure 31. Schematic of a typical geometry where radiation flux between two equal cylinders *O1* and *O2* are blocked symmetrically by two extra equal cylinders, radius *R* and separation gap *d*.

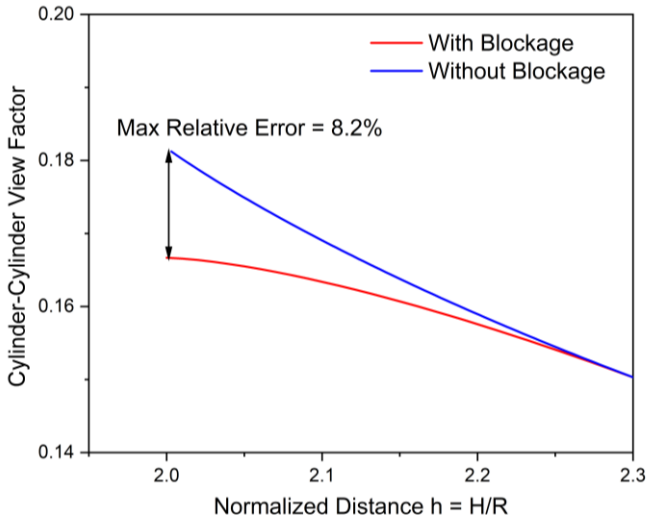

Figure 32. Comparison of viewer factors with and without the blockage between adjacent cells in equally-spaced homogenous array.

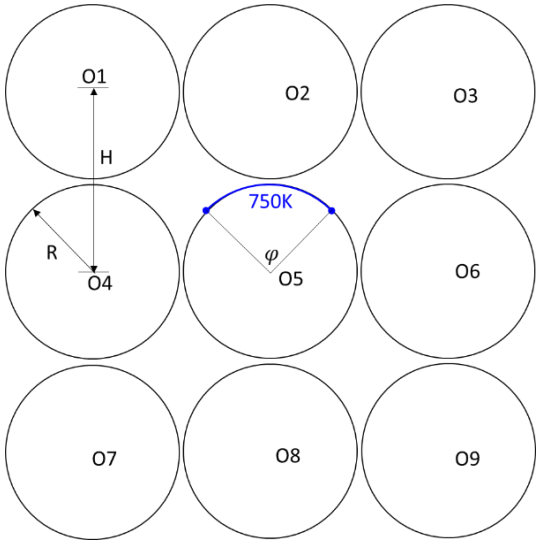

Figure 33. A common orthogonal arrangement of cylindrical battery packs with radius *R* and cell center distance *H*, *h* = *H/R*.

Given the definition of view factor, the sum of view factor from cell 5 to all reachable surfaces must be unity with sufficient small cell gaps. In other words, no radiation emission from cell 5 is able to escape from all the cells around: We hence can obtain:

$$F_{51} = F_{53} = F_{57} = F_{59} = \frac{1}{4} - \frac{\sqrt{h^2 - 4} - h + 2\,arcsin\left(\frac{2}{h}\right)}{2\pi} \qquad (57.)$$

With these view factors analytically obtained, the radiation heat flux from the center Cell 5 to all its adjacent cells with and without blockage can be easily evaluated. A comparison of the view factor in Equations (55.) and (57.) is presented in Figure 34, with Cells 2, 4, 6, and 8 as the closest cells relative to the trigger cell 5, and 1, 3, 7, and 9 being next-closest cells. It is very interesting to see that there is a threshold cell separation distance h ~ 2.7, within which the closest cells receive higher radiation while beyond which the corner cells receive higher radiation. For 18650 cell arrays, this limiting aspect ratio of h = 2.7 corresponds to a cell gap of 6.3 mm. In the other limit of h = 2 where cells directly touch with their closest neighbors, the radiation heat flux on the closest neighboring cell is more than two times higher than that received by the corner ones. With gradually increased spacing, the radiation heat flux drops on the closest cells and increases on the corner cells. This provides direct guidance on battery arrangement in arrays in order to suppress thermal runaway.

3.5 Effects of radiation from localized hot spots

It should be noted that the view factor for radiation heat flux calculation is based on the assumption that Cell 5 has a uniform surface temperature. Under certain conditions,

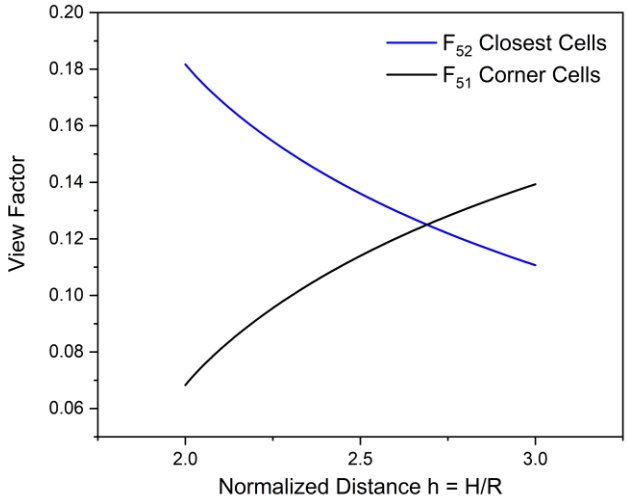

Figure 34. Comparison of viewer factors among different adjacent cells in orthogonal arrangement in Figure 47.

the presence of localized hot spots may result in a non-uniform battery surface temperature, which may complicate the nature of radiative heat transfer. In such a case, the problem is no longer symmetric, similar to the one discussed in the previous sub-section. Therefore, radiative heat flux to each cell must be calculated separately. In order to investigate such effects, localized hot spots are introduced as shown in Figure 33, represented by the blue arc segment on the surface of Cell 5. The size of the hot spot is characterized by the angle φ shown in Figure 33, while the center of the hot spot is located along the center line of Cells 5 and 2. This hot spot is assigned a representative temperature of 750 K, while the rest part of Cell 5 is assumed to be at 300 K. A cell-to-cell gap of 1 mm is assumed. As we change the hot spot size, it is expected that both the radiative surface area and the view factor will vary accordingly.

Figure 35 shows the radiative heat flux per unit receiving surface area for hot spot sizes of 20°, 45°, 90° and 360°. In the 360° case, we observe that each radiative heat flux on Cells 2, 4, 6, and 8 accounts for 17 % of the total radiation, and that each radiative heat flux on Cells 1, 3, 7, and 9 accounts for 8 %, consistent with their corresponding view factors shown in Figure 34. With reduced hot spot size to 90º, more than 60 % of the total radiation is received by Cell 2, the closest one to the hot spot, with a similar radiation heat flux on Cell 2 to the 360°case. With further reduced hot spot sizes to 45° and 20°, the radiation flux is reduced as expected, 80 % and more radiation from the hot spot is directly emitted to the closest Cell 2. This shows that the nature of radiative heat transfer between cells, and thus, the nature of thermal runaway propagation depends on the size of the hot spot. Mitigation strategies, therefore, must account for the nature of the hot spots expected.

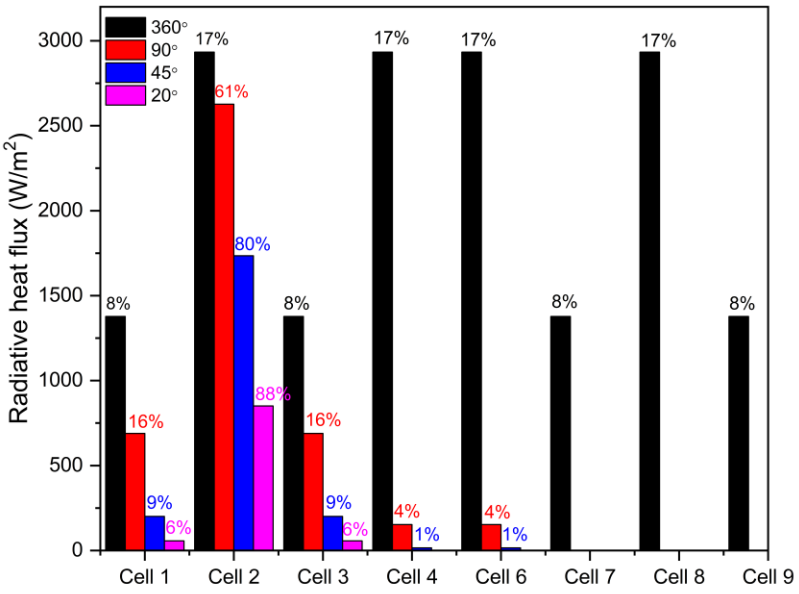

Figure 35. Radiation heat flux in an orthogonal 3×3 battery array with localized hot spot.

In the limiting case of an infinitely small hot spot, it can be shown that the view factor from the hot spot to an adjacent circle degenerates to *R/H*. This theoretical result can be applicable to highly localized hot spots, such as small, hot particles from venting events.

4. Conclusion

Based on carefully designed and validated calculations and numerical simulation, the interplay between radiation and pre-runaway chemistry in battery thermal runaway propagation is identified in the current study. Results evaluate the role of radiative heat transfer from a hot trigger cell to colder neighboring cells in the propagation of thermal runaway.

Results indicate that radiation induced thermal runaway exhibits intrinsic differences between low and high trigger temperature regimes - at high triggering temperatures, thermal runaway is triggered very rapidly close to the battery surface, and the thermal runaway reactions occur simultaneously in space and time. In this case, radiation plays a solely dominant and direct role. In contrast, at low trigger temperature, thermal runaway is triggered much more slowly and deeper in the cell, and the thermal runaway reactions can separate in spatial and temporal domains due to the depletion of certain species.

By investigating the evolution of the net radiation flux during thermal runaway, we have found that the net radiation heat flux has a cross-over instant, beyond which the net radiation heat flux becomes negative. Therefore, radiation can either facilitate or mitigate thermal runaway. For high temperature conditions, the cross-over state is very close to the onset of thermal runaway, as such radiation constantly facilities thermal runaway. In

contrast, under low temperature conditions, the cross-over state can be far ahead of the onset of thermal runaway, therefore radiation facilitates thermal runaway in the earlier stage and mitigates thermal runaway in the later stage.

Results from this work identify the non-monotonic role of radiation in thermal runaway triggering and provide direct insights into the complex interaction of two highly nonlinear phenomena - radiation heat transfer and chemical reactions during thermal runaway. The time-integrated radiation heat flux exhibits a non-monotonic dependence on the triggering temperature. The underlying reasons can be twofold: for one thing, the delay time of thermal runaway is substantially longer for low temperature conditions, albeit with a lower radiation heat flux; for another, the pre-runaway chemistry plays an increasingly significant role in increasing the battery temperature under lower triggering temperature conditions, which must be considered for radiation induced thermal runaway propagation.

We analytically evaluated the view factor accounting for equal-spaced homogenous arrangement and orthogonal arrangement of cells in practical battery packs. It was shown that the blocking effect in the equally-spaced homogenous arrangement can decrease the radiation heat flux by as much as 8.2 %. While in the orthogonal arrangement, a threshold cell separation distance exists, within which, the closest cells receive higher radiation while beyond which the corner batteries receive higher radiation. The results indicate that radiation induced thermal runaway propagation in a pack is not necessarily along the trajectory among closest cells. Radiation effects from a localized hot spot with varying sizes were also investigated, showing the increased focusing effects and necessitating specific thermal runaway prevention methods.

In the context of relatively little past work on radiative heat transfer during thermal runaway propagation, this work makes fundamental contributions in understanding the role of radiation, and its interplay with chemical reactions that cause thermal runaway. The insights gained from this work may help develop strategies for reduced thermal runaway propagation, and hence, safer battery packs.

CHAPTER III

CELL TO CELL VARIABILITY IN LI-ION BATTERY THERMAL RUNAWAY: EXPERIMENTAL TESTING, STATISTICAL ANALYSIS, AND KINETIC MODELING

A version of this chapter was originally published by Liwen Zhang, Shiyou Yang, Lu Liu, Peng Zhao:

L. Zhang, S. Yang, L. Liu, P. Zhao, "Cell-to-cell variability in Li-ion battery thermal runaway: Experimental testing, statistical analysis, and kinetic modeling." *Journal of Energy Storage* 56 (2022): 106024.

CRediT authorship contribution statement

Liwen Zhang: Investigation, Formal Analysis and Writing; Lu Liu: Validation and Editing; Shiyou Yang: Conceptualization and Writing - Review & Editing; Peng Zhao: Conceptualization, Methodology, Investigation and Writing - Review & Editing

Abstract

As one of the most promising energy storage mediums, Lithium-ion batteries (LIBs) have attracted extensive research interest. A major challenge associated with LIB application is thermal runaway, which can be triggered under abused conditions and impose direct threats to lives and properties. Here, we select Li-ion batteries with lithium cobalt oxide cathode and graphite anode (18650, Samsung), with relatively simple chemistry, to revisit thermal runaway. The experiment is conducted using an accelerating rate calorimeter (EV+ ARC, Thermal Hazard Technology) following the heat-wait-seek strategy, and is repeated for 9 similar new cells with 100 % state of charge (SOC). Key features such as onset temperature of self-heating, the onset temperature of thermal runaway, maximum heat release rate, thermal runaway delay time, and maximum temperature are measured experimentally. Although the cells are all brand new and have been initiated similarly, obvious cell-to-cell variability has been observed in the measured exothermic onset temperature, delay time,

and mass losses. It is also shown that the widely used four-step thermal runway model cannot quantitatively capture the activation energy from the heat release rate. To improve the kinetic modeling and accommodate the cell-to-cell variability, statistical analysis is conducted to process the experimental results. Mean and standard error of the frequency factor and activation energy has been acquired to determine the lower and upper bound of the kinetic modeling using a one-step global chemistry. The measured and simulated thermal runaway delay time has reached a reasonable agreement, with the uncertainty of the kinetic model considered. The role of reactant consumption during the heating process is also discussed. The identified cell-to-cell variability should not only be considered for cell-level safety evaluation and modeling, but also in the thermal runaway propagation of battery modules and packs.

1. Introduction

With the global trend of decarbonization and electrification, research and development of Lithium-ion batteries (LIBs) have attracted extensive interest for applications in ground transportation and energy storage [6,7,150–152]. One of the biggest challenges in LIB is thermal runaway, where side reactions among battery materials can occur under abused conditions, such as over-heating, over-charging, collision, and internal short circuits. These side reactions not only release heat to elevate the battery temperature but also release flammable gases and particles that can induce subsequent combustion and fire, which triggers the propagation of thermal runaway on a larger scale. Thermal runaway directly threats lives and properties and is hence a key factor for the design and safety evaluation of future batteries.

Fundamentally, by drawing an analogy between thermal runaway and combustion, a charged battery carries "fuel" and "oxidizer" internally, containing all the reactants needed to be flammable and explosive. Figure 36 shows the thermal runaway mechanism using a typical LIB with $LiCoO_2$ cathode, the electrolyte of ethylene carbonate ($C_3H_4O_3$) and Lithium hexafluorophosphate ($LiPF_6$), and a graphite anode. The solid-electrolyte-interphase layer is thermally unstable and can decompose when it is subject to high-temperature conditions. The lithium in the anode will then directly contact the electrolyte and form lithium carbonate and ethylene. In addition, the cathode and electrolyte can directly react through the oxygen generated from cathode decomposition. Finally, the electrolyte material carbonate and salt can decompose under elevated temperatures. These reactions are largely exothermic and are accompanied by the formation of gases such as ethylene and oxygen. For other battery cathode materials such as NMC, the reactions and the corresponding products can be more complex.

So, what has been done to mitigate thermal runaway initiation? From the modeling aspect, Xu et al. have shown that with an appropriate design of cooling strategy, heat release from the battery can be effectively removed such that it is less likely for thermal runaway to be triggered [78]. Zhang et al. have computationally identified the safety regime boundary for thermal runaway, where the critical heat source intensity and duration time for a hot spot that can trigger self-sustained thermal runaway has been evaluated based on the minimum ignition energy concept [144]. More recently, the concept of mild combustion and stretched S-curve is adopted to inform battery material screening, such that a high heat release rate from a strong ignition event can be fundamentally avoided [145]. From the

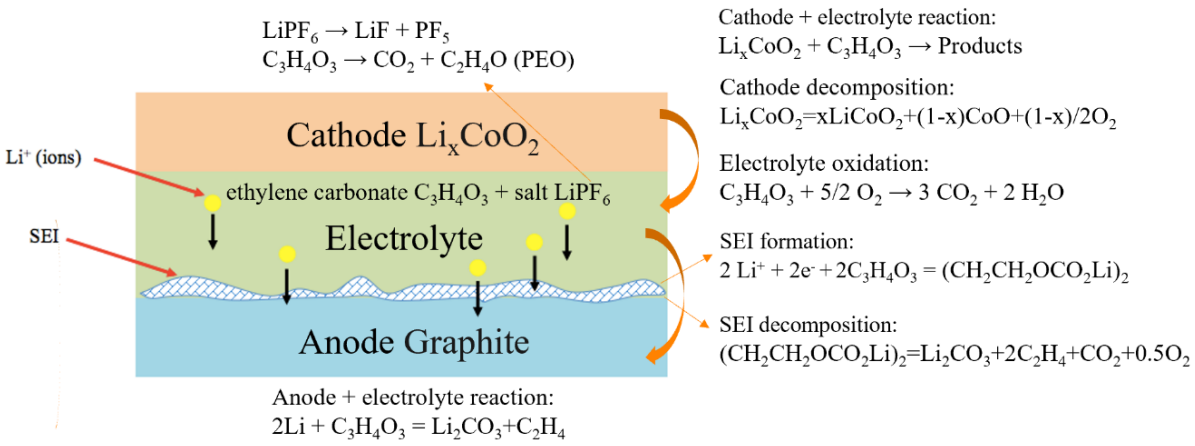

Figure 36. Configuration and thermal runaway reactions for a typical LCO LIB.

battery design aspect, Hou et al. [153] have introduced fire-resistant electrolyte-based LIBs, and shown that unfortunately, they cannot completely avoid thermal runaway. This is because flammability measures the reactivity of electrolytes with oxygen, which doesn't relate to the chemical reactivity of most thermal runaway initiation reactions. Another intriguing design is the solid-state LIBs that utilize thin metal oxide film as Li conductors. According to the testing results by Chen et al. [154], thermal runaway can still occur potentially due to the cross-talk reactions between Li in the anode and the oxygen generated from the decomposition of the metal oxides. In summary, although there is still no universal strategy that can completely avoid LIB thermal runaway, the probability of thermal runaway can be largely reduced through battery material screening, manufacturing, thermal management, and cooling design.

So far, most thermal runaway testing and modeling are based on a single sample experiment. Due to the heterogeneous and multiphase nature of the battery, as well as the multi-physical nature of thermal runaway phenomena, a single sample experiment might not be able to reflect the safety characteristics of batteries with the same chemistry and design in general. In this work, we revisit thermal runaway testing and modeling over the extensively investigated, relatively better-understood LIBs with LCO chemistry, using a recently established, well-calibrated facility EV+ ARC (THT) following the well-controlled heat-wait-seek (HWS) strategy. By repeating the experiment using nine similar cells with near-identical initial conditions, our results conclude that thermal runaway is highly sensitive to the cell-to-cell variations due to manufacturing inconsistency. Therefore, it can be misleading to conduct a safety evaluation or develop thermal runaway

chemistry based on a single set of thermal runaway experiments. Statistical analysis will be a necessary tool to fairly evaluate the tendency of thermal runaway and to interpret the experimental data.

The primary objectives and contribution of the current work are three-fold: first, we have identified the cell-to-cell variability in battery thermal runaway testing; second, we have evaluated the reactant consumption effects during the heating period of the test; last, we would like to demonstrate how statistical analysis can be utilized to interpret thermal runaway testing data and guide modeling.

2. Methodology

2.1 Experimental methodologies

2.1.1 Battery initialization

In this work, commercial 18650 Li-ion batteries with a $LiCoO_2$ (LCO) cathode and graphite anode (Samsung) are used. The technical specification of the battery we used in this study is available at [155]. The basic parameters of the battery are listed in Table 11.

Before thermal runaway testing, all batteries are cycled using a MACCOR 4200 system with an environmental chamber to achieve similar initial conditions. Detailed test procedures for the batteries are summarized in Table 12 and Table 13, respectively. In these test procedures, charging is done via a constant current constant voltage (CCCV) method, which means charging at a given constant current until reaching the maximum voltage given by the manufacturers, followed by charging with the maximum voltage until the current decreases to C/10. Discharging is done with a given constant current until the cut-off voltage 2.75 V is reached. Measurements of mass, voltage, and capacity only show

Table 11. Basic parameters of the test battery.

Parameter (unit)	Value
Model	ICR18650-30B
Chemistry	$LiCoO_2$/Graphite
Height (mm)	65
Diameter (mm)	18
Rated capacity (Ah)	2.95
Nominal voltage (V)	3.78
Charging voltage (V)	4.35
Discharging cut-off voltage (V)	2.75
Max. charge/discharge current (C)	1/2
Operating temperature (^oC)	0~45 (Charge) -20~60 (Discharge)
Cell weight (g)	$\leq$ 48.0

Table 12. Initialization of the batteries.

Battery No.	Test Procedures
Batt 1-3	Step 1: 0.5 C Charge – 0.2 C Discharge – 0.5 C fully Charge at 25 ℃
Batt 4-6	Step 1: 0.5 C Charge – 0.2 C Discharge – 0.5 C fully Charge at 25 ℃. Step 2: 1 C Discharge at 0 ℃~50 ℃, 0.5 C Charge at 25 ℃. Step 3: 0.1 / 0.5 / 1 / 2 C Discharge-0.5 C Charge at 25 ℃. Step 4: 0.5C Charge/Discharge cycle 10 times at 25 ℃.
Batt 7-9	Step 1: 0.2 C Charge – 0.2 C Discharge – 0.2 C Charge – 0.2 C Discharge – 0.2 C Charge at 25 ℃. Step 2: 0.1 C Charge / Discharge cycle 2 times at 25 ℃

Table 13. Mass, voltage, and capacity for the nine 18650 LCO batteries.

Battery No.	Mass (g)	Voltage (V)	Capacity (Ah)
Batt 1	46.262	4.33	2.941
Batt 2	46.312	4.32	2.936
Batt 3	46.312	4.33	2.936
Batt 4	46.109	4.35	2.818
Batt 5	46.261	4.35	2.810
Batt 6	46.264	4.35	2.825
Batt 7	46.326	4.32	2.853
Batt 8	46.279	4.32	2.870
Batt 9	46.217	4.32	2.860
Average	46.260	4.33	2.872
Standard deviation	0.066	0.014	0.053
Standard error	0.022	0.004	0.017

small deviations of initial conditions among the testing cells, as listed in Table 13. Before carrying out the ARC test, all the test batteries are at 100 % state of charge (SOC). It should be noted that although there are slight differences in the initialization procedure of each group, we nevertheless do not expect these normal cycling processes can introduce substantial variations in thermal runaway as we shall demonstrate later. Actually, all the cells exhibit nearly identical voltage, capacity, impedance and charging-discharging curves before thermal runaway experiments. On the other hand, each group of three cells actually goes through exactly the same initialization procedure, the differences in their thermal runaway behavior therefore can serve as strong evidence for cell variability.

2.1.2 ARC testing procedure

The first prototype of accelerating rate calorimetry (ARC) was made commercially available by the Dow Chemical Company in 1980s [156]. The thermal runaway testing facility used in this work is the advanced EV+ARC, manufactured by Thermal Hazard Technology (THT), as shown in Figure 37(a). The calorimeter of the EV+ARC has an internal size of 40 cm in diameter and 44 cm in depth. The physical arrangement of the test cell in the EV+ ARC is shown in Figure 37(b). We first carefully remove the test battery from its shrink wrapping and attach the N-type thermocouple to the middle surface of the test battery with a glass cloth tape. The N-type thermocouple used to continuously detect the battery temperature has been carefully calibrated with standard samples, and the sensitivity of the system is within 0.02 ℃/min. The test battery is then suspended from the aluminum frame with thin iron wire to ensure uniform heating from the top, side, and bottom heaters.

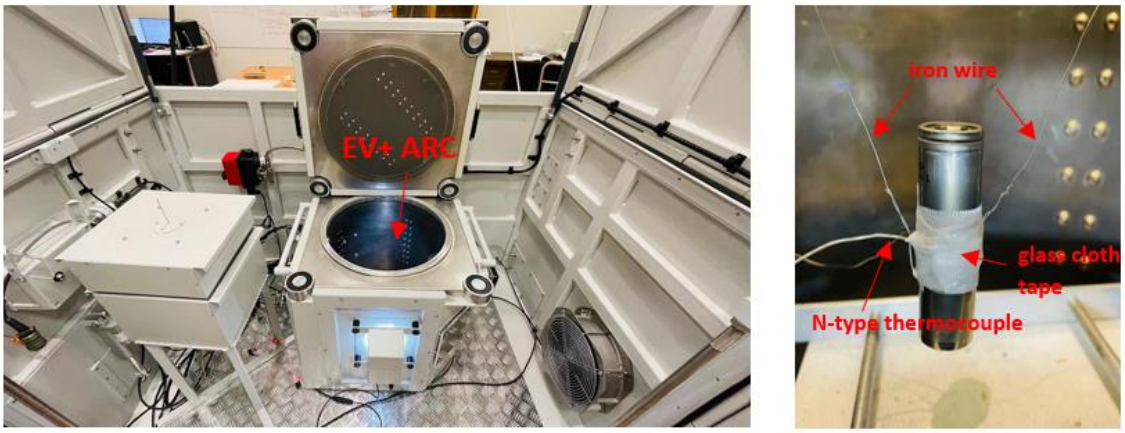

(a) (b)

Figure 37. (a) EV+ARC at UTSI; (b) suspension of 18650 cells in the EV+ chamber.

In this study, the heat-wait-seek (HWS) method is adopted to trigger thermal runaway. The logic flow chart and typical temperature profile and key responses during thermal runaway following the HWS strategy are shown in Figure 38(a) and (b), respectively. At first, the test battery is heated up from ambient temperature until the surface temperature reaches 50 ℃, then the wait mode is activated and will last for 45 min, to ensure thermal equilibrium between the ARC and the battery. Then the system enters "seek" mode to search for the temperature rise rate of exothermic reactions and compare it with the temperature rate sensitivity of 0.02 ℃/min. If the measured temperature rise rate is above the threshold, the system will switch to exotherm mode. This mode allows a nearly adiabatic environment with no temperature difference between the heaters and the sample, especially when the self-heating rate is below a threshold value [157]. As a result, HWS allows tracking of the cell temperature evolution in the near-adiabatic scenario. On the other hand, if the detected temperature rise rate is below the threshold, the system will perform the next HWS step. In our test, each heating step increases the battery temperature by 5 ℃. In either heating or exotherm mode, when the temperature exceeds the given maximum of 300 ℃, the heaters shut down completely and the system starts cooling down by introducing pressurized nitrogen. It is worth noting that the potential effects of internal and external heat transfer during an ARC experiment is carefully analyzed recently in [158].

Based on the ARC test, key parameters of thermal stability of the test battery can be obtained such as self-heating onset temperature (T_{exo}), thermal runaway onset temperature (T_{TR}), maximum temperature (T_{max}), thermal runaway delay time, and the slope

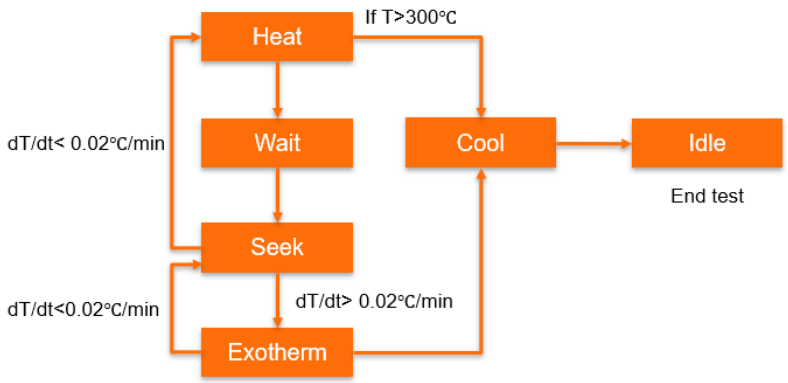

(a)

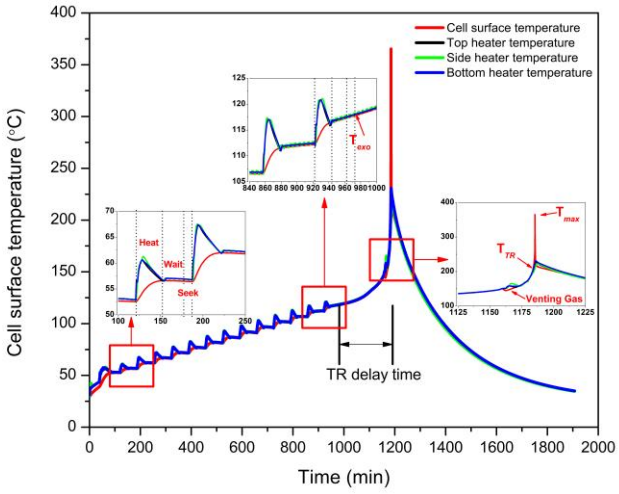

(b)

Figure 38. (a) logic flow chart of the ARC thermal runaway test following HWS strategy; (b) a typical temperature history and key responses during thermal runaway following the HWS strategy.

of the temperature evolution curve – temperature rise rate (dT/dt), as shown a typical thermal runaway test triggered by HWS in Figure 38(b). In this study, the T_{exo} is defined as the temperature when the temperate rise rate of the test battery reaches 0.02 ℃/min, and the T_{TR} is defined as the temperature when the temperate rise rate of the test battery reaches 20 ℃/min. The time duration between T_{exo} and T_{TR} is defined as the thermal runaway delay time. These data will be used to derive the parameters involved in the subsequent thermal runaway model.

2.2 Numerical simulation approaches

2.2.1 ARC simulation strategy

For numerical simulation, both the 0D homogeneous model and the two-dimensional axisymmetric model (2D) have been conducted in COMSOL Multiphysics 5.5, to simulate the ARC experiment. Energy conservation equations for both models are listed in Table 14. For the lumped model, we assume that the battery interior is isothermal with zero temperature gradient. Hence, the energy balance equation can be simplified without considering the heat conduction inside the battery. For the 2D model, due to the axisymmetric geometry of the battery, the temperature inside the battery varies in both radial and axial directions. Both thermal runaway reaction and internal heat conduction are considered.

To predict ARC tests, the thermal boundary conditions in the model are set as adiabatic, ignoring convection and radiation. As explained in the previous section, when the test battery enters exotherm mode, the system achieves adiabatic to prevent the test battery from exchanging heat with its surroundings. The heat source term in the model that

Table 14. Energy balance equation for the lumped model and 2D axis model.

	Lumped Model	**2D axisymmetric Model**
Assumption	Isothermal domain	Thermal stratification exists
Governing Equation	$\rho c_p \frac{dT}{dt} = Q$	$\rho c_p \frac{\partial T}{\partial t} = \frac{1}{r}\frac{\partial}{\partial r}\left(kr\frac{\partial T}{\partial r}\right) + \frac{\partial}{\partial z}\left(k\frac{\partial T}{\partial z}\right) + Q$
Chemical reaction heat	$Q = Q_{sei} + Q_{ne} + Q_{pe} + Q_e$	$Q = Q_{sei} + Q_{ne} + Q_{pe} + Q_e$

triggers the thermal runaway of the battery comes from four commonly used chemical side reactions [75], which will be discussed in detail in the next section.

2.2.2 Four-step reaction model

In the four-step reaction model, the chemical heat release Q inside the battery comes from four semi-global thermal chemical reactions [70,75]. These exothermic reactions include the decomposition of solid-electrolyte-interface (SEI), the reaction between the anode and the electrolyte, the reaction between cathode and electrolyte, and electrolyte decomposition. The quantitative characteristics of these reactions depend on the battery material properties, thermal chemical parameters, and temperature. The reaction model, frequency factor, and activation energy that describe the kinetics between battery materials have been previously obtained by fitting the experimental measurements from accelerating rate calorimetry (ARC) and differential scanning calorimetry (DSC) tests [73]. The chemical reaction rates and heat generation have been widely adopted in literature [70,75] and are summarized in Table 15.

In order to validate the thermal runaway model, we compared the four-step reaction model against literature-reported oven test results [73]. The model parameters used in this study were collected from [75] to describe a fully charged battery with LCO/Graphite chemistry. A major difference from the ARC condition is that oven test simulation strongly relies on the radiation and convection boundary conditions. The comparison is shown in Figure 39, where both lumped and 2D axis model results are in good agreement with the literature result. As shall be shown later, such agreement based on a single cell test does not necessarily indicates the validity of the kinetic model. However, the results suggest an

Table 15. Reaction rates and heat sources of the four-step thermal abuse model.

Reaction term	Equations	
SEI decomposition	$\frac{dc_{sei}}{dt} = -A_{sei} exp\left[-\frac{E_{a,sei}}{RT}\right] c_{sei}^{m_{sei}}$	$Q_{sei} = -H_{sei} W_c \frac{dc_{sei}}{dt}$
Anode-electrolyte reaction	$\frac{dc_{ne}}{dt} = -A_{ne} exp\left[-\frac{t_{sei}}{t_{sei0}}\right] c_{ne}^{m_{ne,n}} exp\left[-\frac{E_{a,ne}}{RT}\right]$	$Q_{ne} = -H_{ne} W_c \frac{dc_{ne}}{dt}$
	$\frac{dt_{sei}}{dt} = A_{ne} exp\left[-\frac{t_{sei}}{t_{sei0}}\right] c_{ne}^{m_{ne,n}} exp\left[-\frac{E_{a,ne}}{RT}\right]$	
Cathode-electrolyte reaction	$\frac{d\alpha}{dt} = A_{pe} \alpha^{m_{pe,p1}} (1-\alpha)^{m_{pe,p2}} exp\left[-\frac{E_{a,pe}}{RT}\right]$	$Q_{pe} = -H_{pe} W_p \frac{d\alpha}{dt}$
Electrolyte decomposition	$\frac{dc_e}{dt} = -A_e exp\left[-\frac{E_{a,e}}{RT}\right] c_e^{m_e}$	$Q_e = -H_e W_e \frac{dc_e}{dt}$
Overall heat generation	$Q = Q_{sei} + Q_{ne} + Q_{pe} + Q_e$	

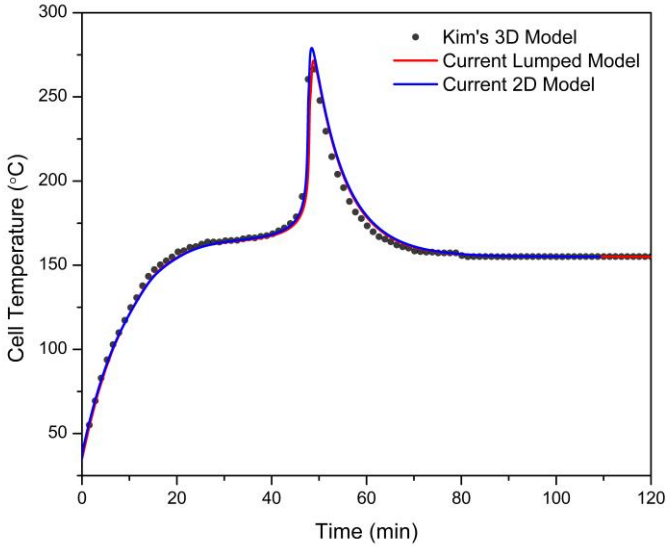

Figure 39. Validation of the four-step model against literature oven test results, radiation, and convection heat flux is applied as boundary conditions.

insignificant role of heat conduction for small 18650 cells, even in the worst case with both surface and internal heat transfer, hence the lumped model will be adopted.

2.2.3 Reactant consumption during the heating period

With a non-negligible duration of cells in a high-temperature environment, reactions such as SEI decomposition can occur even before the system detects the exothermic mode. Such reaction progress can affect the initial condition when the cell starts at the self-exothermic onset condition. From the experimental perspective, due to the temperature rate sensitivity (0.02 ℃/min) setting in the ARC test, it is evident that some chemical reactions have already occurred, but it is difficult to quantify the actual extent of chemical reactions at the exotherm onset temperature. Most previous simulations just neglect the consumption of reactants during the heating period, leading to ambiguities in thermal runaway modeling and prediction.

To investigate the consumption of reactants when the cell just entering exotherm mode, the preheating temperature profile of the ARC test is applied to the four-step reaction model to evaluate potential reactant consumption. Figure 40(a) demonstrates that there are significant changes in the dimensionless parameters during the heating period, especially c_{sei}, which indicates that the SEI decomposition reaction has occurred before the system detects the exotherm mode. The evolution of the battery temperature with and without reactant consumption is compared in Figure 40(b). The state at exothermic onset temperature is considered as time 0 for the delay time calculation. With reactant consumption considered, the pre-runaway heat release is much lower, leading to a substantially elongated thermal runaway delay time. Table 16 provides a summary of

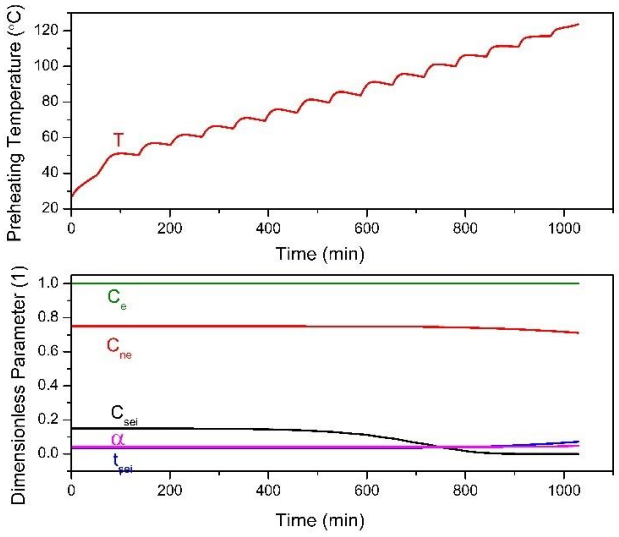

(a)

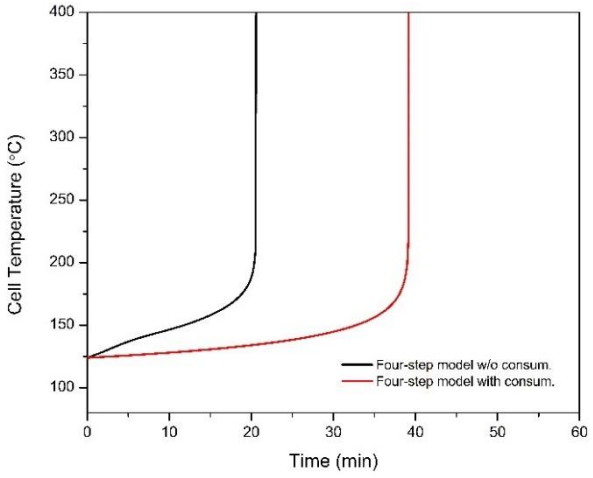

(b)

Figure 40. (a) battery reactant consumption during the heating period, corresponding to a typical HWS temperature trajectory with T_{exo} around 120 °C; (b) effect of heating period reactant consumption on thermal runaway delay time calculation using the four-step model.

Table 16. Model parameters in the four-step thermal abuse model.

Parameters (unit)	Model without reactants consumption	The model with reactant consumption
ρ (kg/m^3)	2780	
c_p (J/(kg·K)	730	
H (J/kg)	H_{sei} / H_{ne} / H_{pe} / H_e 2.57E5 / 1.174E6 / 3.14E5 / 1.55E5	
W (kg/m^3)	W_{sei} / W_{ne} / W_{pe} / W_e 610.4 / 640.4 / 1221 / 406.9	
E (J/mol)	E_{sei} / E_{ne} / E_{pe} / E_e 1.3508E5 / 1.3508E5 / 1.396E5 / 2.74E5	
A (s^{-1})	A_{sei} / A_{ne} / A_{pe}/ A_e 1.667E15 / 2.5E13 / 6.667E13 / 5.14E25	
T_{exo}(°C)	77.54 / 97.73 / 118.17 / 123.83	
c_{sei} (1)	0.15	0.1380 / 0.0511 / 2.55E-6 / 1.52E-9
c_{ne} (1)	0.75	0.749 / 0.7458 / 0.7218 / 0.7112
t_{sei}(1)	0.03	0.0333 / 0.0372 / 0.0612 / 0.0718
α (1)	0.04	0.040026 /0.0404 / 0.0443 / 0.0476
c_e (1)	1	1 / 1 / 1 / 1

parameter values used in the thermal abuse model, and the corresponding reactant consumption at four different experimentally determined self-heating onset temperature (T_{exo}). Different values in Table 16 correspond to the different self-heating onset temperature and heating temperature history of the four batteries Batt 8 (77 ℃), Batt 2 (98 ℃), Batt 1 (118 ℃), and Batt 4 (124 ℃). These are considered as representative heating profiles that cover the temperature range of all experiments. By applying the preheating temperature profile of these four experiments to the four-step kinetic model, we can evaluate the extent of reactant consumption for each condition.

3. Results and discussion

3.1 Experimental thermal runaway data and cell-to-cell variation

The experimental thermal runaway testing results of all the 18650 LCO cells have been summarized in Table 17. The onset temperature of exothermicity, T_{exo}, denotes the temperature when the time rise rate of battery temperature exceeds the threshold of 0.02 °C/min. The onset temperature of thermal runaway, T_{TR}, is defined as the temperature when the battery temperature rise rate is above 20 °C/min. The time duration in between T_{exo} and T_{TR} is defined as the thermal runaway delay time. After each experiment, the mass of the battery is weighted again to quantify the mass reduction during thermal runway, which includes gas and other battery components during the strong venting events. The maximum temperature of the cell during thermal runaway is also recorded, which includes potential error from strong venting and explosion event that may cause the thermocouple to fall off. From the testing results, a most obvious observation is that the cells exhibit substantial variations in all the thermal runaway responses such as the T_{exo}, T_{TR}, T_{max}, TR delay time

Table 17. Self-heating onset temperature, thermal runaway onset temperature, maximum temperature, thermal runaway delay time, and mass change during thermal runaway for all the nine 18650 Samsung LCO cells.

Battey Number	Exothermic onset Temp T_{exo}(℃)	Thermal runaway onset Temp T_{TR}(℃)	Max Temp T_{max}(℃)	TR delay time (min)	Mass change (g)
Batt 1	118.2	211.4	365.4	204.33	N/A
Batt 2	97.7	210.1	716.5	720.50	26.967
Batt 3	67.4	200.0	345.1	1308.96	9.951
Batt 4	123.8	220.9	456.5	121.52	27.131
Batt 5	77.7	201.1	384.2	897.43	21.674
Batt 6	77.4	195.4	392.7	802.80	24.405
Batt 7	76.9	228.6	390.3	1584.35	7.054
Batt 8	776	200.7	726.7	911.74	23.718
Batt 9	77.5	204.2	414.4	1044.03	9.797

and mass change. For example, self-heating starts to occur as low as 67 °C and as high as 123 °C, TR delay time also ranges from around 122 min to 1584 min. In addition, cell variation also exhibits in the detailed runaway process as shown in the cell temperature evolution in Figure 41. Batt 7 even shows a two-stage thermal runaway, which includes two individual exothermic processes separated by a venting event. While for the rest of the cells, the venting nevertheless occurs much closer to the main thermal runaway event. It is worth noting that some of the observed variations are coupled, for example, the TR delay time can be further affected by the uncertainty in T_{exo}. Obviously, the measurement uncertainty of T_{exo} can be as large as the heating step 5 °C, and a temperature rise of 5 °C in the exotherm mode (e.g., ~250 min) can take much longer than in the HWS mode (e.g., < 100 min). However, the observed variation in TR delay time is much larger than the sole effect of measurement uncertainty in T_{exo}. If we look at the results of Batt 5-9, which all exhibit a similar T_{exo} of 77 °C, their TR delay time nevertheless ranges from 802 min to 1584 min, indicating a strong variation much larger than 5 °C duration in different modes.

Since the experimental facility and the HWS heating protocol has been carefully calibrated with high sensitivity of 0.01 °C/min, the observed cell-to-cell variability is most likely induced by the manufacturing inconsistency and occurrence of defects within these cells. The results directly indicate that thermal runaway is very sensitive to manufacture variations even for fresh LIBs. Here cell variability is inevitable even among fresh cells; while for used cells, it is expected that cell variation can be further amplified from various extents of degradation. Consequently, safety evaluation based on a single cell testing is

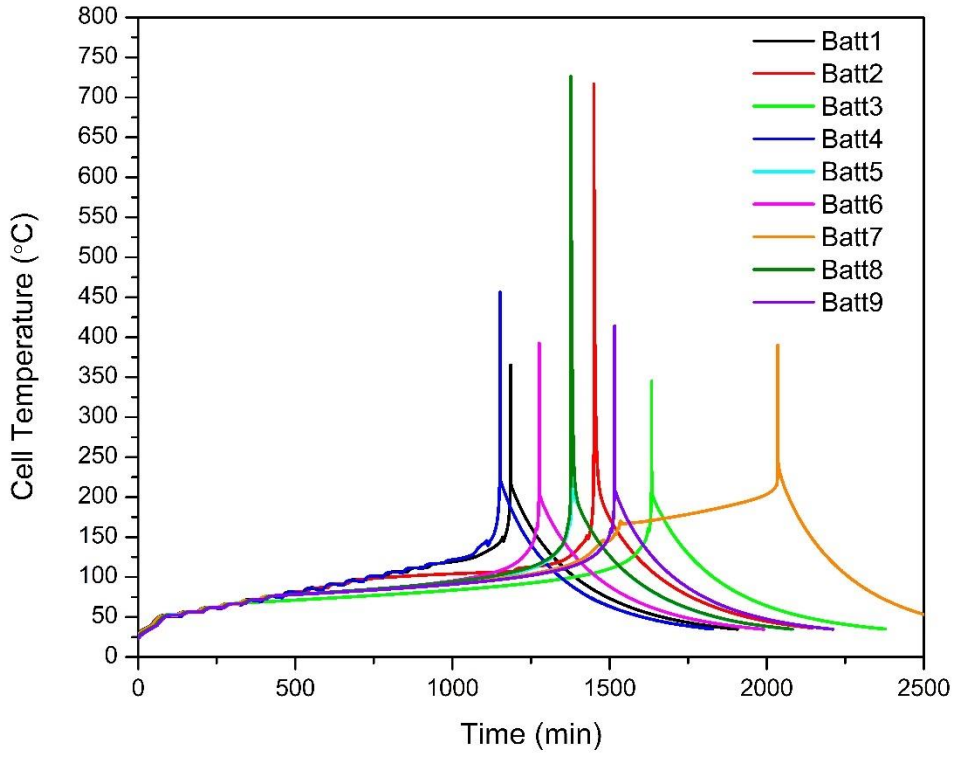

Figure 41. Battery temperature evolution during thermal runaway for all the 18650 LCO cells.

likely not representative of the statistically distributed performance of cells with the same design.

From the temperature evolution, frequency factor and the global activation energy can be readily obtained from the heat release rate. Based on the Arrhenius law, the self-heating rate can be expressed as [123,159,160] assuming adiabatic and ignoring reactant consumption:

$$\ln\left(\frac{dT}{dt}\right) \approx \ln(\Delta T_{ad} A) - \frac{E_a}{k_B T} \quad (58.)$$

where $\frac{dT}{dt}$ is self-heating temperature rate, ΔT_{ad}(K) is the difference between the initial exothermic temperature T_{exo} and the maximum temperature T_{max}, A(min^{-1}) is frequency factor, E_a(eV) is the activation energy, k_B is Boltzmann's constant (8.62E-5 eV·K^{-1}). Figure 42(a) plots the natural logarithm of the self-heating rate versus the inverse of temperature for the cells, except Batt 7 showing a two-stage thermal runaway. By using the linear region on the temperature rate profiles, the activation energy indicated by the slope varies from 0.83 to 1.0 eV and reaches great consistency among cells, confirming the same battery materials. The current data is also compared to the activation energy reported in the literature of 18650 cells with LCO chemistry from different manufacturers produced about a decade ago [159] as shown in Figure 42(b), which ranges from 1.3 to 1.7 eV. The average activation energy of the current cells is about 50 % lower, indicating lower thermal sensitivity.

Figure 43 (a) and (b) show the temperature evolution and heat release rate analysis of Batt 7. Interestingly, the two exothermic periods separated by the venting event share similar activation energy, while the second period exhibits a much larger scattering in heat

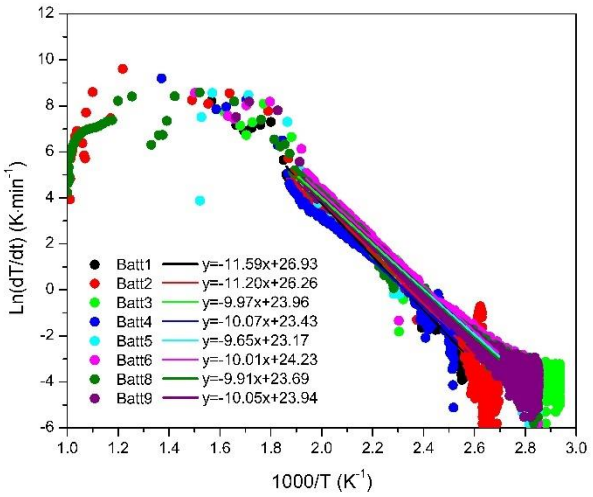

(a)

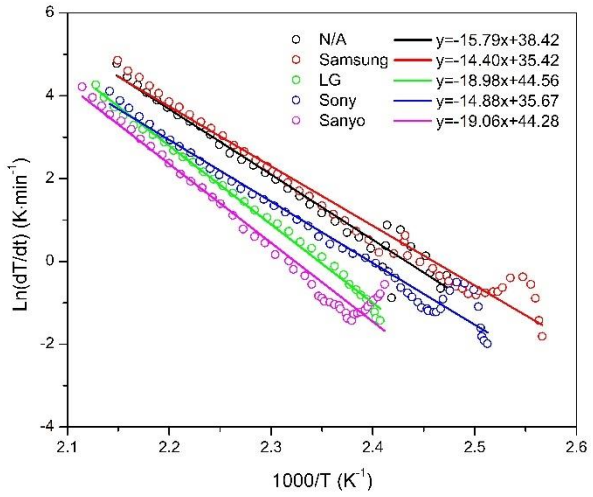

(b)

Figure 42. Frequency factor and activation energy from (a) the 18650 LCO cells utilized in the current work; (b) literature reported 18650 LCO cells.

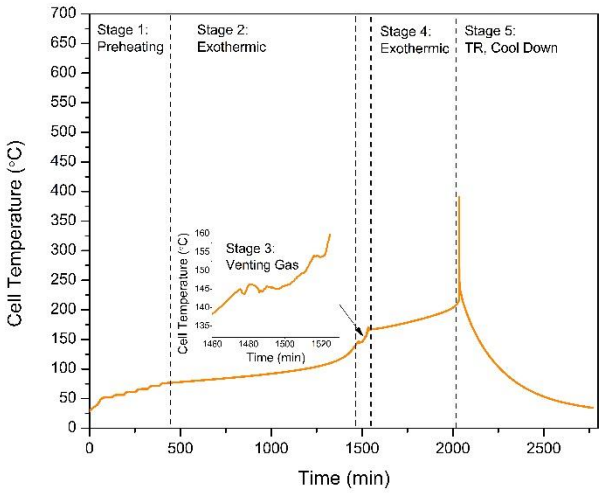

(a)

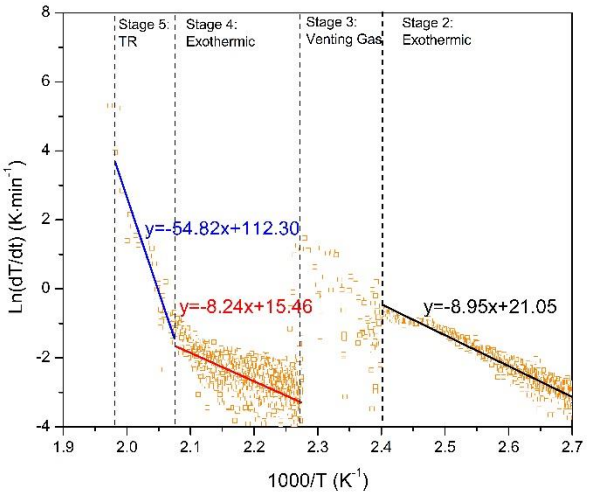

(b)

Figure 43. (a) temperature evolution; (b) activation energy of heat release for battery 7 with two-stage thermal runaway.

release rate. Another observation is that a substantial decrease in heat release rate is seen by the end of venting. The sudden pause of strong chemical reactions may be induced by partial consumption of the battery or by the limitation of some diffusion-controlled phenomena. In practice, although self-heating is triggered around 77 °C in Batt 7, it exhibits a much lower heat release rate when the temperature is above 150 °C and a much longer thermal runaway delay time, and is one of the safest among all the cells tested.

3.2 Challenges in thermal runaway modeling using the four-step model

The first modeling challenge arises when the global activation energy from the simulation fails to agree with that obtained from the ARC experiments. Figure 44 shows numerical simulation using the four-step kinetic model under three different initial temperatures. The simulation results show that there are multiple linear regions on the logarithmic plot with substantially different temperature rate profiles, therefore, we divide each simulation into three regions for separate linear fitting. Taking the experimental result as a reference, we focus on the middle region. As shown in Figure 44, the global activation energy from the simulation results using the four-step model is much higher compared to the current ARC experiments, while they have a closer agreement with the values of previously reported literature results [159] shown in Figure 42(b). This is a common challenge in numerical simulation when modeling results are inconsistent with experimental data. The problem is certainly addressable by tuning the kinetic model parameters, for example, through sensitivity analysis [161] and other optimization methods such as the genetic algorithm [162]. Given the under-constrained nature of this problem, there are multiple free parameters involved in the four-step model and multiple ways may

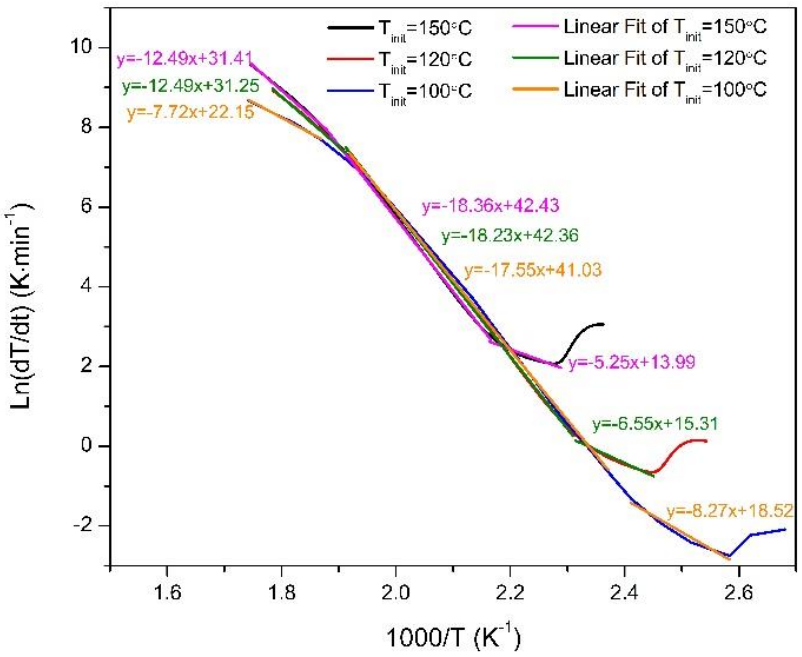

Figure 44. Simulation using the four-step mechanism showing much larger global activation.

exist to adjust the model to achieve similar global activation energy with the experiment. Consequently, one can obtain a set of model parameters that fit their particular thermal runaway testing data, which is however not mathematically unique and cannot be adopted in general even for the same cell materials and design.

Furthermore, the observed cell variability in thermal runaway testing can provide misleading targets for the development of thermal runaway chemistry and modeling. We use the widely adopted four reaction mechanism to simulate the ARC thermal runaway testing results. As shown in Figure 45, both Batt 1 and 4 have an exothermic onset temperature T_{exo} of approximately 120 °C, and they have nearly identical initial SOC, voltage, and capacity. When efforts are made trying to simulate these testing conditions with the LCO thermal runaway model, the first question that arises is that which should be selected as the target condition to compare against the modeling results? Without identifying the target of model performance, it is impossible to further adjust and optimize model parameters. Similar challenges occur when we try to simulate the thermal runaway conditions corresponding to T_{exo} of 77 °C, where Batt 5 to 9 all have similar T_{exo} but distinct runaway processes. As we show in the following, battery safety evaluation must be obtained from statistical analysis of behaviors of multiple cells, rather than from a single test – which is, unfortunately, a common practice in current literature [136,163–165].

3.3 Statistical analysis of thermal runaway results and the one-step model

To address the challenges induced by the parameter optimization of the four-step thermal runaway model, and the inherent cell variability shown from thermal runaway testing, we develop a statistical analysis method of thermal runaway based on a one-step

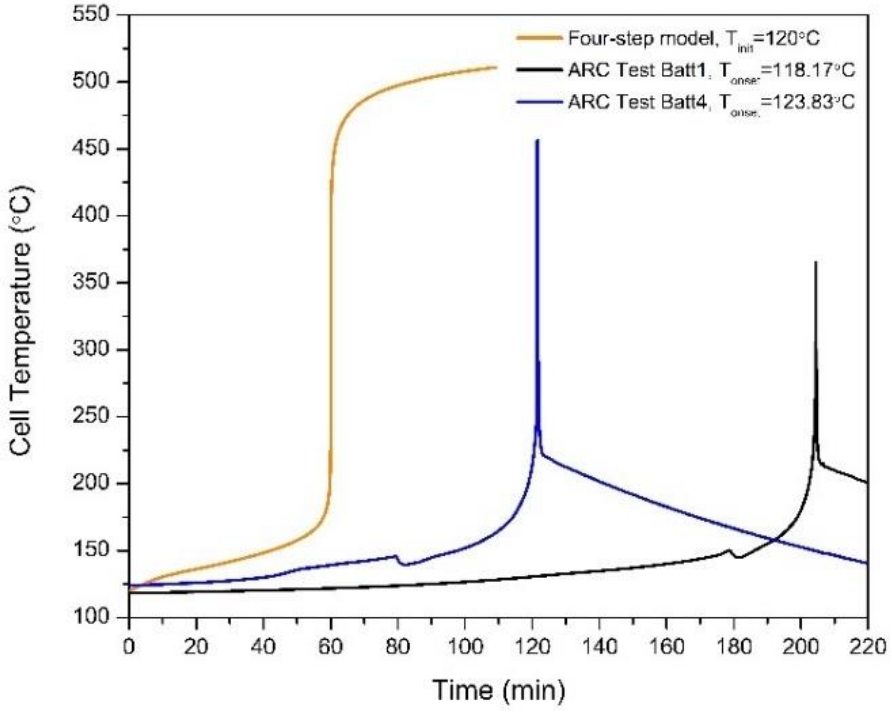

Figure 45. ARC simulation versus experiments (Battery 1 and 4) with onset temperature around 120 °C.

overall chemical model. The idea is rather straightforward: from the heat release profile of each ARC experiment, a one-step global chemical model in the Arrhenius form can be uniquely determined. By direct statistical analysis of the one-step global mechanism from each cell, the mean value and standard error of both the frequency factor and the activation energy can be readily obtained. The variations of the frequency factor and the activation energy can then be utilized to quantify the uncertainty range of the thermal runaway chemistry. By comparing the experimental data with the nominal value and uncertainty range of the modeling, a more rigorous evaluation of cell safety evaluation can be made on the basis of statistical analysis. Due to limited resources, our data reported in this work only cover 8 cells, the results are nevertheless sufficient to demonstrate the nature of cell variability as well as the usefulness and application of the statical analysis method.

The one-step global model will adopt the following species and energy conservation equations:

$$\frac{dc}{dt} = -Ace^{-\frac{E}{RT}} \tag{59.}$$

$$c_p \frac{dT}{dt} = HAce^{-\frac{E}{RT}} \tag{60.}$$

where the values of thermal chemical parameters are provided in Table 18. It should be noted that the specific total formation enthalpy satisfies $H = c_p \Delta T_{ad}$ under the current adiabatic condition. Therefore, the model results are independent of the choice of c_p, and the parameters including *A, E* and ΔT_{ad} can be uniquely determined from each experimental measurement. Through the statistical analysis, the frequency factor *A* can be expressed as 3.49E8$\pm$2.46E8 min^{-1}, and the global activation energy *E* is 8.58E4$\pm$2.05E3

Table 18. Statistical analysis of frequency factor and global activation energy of all 18650 Samsung LCO cells.

	ΔT_{ad} (K)	c_p (J/kg·K)	H (J/kg)	E (J/mol)	A (min^{-1})	Self-heating onset Temp T_{exo}(℃)	TR delay time (min)
Batt 1	247.2	730	1.80E5	9.65E4	2.00E9	118.2	204.33
Batt 2	618.7	730	4.52E5	9.33E4	4.10E8	97.7	720.50
Batt 3	277.8	730	2.03E5	8.30E4	9.00E8	67.4	1308.96
Batt 4	332.7	730	2.43E5	8.39E4	4.50E7	123.8	121.52
Batt 5	306.5	730	2.24E5	8.03E4	3.77E7	77.7	897.43
Batt 6	315.3	730	2.30E5	8.33E4	1.06E8	77.4	802.80
Batt 8	649.1	730	4.74E5	8.24E4	2.99E7	77.5	911.74
Batt 9	336.9	730	2.46E5	8.36E4	7.40E7	77.5	1044.03
Average	ΔT_{ave}: 385.5	$c_{p_{ave}}$: 730	H_{ave} : 2.29E5	E_{ave}: 8.58E4	A_{ave}: 3.49E8	T_{ave} : 89.7	t_{ave}: 751.41
Standard deviation	ΔT_{SD}: 156.3	$c_{p_{SD}}$: 0	H_{SD}: 1.73E4	E_{SD}: 5.80E3	A_{SD}: 6.95E8	T_{SD}: 21.2	t_{SD}: 404.12
Standard error	ΔT_{SE}: 55.3	$c_{p_{SE}}$: 0	H_{SE}: 6.12E3	E_{SE}: 2.05E3	A_{SE}: 2.46E8	T_{SE}: 7.5	t_{SE}: 142.9

J/mol. The global activation energy exhibits a much smaller percentage variation compared to the frequency factor. Also, due to the substantially different two-stage thermal runaway behavior, Batt 7 is not included in the statistics and is separately analyzed as shown in Figure 43.

3.4 Comparison of the modeling accounting for uncertainty from cell variability

With the nominal value and uncertainty available for the kinetic parameters obtained from the experimentally measured heat release rate, we can readily evaluate the uncertainty of the modeling results of other thermal runaway responses. The first key thermal runaway parameter we would like to predict is the exothermic onset temperature T_{exo}. According to the definition of T_{exo}, we can set the value of temperature rise rate in Equation (60.) to be 0.02 °C/min and solve the temperature. It is straightforward to see that the upper limit of the predicted exothermic onset temperature T_{exo} (110.24 °C) occurs when A takes minimum and E takes maximum, and that the lower limit of T_{exo} prediction (71.75 °C) occurs when A takes maximum and E takes minimum. The nominal value of the onset temperature (86.50 °C) is obtained when both A and E adopt their average values. The comparison of the experimental measured T_{exo} and model prediction accounting for uncertainty is shown in Figure 46, achieving reasonable agreement. The experimental measurement is either bounded by or very close to the upper and lower limits of the kinetic modeling. It should be noted that for each battery, if the reactant consumption effect is accounted for, then that the upper limit of onset temperature prediction will be further extended.

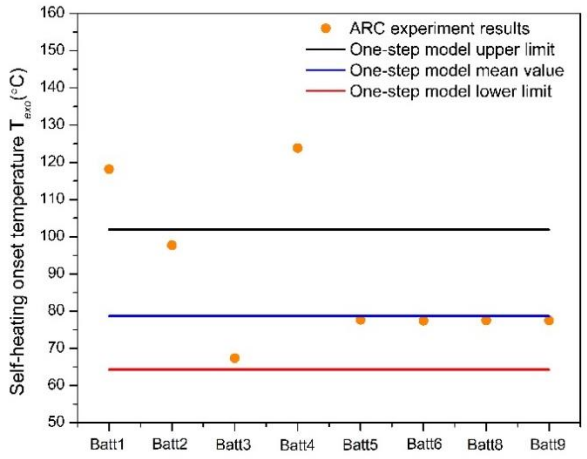

(a)

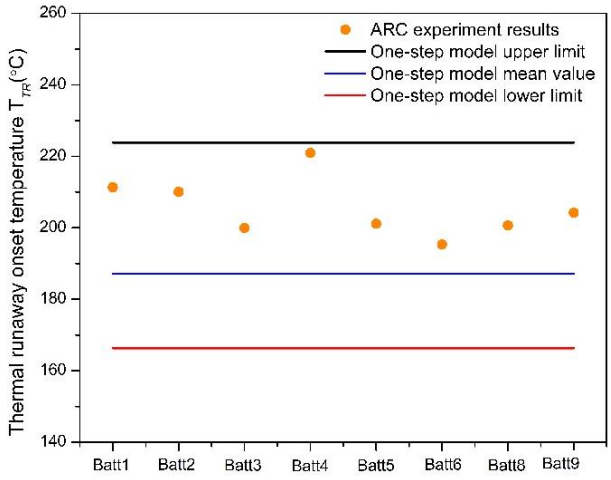

(b)

Figure 46. Comparison of the modeling and experiment for (a) exotherm onset temperature; (b) thermal runaway onset temperature, accounting for the variation in reaction kinetic parameters.

The next key thermal runaway parameter to be predicted is the thermal runaway delay time. Following the modeling procedure described in Sec. 2.2.3, the modeling effort includes both the four-step model and the one-step global model, accounting for the effect of potential reactant consumption during the heating period. Due to the non-negligible duration of cells in the high-temperature environment, reactions such as SEI decomposition can occur even before the system detects the exothermic mode. Such reaction progress can affect the initial condition when the cell starts at the self-exothermic onset condition. Figure 47(a) and (b) show the reactant concentration at the end of the heating process using both the four-step and one-step models following the experimental temperature profiles of a few representative tests. It is seen that reactant consumption is non-negligible for conditions with sufficiently high self-heating onset temperatures. For the one-step model, up to 25 % of the reactant can be consumed already before the system detects the exothermicity threshold, when T_{exo} is beyond 120 °C.

Figure 48 shows the comparison of the experimentally measured thermal runaway delay time and numerical simulations under various conditions. The most interesting set of comparisons is with the simulation results of the one-step model accounting for the uncertainty of the kinetic parameters. The upper limit of thermal runaway delay time is obtained by the combination of minimum value of *A* and maximum of *E*, while its lower limit is given by maximum *A* and minimum *E*. These two limits span by about one order of magnitude, indicating a large uncertainty for the thermal runaway delay time predicted by the one-step model. Through this comparison, it is intriguing that the experimental data are well within the upper and lower limits of the one-step kinetic modeling. With reactant

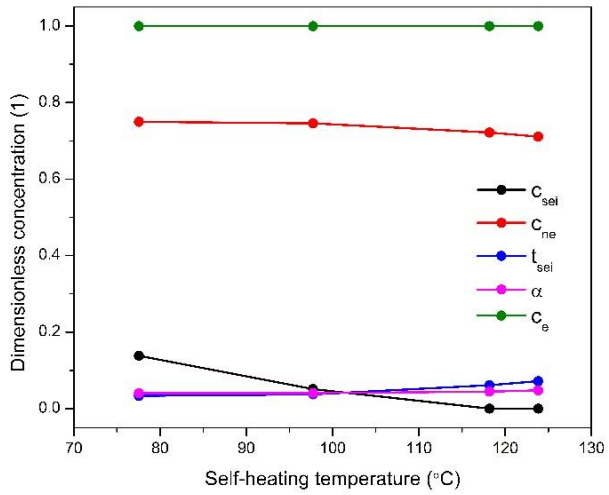

(a)

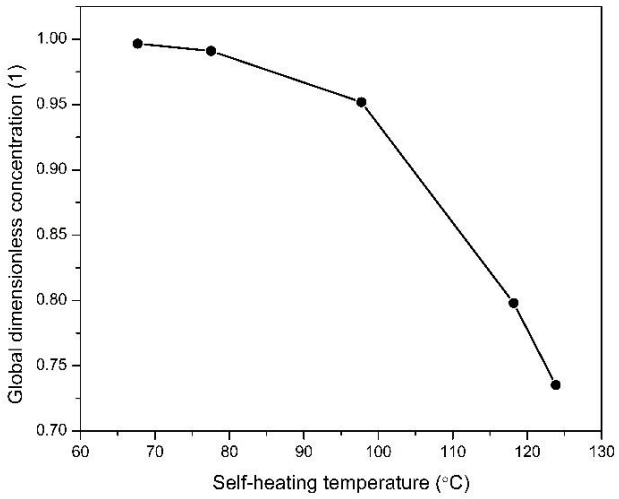

(b)

Figure 47. Change of dimensionless reaction concentration during the heating period for different exotherm temperatures (a) four-step model; (b) one-step model.

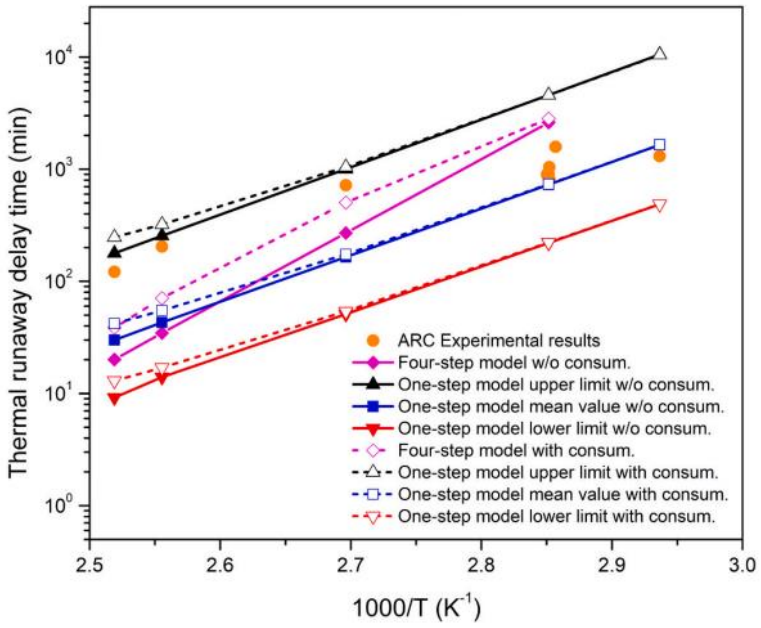

Figure 48. Comparison of the modeling and experiment for thermal runaway delay time, accounting for the variation in reaction kinetic parameters and the reactant consumption during heating.

consumption during heating further taken into account, the thermal runaway delay time can be elongated by a factor of two under the higher end of T_{exo}. Similar simulation conducted using the four-step thermal runaway model shows a stronger effect considering reactant consumption. Furthermore, it is seen that the thermal runaway delay time predicted by the four-step chemistry also lies in the uncertainty of the one-step model, which nevertheless exhibits a stronger temperature sensitivity.

3.5 Reflection on the thermal runaway experiment and data interpretation

Through the statistical analysis and detailed comparison between numerical simulation and experiment, it can be seen that safety evaluation based on a single cell testing is very likely not representative of the statistically distributed performance of cells with the same design, and can even provide misleading targets for the development of thermal runaway chemistry and modeling. This issue is unfortunately not carefully addressed in the vast volume of existing battery safety testing literature. By incorporating statistical analysis and uncertainty quantification, we can achieve rigorous and consistent safety evaluation, including a reasonable description of the scattered exothermic onset temperature and the thermal runaway delay time. It is expected that with more cells included, the uncertainty of the kinetic parameters can be further reduced, leading to improved accuracy of the prediction.

From the experimental observation, we note that a few key factors that can affect the interpretation and accuracy of the measured data. First of all, difference in the measured adiabatic temperature rise ΔT_{ad} is not necessarily a measurement error. LCO cells exhibit strong venting events, and these venting events are quite different among each test. Not all

the venting events lead to combustion and substantial heat release. Part of the heat released with the venting materials will not contribute to the heating of the battery. Eventually, the measured mass reduction of cells cannot be directly used in the energy balance. Thermodynamically we therefore should not expect the same ΔT_{ad} for LCO cells, unless we can ensure complete reaction of all materials and adiabatic heating on the battery and residuals. This is also confirmed by [166]. Secondly, there does exist a non-negligible experimental error associated with the measurement of the adiabatic temperature rise ΔT_{ad}, which will further affect the evaluation of the frequency *A* factor. For one thing, due to the design and control strategy of the EV+ ARC, heat loss is activated when the battery temperature reaches 300 °C. For another, the strong venting and explosion can cause the cell to swing in the chamber and collide with the chamber wall. This can lead to the potential failure of the glass cloth tape, where the thermocouple can fall off during such an intense thermal runaway. Both of these factors can lead to ambiguities in the maximum cell temperature measurement, and subsequent error propagation in the data processing. However, error from the maximum cell temperature measurement does not affect the measurement of the exothermic onset temperature, thermal runaway onset temperature, thermal runaway delay time, and the activation energy. Variations among these properties are substantial evidence of cell variability and necessitate statistical analysis and uncertainty quantification of battery safety evaluation.

Furthermore, cell degradation, heating rate and cell chemistry will certainly affect the observed cell variability. Firstly, fresh cells are utilized in the current testing, with negligible degradation. Stronger cell variability will be observed when comparing cells

with different extent of degradation. Secondly, the slow heating rate adopted in current HWS experiment allows longer residence time to observe the cell variability. In the scenario of ramp heating or conditions with much higher heating rate [167], we should expect weaker cell variability in thermal runaway. Thirdly, higher cell variability can be expected for cells with more sensitive and reactive materials.

Last but the not least, the current single cell thermal runaway experiment shed light on the complexity of the thermal runaway propagation. In the current statistical analysis, we have attributed all the factors leading to variability such as defects, particle size, manufacturing inconsistency to the thermal runaway chemistry. Consequently, there is an uncertainty in thermal runaway kinetics among all the cells with nearly identical initial conditions. Therefore, it is not feasible to predict which cell starts thermal runaway first when a battery module of similar cells is exposed to similar heating condition. Eventually, it is not quite feasible to predict the path of thermal runaway propagation that leads to a great safety concern.

4. Conclusion

Through carefully conducted ARC thermal runaway experiments via step heating, the current work has provided solid evidence for the cell-to-cell variability in fresh commercial 18650 LCO cells with similar initial conditions. These variations include non-negligible differences in the measured thermal runaway responses including exothermic onset temperature, thermal runaway onset temperature delay time, maximum temperature, and mass reduction, as well as in the observed venting events. These variations suggest that thermal runaway can be very sensitive to manufacture inconsistency and defects generated

during thermal runaway, as such, the behavior of a single cell might not be representative of the average performance of multiple cells. Therefore, battery safety evaluation must be based on the statistical analysis of multiple cells of similar conditions.

By analyzing the heat release rate during the thermal runaway test, the frequency factor and the activation energy based on one-step global chemistry are obtained for each battery. By fully attributing the observed cell variability to thermal runaway chemistry, statistical analysis is then applied to the dataset, to acquire the mean and standard error of the frequency factor and global activation. With uncertainty quantification, the modeling work has reasonably captured the range of the exothermic onset temperature distribution. The measured thermal runaway delay time is also found to be bounded by the upper and lower threshold of the model prediction.

In addition to the uncertainty of chemistry induced by cell-to-cell variations, another effect that needs to be properly considered for safety evaluation is the different extent of battery material consumption during the heating period of the test. Due to the non-negligible duration of cells in the high-temperature environment, reactions such as SEI decomposition can occur even before the system detects the exothermic mode. Such reaction progress can affect the initial condition when the cell starts at the self-exothermic onset condition. Results show that reactant consumption can induce a difference in the delay time up to a factor of two.

The variation in the measured maximum temperature is not necessarily an experimental error, due to the variations in venting, combustion, and the actual of thermal energy heating up the cell. However, some error does exist in the measurement of the

maximum temperature, due to applied cooling from the ARC system, and also the potential falling-off of thermocouples during strong venting. Such error can lead to a quantitative difference in the kinetic evaluation, but will not affect the observation of the cell variability and the necessity to accommodate statistical analysis of battery safety evaluation.

It is expected that the observed cell variability also depends on degree of degradation, heating rate and cell chemistry, and that the observed cell variability will fundamentally affect the thermal runaway propagation path in a module or pack. These aspects certainly merit future investigations.

CHAPTER IV

THERMAL RUNAWAY OF LI-ION BATTERY WITH DIFFERENT AGING HISTORIES

A version of this chapter was originally published by Liwen Zhang, Lu Liu, Alexander Terekhov, Douglas Warnberg, Peng Zhao:

L. Zhang, L. Liu, A. Terekhov, D. Warnberg, P. Zhao, " Thermal runaway of Li-ion battery with different aging histories." *Process Safety and Environmental Protection*.

CRediT authorship contribution statement

Liwen Zhang: Investigation, Methodology, Formal Analysis and Writing; Lu Liu: Validation and Editing; Alexander Terekhov: Conceptualization; Douglas Warnberg: Conceptualization; Peng Zhao: Conceptualization, Methodology, Investigation and Writing - Review & Editing

Abstract

Safety issues associated with thermal runaway (TR) in batteries have attracted extensive research attention. However, understanding and predicting TR encounter significant challenges due to the complexities of chemical reactions, venting events, thermal stratification, multiphase interactions, and variable boundary conditions. These challenges are further complicated by intrinsic battery degradation, a phenomenon often insufficiently characterized and governed by multiple mechanisms. These primarily include the depletion of electrolyte and active materials, thickening of the solid-electrolyte-interphase (SEI), and formation of lithium plating and dendrites. Such degradation alters the battery's materials and structure, directly causing electrochemical performance penalties and potentially affecting its TR behavior. This study examines the TR behavior of commercial 18650 cells with lithium nickel cobalt manganese oxide (NCM) cathodes, focusing on degradation associated typical usage scenarios: long-term cycling, low-temperature cycling, dynamic

cycling with calendar aging. We employ Electrochemical Impedance Spectroscopy (EIS) to probe internal changes in the electrochemical properties of aged cells compared to fresh counterparts. The EIS results reveal pronounced SEI impedance and substantially increased charge transfer impedance in long-term cycled cells. TR tests were conducted using an Accelerating Rate Calorimeter (EV+ ARC, Thermal Hazard Technology) following the heat-wait-seek (HWS) strategy. Our findings indicate a significant impact of aging mechanisms on second-life battery safety. Specifically, cells subjected to low-temperature cycling demonstrated a considerably lower onset temperature for exothermic reactions, and shorter TR delay time, despite all aged cells showing similar state of health. Furthermore, the temperature corresponding to the cell voltage drop is consistently much lower for aged cells with dynamic cycling and calendar aging.

1. Introduction

Li-ion batteries (LIB) stand out as a most promising electrochemical energy storage for vehicle electrification and energy storage technologies, owing to their high energy density and long cycle life [168,169]. Although their potential, the occurrence of safety incidents related to TR has been identified as a major concern for the widespread adoption of high energy density LIB [117,170,171]. Consequently, efforts are urgently needed to understand and prevent TR. In general, undesired chemical reactions among various battery components can be triggered under abusive conditions, which are not only highly exothermic but can also release substantial amounts of flammable materials [131,172,173]. TR observed in LIB can be attributed to a complex interplay factor such as variations in battery materials [174,175], state of charge (SOC) [136,176–178], state of health (SOH)

[36,51], as well as external conditions like temperature [179,180] and the effectiveness of cooling systems [181–183].

In addition, there is growing interest to utilize second life batteries, which have reached the end of their "automotive" life but still have a remaining capacity of about 80% of fresh cells, for stationary electrical energy storage systems. For such batteries, aging has a significant impact on their thermal stability. As batteries undergo prolonged cycles and usage, changes in their internal structure and chemical properties may occur, such as creak of particles [184], the formation of SEI [185,186], lithium plating [187], the reaction of the active material with electrolyte [188], resulting in loss of active material (LAM) [189], loss of lithium inventory (LLI) [190] and increase in resistance, which contribute to the capacity fade and power fade [16], potentially posing risks of TR. The changes in the battery TR performance during the aging process are strongly dependent on the degradation paths and aging mechanism [191]. Aging mechanisms are also influenced by various factors such as chemical reactions within the battery, temperature variations, charge-discharge cycles, and the materials used in the battery's construction. Moreover, the aging mechanisms vary significantly under low and high temperatures. Therefore, a thorough investigation into the TR variations of batteries with different aging histories is crucial for enhancing the safety and stability of battery systems.

To gain a comprehensive understanding of this issue, Kong et al. [192] have confirmed that irreversible lithium consumption due to lithium plating at the anode is a primary concern for temperatures below 25 ℃ and proposed the detrimental impact of lithium plating on battery safety at low temperatures. Conversely, for temperature

exceeding 25 ℃, the growth of SEI becomes a predominant factor in battery aging. Previous studies, such as the work conducted by Feng et al. [193], also have investigated the impact of aging paths. They explored two distinct aging tests, namely high-temperature storage and low-temperature cycling, and observed that while capacity retentions may exhibit similarities, cells subjected to high-temperature storage demonstrated superior thermal stability. Conversely, low-temperature cycling led to lithium plating on the anode surface, resulting in a deterioration of thermal stability.

In order to deepen the understanding of aging histories on TR behavior of Li-ion batteries, in this study, we adopt commercial NMC 18650 cells, which are cycled at a temperature of 25 ℃ and -5 ℃ until the discharge capacity decreased to 80 % of the initial discharge capacity, mirroring the capacity retention observed in the same aged cells sourced from a vacuum machine. Also, the fresh cells were also included in the study, serving as a baseline for comparison. Although many studies have explored the impact of low-temperature and high-temperature on battery aging and thermal stability, our research stands out by in-depth study of aged cells under more realistic conditions. It is worth noting that we studied the cells from a used Dyson Vacuum cleaner, which represents actual usage scenarios incorporating both dynamic cycling and calendar aging. This approach includes the complex, real-word aging mechanisms, and is crucial to understanding the impact of aging on thermal runaway in practical applications. Subsequently, a series of TR tests were performed on cells that had degraded under different aging paths using EV+ ARC. The comparative analysis of these TR tests established a correlation between aging history and safety characteristics of commercial 18650 NMC cells.

2. Experimental methodology

2.1 Battery type and initialization

In this study, commercial 18650 Li-ion batteries with NMC cathode and graphite anode manufactured by Sony are used. Table 19 lists the detailed specifications of the battery sample.

Before TR testing, all cells from the same vendor (Sony) were characterized using MACCOR 4200 system with an environmental chamber. Post-characterization, the cells were segregated into four groups: 'fresh cells' (serving as the baseline), 'cycled at 25 ℃' (exposed to ambient temperature cycling), 'cycled at -5 ℃' (undergoing low-temperature cycling), and cells of the same model obtained from a used Dyson Vacuum cleaner, which has experienced dynamic cycling conditions of several years. This grouping allows for a comprehensive exploration of TR response under varying aging histories, including both controlled experimental setting and real-word scenarios, where the dominant aging mechanism under each condition can be different. For example, low temperature cycling facilitates the growth of lithium plating and dendrite. Detailed cycling procedures for all cells as described in Table 20. It should be noted that despite their differing aging histories and cycle numbers, all aged cells exhibit similar capacity retention. Additionally, to ensure a consistent baseline, all cells are fully charged to 100 % SOC before carrying out the ARC test. Typical charging/discharging curves of voltage versus discharge capacity for all groups of cells are illustrated in Figure 49, providing a comprehensive overview of their voltage performance under distinct aging histories. Compared with fresh cells, the voltage curve of aged cells shifts to left, which implies the capacity fade and can be used as an

Table 19. The specifications of the battery sample involved in this study.

Parameter (unit)	Value
Model	US18650VTC4
Chemistry	NMC/Graphite
Height (mm)	65
Diameter (mm)	18
Rated capacity (Ah)	2.1
Nominal voltage (V)	3.7
Charging voltage (V)	4.2±0.05
Cell weight (g)	45.0 average

Table 20. Different aging history of the batteries.

Battery No.	Test Procedures
Cell 1-3	Step 1: Characteristic (initialization before ARC test
Fresh cells	• Charge: Ambient, 2 A(CC/CV), 2.5 h, 4.2 V
	• Discharge: Ambient, 0.4 A, 2.5 V cut off 5 times
	Step 2: ARC test
	• HWS strategy, 5 ℃ heating step, 0.02 ℃/min temperature sensitivity
Cell 4-6	Step 1: Same as Cell 1-3 (Characteristic)
Cycled at 25℃	Step 2: Cycling at normal temperature.
	• Charge: 25 ℃, 4 A(CC/CV), 2.5 h, 4.2 V
	• Discharge: 25 ℃, 10 A, 2.5 V cut off, 750 times
	Step 3: Same as Step 1 (Capacity check, initialization)
	Step 4: Same as Cell 1-3 (ARC test)
Cell 7-9	Step 1: Same as Cell 1-3 (Characteristic)
Cycled at -5℃	Step 2: Cycling at low temperature.
	• Charge: -5 ℃, 2 A(CC/CV), 2.5 h, 4.2 V
	• Discharge: -5 ℃, 10 A, 2.5 V cut off, 500 times
	Step 3: Same as Step 1 (Capacity check, initialization)
	Step 4: Same as Cell 1-3 (ARC test)

Table 20 continued

Battery No.	Test Procedures
Cell 10-12	Same battery brand, work for 6 years, unknown charge/discharge process
Unknown dynamic cycled conditions	Same battery brand from a used Dyson Vacuum cleaner Same as Cell 1-3

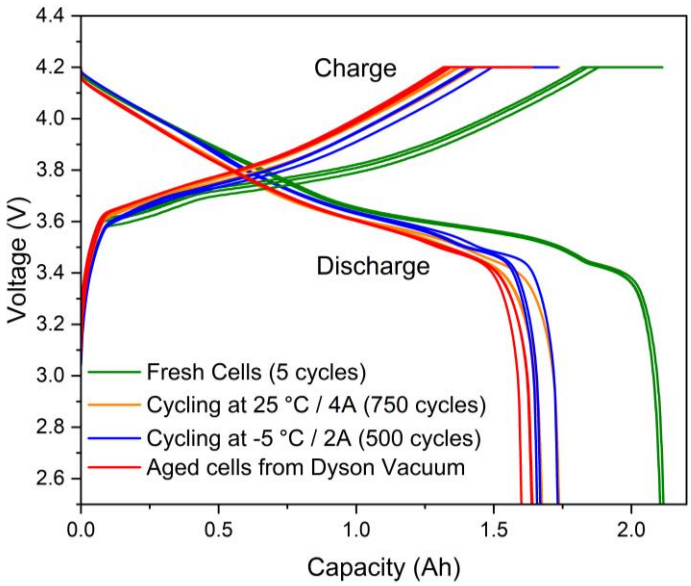

Figure 49. Degradation voltage evolution across four groups of cells with varied aging histories.

indicator of the SOH of the cell. Figure 50 shows a summarized SOH for all cells, commonly defined as:

$$SOH = \frac{Q}{Q_0} \times 100\% \quad (61.)$$

where Q is the discharge capacity, Q_0 is the initial capacity of the cell.

2.2 EIS measurement

EIS is an invaluable tool for the non-destructive, rapid assessment of battery health and is extensively utilized in LIB research. In this study, EIS tests were conducted on all cell groups at both the beginning of life (BOL) and end of life (EOL, 80 % SOH [194]) using the potentiostat/galvanostat instrument PASTAT 4000A (Princeton Applied Research). This instrument implements a small AC current signal perturbation through the cell. Measurements were performed on fully charged cells with a 10-mV amplitude, scanning 30 logarithmically spaced points between 3 kHz and 0.1 Hz using the working/sense electrode and reference/counter electrode terminal setup. The impedance profiles of cells at the BOL and EOL are expressed as the Nyquist plot shown in Figure 51. Nyquist plot can reveal valuable information about electrochemical processes and provides insights into phenomena such as solid electrolyte interface (SEI) growth, charge transfer resistance and diffusion limitations [195]. According to the Randles battery model, the high-frequency intersection on the horizontal axis indicates ohmic resistance, the semicircle's diameter corresponds to charge transfer resistance, and the straight line in the low frequency range denotes the diffusion process. To gain a more instinctive observation of the changes in ohmic resistance and charge transfer resistance in aged cells, effective

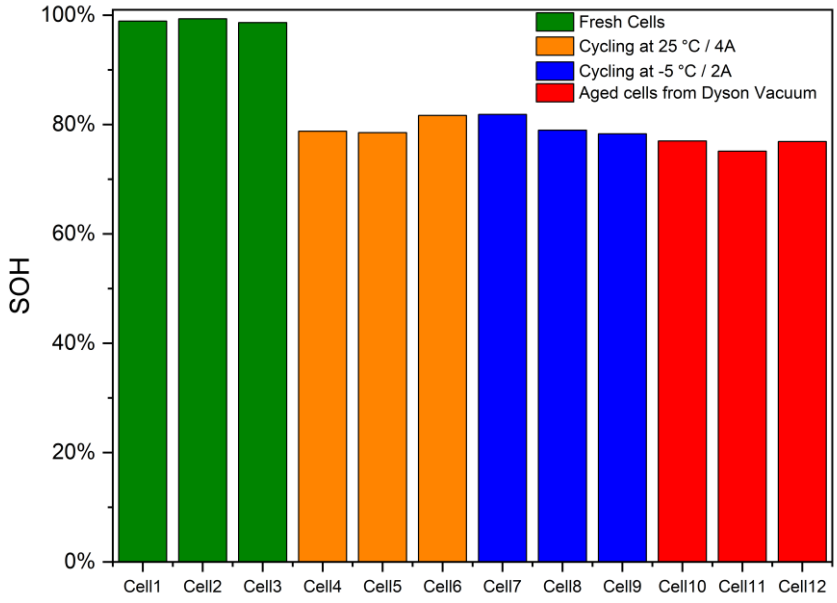

Figure 50. SOH of four groups of cells with varied aging histories.

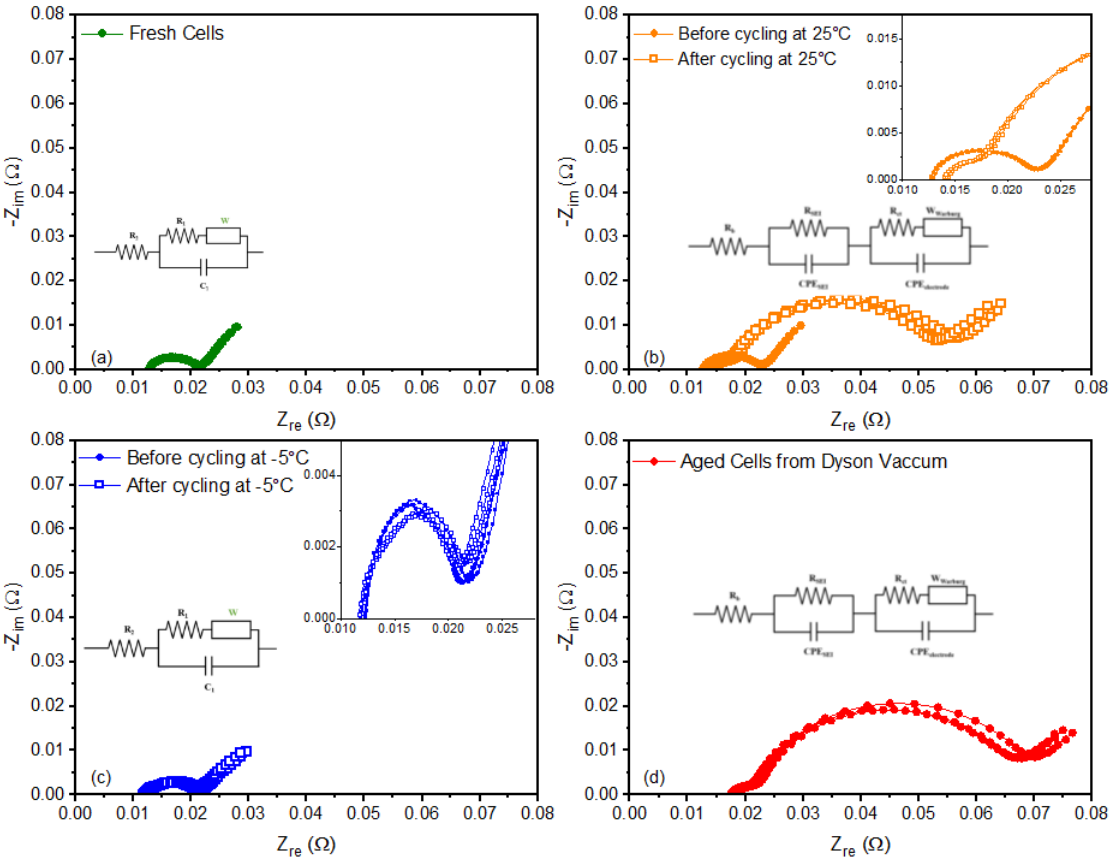

Figure 51. Nyquist plot of NMC cells at BOL and EOL (a) fresh cells (baseline); (b) aged cells cycled at 25 °C; (c) aged cells cycled at -5 °C; (d) aged cells from a used Dyson Vacuum cleaner.

equivalent circuit models (ECM) were employed to fit the EIS data. The resistance values of all cell groups are illustrated in Figure 52, and cells with different aging histories exhibited different impedance changes. Aged cells cycled at 25 ℃ demonstrated a rightward shift in the overall Nyquist plot, characterized by two discernible semicircles. The smaller semicircle suggests SEI thickening during prolonged cycling, resulting in a slight increase in ohmic resistance. In addition, there is a pronounced increase in charge transfer resistance. In contrast, cells cycled at -5 ℃ showed minimal changes in both ohmic and charge transfer resistance, with no obvious dual semicircles, indicating the predominant aging mechanism at low temperatures is lithium plating. Interestingly, cells from a used Dyson Vacuum cleaner, subjected to dynamic cycling conditions, exhibited EIS curves similar to those cycled at 25 ℃, including noticeable dual semicircles. These cells showed significant increases in both ohmic and charge transfer resistances, even surpassing those observed in cells cycled at 25 ℃. This could be attributed to the complex dynamic working conditions and extended calendar life associated with Dyson Vacuum cleaner cells.

2.3 TR testing in ARC

In order to comprehensively study the influence of the aging histories on the TR features of Li-ion batteries, TR tests are performed using the EV+ ARC, manufactured by Thermal Hazard Technology (THT). Our focus is directed towards assessing the impact of different aging histories on three key temperature parameters: self-heating onset temperature, TR temperature and maximum temperature, as well as TR delay time. To determine the self-heating onset temperature, the standard heat-wait-seek (HWS) method

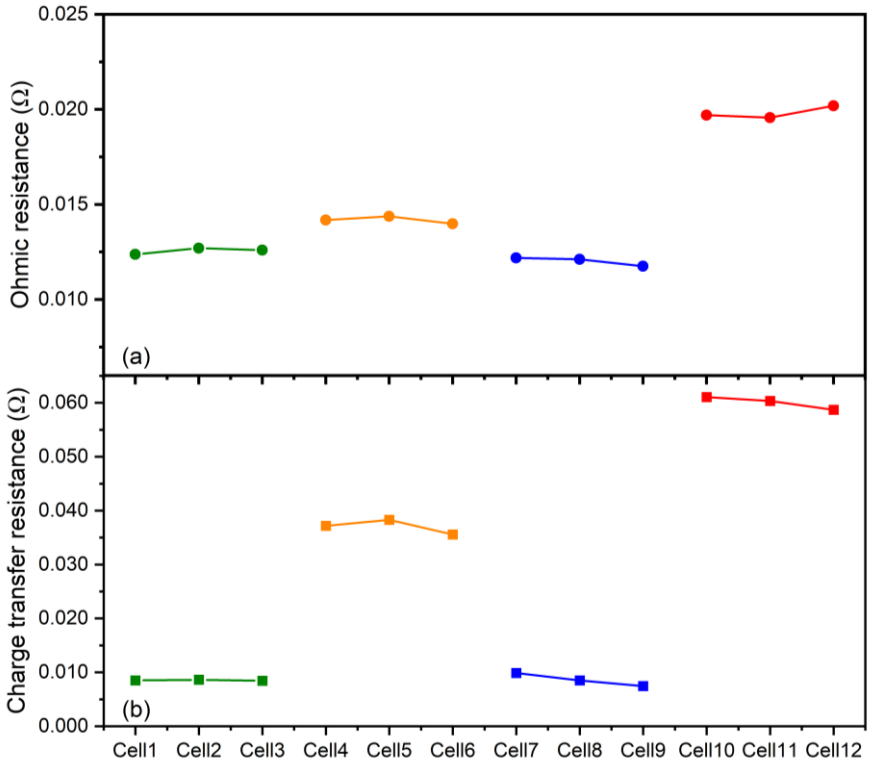

Figure 52. Fitting values of resistance (a) ohmic resistance; (b) charge transfer resistance.

is adopted for all measurements. Detailed procedures are outlined in our previous work [143]. Subsequently, the relationship between aging histories and TR features are discussed.

3. Results and discussion

3.1 Mass loss during thermal runaway

Figure 53 illustrates the percentage of mass loss in cells under different aging conditions after TR. The mass loss during the TR tests ranges from 22 % to 29 % for the cells, with a higher total mass loss observed in fresh cells. This phenomenon can be attributed to the degradation of cell capacity and the loss of active materials in aged cells, leading to a decrease in thermal runaway intensity and less materials being ejected during TR.

3.2 Temperature and voltage characteristics

During the ARC test process, both surface temperature and voltage are monitored, in order to comprehensively monitor the thermo-electrical change of cells during TR. Figure 54(a) and (b) illustrates the typical surface temperature and voltage variations of fresh cells and different aged cells. From Figure 54(a), it can be observed that aged cells cycled at low-temperature exhibit significantly earlier TR, emphasizing the distinct impacts of different aging conditions.

From the voltage profiles of Figure 54(b), it is evident that when the tested cell reaches a certain temperature, the voltage undergoes a sudden drop but does not immediately reach zero. Instead, it maintains at a certain level for a period. Subsequently,

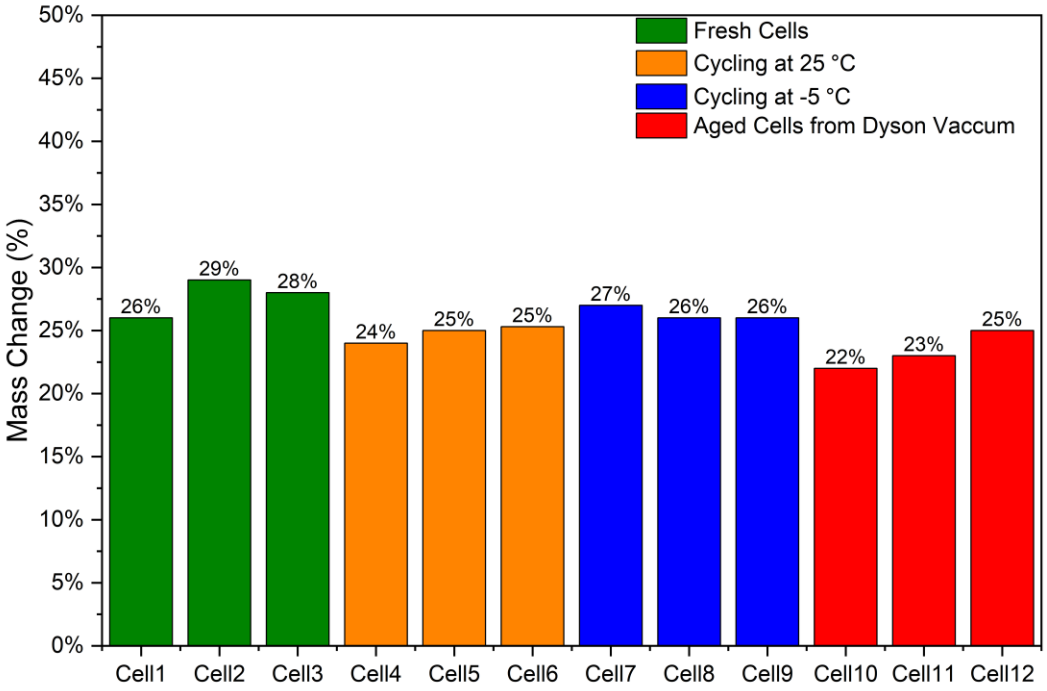

Figure 53. The mass loss percentage of cells at different cycle conditions.

when a substantial internal short circuit occurs, the cell voltage rapidly drops to 0V, triggering an immediate onset of TR. Also, Figure 54(c) illustrates the corresponding temperatures (indicated by dots with line on the graph) when different aged cells experience a sudden voltage drop. It can be seen that the voltage drop occurs before a sharp increase in cell temperature, particularly in the case of aged cell from a used Dyson Vacuum cleaner, where the voltage drops first at relatively low temperatures compared to other aging conditions. This phenomenon suggests that these cells with dynamic cycling with calendar aging are more sensitive to internal short circuit triggers, indicating a correlation with its complex aging mechanisms, potentially due to the cumulative effects of stress and degradation mechanisms of their aging process, resulting in more fragile internal structure prone to early short circuit. As the temperature continues to rise, the complex chemical reactions inside the cells continuously generate gas, driving fluctuations in the cell voltage. Ultimately, when a significant internal short circuit occurs, the voltage rapidly drops to 0 V. It is worth noting that there is a clear correlation between the aging method and the temperature at which voltage drops occur. Cells aged under dynamic and calendar aging conditions demonstrate accelerated degradation processes that may be affected by factors such as the growth of lithium dendrites, electrolyte decomposition, or cathode material degradation. These degradation processes may change the internal structure and chemistry of the cells, thereby impacting their thermal and electrical response patterns. Furthermore, the fact that the voltage of aged batteries undergoing low-temperature cycling drops to 0V first further emphasizes the role of lithium dendrites in accelerating the occurrence of short circuits. A comparative analysis of cells under different aging conditions reveals diverse

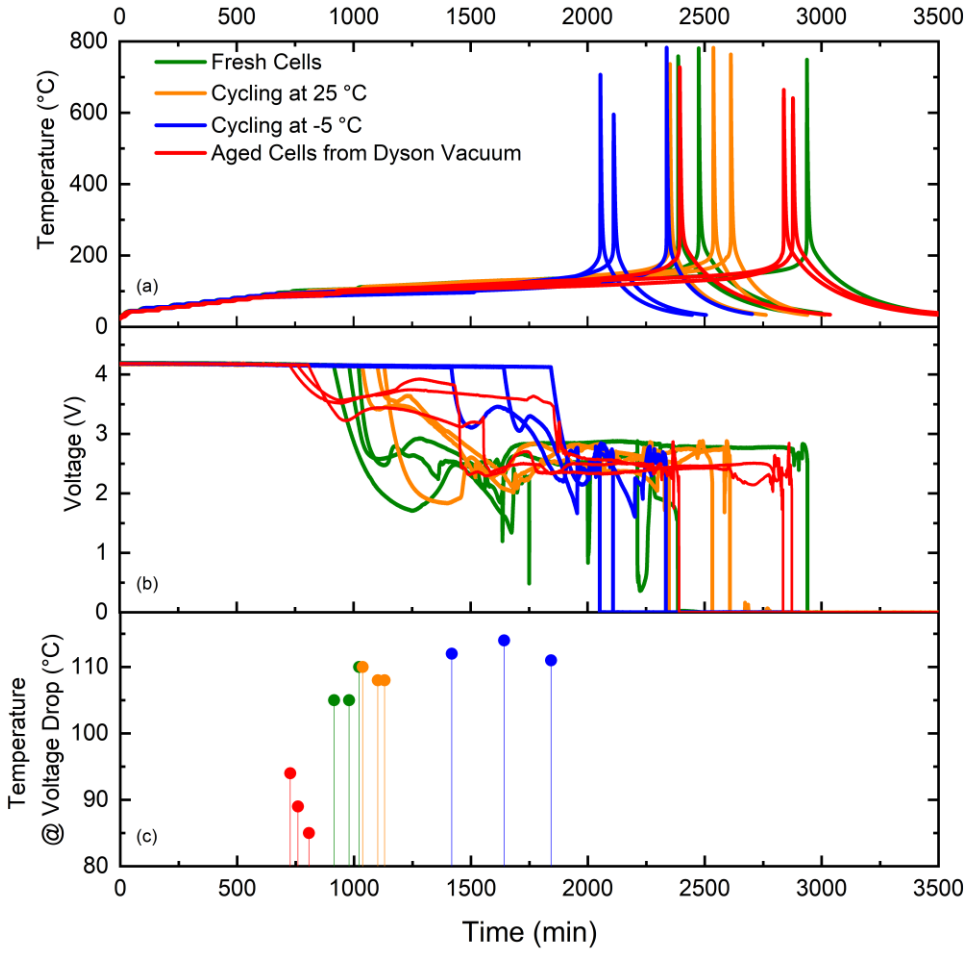

Figure 54. (a) cell surface temperature during TR; (b) voltage evolution during TR; (c) corresponding temperature during when cell experiences a sudden voltage drop.

thermal and voltage behaviors, each correlating with specific degradation processes inherent in the aging method.

3.3 Critical temperature

During the ARC test, three characteristic temperatures, namely self-heating onset temperature (corresponding to 0.02 ℃/min), TR temperature (corresponding to 20 ℃/min), and maximum temperature, are identified to quantify the thermal stability performance of the battery. Figure 55 shows the critical temperatures for different aging conditions. It can be observed that under different conditions, the self-heating onset temperature of the cell remains within the range of 82–102 °C. Aged cells cycled at 25 °C almost equal with the self-heating onset temperature of fresh cells. However, the self-heating onset temperature was lower for cells cycled at temperatures of -5 °C, showing a decrease from 102 °C to 82 °C, a difference of approximately 20 ℃. This variance may be attributed to the exothermic reaction between deposited lithium on the anode surface and the electrolyte occurring at a lower temperature. Additionally, the self-heating onset temperature of aged cells from a used Dyson Vacuum cleaner is significantly lower than that of fresh cells, suggesting a correlation with the more complex aging mechanisms inherent in Dyson Vacuum cleaner cells, and it is much easier to thermally trigger internal short circuit in these cells. It is worth noting that in the group of cells subjected to low temperature cycling, as well as those aged cells from Dyson Vacuum cleaner, individual cells show different self-heating onset temperature. For example, while Cell 9 may have demonstrated a different value than Cell 7 and 8 within the same low-temperature cycling, this temperature deviation is not unexpected, accounting for cell-to-cell variation, even existing within fresh cells, is a key

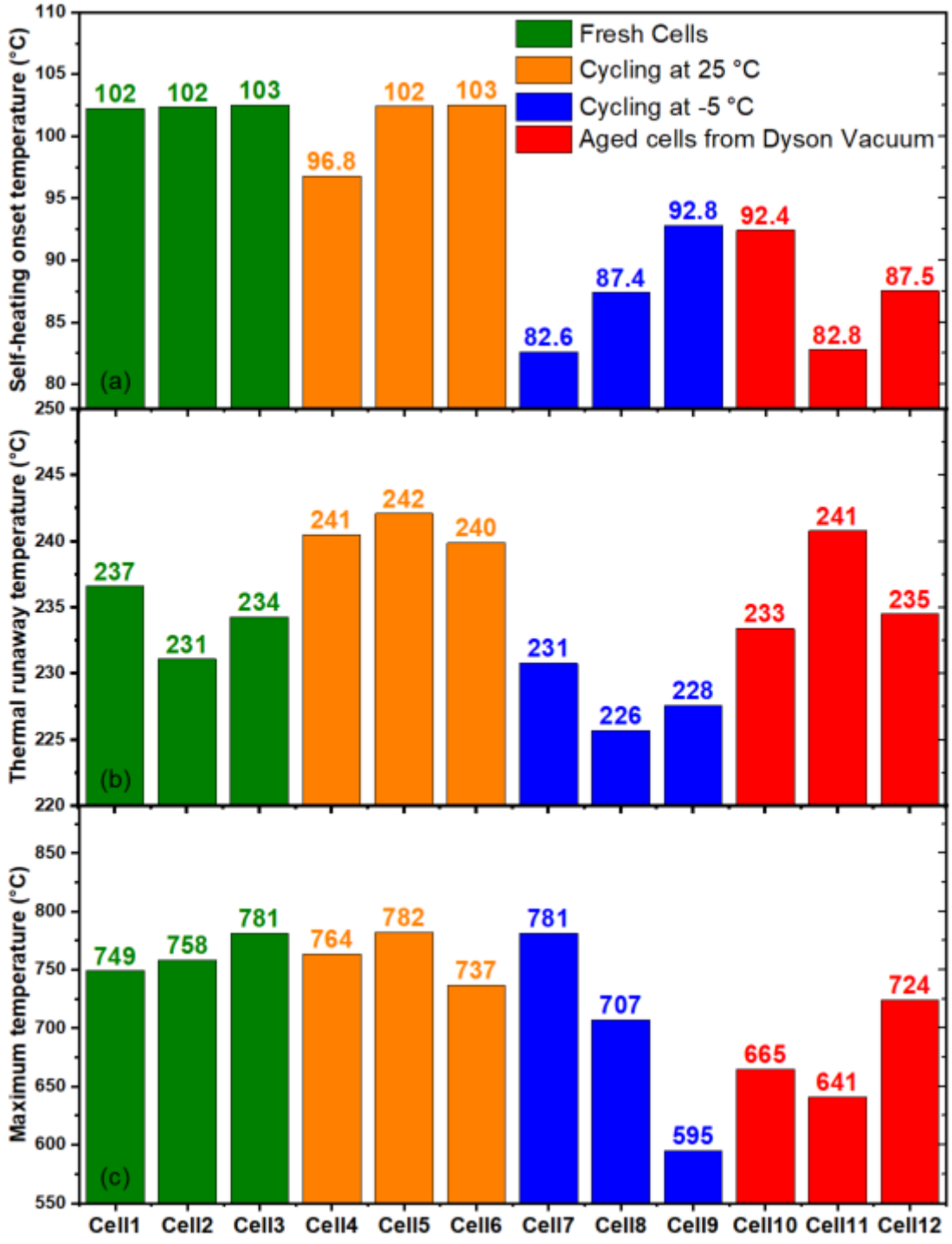

Figure 55. Critical temperatures at different aging conditions (a) self-heating onset temperature; (b) TR temperature; (c) maximum temperature.

factor that can lead to differences in self-heating onset temperature during thermal runaway. Under specific degradation conditions, even if the overall state of health (SOH) evaluated from capacity is largely similar, the microstructure and local level of degradation within each cell can still be quite different. Additionally, the uncertainty in measuring the self-heating onset temperature could be as large as the 5 ℃ increments during the heating step, consequently, variation in the self-heating onset temperature of aged cells under low-temperature cycles fall within a reasonable margin of error.

In low-temperature aged cells, not only is the self-heating onset temperature lower compared to other groups of cells, but the TR onset temperature also exhibits a lower performance. The declining trends of self-heating onset temperature and TR onset temperature indicate a deterioration in the thermal stability of the lithium-ion battery following low-temperature cycling. However, there is no clear pattern observed in the maximum temperature and there was a significant difference in maximum temperature. It's crucial to note that this difference does not impact the determination of the self-heating onset temperature. Additionally, as we have pointed out in our precious work [35], even for fresh cell, we should not expect that the maximum temperature to be the same due to (a) difference in the amount of injection and hence residual mass of the cell to be heated up (b) difference in the amount of heat released to heat up the cell. In short, not all the injected mass is reacted, and not all the heat release is used to heat up the cell. Not to mention that these complexities are often exacerbated by the aging process. Specifically, for the low-temperature cells, different microstructure and distribution of the lithium dendrite can potentially probably lead to different reaction rates and heat release during

thermal runaway. Recognizing and addressing the impact of aging on battery variability is a key consideration.

3.4 Thermal runaway kinetics of aged cells

After getting the temperature evolution from ARC test, activation energy of the TR reaction and frequency factor can be readily calculated from the heat release rate. Based on the Arrhenius law, the self-heating rate can be expressed in Equation (62.) [159,160], assuming adiabatic and ignoring reactant consumption:

$$\ln\left(\frac{dT}{dt}\right) \approx \ln(\Delta T_{ad} A) - \frac{E_a}{k_b T} \qquad (62.)$$

where $\frac{dT}{dt}$ is self-heating temperature rate, ΔT_{ad} is the difference between the initial self-heating onset temperature and the maximum temperature, k_b is Boltzmann's constant (8.62E-5 eV·K^{-1}), A is frequency factor and E_a is activation energy of TR reactions. Figure 56 plots $\ln\frac{dT}{dt}$ versus $\frac{1000}{T}$ to calculate frequency factor A and activation energy E_a for four groups of cells with varied aging histories. By using the linear fitting on the temperature rate profiles, the activation energy E_a indicated by the slope and frequency factor A indicated by the intercept are obtained and summarized in Figure 57. The bar chart reveals correlated consistency in the variation of calculated activation energy E_a and frequency factor A. Cells with higher activation energy also exhibit larger frequency factors. Additionally, there are observable trends in activation energy and frequency factor variations between different cell groups, ranging from new cells to those subjected to cycling at 25 °C, aged cells from a used Dyson Vacuum cleaner, and low-temperature cycling aging cells. Notably, the activation energy and frequency factor of cells aged

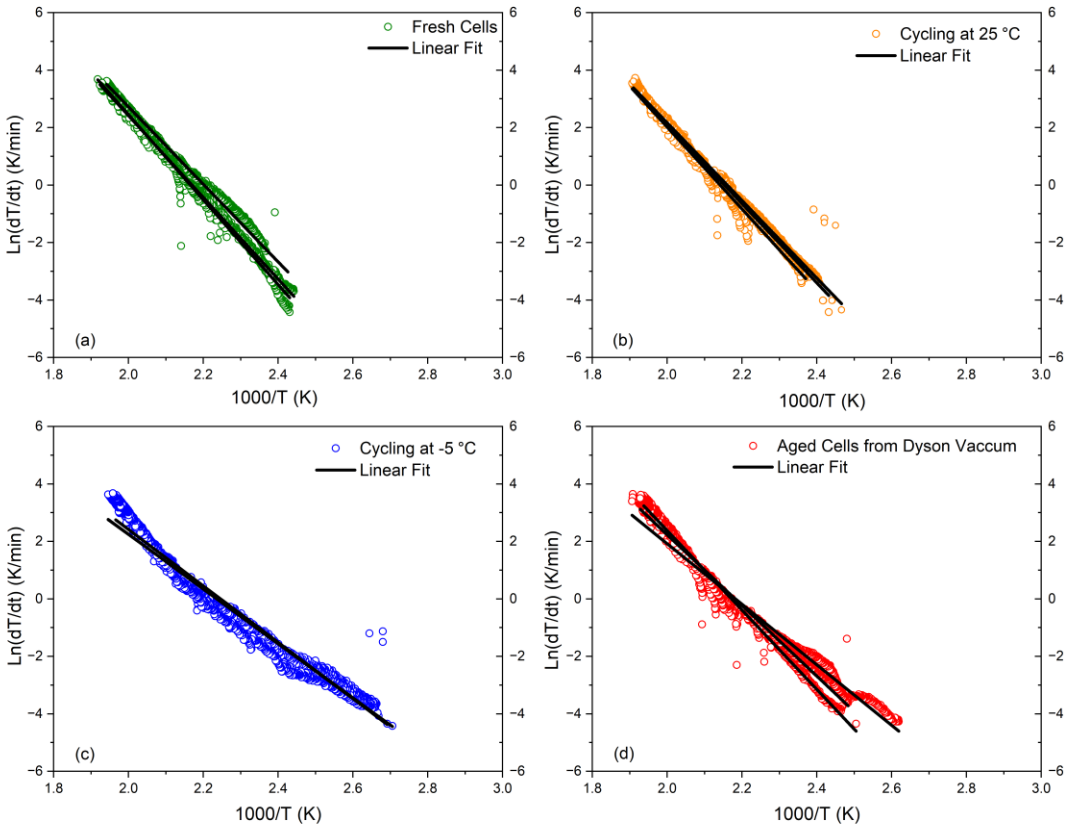

Figure 56. ln(dT/dt) versus 1000/T during TR of four groups of cells with varied aging histories (a) fresh cells (baseline); (b) aged cells cycled at 25 °C; (c) aged cells cycled at -5 °C; (d) aged cells taken from a used Dyson Vacuum cleaner.

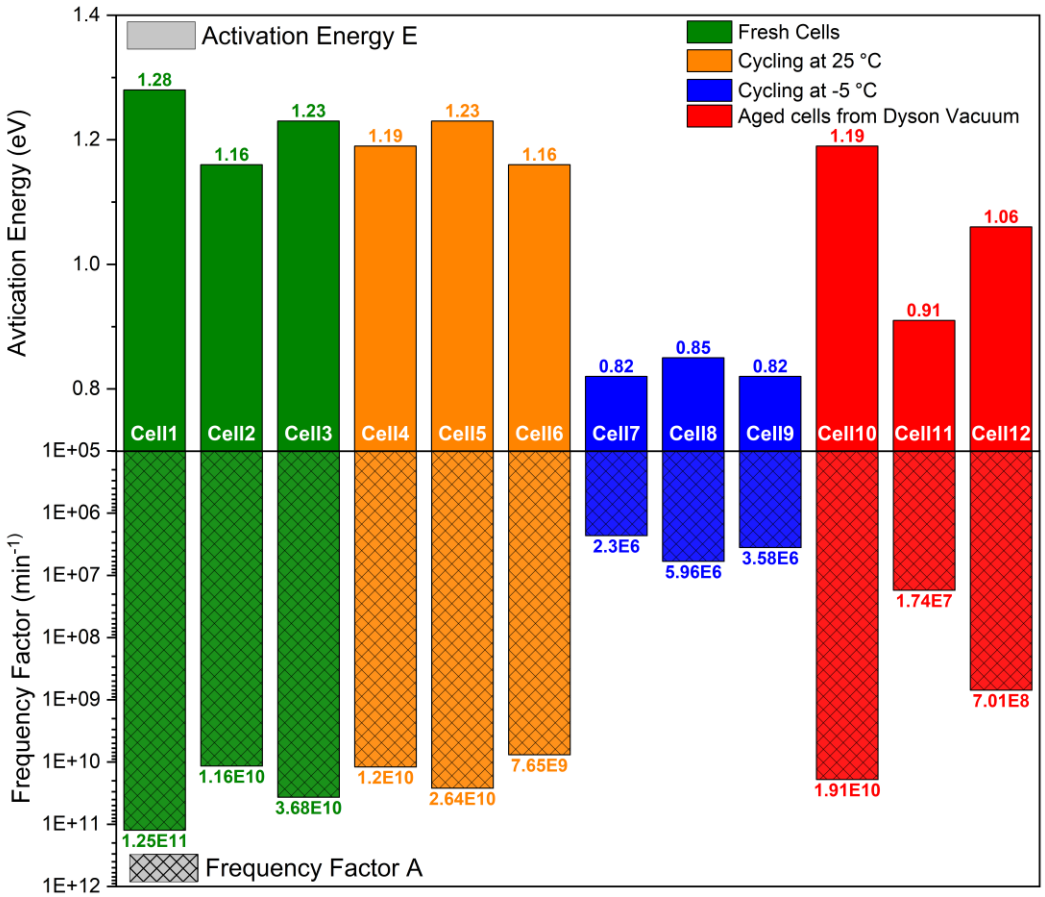

Figure 57. Activation energy and frequency factor of four groups of cells with varied aging histories.

through cycling at 25 °C are nearly identical to those of fresh cells, indicating minimal differences. In contrast, the aged cells from a used Dyson Vacuum cleaner show variations in activation energy, emphasizing the significant impact of different aging mechanisms on battery TR. It is essential to highlight those cells aged through low-temperature cycling exhibit a substantial decrease in activation energy compared to other groups. This aligns with the observation that cells undergoing low-temperature aging enter self-heating mode earlier.

4. Conclusion

In this work, commercial 18650-type LIB based on NMC were tested using EIS and ARC to comprehensively investigate the TR behavior of Li-ion batteries under varied aging histories to reveal the key aspects affecting the safety and stability of batteries. The observed variations in critical temperatures, mass loss, and kinetic TR parameters underscore the importance of understanding aging mechanisms in mitigating potential risks associated with Li-ion battery applications. This study reveals that cells subjected to low-temperature cycling exhibit a significantly earlier onset of TR, emphasizing the role of lithium dendrites/plating in accelerating short circuits. The lower self-heating onset temperatures for cells cycled at low temperatures and those from a used Dyson Vacuum cleaner compared with fresh cells signifying the impact of real-word usage patterns on battery aging and thermal stability. This highlights the impact of diverse aging mechanisms on thermal stability and demonstrates the insufficiency of traditionally defined SOH in the characterization of thermal runaway of aged cells.

Furthermore, the kinetic analysis of TR provides valuable insights into the activation energy and frequency factor variations among different aging groups. The substantial decrease in activation energy for cells aged through low-temperature cycling aligns with their earlier entry into self-heating mode, emphasizing the need for tailored safety concern in such scenarios.

In conclusion, the research highlights the complexity of aging effects on Li-ion battery thermal behavior and underscores the necessity for tailored safety strategies based on specific aging conditions. In this study, aged cell from a used Dyson Vacuum cleaner (representing a portable device with dynamic cycling and calendar aging) displayed different thermal stability characteristics during thermal runaway, demonstrating the variability in aging effects on thermal runaway in commonly used consumer electronics. This observation is particularly important as it illustrates that if such differences in thermal stability exist in small portable devices, the implications for large-scale applications such as electric vehicles are even more significant. As Li-ion batteries continue to be integral to various applications, ranging from electric vehicles to energy storage, a nuanced understanding of the interplay between aging mechanisms and thermal stability is essential for advancing the safety and reliability of these energy storage systems. This work contributes valuable insights to the ongoing efforts aimed at enhancing the robustness of Li-ion battery technology in real-world applications.

In future experiments, we can consider conducting ARC experiments specifically for cells with different capacity retentions under low-temperature cycling. We aim to evaluate the potential correlation between lithium plating quantity and ARC parameters,

such as activation energy. This targeted approach will allow for a more detailed examination of the relationship between lithium plating and thermal runaway in varying conditions. Future work will also incorporate non-intrusive quantification of cell variation induced by lithium plating and dendrite before the detrimental thermal runaway test, and identification of potential structure-performance relationship in aged cells.

CHAPTER V

THE HOTSPOT IGNITION NATURE OF THERMAL RUNAWAY IN LI-ION BATTERIES CYCLED UNDER LOW TEMPERATURES

Abstract

Thermal runaway remains as a major safety issue for lithium-ion batteries (LIBs), causing concerns in their broader adoption in applications such as electric vehicles and energy storage systems. Lithium plating/dendrites, frequently observed in LIBs after low-temperature and/or fast cycling, not only play the role of a major aging mechanism, but also lead to substantial changes in the thermal runaway behavior, thereby presenting a significant challenge to cell performance and reliability. This study focuses on analyzing thermal runaway in aged batteries with dominant degradation from Li plating and dendrite, which is promoted through cycling at low temperatures. We employed the commercial batteries for experiments: 18650 cells with positive electrodes of Lithium Phosphate (LFP). cells were subjected to low temperature cycling until they aged to 60% of cycle life, followed by thermal runaway testing using an accelerating rate calorimeter (EV+ ARC, Thermal Hazard Technology) at 100% state of charge. The results show that thermal runaway of these aged cells occurs earlier than fresh batteries, with a notable decrease in self-heating onset temperature, indicating a higher susceptibility to thermal runaway. The aged cells enter exothermicity much earlier, with a cell surface temperature as early as 55 ℃. Meanwhile, in the early stages of self-heating for LFP batteries, venting gas and white smoke phenomena were prominently observed. This indicates a much higher internal temperature within the cells such that intense electrolyte vaporization and gas generation is feasible. Detailed numerical simulation has been performed to interpret the mode of thermal runaway for cells with lithium dendrite, which bears inherent similarity to hot-spot induced ignition. These observations provide novel understanding of the combustion mode

for the thermal runaway of aged cells with plating and dendrites, offering insights into the application and management of secondary life batteries, with combined aging and safety challenges.

1. Introduction

The growing demand for renewable energy and the global trend towards electrification have greatly promoted the development of Li-ion batteries (LIBs) in various fields, especially in electric vehicles (EVs) and energy storage systems. Although lithium-ion batteries are widely adopted and offer many advantages, such as high energy density, low memory effect and long cycle life [196–198], they still have safety concerns, particularly the risk of thermal runaway, a catastrophic failure that can lead to subsequent combustion [199–202]. The initiation of thermal runaway bears inherent similarity to an ignition event, where exothermicity from side reactions, if not dissipated sufficiently fast, can eventually drive the cell temperature to the thermal runaway onset, companioned with very high heat release rate, gas/particle emissions, and even fires. Thermal runaway is being extensively investigated by combining sub-cell, cell, and pack level experiments [203–211], multiphysical modeling and numerical simulation [212–218], and theoretical analysis [219–222] for cells with different materials, aspect ratio, state of charge (SOC), and state of health (SOH). It is worth noting that combustion concepts and research tools can be very helpful in the mechanistic study and prevention of thermal runaway [221,223–227].

Beyond safety, another inherent challenge of battery is that a cell fundamentally suffers from irreversible degradation after hundreds and thousands of cycles, as manifested

by reduced cell capacity and increased internal resistance [228–232]. Such degradation frequently involves various physical, chemical and material aspects, for example, loss of active materials [233,234], thickening of solid-electrolyte interphase layer [235–238], lithium plating and dendrite [239–242], and cracking of electrodes [243–249], etc. Concerns on performance decline from cell degradation has attracted interests in battery second life, where dynamic cells approach the end of their automotive life typically with a residual capacity of 70-80%, can still be utilized in less demanding but still effective applications, such as stationary energy storage [244,245,248,249]. The extension of battery second life effectively reduces the overall carbon footprint and increases the renewable energy available to the grid, however, can be challenged even more from thermal runaway and safety concerns. It is highly possible that a degraded cell can lead to easier occurrence of thermal runaway, which of course, depends on the extent and dominant pathway of degradation [200,250–254].

Thermal runaway becomes more concerning in the context of battery second life. A dominant degradation mechanism that is facilitated under low temperature cycling and/or high current fast charging conditions is the production of lithium plating and dendrites, where lithium atoms are deposited on the anode surface, forming metallic lithium instead of being embedded in the anode material [255,256]. Over time, these deposits can grow into dendritic structures that can potentially puncture the separator and cause internal short circuits, increasing the risk of thermal runaway [257–259]. Zhao et al. [260] presented a numerical model for thermal runaway in low temperature cycling Nickle-Cobalt-Aluminum (NCA) 18650 cylindrical lithium-ion batteries, including lithium metal reaction,

and validated it against oven test results. Wu et al.[261] conducted adiabatic thermal runaway tests on lithium cobalt oxide (LCO) pouch cells cycled at -10 ℃ with varying states of health and developed a model to predict the thermal runaway at different SOH conditions. Kong et al. [262] conducted thermal abuse test of NCA 18650 cells and revealed that lower operating temperatures and higher cycling rates significantly affect the thermal runaway behavior, leading to earlier onset of thermal runaway, and altered venting flame characteristics. Ng et al. [258] explored the effects of low temperature cycling on lithium-ion batteries, focusing on lithium plating and corrosion hazards, where material characterization revealed exacerbate stress in certain regions of the battery, leading to significant lithium deposition, severe gassing, and in some cases, catastrophic failure through thermal and nonthermal runaway. Zhou et al. [263] investigated the critical safety concern of lithium plating in lithium-ion batteries, and tried to correlate thermal runaway chemical kinetics with the quantification of lithium plating. Their experiments show that the worst lithium plating scenario is sufficient to cause a secondary thermal runaway ahead of the main thermal runaway event. Despite the useful insights gained from these valuable studies, none of them provide guidance into the combustion mode of thermal runaway of cells with substantial dendrite formation.

This work focuses on the combustion mode of thermal runaway in aging Li-ion batteries with dominant degradation from lithium plating and dendrite, induced by low temperature cycling. The commercial 18650 Lithium Iron Phosphate (LFP) are utilized. Subsequently, a series of thermal runaway tests are conducted by utilizing Accelerating Rate Calorimetry (ARC), following the wait-heat-seek thermal abuse strategy [143]. To

further justify the combustion mode, detailed numerical simulations were conducted in the internal hotspot induced thermal runaway, achieving both qualitative and quantitative comparison with the experiment. Our results shed light on the role of dendrites in initiating thermal runaway, which bear similar nature of hot spot induced ignition.

2. Experimental approach

2.1 Battery preparation and electrochemical performance test

To understand the thermal runaway behavior of aged batteries with different chemistries under low temperatures cycling, this study utilized the type of 18650 commercial batteries known as the JGNE LFP cell. Table 21 lists the detailed specifications of these test cells.

Before thermal runaway experiments, all cells underwent various preconditioning using a MACCOR 4200 system with an environmental chamber to achieve the required conditions. In this study, both low temperature cycle aging and ambient temperature short-term cycling are considered. The cells were divided into three groups, with the specific cycling protocols detailed in Table 22. Cells 1-2 underwent 50 cycles at low temperature (0 °C); Cells 3-4 were cycled 50 times at room temperature; Cell 5 served as a fresh cell baseline. After cycling, all cells were subjected to a final standardization process at room temperature to ensure a full charge and a state of charge (SOC) of 100 %. The charging / discharging curves of voltage versus discharge capacity for test cells are illustrated in Figure 58. It is apparent that the voltage curve of an aged cell is shifted to the left compared to a fresh cell, indicating capacity fading. This transition can be used as an indicator of

Table 21. Basic parameters of JGNE LFP test cells.

Parameter (unit)	JGNE
Model	HTPFR18650
Chemistry	LFP/Graphite
Height (mm)	65
Diameter (mm)	18
Rated capacity (Ah)	1.1
Nominal voltage (V)	3.2
Charging voltage (V)	3.65
Discharging cut-off voltage (V)	2.5
Max. charge/discharge current (A)	5.5/33
Operating temperature (^{o}C)	0~55 (Charge)
	-20~60 (Discharge)

Table 22. Cycling protocol of the JGNE LFP cells.

Battery No.	Test Procedures
Cell 1-2	Step 1: 0.5C Charge/Discharge 2 times at ambient temperature Step 2: 0.5/1/3/5/0.5C Charge/Discharge at ambient temperature Step 3: 1C-Charge 5C-Discharge 50 times at 0℃ Step 4: 0.5/1/3/5/0.5C Charge/Discharge at ambient temperature Step 5: 0.1C Discharge-Charge cycle 3 times at ambient temperature
Cell 3-4	Step 1-2: Same as Cell 1-2 Step 3: 1C-Charge 5C-Discharge 50 times at ambient temperature Step 4-5: Same as Cell 1-2
Cell 5	Step 1: 0.1C Discharge-Charge cycle 3 times at ambient temperature

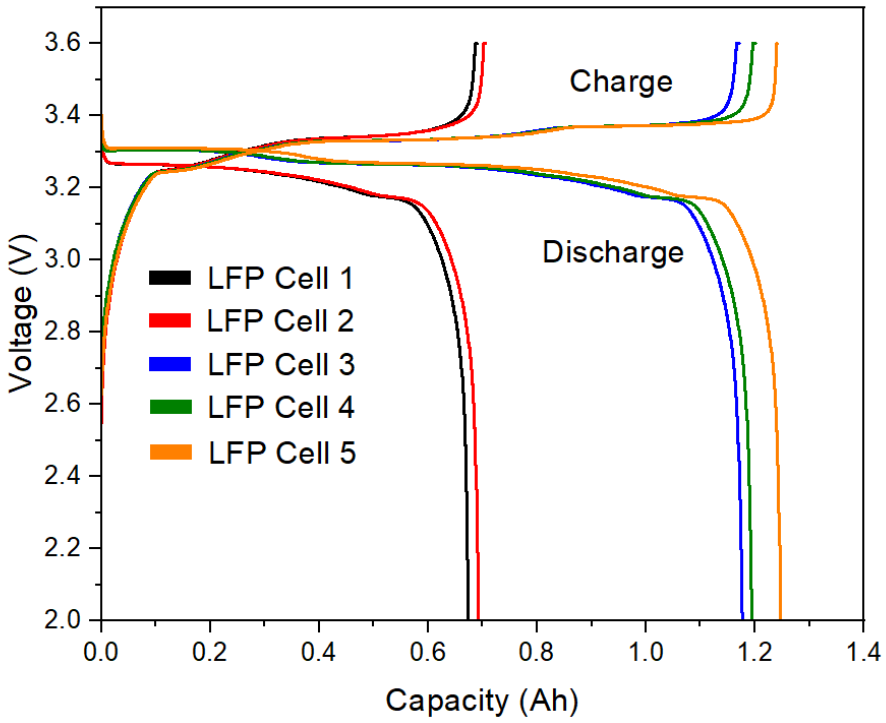

Figure 58. Voltage evolution before ARC test.

state of health (SOH), which is commonly used to represent the remaining capacity of a battery relative to its original capacity, and is typically expressed as a percentage:

$$SOH = \frac{Q}{Q_0} \times 100\% \quad (63.)$$

where Q is the discharge capacity, Q_0 is the initial capacity of the cell. Figure 59 summarizes the SOH of JGNE LFP cells, showing that Cells 1-2, after undergoing 50 cycles at low temperatures, experienced significant capacity degradation with an SOH slightly below 60%, while the remaining cells maintained an SOH close to 100%.

Following the initialization of all cells, Electrochemical Impedance Spectroscopy (EIS) measurements were conducted using the PARSTAT 4000A system by Princeton Applied Research. This provided key data on the electrochemical properties of the cells, as illustrated by the Nyquist plot in Figure 60. The Nyquist plot serves as an essential analytical tool for evaluating the electrochemical behavior of cells, offering deep insights into their operational efficiency and internal mechanisms [195]. According to the interpretation based on the Randles cell model, as presented in the Nyquist plot, the point where the semicircle intersects the real axis in the high-frequency domain indicates the ohmic resistance. This resistance is attributed to the combined resistances of the electrolyte, separator, and the battery electronic components. The diameter of the semicircle represents the charge transfer resistance, which reflects the electrochemical reaction kinetics at the electrode interface. Meanwhile, the straight line observed in the low-frequency region is indicative of the diffusion process, demonstrating the movement of ions within the battery. It can be seen that the initial EIS results show that the cells perform very similarly, with only slightly different impedances. As shown in Figure 60, the EIS results exhibited more

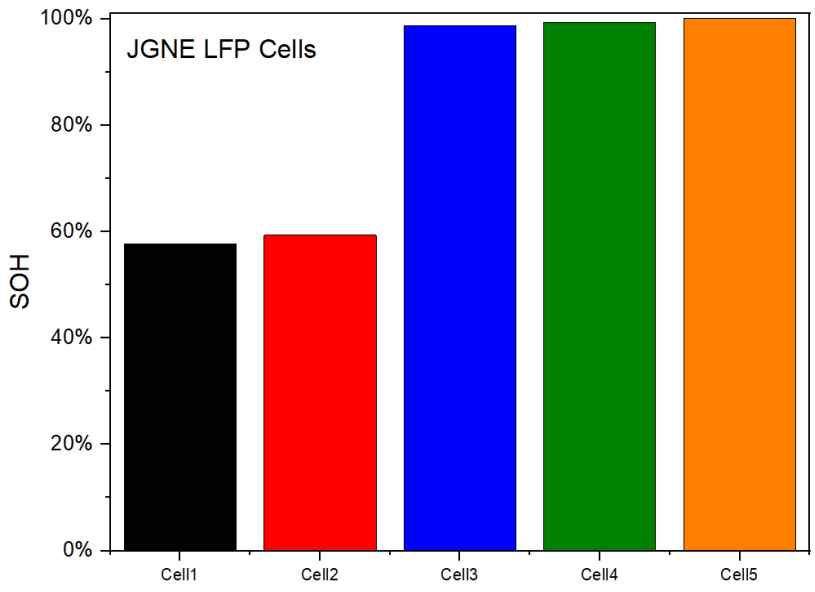

Figure 59. SOH of test cells.

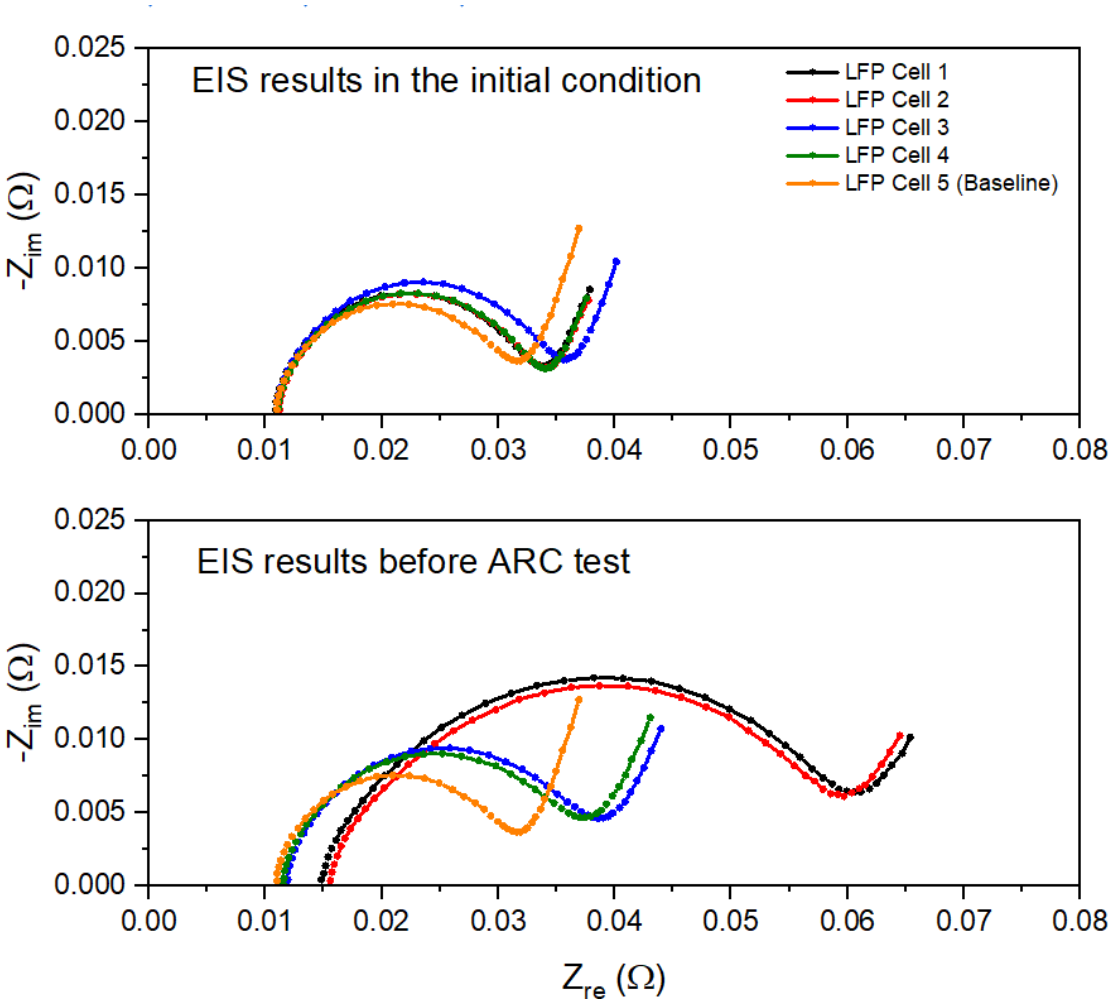

Figure 60. Nyquist plot changes of test cells before cycling and before ARC test.

pronounced differences after experiencing various cycling conditions, indicating changes in their electrochemical performance. Specifically, cells cycled at low temperatures exhibit not only changes in ohmic resistance but also increases in charge transfer resistance.

2.2 Thermal runaway test in ARC

In order to study the effect of low temperature cycling on the thermal runaway (TR) characteristics of lithium-ion batteries, the EV+ acceleration calorimeter (ARC), provided by Thermal Hazard Technology (THT), was used to conduct thermal runaway tests. This study aims to evaluate the impact of aging batteries under low temperature cycling on key temperature parameters, including self-heating onset temperature, TR temperature, maximum temperature, and TR delay time. The self-heating onset temperature was determined in all experiments using the established heat-wait-seek (HWS) method, with the detailed method described in our previously published work [143].

2.3 Analysis of thermal runaway experimental data

During thermal runaway experiments, we collected data on surface temperature and voltage changes for batteries involved in the tests. The results, as shown in Figure 61, are compared. This figure illustrates the evolution of temperature and voltage for fresh LFP cells, those cycled at low temperature, and those at ambient temperature. It can be observed that Cell 1 and Cell 2, which were cycled at low temperature, were the first to enter the self-heating mode, at approximately 55 ℃, accompanied by venting gas and the emission of white smoke, as illustrated in Figure 62. The production of white smoke is primarily attributed to the decomposition of electrolyte and internal materials, resulting in the release

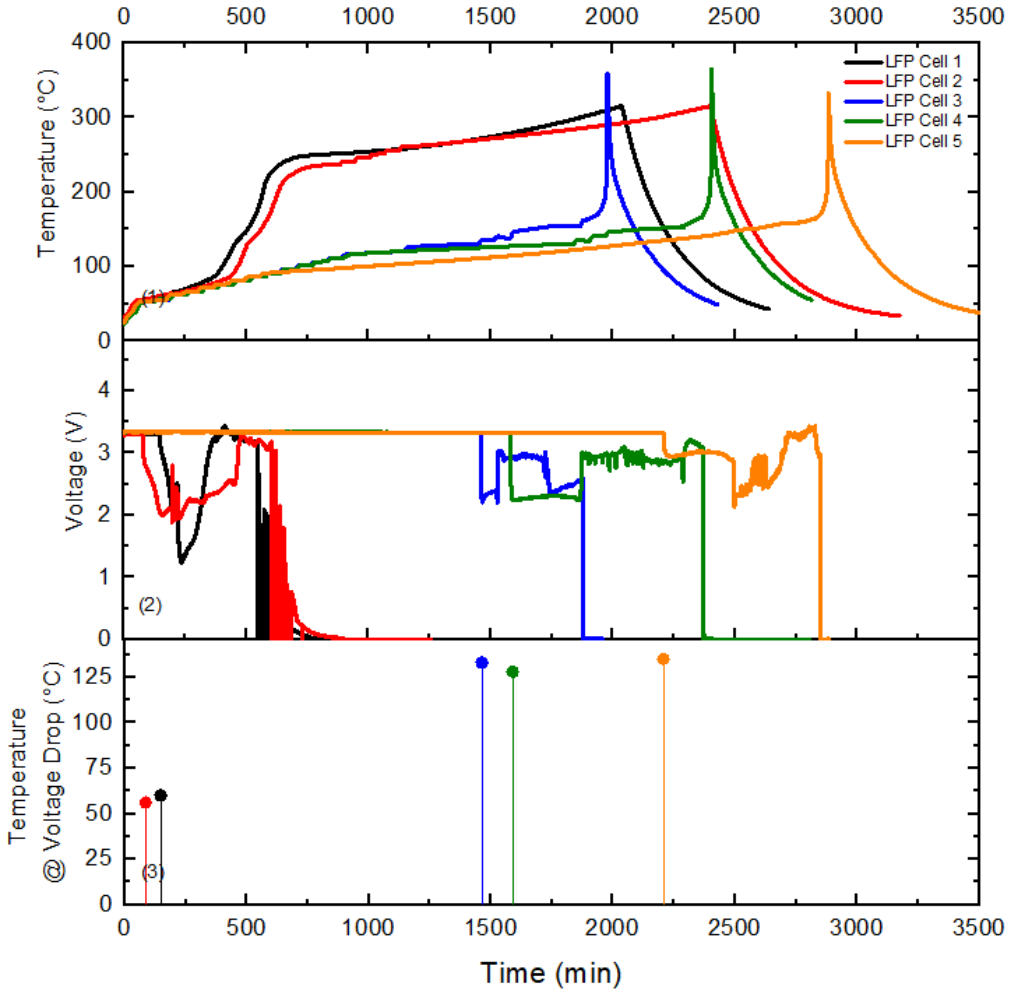

Figure 61. Cell surface temperature, voltage evolution, corresponding temperature during when cell experiences a sudden voltage drop.

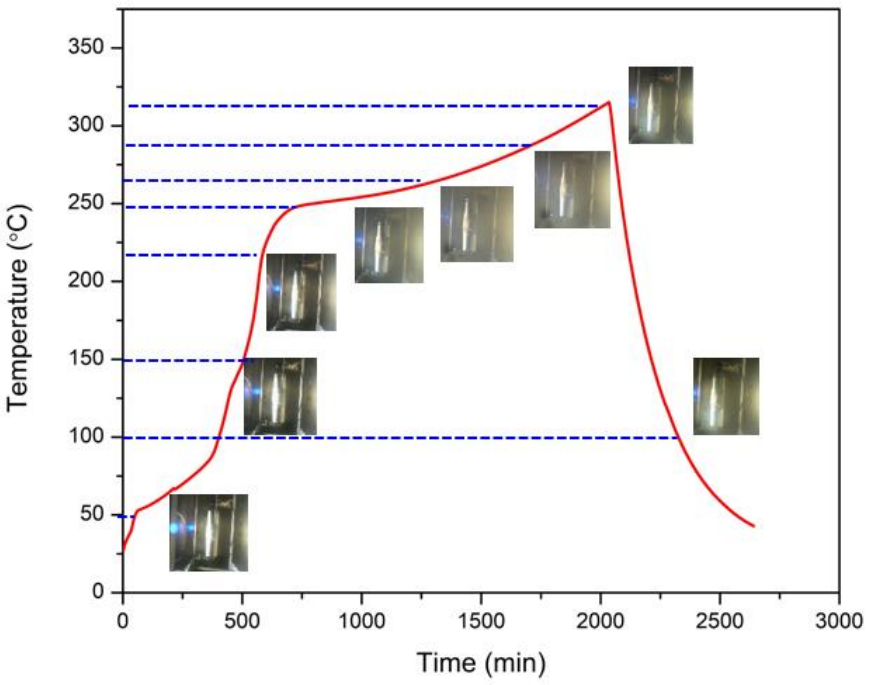

Figure 62. Venting gas and the emission of white smoke observed at around 55 ℃.

of gases and particles from the battery during overheating. However, with the surface temperature of the battery only reaching 55°C at this point, it implies the formation of high temperature spots internally. This leads to a non-homogeneous temperature distribution inside the cell, which in turn causes the observed emission of white smoke from the battery.

From the voltage evolution presented in Figure 61, it is clear that after reaching a certain temperature, the voltage suddenly drops, but it does not drop to zero immediately. Instead, it stabilizes at a certain level for a while before severe internal short cause the voltage to plummet to 0V, immediately triggering thermal runaway. Additionally, Figure 61 shows the corresponding temperatures (marked by dots with lines on the graph) when various aged batteries experience sudden voltage drops. It is observed that the cells cycled at low temperatures exhibit a voltage drop first, around 60 ℃, compared to other cells, whose voltage drops at approximately 130 ℃. This suggests that lithium dendrites formed during low temperature cycling create localized hot spots, accelerating internal short circuits.

During thermal runaway testing, three characteristic temperatures are identified to quantify the thermal stability performance of the cells: the self-heating onset temperature (corresponding to 0.02°C/min), TR temperature (corresponding to 1°C/min for JGNE LFP cell), and the maximum temperature. Figure 63 displays the critical temperatures collected during the thermal runaway experiments. It was observed that for LFP cells, the self-heating onset temperature ranged from 55 to 120 °C. Cells cycled at 0°C showed a lower self-heating onset temperature, dropping from 120°C to 55°C, a difference of approximately 70°C. In cells aged at low temperatures, not only is the self-heating onset

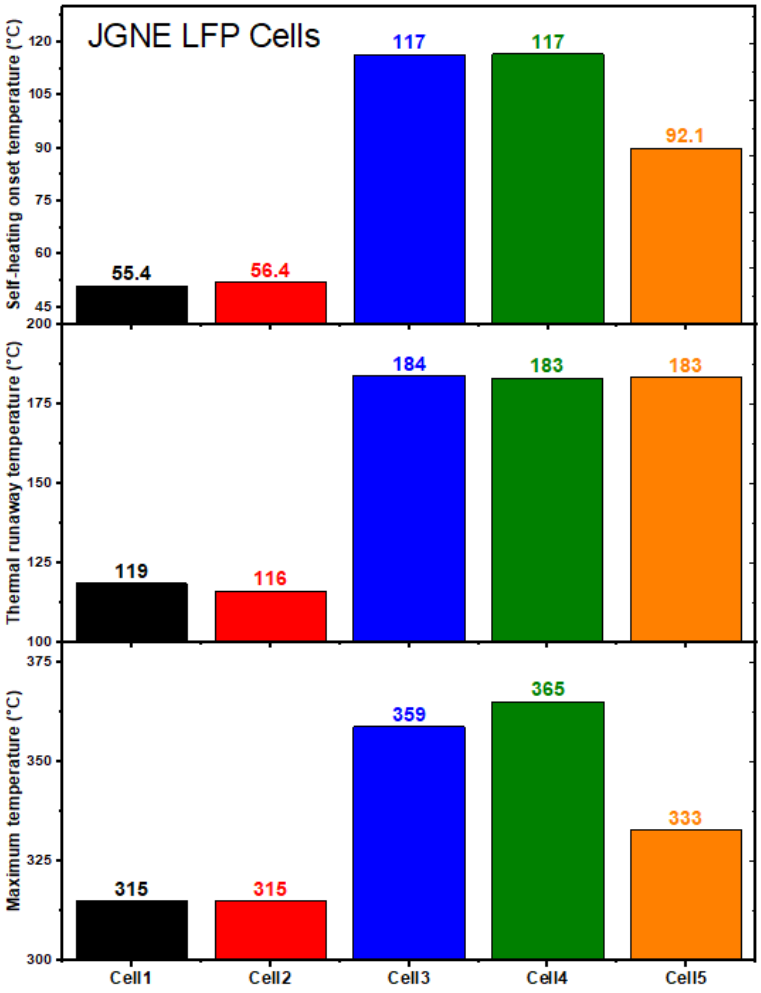

Figure 63. Critical temperatures at different aging conditions.

temperature lower, but the TR onset temperature also shows reduced performance. The decreasing trend in both self-heating and TR onset temperatures indicates a deterioration in the thermal stability of lithium-ion batteries after low temperature cycling. Additionally, the maximum temperature also shows reduced performance, which may be attributed to the loss of active material during the aging process.

In the thermal runaway experiments, we not only obtain characteristic temperature data but also derive the activation energy of the TR reaction and the frequency factor based on the temperature evolution curves and the temperature rise data, following the Arrhenius law [159,160]. The specific expression is shown below:

$$\ln\left(\frac{dT}{dt}\right) \approx \ln(\Delta T_{ad} A) - \frac{E_a}{k_b T} \tag{64.}$$

where $\frac{dT}{dt}$ is self-heating temperature rate, ΔT_{ad} is the difference between the initial self-heating onset temperature and the maximum temperature, k_b is Boltzmann's constant (8.62E-5 eV·K^{-1}), A is frequency factor and E_a is activation energy of TR reactions. Figure 64 plot $\ln\frac{dT}{dt}$ versus $\frac{1000}{T}$ for LFP cells to calculate frequency factor A and activation energy E_a under different conditions. It is observed that the performance of LFP batteries cycled at low temperatures differs significantly from other cells, not showing a linear relationship, thus making it challenging to derive specific values for frequency factor A and activation energy E_a in this study. However, the remaining cells displayed a linear relationship. By linearly fitting the temperature rate curves, the activation energy E_a, represented by the slope, and the frequency factor A, represented by the intercept, were obtained and summarized in Figure 65. The bar chart reveals a correlated consistency in the variation of

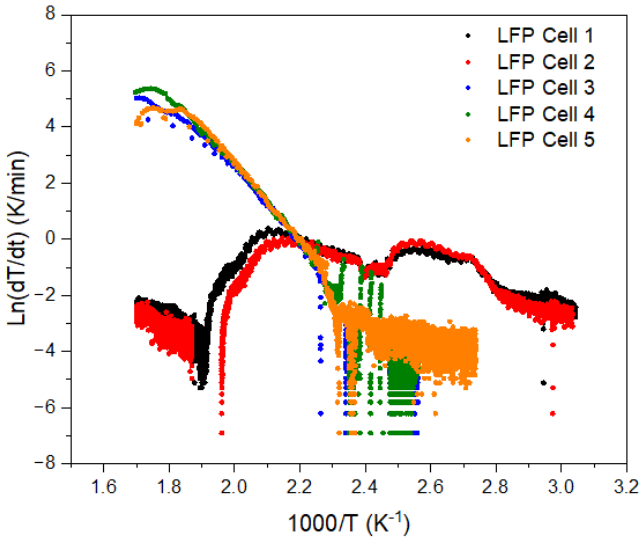

Figure 64. Natural logarithm of the self-heating rate versus inverse of temperature curves.

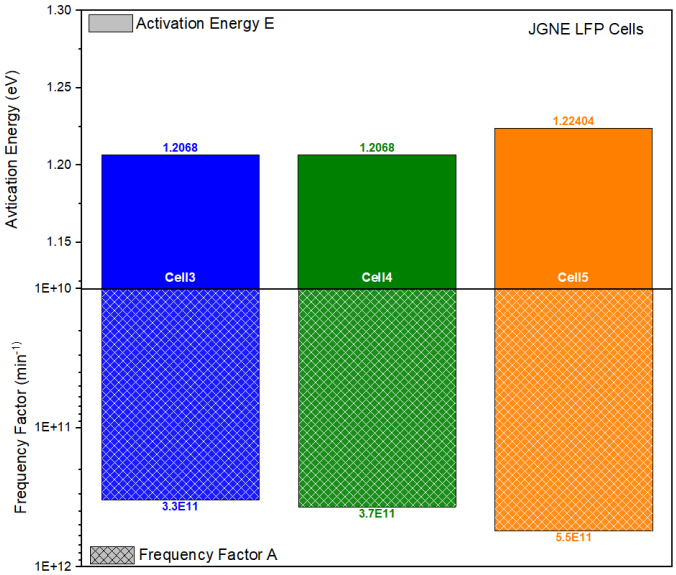

Figure 65. Activation energy and frequency factor of test cells.

calculated activation energy E_a and frequency factor A. Cells with higher activation energy also exhibit larger frequency factors. Since the LFP cells cycled at low temperatures did not yield calculable E_a and A values, they cannot be compared with fresh cells.

3. Numerical simulation approach

3.1 Hot spot simulation strategy

It is well known that short circuits within batteries can create hot spots, leading to thermal runaway. The growth of lithium dendrites can trigger these internal short circuits, thereby forming hot spots within the battery that generate localized high temperatures. The increase in battery temperature also triggers exothermic reactions between the electrolyte, the active material and solid electrolyte interface (SEI), further exacerbating the temperature increase.

Based on the experiments on battery thermal runaway described in the previous Section 2, it was observed that cells undergoing low temperature cycling enter the self-heating mode earlier, a phenomenon particularly evident in LFP batteries. At 55 ℃, these cells entered the self-heating mode, likely due to the formation of lithium dendrites caused by low temperature cycling. As the cell heats up and expands internally, lithium dendrites in some areas may puncture the separator, leading to partial internal short circuits. This forms a local hot spot, triggering the battery to enter the self-heating mode prematurely. To understand how local hot spots affect battery thermal runaway, this study developed a simple thermal runaway model with a local hot spot for a cylindrical 18650 LFP/Graphite cell.

For the numerical simulation, a two-dimensional axisymmetric model (2D) was developed in COMSOL Multiphysics 5.5 to simulate ARC experiments with a hot spot. The energy conservation equation of this model is shown in Table 23. Due to the axisymmetric geometry of the battery, the internal temperature of the battery varies both radially and axially, taking into account both thermal runaway reactions and internal heat conduction.

To better study the impact of local hot spots on thermal runaway, an initial simplified thermal runaway model was used to simulate scenarios without local hot spots. In this study, the LFP Cell 5 serves as a validation tool to ensure the functionality of the model. Based on ARC experimental results, the cell underwent a heating process for up to 700 minutes. During this period, the cell temperature curve from the ARC experiments, as shown in Figure 66, was applied as a boundary condition to the model, which also considered convection and radiation. The heat transfer coefficient, h_{conv} was set to 20 $W/m^3 \cdot K$, and surface emissivity, ε_{rad} was set to 0.8. After 700 minutes, the cell entered the self-heating mode, and the thermal boundary conditions of the model were set to adiabatic, neglecting convection and radiation. This adjustment was made because, when the test cell enters the exothermic mode, the system is insulated to prevent thermal exchange with the surrounding environment.

The heat source term in the model that triggers thermal runaway comes from four commonly used chemical side reactions [75]. The chemical heat release Q, inside the battery stems from four semi-global thermal chemical reactions, including the decomposition of the solid-electrolyte interface (SEI), the reaction between the anode

Table 23. Energy balance equation for 2D axis model.

	2D axisymmetric Model
Assumption	Thermal stratification exists
Governing Equation	$\rho c_p \frac{\partial T}{\partial t} = \frac{1}{r}\frac{\partial}{\partial r}\left(k_r r \frac{\partial T}{\partial r}\right) + \frac{\partial}{\partial \theta}\left(k_\theta \frac{\partial T}{\partial \theta}\right) + Q$
Chemical reaction heat	$Q = Q_{sei} + Q_{ne} + Q_{pe} + Q_e$
Boundary condition	$q_{conv}'' = h_{conv}(T - T_{ARC})$
	$q_{rad}'' = \varepsilon_{rad}\sigma(T^4 - {T_{ARC}}^4)$

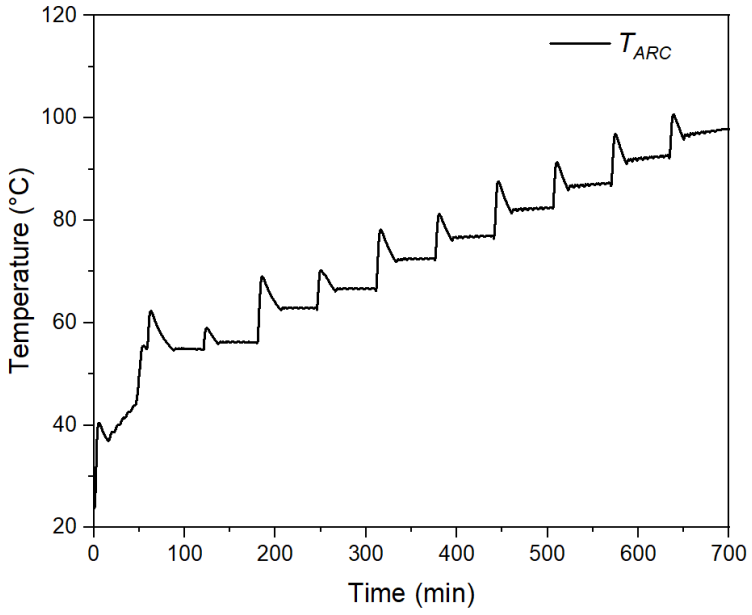

Figure 66. Temperature profile of LFP Cell 5 during the heating process in the thermal runaway experiment.

and electrolyte, the reaction between cathode and electrolyte, and electrolyte decomposition. The quantitative characteristics of these reactions depend on the battery material properties, thermal chemical parameters, and temperature. The reaction model, frequency factor, and activation energy describing the kinetics between battery materials have been previously determined by fitting experimental measurements from accelerating rate calorimetry (ARC) and differential scanning calorimetry (DSC) tests [73]. The chemical reaction rates and heat generation are widely recognized in the literature [70,75] and summarized in Table 24.

To validate the thermal runaway model, the four-step reaction model was compared with experimental results from LFP Cell 5, as described in Section 2. The model parameters, derived from [264], describe a fully charged battery with LFP/Graphite chemistry. As illustrated in Figure 67, although there are some discrepancies between the model and experimental results, previous study [143] has highlighted the challenges posed by cell-to-cell variation in model predictions. Furthermore, Cells 3 and 4, despite being identical batteries, exhibited slightly different thermal runaway behaviors, as noted in Section 2. Additionally, the temperature curve of the model does not decrease after thermal runaway occurs, contrasting with the rapid decrease in temperature observed in the experimental cells post-thermal runaway. This inconsistency is attributable to the adiabatic boundary conditions of the model. Given that our focus is on the impact of local hot spots on thermal runaway, the deviation of model falls within a reasonable range of acceptance. This model will be utilized further to investigate the effects of local hot spots on thermal runaway.

Table 24. Reaction rates and heat sources of the four-step thermal abuse model.

Reaction term	Equations	
SEI decomposition	$\frac{dc_{sei}}{dt} = -A_{sei} exp\left[-\frac{E_{a,sei}}{RT}\right] c_{sei}^{m_{sei}}$	$Q_{sei} = -H_{sei} W_c \frac{dc_{sei}}{dt}$
Anode-electrolyte reaction	$\frac{dc_{ne}}{dt} = -A_{ne} exp\left[-\frac{t_{sei}}{t_{sei0}}\right] c_{ne}^{m_{ne,n}} exp\left[-\frac{E_{a,ne}}{RT}\right]$	$Q_{ne} = -H_{ne} W_c \frac{dc_{ne}}{dt}$
	$\frac{dt_{sei}}{dt} = A_{ne} exp\left[-\frac{t_{sei}}{t_{sei0}}\right] c_{ne}^{m_{ne,n}} exp\left[-\frac{E_{a,ne}}{RT}\right]$	
Cathode-electrolyte reaction	$\frac{d\alpha}{dt} = A_{pe} \alpha^{m_{pe,p1}} (1-\alpha)^{m_{pe,p2}} exp\left[-\frac{E_{a,pe}}{RT}\right]$	$Q_{pe} = -H_{pe} W_p \frac{d\alpha}{dt}$
Electrolyte decomposition	$\frac{dc_e}{dt} = -A_e exp\left[-\frac{E_{a,e}}{RT}\right] c_e^{m_e}$	$Q_e = -H_e W_e \frac{dc_e}{dt}$
Overall heat generation	$Q = Q_{sei} + Q_{ne} + Q_{pe} + Q_e$	

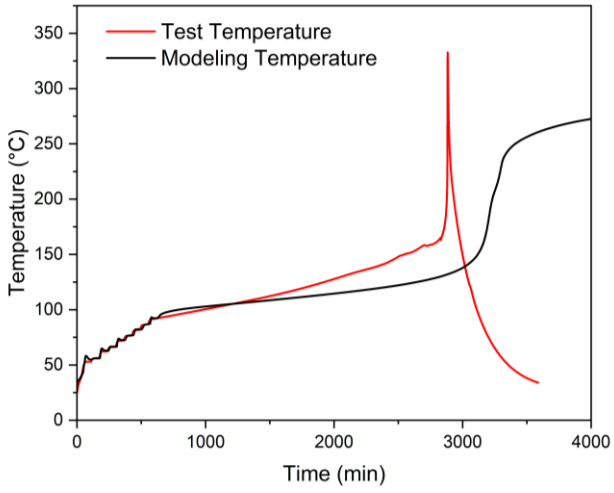

Figure 67. Comparison of temperature profiles: model predictions vs. experimental data for LFP Cell 5.

To understand the impact of local hot spots on thermal runaway, we selected a small area within the battery to simulate the local hot spots, based on the validated model, as illustrated in Figure 68. The specific meshing parameters for the model are as follows: the minimum element size is set at 1.38E-8 m, the element growth rate for the mesh at 1.4, and the boundary layer properties include 8 layers with a stretching factor of 1.2. The remaining domain size properties are configured with a maximum element size of 6.9E-4 m, a minimum element size of 1.38E-6 m, and an element growth rate of 1.1. The model comprises 15186 domain elements and 654 boundary elements. Subsequently, we applied three different heat sources to this hot spot region, as shown in Figure 69, to observe the influence of the hot spots on thermal runaway.

3.2 Hot spot modeling results

The temperature evolution of the cell after applying a heat source to the small hot spot region is shown in Figure 70. It can be noted that local heat sources can indeed cause the battery to experience thermal runaway earlier, and the greater the intensity of the heat source, the earlier the thermal runaway occurs. It is observed that when the localized heat source intensity is set to 1.5E8 W/m^3, the thermal runaway behavior of model closely mimics the thermal runaway behavior of aged LFP cells cycled at low temperatures. This further confirms that the earlier onset of thermal runaway in LFP cells may be attributed to excessive lithium dendrite formation during the aging process, leading to internal short circuits and hot spots. Additionally, if the localized heat source is particularly small, it does not accelerate the occurrence of thermal runaway. This simplified model provides valuable insights into the impact of local hot spots on thermal runaway.

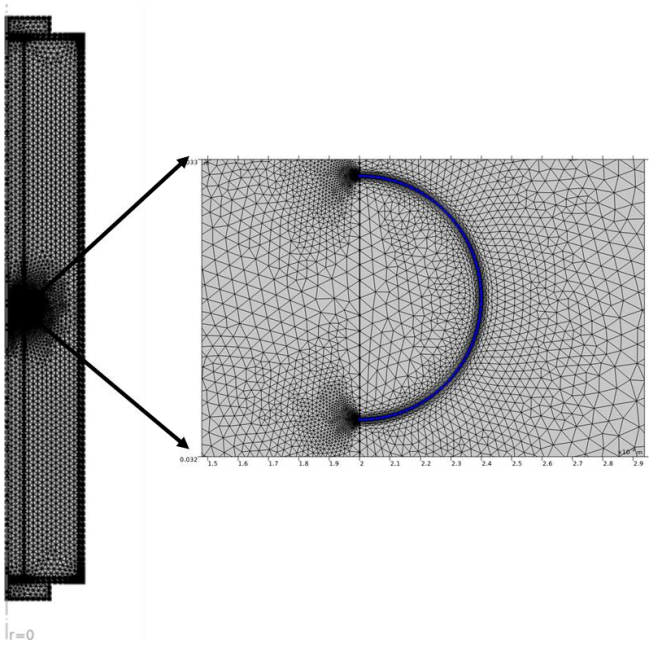

Figure 68. Numerical simulation model incorporating a small hot spot region.

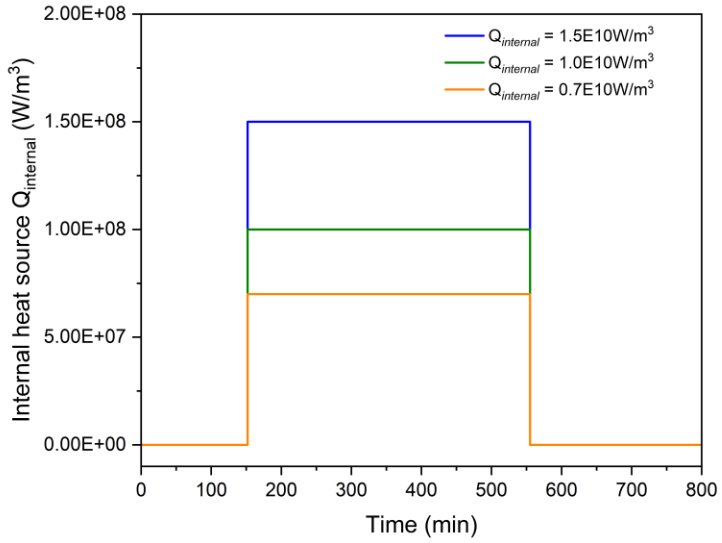

Figure 69. Three different intensities of heat source applied to small hot spot.

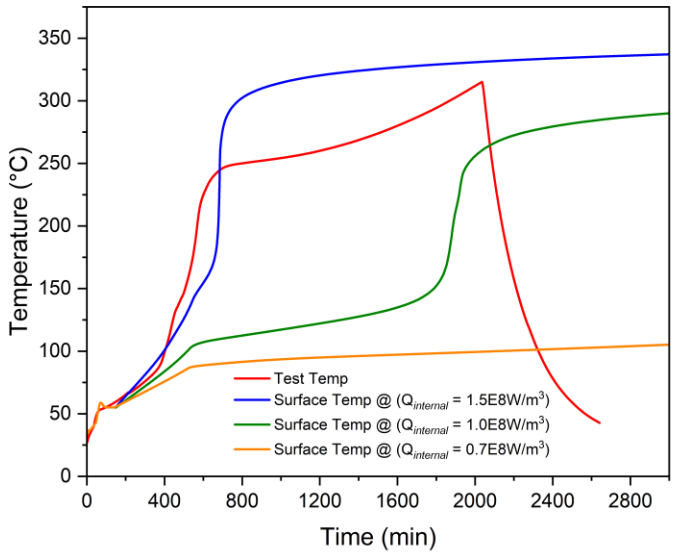

Figure 70. Temperature evolution under different applied internal heat source.

4. Conclusion

This study investigated the thermal runaway phenomenon in lithium-ion batteries, particularly focusing on the significant effects of lithium plating and dendrites resulting from low temperature cycling. Commercial 18650 LFP cells were employed. It demonstrated an earlier onset of thermal runaway after aging through low temperature cycling compared to fresh cells, which was attributed to the formation of lithium plating and dendrites. Experiments revealed that low temperature cycling significantly accelerated the thermal runaway process. This was apparent in LFP batteries, which entered to the self-heating mode much earlier, around 55°C, indicating that the degree of aging and lithium dendrite formation significantly impacts the thermal stability of the batteries. It is worth noting that the early self-heating mode of LFP is characterized by gas emissions and white smoke, which suggests increased risks associated with aging cells. To better understand the initiation and progression of thermal runaway caused by internal hot spots due to lithium dendrites, the study utilized a simplified model, applying heat sources of varying intensities to a small hot spot within the battery. The model confirmed that while larger heat sources indeed accelerate thermal runaway Although simplified, the results provide valuable insights into the potential effects of localized thermal hot spots on the overall thermal runaway in lithium-ion batteries. This model helps to propose a mechanism of thermal runaway similar to hot spot induced ignition.

CHAPTER VI

AEROSOL EMISSION CHARACTERISTICS DURING LI-ION BATTERY THERMAL RUNAWAY

Abstract

Aerosol emission during battery thermal runaway can serve as hot spots and lead to subsequent thermal runaway propagation in nearby cells and gas phase explosions. Furthermore, such submicron particles can potentially be toxic, leading to greater concerns for environmental pollution and inhalation hazards. While thermal runaway has been extensively characterized, aerosol emission from thermal runaway is largely unknown. In this work, two major equipment for aerosol measurement — Engine Exhaust Particle Sizer (EEPS) and Aerodynamic Particle Sizer (APS) — are utilized to quantify the number density, peak diameter, and time evolution of aerosol emission during thermal runaway. The EEPS captures particles ranging from 5.6 nm to 560 nm, while the APS captures particle size from 0.5 to 20 microns. Thermal runaway experiment is conducted via well-controlled rapid heating strategy in an accelerating rate calorimeter (ARC), to which the EPPS and APS are connected. This work reports novel data on the distribution and time evolution of aerosol emission from various Li-ion batteries.

1. Introduction

With the acceleration of industrial development, the spread of pollution has been exacerbated. Finding alternative methods to reduce environmental pollution has become an important task for industries. Lithium-ion batteries (LIBs) have been widely used in various industries and daily life due to their high energy density, long cycle life, high efficiency, and minimal environmental impact [265–268]. These attributes are driving the global shift towards decarbonization and electrification. However, despite their advantages, LIBs also present significant safety challenges, particularly in terms of thermal runaway [269–272].

Thermal runaway of lithium-ion batteries is a complex, exothermic reaction that can release a large amount of energy, emit toxic gases and aerosols, and result in smoke, fire, and explosion, thereby causing pollution and unavoidable environmental harm. This phenomenon has attracted widespread attention from researchers. For example, Wang et al. [273] investigated the thermal hazard characteristics of gases released from batteries with different cathode materials during thermal runaway. They verified the combustion and explosion properties through experiments to assess associated risks. Chen et al [274] investigated the hazardous components of powder ejected during the thermal runaway of a fully charged lithium-ion battery. They found that it primarily consists of carbon, organosilicon, small organic molecules, silicon dioxide, carbonates, and metals, with the composition influenced by the state of charge, heating temperature, and atmosphere, highlighting the potential danger this powder poses to human health under varying conditions. Zhang et al. [275] studied vent gas and particulate matter (PM) emissions

during thermal runaway in lithium-ion batteries. They demonstrated that boiling point classification effectively identifies vent gas compositions, with significant portions of emissions being quantifiable and settleable PM below 0.5 mm dominating PM mass, leading to a total emission representing 28.53% of the cell mass. Premnath et al. [276] investigated particle and gaseous emissions from thermal runaway events in LFP and NMC lithium-ion battery systems. revealing that both battery chemistry and the initiation mechanism of thermal runaway significantly affect the magnitude and profile of particle emissions. They also found that the emission of PM2.5 and total particulate number (PN) at rates far exceeding those from diesel engine exhaust. Wang et al [277] demonstrated that smaller smoke particles from Li-ion battery thermal runaway exhibit higher oxidation reactivity, suggesting that capturing or neutralizing these particles could enhance battery safety by mitigating fire risks. Sturk et al [278] highlighted the significant differences in chemical reactivity, venting duration, maximum temperature, and gas emissions between NMC/LMO and LFP lithium-ion cell chemistries. They showed NMC/LMO cells are more reactive with faster venting, higher temperatures, and greater CO_2 emissions, but have similar HF releases compared to LFP cells, emphasizing the importance of cell chemistry in battery safety evaluations. Zhang et al. [279] revealed the particle size distribution and elemental composition of the settleable solid particles, which contain significant amounts of carbon, nickel, copper, cobalt, manganese, aluminum, and lithium.

While some studies have focused on vent gases emission and particle ejection from Li-ion batteries during thermal runaway, there are relatively few studies that specifically focus on the characteristics of aerosol emissions during thermal runaway events. These

emissions represent significant health and environmental pollution risks and necessitate extensive research to inform safety standards and mitigation policies. This gap in research highlights the need for a focused investigation into the aerosol generated during Li-ion battery thermal runaway, to better understand their composition, behavior, and impact on both health and the environment.

This paper aims to conduct an in-depth study of the aerosol emissions characteristics during Li-ion battery thermal runaway. By exploring the peak diameter, particle size distribution, and time evolution of aerosol emission during thermal runaway, this study attempts to provide valuable insights into the aerosol generated in these hazardous scenarios. Understanding the specifics of aerosol emissions during thermal runaway is crucial for developing safer battery technologies, enhancing emergency response measures, and minimizing the impact on human health and the environment. Through experimental analysis and a review of existing literature, this study contributes to knowledge about Li-ion battery safety and presents a step forward in addressing one of the critical challenges in the field of energy storage.

2. Experimental Methodology

2.1 Battery types and characteristics

In this study, we utilized six commercial cells from different manufactures to investigate their thermal runaway behavior and aerosol emission distribution during thermal runaway. These included lithium nickel cobalt manganese oxide (NMC) batteries from Sony, LG and Samsung; lithium nickel cobalt aluminum oxides (NCA) batteries from

Panasonic; and lithium iron phosphate (LFP) batteries from A123 and JGNE. Table 25 lists the detailed of specifications of each battery for clarify and reference.

Before TR testing, all cells were cycled three times followed by the standard charge / discharge condition based on their datasheet, ensuring they all reached 100 % SOC. The charging / discharging protocols were conducted using a MACCOR 4200 system with an environmental chamber. After initialization, Electrochemical Impedance Spectroscopy (EIS) tests were performed using the PARSTAT 4000A (Princeton Applied Research). Fundamental data such as discharge capacity and Nyquist plot for these cells are displayed in Figure 71(a) and Figure 71(b), providing insights into their baseline performance and electrochemical properties.

The Nyquist plot is a valuable tool for analyzing the electrochemical properties of batteries, offering insights into their performance and internal processes [195]. According to the Nyquist plot based on a Randles cell model, the intersection of the semicircle with the real axis in the high frequency range represents the ohmic resistance, associated with resistance of the electrolyte, separator, and electronic components of the battery. The diameter of the semicircle represents the charge transfer resistance, influenced by the kinetics of electrochemical reactions at the electrode interfaces, and the straight line in the low frequency represents the diffusion process [195].

It can be seen that LG and Panasonic batteries exhibit higher capacities, which are desirable for applications requiring extended usage times, such as EVs and portable electronic devices. However, both start at a slightly higher Z_{re}, suggesting higher ohmic resistance, which could impact efficiency, especially at high discharge rates. Additionally,

Table 25. The specifications of the battery sample involved in this study.

Property (unit)	Sony	LG	Samsung	Panasonic	A123	JGNE
Model number	US 18650VTC4	INR 18650MJ1	INR 18650-25B	NCR 18650B	APR 18650M1B	HTPFR 18650
Chemistry	NMC	NMC	NMC	NCA	LFP	LFP
Height (mm)	65	65	65	65	65	65
Diameter (mm)	18	18	18	18	18	18
Rated capacity (Ah)	2.1	3.5	2.5	3.2	1.2	1.1
Nominal voltage (V)	3.7	3.635	3.6	3.6	3.3	3.2
Charging voltage (V)	4.2	4.2	4.2	4.2	3.6	3.65
Discharging cut-off voltage (V)	2.5	2.5	2.5	2.5	2.0	2.5
Max. charge/discharge current (A)	N/A / 30	3.4 / 10	4 / 20	N/A	4 / 30	5.5 / 33
Suggested operating temperature (ºC)	0~45 (Charge) -20~75 (Discharge)	0~45 (Charge) -20~60 (Discharge)	0~45 (Charge) -20~75 (Discharge)	10~45 (Charge) -20~60 (Discharge)	0~55 (Charge) -30~55 (Discharge)	0~55 (Charge) -20~60 (Discharge)

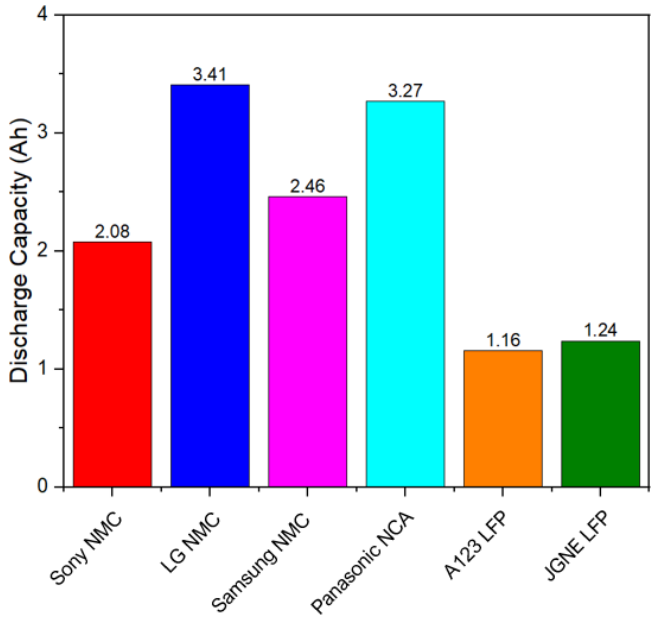

(a)

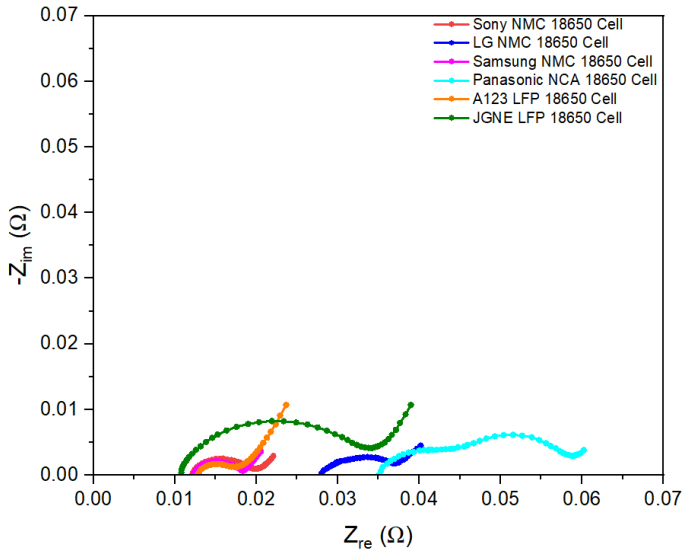

(b)

Figure 71. (a) Competitive discharge capacity of commercial cells from various manufacturers; (b) competitive Nyquist plot of commercial cells after initialization.

the Nyquist Plot for the Panasonic cell shows a more elongated curve, which may indicate different kinetics or diffusion characteristics, possibly affecting its performance under varying load conditions. In contrast, Sony and Samsung batteries display moderate capacities, starting at a slightly lower Z_{re} compared to LG, which implies lower ohmic resistance and could enhance efficiency. They also have a similar semicircle size, indicating comparable charge transfer resistances. A123 and JGNE batteries, on the other hand, have relatively lower capacities compared with the other cells, limiting their suitability for applications requiring prolonged usage. These batteries are potentially more suited for energy storage systems, where stability, safety, and long-term reliability are more critical than immediate power delivery.

2.2 Thermal runaway-aerosol experimental setup

The thermal runaway-aerosol test integrates thermal runaway testing, performed using the EV+ accelerating rate calorimetry (ARC) manufactured by Thermal Hazard Technology (THT), with aerosol measurements employing two major equipment from TSI: Engine Exhaust Particle Sizer (EEPS) and Aerodynamic Particle Sizer (APS). The setup combination schematic is shown in Figure 72. The detailed operational principle of the ARC and the physical arrangement of the test cell in the EV+ AR can be referred to our previous work [143].

The EEPS and APS are instruments designed for detailed particle size distribution measurements. The EEPS measures particles ranging from 5.6 to 560 nm, which is useful for capturing submicron particles typically associated with combustion processes or chemical reaction [280]. It provides high temporal resolution, allowing for real-time

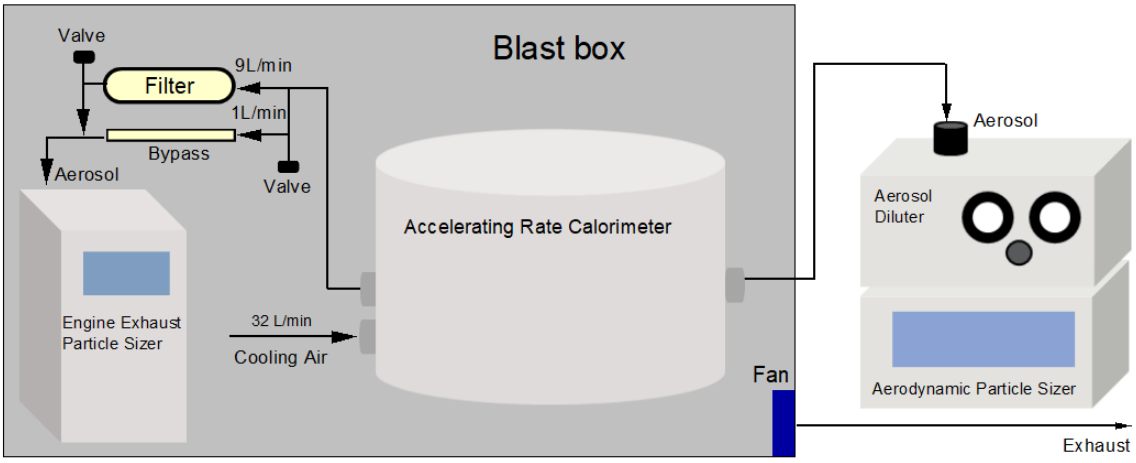

Figure 72. Schematic of thermal runaway – aerosol measurement setup for Li-ion batteries.

analysis of dynamic processes. On the other hand, the APS measures micron particles, typically ranging from 0.5 to 20 μm, making it suitable for assessing a broader spectrum of aerosol emissions [281]. Both instruments are critical in evaluating aerosol and particulate emissions from thermal events in battery testing, offering insights into particle size distribution and concentration during thermal runaway scenarios.

In this study, the rapid heating method is adopted to trigger thermal runaway. All cells are heated from ambient temperature to a surface temperature of 150 ℃ quickly, differing from the standard heat-wait-seek (HWS) heating mode to save time. Based on previous experimental observations, we have determined that cell will enter the exothermic mode at 150 ℃. After the ARC system switches to exotherm mode, it maintains a nearly adiabatic environment, ensuring no temperature difference between the heaters and the test cell until the cell triggers thermal runaway. Simultaneously, the EEPS and APS begin sampling.

To ensure accurate and precise measurement, we carefully set the dilution at 10:1 for EEPS and 20:1 for the APS. The purpose of this dilution is to mix the aerosol samples with clean air, effectively reducing their concentration. It is critical to avoid overloading the sensors and to guarantee that the particle size data collected reflects true aerosol emission during Li-ion battery thermal runaway.

3. Preliminary results and discussion

3.1 Thermal runaway characterization

In this study, we monitored the evolution of temperature and voltage of different 18650 cells during thermal runaway testing, as illustrated in Figure 73. From the

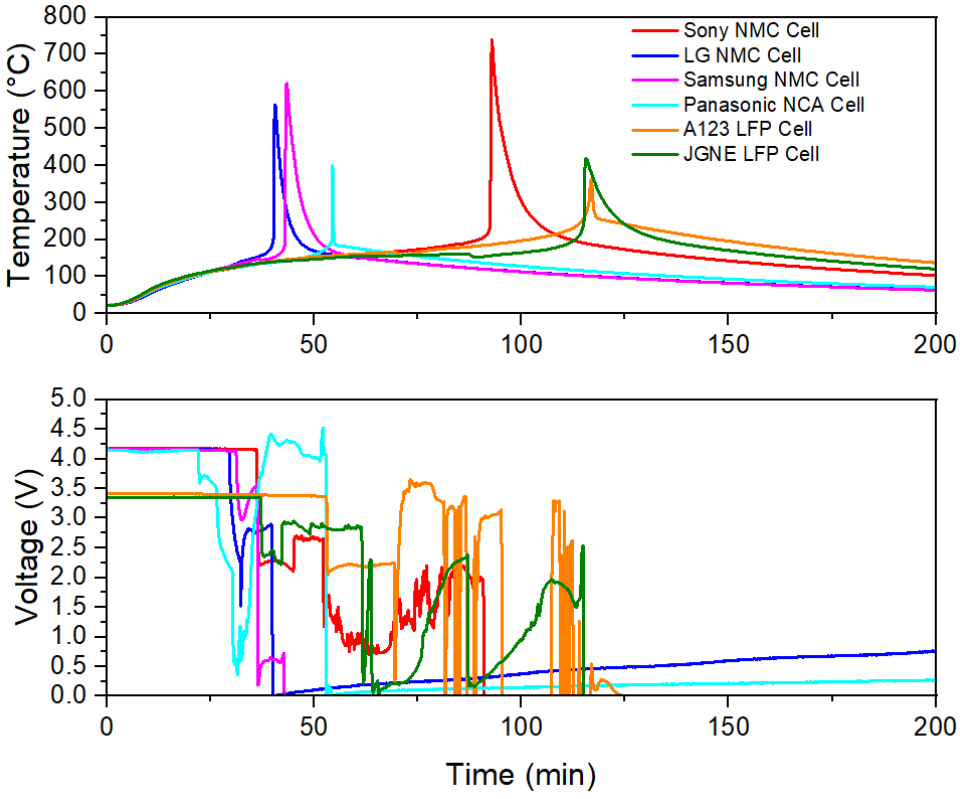

Figure 73. Cell surface temperature and voltage evolution for different cells during ARC experiments.

temperature evolution diagram, it is apparent that LG cell experienced thermal runaway first, which may be related to its higher capacity. This was followed by the Samsung cell, then the Panasonic and Sony cells, and finally, the more stable LFP cells.

Looking at the voltage evolution diagram, there is no clear sequential pattern. The voltage of the Panasonic cell starts to drop first, followed by LG, Samsung and Sony. This inconsistency can be attributed to several factors, such as internal short circuits, electrolyte decomposition, or thermal degradation of the electrode material. Given that the cells come from different manufacturers, it is challenging to analyze the specific cause, resulting in a weak correlation between voltage drop curves and thermal runaway behavior. Nonetheless, the voltage of all batteries fluctuates over a period of time and eventually drops to zero at the moment of thermal runaway.

After the experiment, the mass loss of all cells was measured, and the percentage of mass loss is shown in Figure 74, it can be observed that the LG cell suffered the most mass loss, followed by Samsung, Panasonic and Sony, with A123 and JGNE experiencing the least. This trend indicates a positive correlation with the sequence in which thermal runaway occurred among the cells.

Regarding the temperature evolution from ARC test, activation energy of the TR reaction can be calculated from the heat release rate. Based on the Arrhenius law, the self- heating rate can be expressed in Equation (63.) [159,160], assuming adiabatic and ignoring reactant consumption:

$$\ln\left(\frac{dT}{dt}\right) \approx \ln(\Delta T_{ad} A) - \frac{E_a}{k_b T} \qquad (65.)$$

where $\frac{dT}{dt}$ is self-heating temperature rate, ΔT_{ad} is the difference between the initial self-

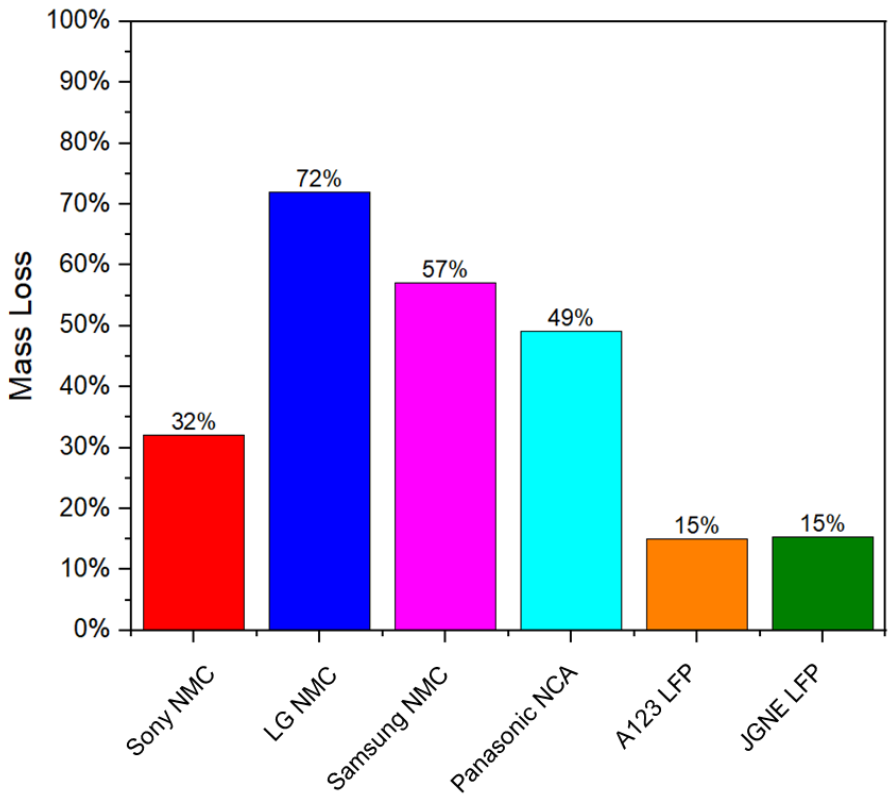

Figure 74. The mass loss percentage of different cells.

heating onset temperature and the maximum temperature, k_b is Boltzmann's constant (8.62E-5 eV·K^{-1}), A is frequency factor and E_a is activation energy of TR reactions. Figure 75(a) plots $\ln\frac{dT}{dt}$ versus $\frac{1000}{T}$ to calculate frequency factor A and activation energy E_a for six cells with different manufactures. By using the linear fitting on the temperature rate profiles, the activation energy E_a indicated by the slope and frequency factor A indicated by the intercept. However, since this experiment directly and rapidly heated the cells to 150 ℃— bypassing the initial self-heating onset temperature, a key temperature parameter of ARC test — the calculation of frequency factor A was not considered in this study. The calculated activation energy E_a for six different cells are summarized in Figure 75(b).

Activation energy E_a for NMC, NCA and LFP battery materials may vary due to differences in specific chemical compositions, manufacturing methods, and testing conditions. As illustrated in Figure 75(b), even cells with the same chemistry can exhibit variations in activation energy due to being sourced from different manufacturers. Although theoretically, a higher activation energy suggests better thermal stability, the actual performance and safety of the battery are affected by multiple factors, including material properties, battery design and operating conditions. This explains why the activation energy of LFP cells is relatively low, yet they provide excellent thermal stability and safety through their unique chemical and structural properties.

3.2 Aerosol distribution analysis

During the experimental process of aerosol sampling, we encountered certain inevitable technical challenges. Our goal was to capture the aerosol emission distribution

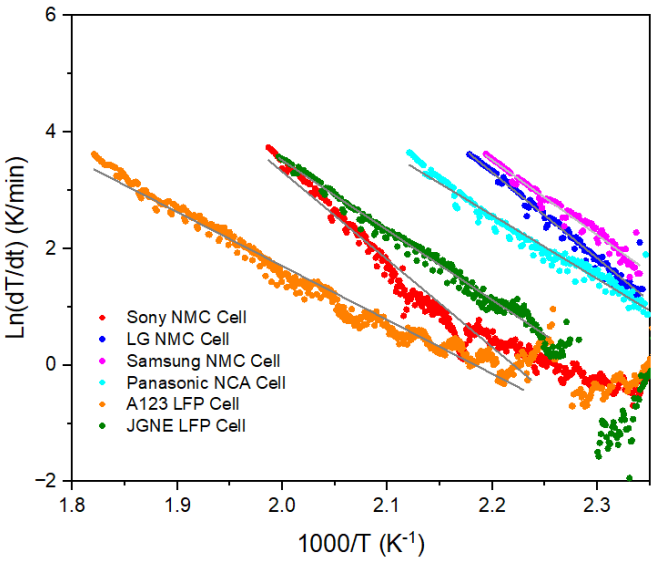

(a)

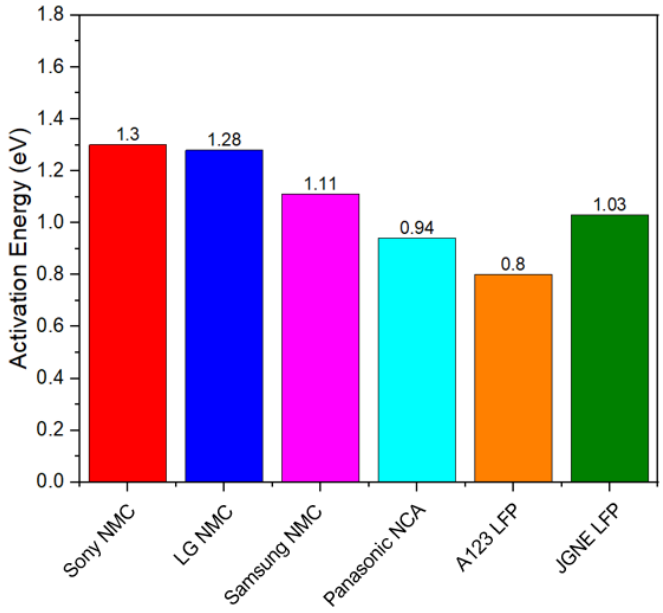

(b)

Figure 75. (a) ln(dT/dt) vs. 1000/T during TR of six different cells; (b) activation energy of six different cells.

during thermal runaway. For this purpose, EEPS and APS were utilized for collection. These instruments require airflow to collect data. However, the ARC instrument, which is designed to maintain an internal adiabatic environment during thermal runaway experiments, does not allow for airflow. The ARC only activates its cool down mode, introducing air into the chamber, when the temperature of the cell reaches the upper limit of 315 ℃ after thermal runaway has occurred.

Consequently, EEPS and APS begin sampling only after the ARC triggers its cooldown mode. Furthermore, due to the startup response time of approximately 10 seconds for EEPS and APS, the aerosol signal is collected within one minute after thermal runaway, rather than at the moment of occurrence. This delay may affect our sampling results. However, we ensured consistency across all cells by standardizing the collection start point relative to each cell thermal runaway event. In future experiments, we will explore methods to address this delay more effectively.

Figure 76 shows the normalized sampling onset relative to the corresponding cell temperature profile. All samples were collected for 600s when the temperature started to drop after thermal runaway.

As previously mentioned, the EEPS primarily measures particle sizes ranging from 5.6 to 560 nm, while the APS focuses on measuring particle sizes from 0.5 to 20 μm. To address the resolution problem encountered when comparing particle concentration data from instruments with different resolutions, the concept of normalized concentration is introduced. Normalizing the concentration data by the logarithmic particle size interval allow allows for a fair comparison between different data sets by removing dependency on

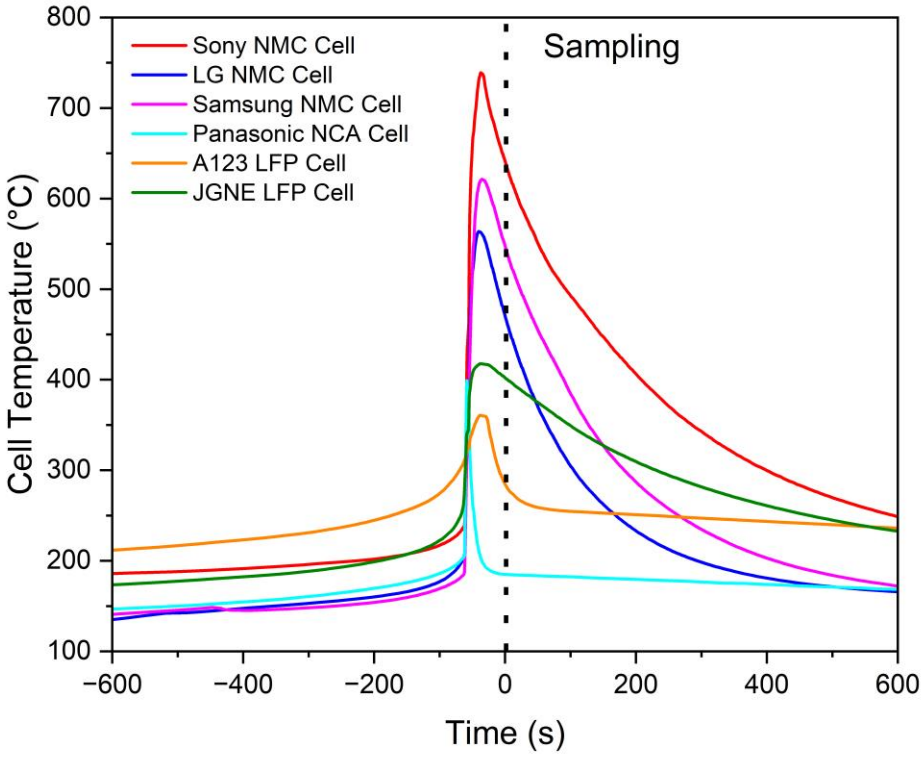

Figure 76. Normalized sampling onset after Li-ion battery thermal runaway.

bin width [282]. The normalized concentration is expressed as:

$$dN/dlogD_p = \frac{dN}{dlogD_p} = \frac{dN}{dlogD_{p,u} - dlogD_{p,l}} \quad (66.)$$

where dN is particle concentration, $dlogD_p$ is the difference in the log of the channel width, D_p is midpoint particle diameter, $D_{p,u}$ is upper channel diameter, $D_{p,l}$ is lower channel diameter.

3.2.1 *Total concentration analysis*

Figure 77 displays the aerosol total concentration over time for each of six cells, using EEPS (red line on the top plot), APS (blue line on the middle plot), and the combined total of both (black line on the bottom plot) to provide a more complete understanding of the particle concentration in the sample. Figure 77 (a), (b) and (c) present the data of total concentration changes over time for NMC cell from Sony, LG, and Samsung, respectively.

The EEPS and APS of those three brands of NMC cells exhibit a similar pattern. The particle behavior can be characterized in three stages: In stage 1, micron and submicron particles coexist and both decreases. In stage 2, submicron particles rise to a plateau, while micron particles peak and then decline. In stage 3, submicron particles become dominant and continue decreasing. However, the significance of micron sized particles is not always consistent; for LG and Samsung, the total concentration of micron sized particles is lower than that of submicron particles by one to two orders of magnitude.

Moreover, the global pattern of concentration is not uniformly consistent across all cell types. For instance, the Samsung cell exhibits a distinct spike in concentration, indicating unique emission behavior compared to the other cells. This variability underscores the complexity of thermal runaway phenomena and highlights the diverse

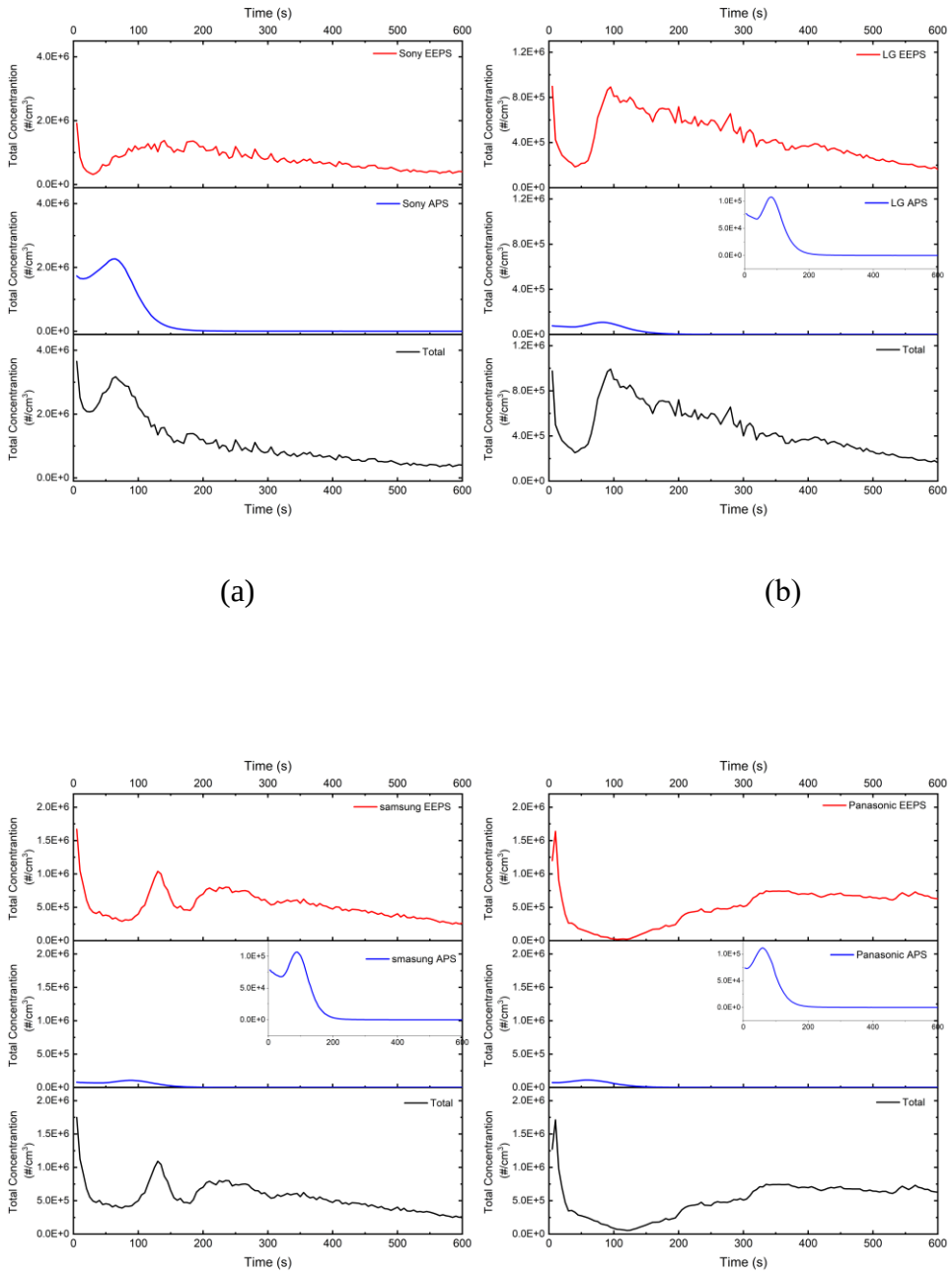

(a) (b)

(c) (d)

Figure 77. Total concentration of aerosols emission after thermal runaway measured using EEPS and APS (a) Sony NMC cell; (b) LG NMC cell; (c) Samsung NMC cell; (d) Panasonic NCA cell; (e) A123 LFP cell; (f) JGNE LFP cell.

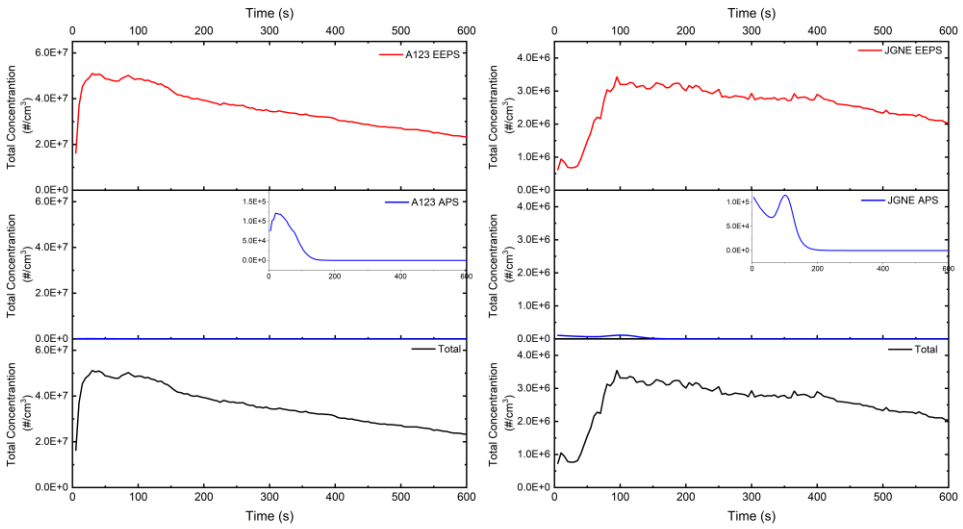

(e) (f)

Figure 77 continued

aerosol emission patterns that can emerge depending on the battery chemistry and manufacturing differences.

Figure 77(d) displays the data of total concentration changes over time for Panasonic NCA cell. The trend of EEPS data for this cell starts with a small rise, followed by a sharp decline, and then stabilizes over time, which is slightly different from that of NMC cells. In contrast, the APS data for the Panasonic cell is almost identical to that of the NMC cells. It is noted that the global trend is dominated by submicron particles, highlighting a consistent pattern with the NMC cells.

Figure 77(e) and (f) reveal that LFP cells exhibit a different emission pattern compared to both NMC and NCA cells. The EEPS data for LFP cells indicates slightly higher variability in submicron particle emission, with total concentration showing a consistent increasing trend before stabilizing. This behavior suggests that LFP cells have a distinct particle emission profile compared to the other chemistries studied. Additionally, it is observed that the micron particle number density is one or two orders of magnitude lower than that of submicron particles. The global trend is dominated by submicron particles, which first increase and then decrease over time, further highlighting the unique characteristics of aerosol emissions from LFP cells.

3.2.2 *Particle size distribution analysis at specific time*

Figure 78 displays a series of particle size distribution measured by EEPS and APS at different specific time points (t = 5s, 10s, 30s, 45s, 60s, 90s, 180s, 300s and 600s) after thermal runaway. Figure 78(a) illustrated that at = 5 s, the Sony NMC cell exhibits a diverse

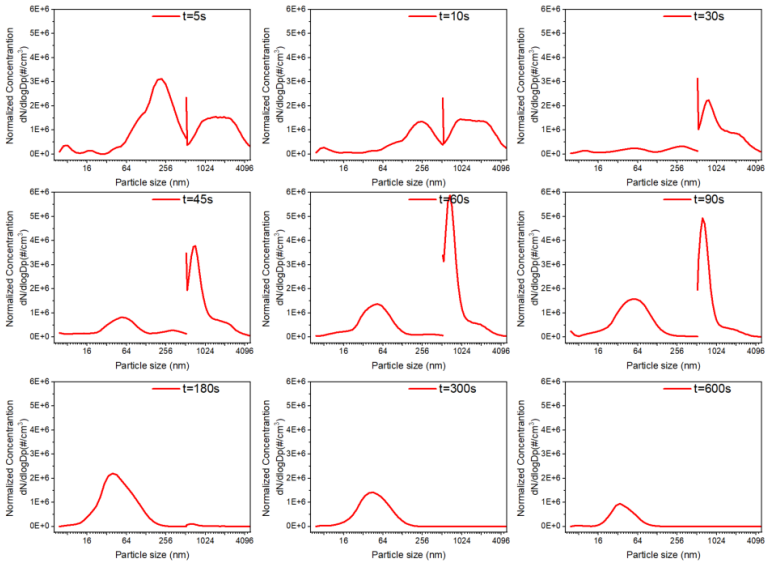

(a)

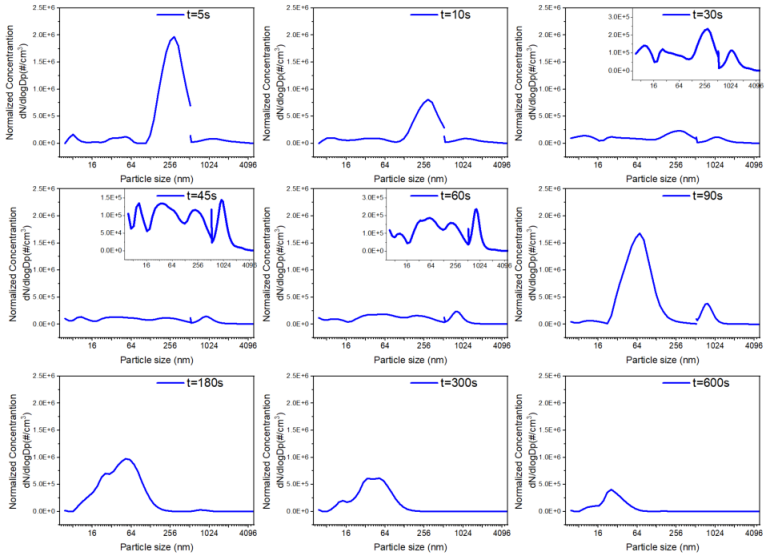

(b)

Figure 78. Particle size distribution measured by EEPS and APS at different time (t = 5s to t = 600s) (a) (a) Sony NMC cell; (b) LG NMC cell; (c) Samsung NMC cell; (d) Panasonic NCA cell; (e) A123 LFP cell; (f) JGNE LFP cell.

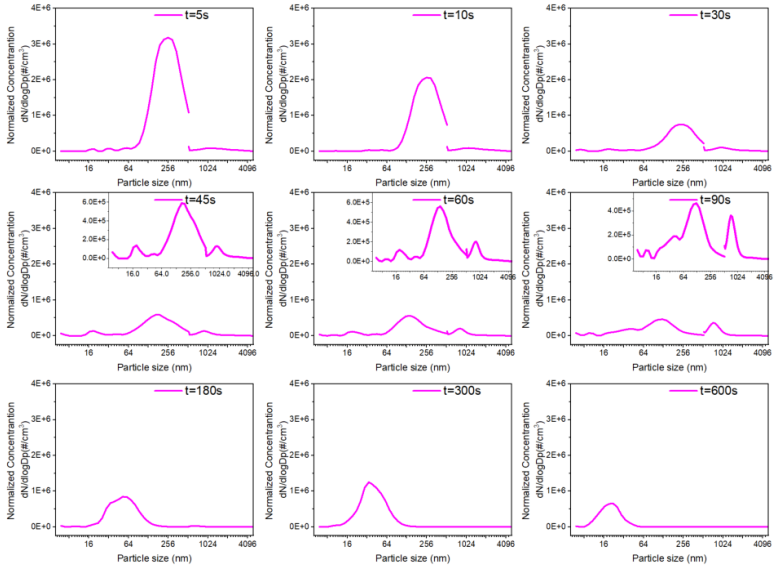

(c)

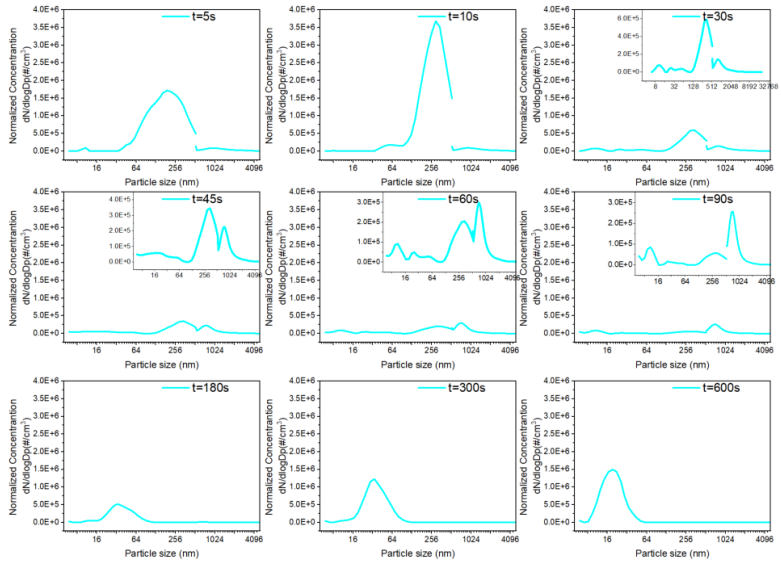

(d)

Figure 78 continued

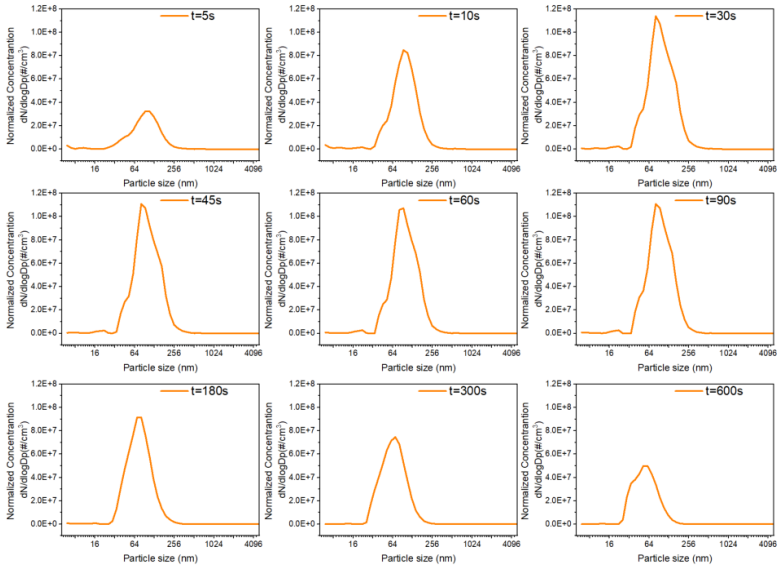

(e)

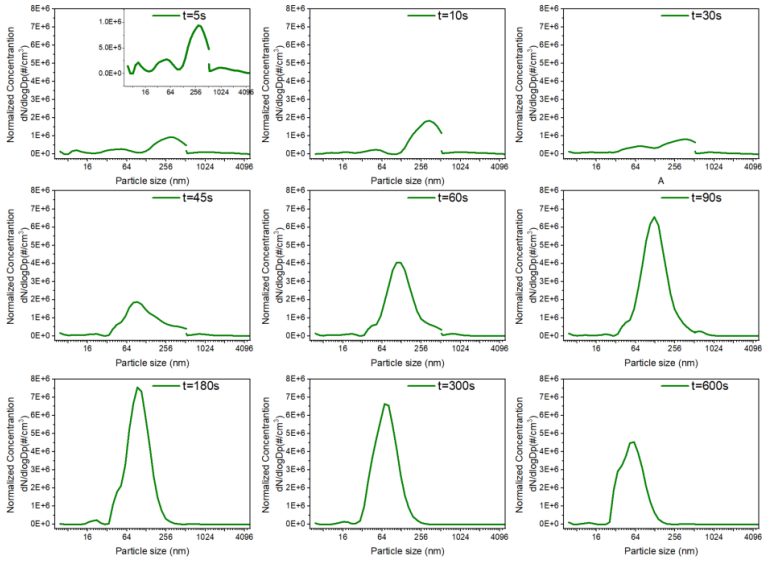

(f)

Figure 78 continued

distribution with multiple peaks, indicating the release of particles of different sizes, with significant peaks around 256 nm and 2 μm, possibly due to initial rupture or breakdown of materials. From t = 10 s to t = 90 s, the peak around 256 nm and 2 μm begins to weaken, with a significant peak appearing near 64 nm and 1 μm and gradually strengthening, especially the peak at 1 μm becomes dominant, which may be due to smaller particles agglomerating into larger ones or changes in reaction kinetics. After t = 180 s, the larger particles have disappeared, leaving only a stable peak around 64 nm. This suggests that there may not be enough small particles remaining to continue forming larger agglomerates. From t = 300 s to t = 600 s, the peaks become less pronounced, indicating reduced particle production or the near end of the thermal runaway event.

Figure 78(b) and (c) show that LG and Samsung NMC cells exhibited similar trends in particle distribution over time. At t = 5 s, both LG and Samsung NMC cells exhibit a significant peak at around 256 nm, differing from the dual peaks of the Sony NMC, suggesting an initial surge of particles at this size. From t = 10 s to 90 s, the peaks shift and change in intensity, with both exhibiting phenomena of three peaks at approximately 16 nm, 256 nm, and 1 μm, respectively, indicating varying dominance of different particle size ranges. After t = 90 s, both LG and Samsung NMC cells displayed two peaks; for LG, the peaks are around 64 nm of small particles and around 1 μm of large particles, while for Samsung, the peaks were approximately 120 nm and 1 μm. Subsequently, the peak of large particles in both LG and Samsung NMC disappears, and the concentration of small particles declines.

Figure 78(d) illustrates that the Panasonic NCA cell displayed some characteristics distinct from the LG and Samsung NMC batteries. Although at t = 5 s, LG, Samsung and Panasonic all have obvious peaks near 256 nm, by t = 10 s, the peak intensity for LG and Samsung decreased, whereas for Panasonic, it increases instead. From t = 30 s, the peak behavior of Panasonic begins to resemble that of LG and Samsung, starting to shift and change intensity, with multiple peaks appearing. In the final periods, the peak remains within the range of smaller particles and tends towards stability.

Figure 78 (e) and (f) indicate that the particle size distribution of LFP cells at different specific times is distinctly different from the previous NMC and NCA cells. Throughout the process, except for JGNE which had several small peaks at t = 5 s, at all other times, both A123 and JGNE exhibited only one peak, with a peak width of approximately ranging from 32 nm to 100 nm.

3.2.3 *Particle size distribution contour*

Figure 79 displays the contour plots of particle size distribution over time, captured by APS (top) and EEPS (bottom) during the thermal runaway-aerosol tests.

From the analysis of the Sony NMC cell in Figure 78(a), and corroborated by the contour plot in Figure 79(a), we observed that both large and small particles are significantly concentrated at the start of the test. Over time, small particles rapidly disperse, allowing large particles to dominate briefly before they too quickly dissipate. Subsequently, the peak shifts back to smaller particles, with the concentration of small particles remaining stable and then gradually decreasing over time. It is worth noting that the white areas on the contour plots indicate oversaturation.

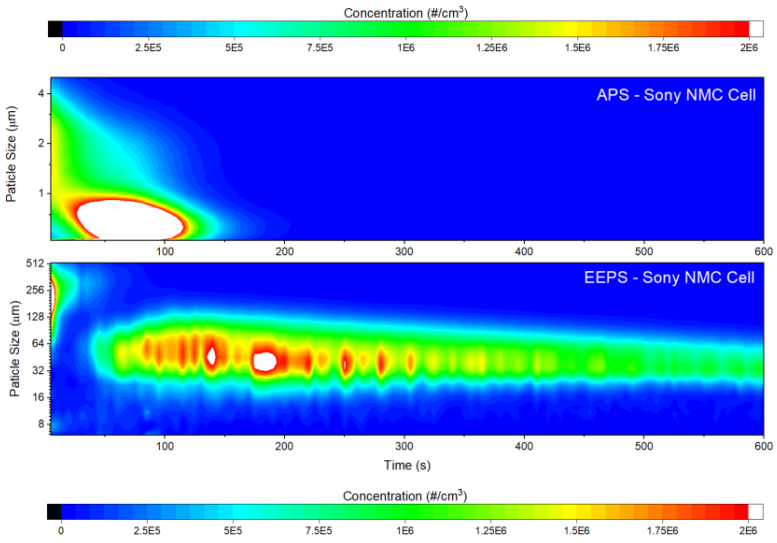

(a)

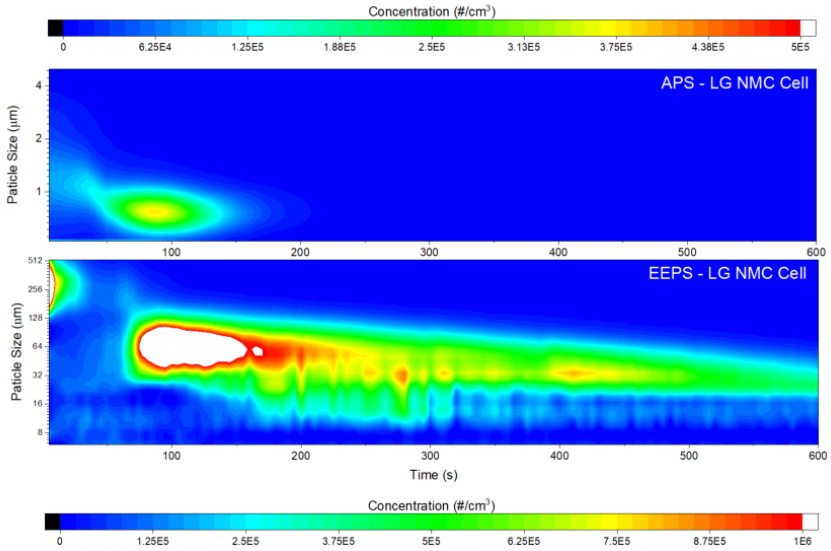

(b)

Figure 79. Contour plots of particle size distribution over time, measure by APS (top) and EEPS (bottom) (a) Sony NMC cell; (b) LG NMC cell; (c) Samsung NMC cell; (d) Panasonic NCA cell; (e) A123 LFP cell; (f) JGNE LFP cell.

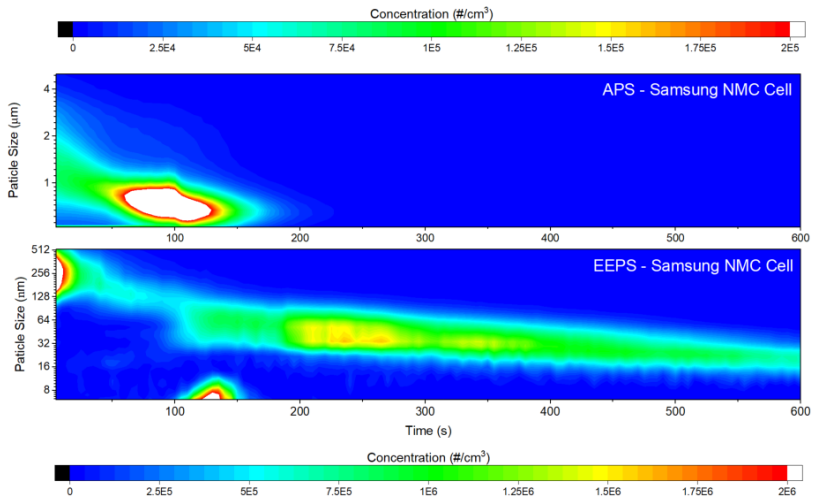

(c)

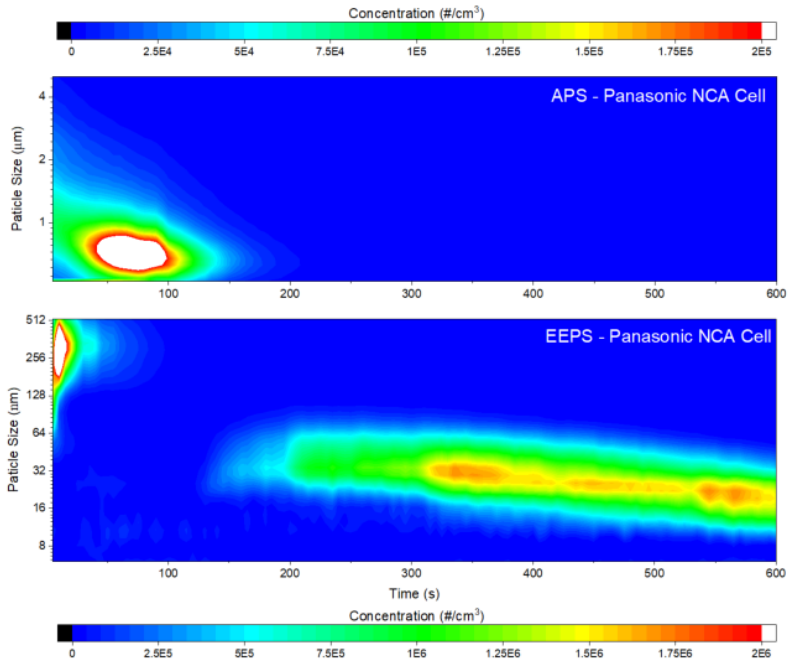

(d)

Figure 79 continued

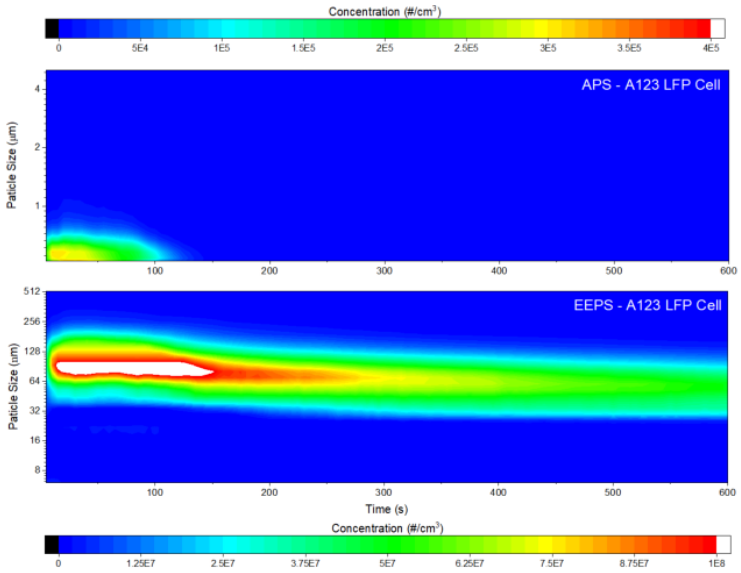

(e)

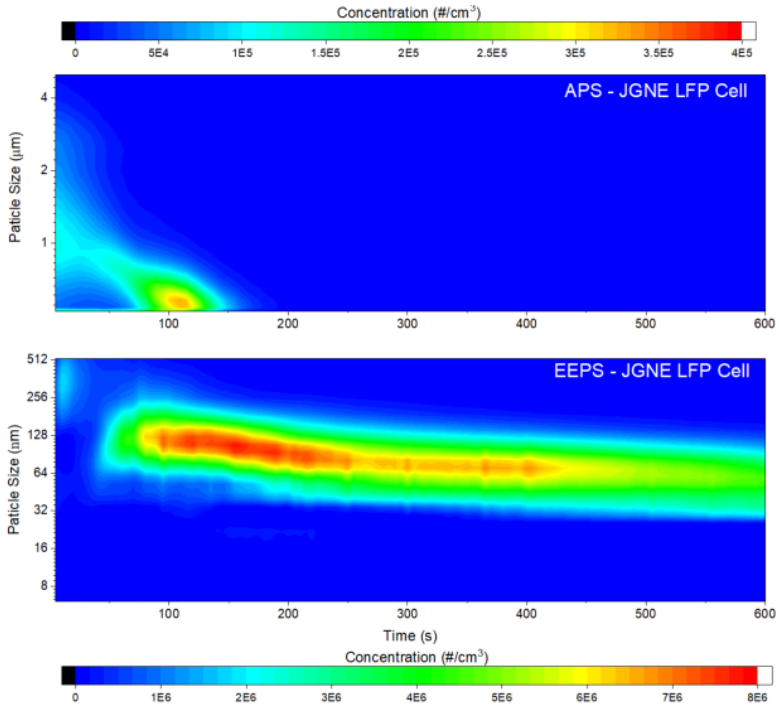

(f)

Figure 79 continued

The particle size distribution trends of NMC and NCA cells are very similar, as shown in Figure 79(a), (b), (c) and (d). At the beginning, the EEPS contour shows the distribution of smaller particles, which then gradually decreases, possibly due to particle agglomeration. This enhances the distribution of larger particles. All four cells exhibit a transition from a distribution dominated by small particles to large particles and then back to small particles, eventually stabilizing at a distribution dominated by smaller particles. The only difference is that the normalized concentration of large particles of Sony NMC cell is significantly higher than that of the other three cells. Unlike NMC and NCA cell, Figure 79(e) and (f) show that for LFP cells, smaller particles around 128 nm dominate the distribution consistently after thermal runaway.

3.2.4 *Metal emissions during thermal runaway*

Thermal runaway in Li-ion batteries presents not only a significant risk of fire and explosion but also the less obvious but equally critical hazard of metal emissions. As batteries are exposed to extreme conditions that lead to thermal runaway, the integrity of the materials inside can be compromised, leading to the release of potentially toxic metal particles into the environment. Understanding the hazards associated with metal emissions during thermal runaway events is thus a crucial aspect of comprehensive battery safety studies.

In this study, we analyzed the materials ejected from a Sony NMC cell during thermal runaway by employing Scanning Electron Microscopy (SEM) and Energy Dispersive Spectroscopy (EDS). The SEM/EDS analysis provides a visual and elemental mapping of the post-event residues, as shown in Figure 80. The micrographs show the

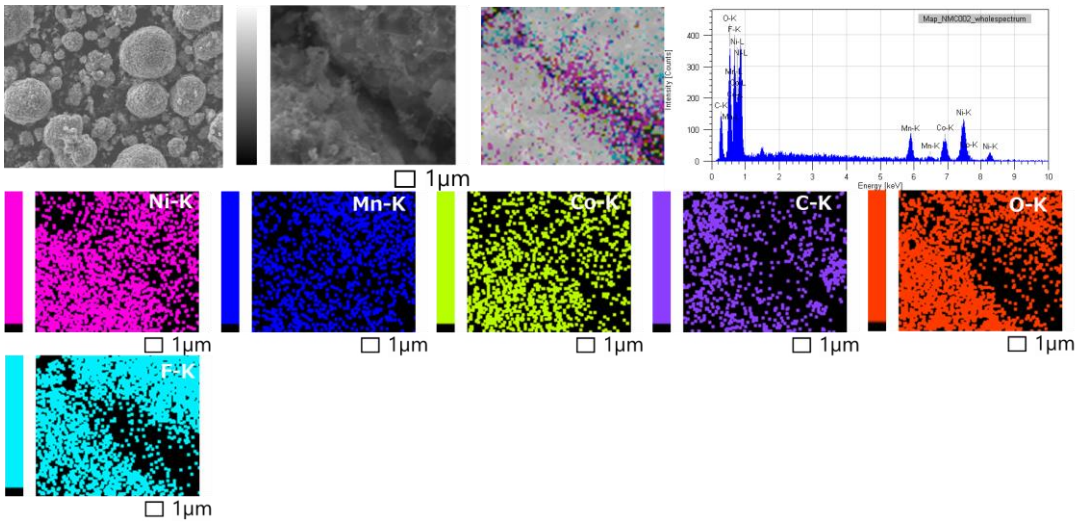

Figure 80. SEM/EDS analysis of material from Sony NMC cell thermal runaway event.

cathode material exhibits signs of melting and agglomeration, which are indicative of high temperature exposure consistent with thermal runaway conditions. The EDS spectrum analysis supplements the SEM image by offering quantitative data on the elemental composition. The multicolor mapping illustrates a spatial distribution of key elements such as Nickel (Ni), Manganese (Mn), Cobalt (Co), Carbon (C), and Oxygen (O), all of which are crucial to the composition of lithium-ion batteries cathode.

After thermal runaway, aerosolized metal particles can cause acute and chronic health problems due to their tiny size and potential toxicity. Furthermore, the long-term environmental impact of these particles is a concern, with implications for soil and water contamination. The findings highlight the need for enhanced safety protocols and battery designs, as well as further research into strategies to reduce metal emissions during such critical events.

4. Conclusion

This work presents a comprehensive analysis of aerosol emissions during Li-ion battery thermal runaway. highlighting critical insights into the peak concentration, particle size distribution, and time evolution of aerosol emission. By utilizing advanced aerosol measurement techniques, specifically the Engine Exhaust Particle Sizer (EEPS) and Aerodynamic Particle Sizer (APS), we have successfully captured the complex dynamics of aerosol generation and quantified emissions across a range of particle sizes from 5.6 nm to 20 μm. The experiments were conducted using a well-controlled rapid heating strategy in an accelerating rate calorimeter (ARC), obtaining new data on the distribution and time

evolution of aerosol emissions from various lithium-ion batteries. This significantly contributes to our understanding of hazards associated with battery failures.

Our findings reveal considerable variations in aerosol emission patterns among different battery chemistries and manufacturers, highlighting the complexity of the thermal runaway process and subsequent aerosol emission. In this study, a rapid heating strategy was employed to observe thermal runaway events using ARC, revealing changes in the temperature and voltage evolution of different battery cells. Experiments on 18650 cells from various manufacturers highlight the role of cell capacity and chemistry in determining the sequence of thermal runaway. LG NMC cells, with higher capacity, experienced thermal runaway first, followed by Samsung, Panasonic, and Sony cells, and finally the more stable LFP batteries. This sequence is reflected in the mass loss measurements, indicating a correlation between thermal runaway and aerosol emissions.

Activation energy calculations based on Arrhenius law provide insight into the thermal stability of different battery chemistries. Although higher activation energies theoretically suggest better thermal stability, the actual thermal performance and safety of batteries are influenced by multiple factors, including material properties, design, and operating conditions. This is evidenced by the lower activation energy of LFP cells, which exhibit excellent thermal stability and safety due to their unique chemical and structural advantages.

Technical challenges encountered in aerosol sampling due to adiabatic conditions within the ARC during thermal runaway testing were addressed through a delayed sampling strategy. While this introduces a sampling delay, it allows for consistent and

comparative analysis across different cell types. The use of normalized concentrations for particle size comparisons provides a more accurate representation of aerosol emissions, revealing distinct emission patterns between the cells tested. Detailed particle size distribution and time evolution analysis revealed differing aerosol emission profiles, with NMC and NCA cells showing similar trends, while LFP cells displayed a distinct pattern. This emphasizes the importance of understanding aerosol emissions at different stages of thermal runaway for both safety and environmental reasons.

This study also raises the challenge of hazards from metal emissions during thermal runaway. The degradation of internal battery materials can lead to the release of toxic metals, presenting significant environmental and health risks. These metal emissions, characterized through SEM/EDS analysis, add another potential danger of battery failure and highlights the need for further research to mitigate these risks.

Overall, this study enhances our understanding of aerosol emissions during thermal runaway in lithium-ion batteries, offering valuable insights for developing safer battery technologies and mitigating health and environmental impacts. New data on aerosol distribution and evolution contribute to the growing knowledge on battery safety and highlight the importance of addressing aerosol emissions in the context of energy storage systems. Future research should aim to further elucidate the mechanisms of aerosol formation and explore strategies to minimize the risk of thermal runaway in lithium-ion batteries.

CHAPTER VII

EXPERIMENTAL INVESTIGATION ON THERMAL RUNAWAY SUSPENSION WITH BATTERY HEALTH RETENTION

A version of this chapter was originally published by Liwen Zhang, Lu Liu, Shiyou Yang, Zhiqiang Xie, Feng-Yuan Zhang, Peng Zhao:

L. Zhang, L. Liu, S. Yang, Z. Xie, F. Zhang, P. Zhao, "Experimental investigation on thermal runaway suspension with battery health retention." *Applied Thermal Engineering* 225 (2023): 120239.

CRediT authorship contribution statement

Liwen Zhang: Investigation, Formal Analysis and Writing; Lu Liu: Validation and Editing; Shiyou Yang: Conceptualization and Writing - Review & Editing; Zhiqiang Xie: Conceptualization and Writing - Review & Editing; Feng-Yuan Zhang: Conceptualization and Writing - Review & Editing; Peng Zhao: Conceptualization, Methodology, Investigation and Writing - Review & Editing

Abstract

With growing applications of Li-ion batteries in ground transportation and energy storage, thermal runaway of Li-ion batteries has become a major concern for energy and public safety. Existing studies on thermal runaway mitigation methods are largely passive, in that most of them focus on propagation mitigation and fire extinguish after thermal runaway has been triggered. In this work, we presented experimental results on thermal runaway suspension with battery health retention, for the first time. By analyzing the temperature and voltage evolution of commercial 18650 cells with Lithium iron phosphate chemistry during step-heating thermal runaway test in an accelerating rate calorimeter, it is found that the voltage signal has a sudden drop corresponding to a similar temperature of 135 ℃, before the occurrence of thermal runaway. Thermal runaway suspension experiments are

then conducted by activating cooling when either the voltage drop or the target temperature signal is reached. It is observed that thermal runaway suspension from the target voltage drop signal fails to prevent the battery from further damage, even with fast liquid N_2 cooling. For thermal runaway suspension at the temperature signal 130 ℃ batteries are successfully saved regardless of fast cooling with liquid N_2, or slow cooling using N_2 gas. Further electrical impedance spectrum testing shows that the batteries survived from thermal runaway suspension have increased bulk resistance while polarization resistance remains unchanged. The cycling performance of the saved batteries has demonstrated identical voltage but reduced capacity by around 20 %. This research can provide useful guidance on thermal runaway prevention and health retention of Li-ion batteries.

1. Introduction

With the growing interest in Lithium-ion batteries (LIBs) applications in vehicle electrification and energy storage technologies, thermal runaway of LIBs has attracted extensive research efforts [283–285]. In general, undesired chemical reactions among battery components can be triggered under abusing conditions, which are largely exothermic and meanwhile can release large amount of flammable materials [173,286–288]. Abuse conditions leading to thermal runaway include over-heating, over-charging, collision, penetration, short circuit, etc. It has also been shown that LIB thermal runaway depends on battery materials [175,289,290], state of charge [291–293], state of health [294–296], and the effectiveness of cooling systems [182,297,298].

A large volume of literature has been dedicated to experimental, modeling and theoretical analysis of LIB thermal runaway [299–303]. From the experimental aspects,

cell-level oven and calorimetry tests have provided global thermal targets to constrain the thermal runaway behavior [304–306]. Non-intrusive in operando diagnostics of cell-level thermal runaway also becomes feasible with the help of synchrotron-based X-ray diffraction [307,308]. Meanwhile, sub-cell level heat and gas release analysis further provides more detailed information on the thermal runaway chemical kinetics. From modeling aspects, a wide range of thermal runaway kinetic mechanisms have been developed, including the one-step [145], four-step [75], six-step [309], and more detailed reaction mechanisms [125]. For theoretical analysis, thermal runaway has been modeled and analyzed based on the classical thermal-explosion criterion [310], linearized reaction rate [311], effective reactant consumption [312], minimum ignition energy [144], mild combustion [145] and reaction front initiation and propagation [313,314]. These studies have all shed light on the fundamental nature of thermal runaway from different aspects.

From the practical perspective, nothing will be more beneficial than complete prevention of thermal runaway. A significant amount of innovative work is dedicated to the improvement and design of battery material and structure. Hou et al.[153] have introduced anti-fire electrolyte-based LIBs, which however cannot completely avoid thermal runaway. Another intriguing design is the solid-state LIBs that utilize thin metal oxide film as Li conductors, where thermal runaway can still occur potentially due to the cross-talk reactions between Li in the anode and the oxygen generated from metal oxide decomposition [315]. Clearly, there has not been a universal strategy that can completely avoid thermal runaway. On the other hand, post-intervention of fire hazards from thermal runaways have been investigated through cooling designs. Xu et al. [78] have

computationally shown that heat release from the battery pack can be largely removed with an appropriate design of a mini-channel cooling strategy. As reviewed in [316], various advanced battery thermal management systems have been designed to reduce the risk of thermal runaway, utilizing various combination of phase change material, metal foam, fins, thermoelectric cooling, etc. [317–319]. Extreme cooling methods such as liquid N_2 cooling have been investigated for cryogenic storage and transportation of Li-ion batteries [320] and battery thermal runaway suppression and fire extinction [129,321].

So far, almost all of the thermal runaway mitigation methods are passive, in that they focus on the prevention of thermal runaway propagation and fire extinguishment after thermal runaway has been triggered. Given the fact that Li can react with H_2O, CO_2, O_2, and those venting gases of battery thermal runaway frequently include highly explosive and flammable gases including H_2 and C_2H_4, existing mitigation methods after thermal runaway occurrence is still risky and potentially ineffective. Furthermore, in such scenarios the health of the battery is always not protected, adding to substantially cost for replacement. This triggers the current work based on intervention of thermal runaway and meanwhile retain the functionality of the battery.

The specific objectives of the current work are three-fold. First of all, we aim to investigate the thermoelectrical signal during thermal runaway and identify a reliable warning sign to stop thermal runaway before the main thermal runaway event, and meanwhile retain the battery's major functionality. Second, we would like to test the effectiveness of different cooling strategies to stop thermal runaway, including liquid N_2 to represent super-fast cooling, and room temperature gaseous N_2 as slow cooling. Last, we

would like to investigate if the battery that survives from a suspended thermal runaway experiment is still functional, and to what extent its cycling performance differs from those of regular cells. In this study, we shall adopt two different types of commercial LFP 18650 cells, which in general are considered to be much safer compared to other cathode materials such as LCO and NMC. We will utilize a well-calibrated EV+ accelerating-rate calorimetry (ARC) testing platform to perform thermal runaway triggering and suspension testing following the heat-wait-seek strategy. Re-evaluation of cell performance is conducted by cycling over a wide range of C rates and through electrochemical impedance spectrum (EIS) measurement.

2. Experimental Methodology

2.1 Battery type and initialization

In this study, two types of commercial 18650 Li-ion batteries with LFP cathode and graphite anode manufactured from A123 and JGNE are used. Table 26 lists the specifications of the battery sample involved in this work.

These batteries were cycled three times using the constant current constant voltage (CCCV) method at a low C-rate of 0.1 C and 20 ℃. By the 4^{th} charge, all the cells achieve similar initial conditions at 100 % SOC. Figure 81 shows the 3^{rd} discharge / 4^{th} charge profiles obtained from the cycling test at 0.1C rates of discharge / charge. All seven batteries exhibit similar voltage evolutions and capacities. Measurements of mass and voltage before the ARC test also exhibit small deviations among the batteries, as listed in Table 27.

Table 26. The specifications of the battery sample involved in this study.

Property (unit)	A123	JGNE
Model number	APR18650M1B	HTPFR18650
Height (mm)	65	65
Diameter (mm)	18	18
Rated capacity (Ah)	1.2	1.1
Nominal voltage (V)	3.3	3.2
Charging voltage (V)	3.6	3.65
Discharging cut-off voltage (V)	2.0	2.5
Max. charge/discharge current (A)	4/30	5.5/33
Suggested operating temperature (^{o}C)	0~55 (Charge)	0~55 (Charge)
	-30~55 (Discharge)	-20~60 (Discharge)

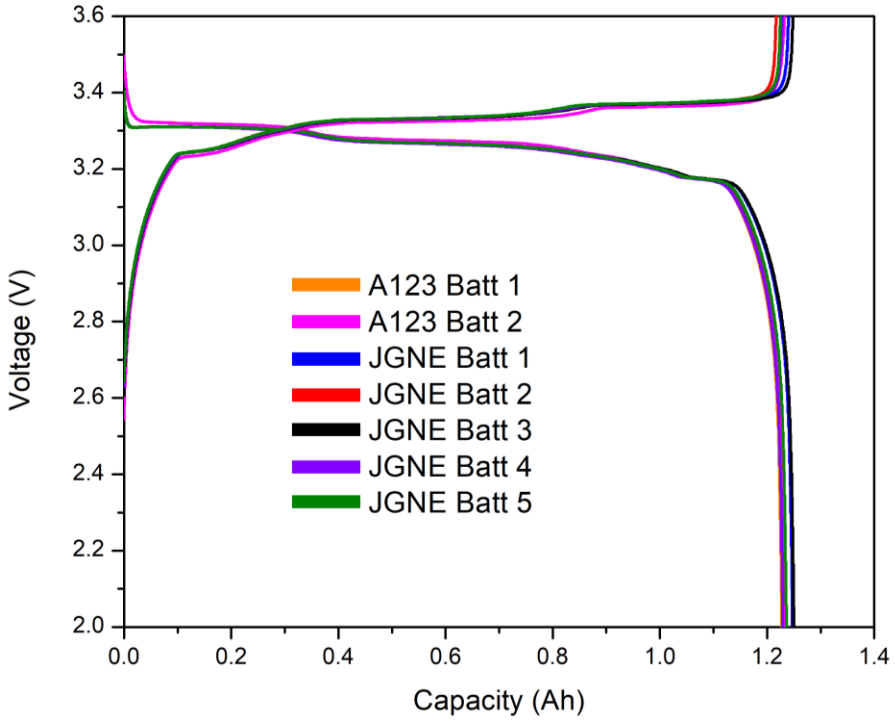

Figure 81. Voltage evolution during 0.1 C discharge and charge of seven 18650 LFP cells.

Table 27. Mass, voltage, and capacity for the 18650 LFP batteries.

Battery No.	**Mass (g)**	**Voltage (V)**	**Capacity (Ah)**
A123 Batt 1	41.484	3.340	1.233
A123 Batt 2	41.512	3.433	1.233
JGNE Batt 1	39.240	3.335	1.241
JGNE Batt 2	39.396	3.357	1.218
JGNE Batt 3	39.454	3.355	1.249
JGNE Batt 4	39.206	3.364	1.230
JGNE Batt 5	39.545	3.359	1.226

2.2 EIS measurement

Electrochemical Impedance Spectroscopy (EIS) is a powerful diagnostic method for quickly and non-destructively assessing battery health and has been widely used in LIB research. In this work, EIS tests are performed with the instrument PARSTAT 4000A (Princeton Applied Research) which applies a small AC current signal perturbation through the cell. The measurements are carried out at the fully charged state with 10 mV amplitude and are obtained by scanning 30 points logarithmically spaced between 3 kHz to 0.1 Hz using two electrode terminal connections with the working/sense electrode and reference/counter electrode. EIS results are expressed as the Nyquist plot as shown in Figure 82, which consists of a semicircle in high and medium frequency ranges and a straight line at a 45 angle to the real axis in the low-frequency range. Based on the widely adopted Randles battery model, the intersection point on the horizontal axis in the high-frequency range represents the ohmic resistance, the diameter of the semicircle represents the charge transfer resistance, and the straight line represents the diffusion process [195]. Compared with the JGNE batteries, the bulk ohmic resistance of A123 battery is only about 10 % higher while its polarization resistance from charge transfer is much smaller.

2.3 Thermal runaway testing and suspension in ARC

The thermal runaway tests are performed using the EV+ accelerating rate calorimetry (ARC), manufactured by Thermal Hazard Technology, as shown in Figure 83(a). The standard heat-wait-seek (HWS) method is adopted for all measurements. At first, the test battery is heated up from ambient temperature until the surface temperature reaches 50 ℃, then the wait mode is activated and will last for 45 min, to ensure thermal

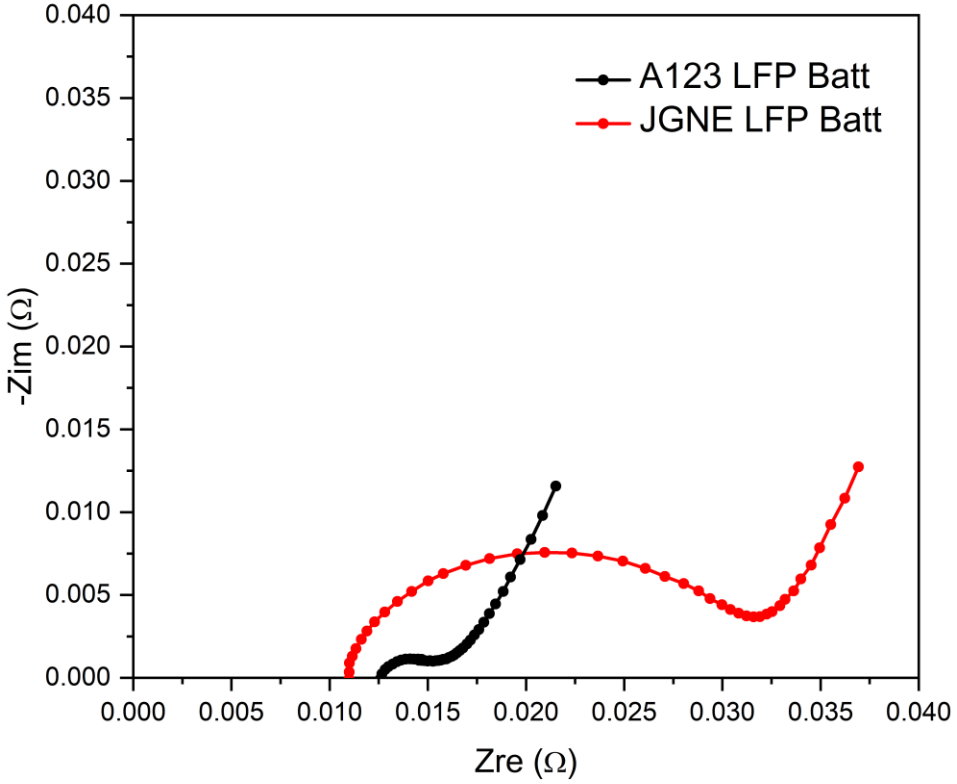

Figure 82. Nyquist plot of the 18650 LFP cells used after initialization.

equilibrium between the ARC and the battery. Then the system enters “seek” mode to search for the temperature rise rate of exothermic reactions and compare it with the temperature rate sensitivity of 0.02 ℃/min. If the measured temperature rise rate is above the threshold, the system will switch to exotherm mode. This mode allows a nearly adiabatic environment with no temperature difference between the heaters and the sample, hence no heat exchange. As a result, HWS allows tracking of the cell temperature evolution in the worst-case adiabatic scenario. On the other hand, if the detected temperature rise rate is below the threshold, the system will perform the next HWS step. In our test, each heating step increases the battery temperature by 5 ℃. In either heating or exotherm mode, when the temperature exceeds the given maximum of 300 ℃, the heaters shut down completely and the system starts cooling. The typical temperature evolution and key responses of an LFP 18650 battery during thermal runaway following the HWS strategy are shown in Figure 83(b). More details about the experimental set-up and methodology are available in our recent work [143].

In the current experiment, two cooling strategies are involved. One is to turn on the fan and valve to purge pressurized N_2 gas under room temperature into the chamber. This cooling strategy is rather slow, which can take a couple of hours for the system to cool down to room temperature and hence can be used to represent the slow cooling limit. Another way is to directly introduce liquid N_2 (-196 ℃) via a separate system such that very fast cooling can be achieved. From the comparison of these two cooling strategies in the fast and slow limits, the effectiveness of cooling in thermal runaway suspension can be clearly identified.

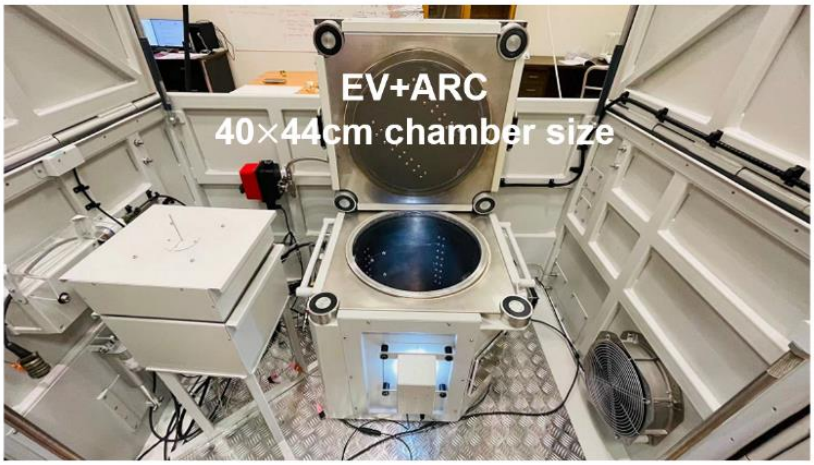

(a)

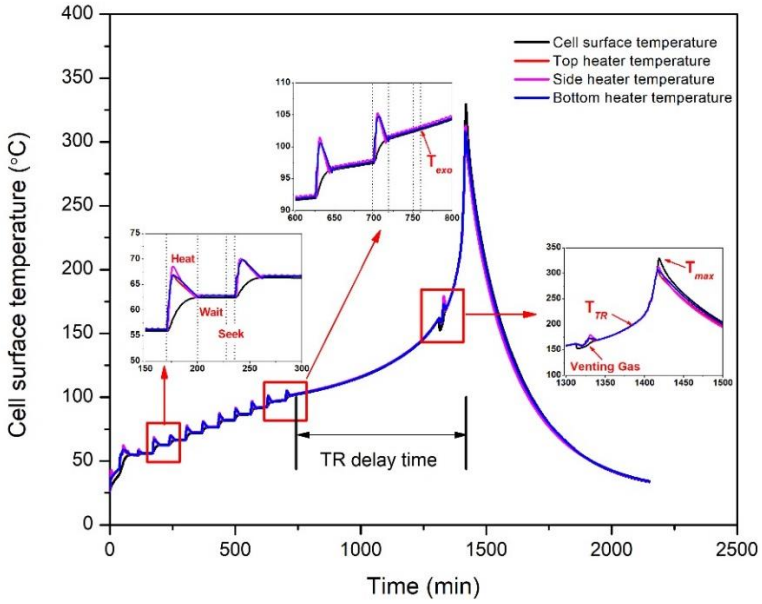

(b)

Figure 83. (a) experimental facility of the EV+ ARC system; (b) typical temperature evolution during ARC experiments following HWS step heating (LFP, 18650 cylindrical cells).

3. Results and discussion

3.1 Thermal runaway suspension

Figure 84 shows the evolution of temperature and voltage of three LFP 18650 cells during thermal runaway testing, following the standard heat-wait-seek strategy. It is seen that for all three cells, exothermicity occurs at around 100 ℃. Starting from the onset of exotherm, the main thermal runaway event does not occur until around 3000 min or later, eventually leading to a maximum temperature of around 330 ℃. The deviations in the temperature evolution of two similar cells A123 Batt 1 and 2 further confirm the recent experimentally observed cell variability during thermal runaway [143]. During this period, the ARC remains in thermal equilibrium with the cell, such that thermal runaway is contributed solely by the heat release from the thermal runaway chemical reactions. In addition, the voltage signal indicates that a sudden voltage drop occurs before thermal runaway. Such voltage drop occurs in less than half a minute, followed by a plateau, and the magnitude of the drop can be as large as about 1 V. Furthermore, one of the most important observations is that the voltage drop occurs at a similar temperature of 135 ℃ for all the cells. This is most likely due to the failure of the separator material (e.g., PE decomposition) [322] and the triggering of internal short circuit.

The characteristics of the temperature and voltage signal then provide the rationale to perform the thermal runaway suspension experiments. It becomes possible to select a suitable voltage or temperature-based criterion as the last warning sign to stop thermal runaway and meanwhile to retain the functionality of the battery. Table 28 lists the suspension signal and cooling strategy of the thermal runaway experiments for 4 batteries

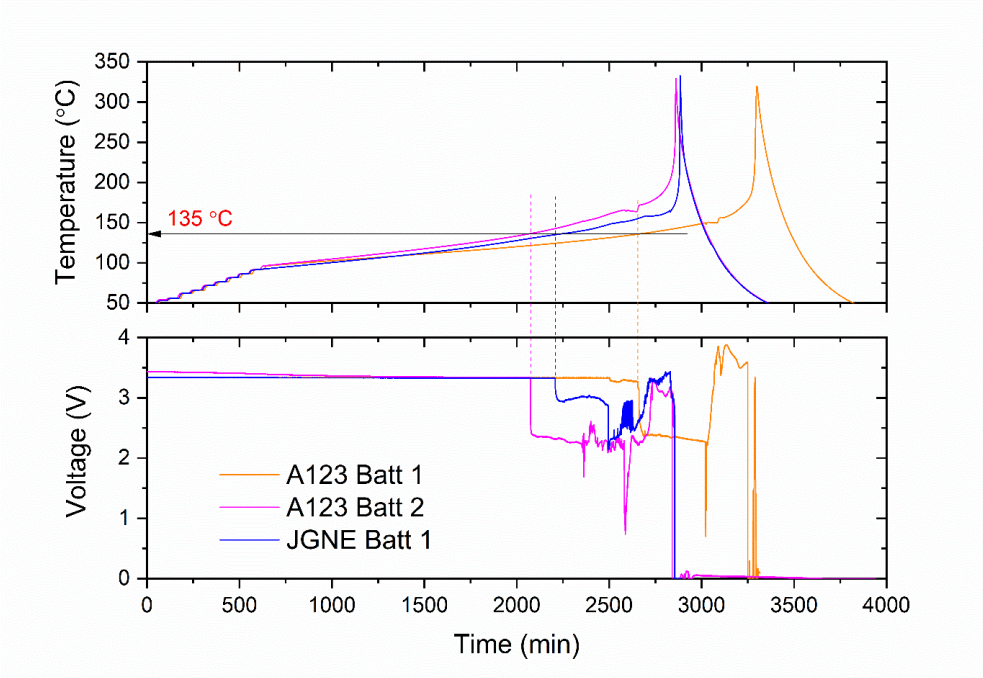

Figure 84. Temperature and voltage evolution during ARC experiments, showing that a sudden drop of voltage occurs at 135 °C.

Table 28. Thermal runaway suspension signal and cooling strategy.

LFP Battery (18650)	TR suspension signal	Cooling strategy	Final battery functionality
JGNE Batt 2	Voltage drops rate > 0.02 V/min	N_2 gas cooling	No
JGNE Batt 3	Voltage drops rate > 0.02 V/min	Liquid N_2 cooling	No
JGNE Batt 4	Temperature = 130 ℃	Liquid N_2 cooling	Yes
JGNE Batt 5	Temperature = 130 ℃	N_2 gas cooling	Yes

with similar initial conditions. For two of them, JGNE Batt 2 and 3, a voltage drop rate beyond 0.02 V/min is defined as the threshold to suspend the experiment, and for the other two, a temperature-based criterion of 130 ℃ right before the voltage drop is selected as the suspension signal. Once the thermal runaway suspension criterion is satisfied, the system fan will be turned on, and direct convective cooling of either N_2 gas under room temperature or liquid N_2 is introduced to the chamber. For JGNE Batt 2 and 5, N_2 gas cooling is adopted while the other two utilize liquid N_2 cooling.

The evolution of temperature and voltage of these 4 sets of thermal runaway suspension experiments are shown in Figure 85. For JGNE Batt 2, N_2 gas cooling is applied when the voltage drop criterion is satisfied. A zoom-in plot of the voltage signal shows that as cooling starts, the voltage also reaches to a plateau. It takes about 6 hours to cool down the cell temperature to 30 ℃ during which period the voltage keeps dropping. Eventually, JGNE Batt 2 drops to 2 V and is not able to be cycled anymore. For JGNE Batt 3, liquid N_2 cooling is introduced immediately when voltage drop meets the criterion. Although liquid N_2 cooling is fast and effective, which brings down the battery temperature to room temperature within a few minutes, the voltage of Batt 3 also decreases quickly and drops by more than 1 V. As a result, JGNE Batt 3 cannot be charged anymore. For JGNE Batt 4, liquid N_2 cooling is applied as soon as the battery temperature reaches to 130 ℃. Negligible voltage drop is observed for this cell, and it is still functional. For the last cell, JGNE Batt 5, N_2 gas cooling is applied at cell temperature 130 ℃ and it takes about 6 hours to cool down the cell to 30 ℃. Negligible voltage drop is observed during this slow cooling process, and the battery is found to be still functional.

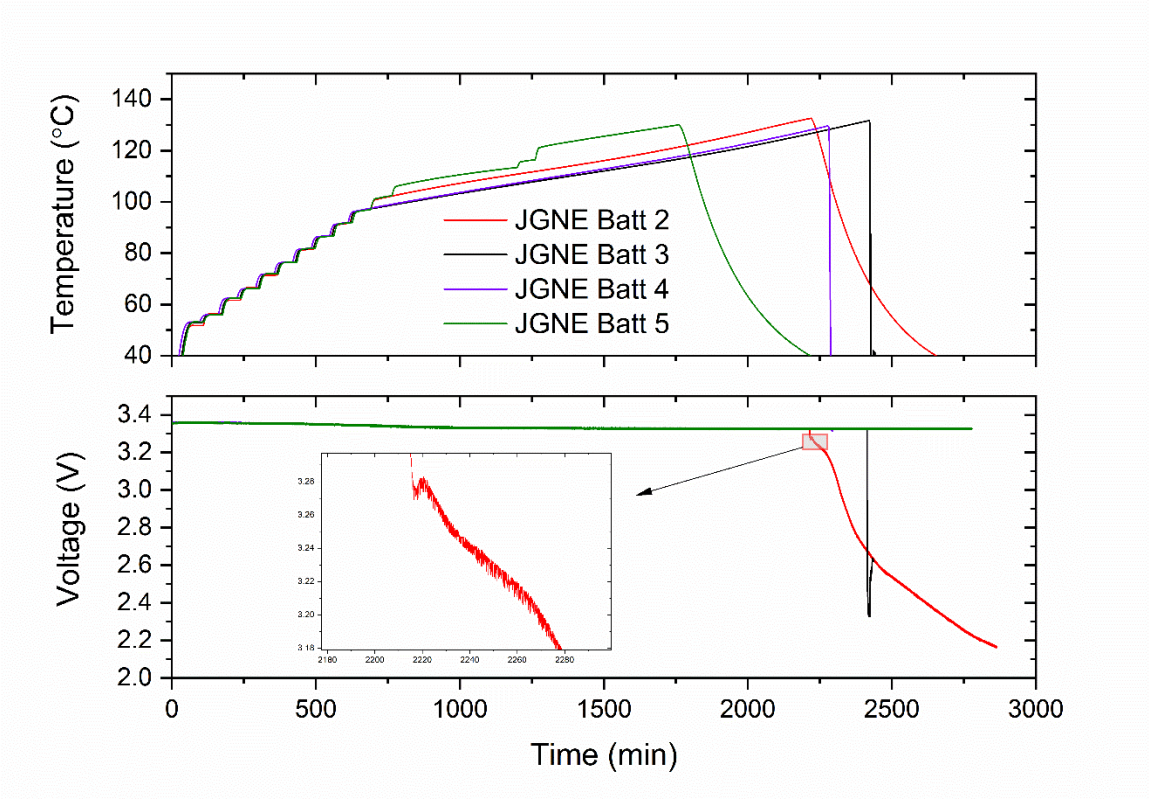

Figure 85. Temperature and voltage evolution during thermal runaway suspension experiments for JGNE Batt 2-5.

From the test results of JGNE Batt 2 and JGNE Batt 3, it can be seen that the voltage drop might not be a reliable signal as a final warning to protect the battery from thermal runaway. It is unclear how much the voltage will drop. At the onset of thermal runaway prevention, the magnitude of the voltage drop is around 0.1 V for JGNE Batt 2 and 1 V for JGNE Batt 3. In case of a large voltage drop, e.g., JGNE Batt 3, even liquid N_2 cooling is not able to save the battery from internal damage. By comparison, no voltage drops are observed for JGNE Batt 4 and JGNE Batt 5. No matter the cooling rate is fast or slow, both batteries survive from the thermal runaway suspension test. The above results indicate that the temperature criterion of 130 ℃ can be used as a reliable last warning signal to suspend thermal runaway.

Also, if we consider that the adiabatic combustion temperature for thermal runaway is around 330 ℃, which leads to an adiabatic temperature excess of 230 ℃ starting from the onset temperature of exothermicity at 100 ℃. At 130 ℃, the heat release rate from thermal runaway chemistry has raised the battery temperature by 30 ℃. The ratio of temperature increment to the adiabatic temperature excess therefore corresponds to approximately 13 % of battery material consumption during thermal runaway. The fact that JGNE Batt 4 and JGNE Batt 5 are still functional indicates that 13 % of battery material consumption does not affect the functionality of those batteries. However, it is expected that the electrochemical performance of the cells saved from thermal runaway suspension will not be identical to the original cells.

It is worth noting that the functionality of a cell is generally defined by characteristics such as battery capacity, internal resistance, voltage, self-discharge rate,

columbic efficiency, cycle life and safety. In the current study, we measured the battery capacity, internal resistance, voltage, cycling capability to confirm functionality. In future follow-up work, we will further consider the self-discharge and cycle life as well as re-running the thermal runaway test to evaluate the safety limit of the battery.

3.2 Re-evaluation of electrochemical performance after thermal runaway suspension

Figure 86 shows the comparison of EIS data of JGNE Batt 4 before and after the thermal runaway suspension experiment. Fittings of the EIS data based on the overall simplified equivalent circuit are also conducted to determine the values of the resistances, as shown in Table 29. The major observation is that the Nyquist plots mainly shift toward the right-hand side after the thermal runaway suspension. A larger intersection value on the horizontal axis indicates a nearly doubled internal ohmic resistance of the saved batteries. The nearly unchanged diameter of the semicircle indicates similar polarization resistance. The large internal resistance increase after ARC test is probably attributed to the following three aspects. First, the electrolyte's evaporation and decomposition occur between 100 and 130 ℃ during the ARC process, leading to newly formed inorganic layers on the electrode surface. Second, the SEI film on the battery active materials may decompose and reform to the inorganic layer on electrode surface, resulting in reduced ion conductivity in the battery active materials [323,324]. Third, the generated gases from chemical parasitic reactions during ARC may also cause swelling or deformation inside the battery and thus induce increased interfacial contact resistance [325]. The EIS measurement and analysis of the other survived cell JGNE Batt 5 show quantitatively similar results.

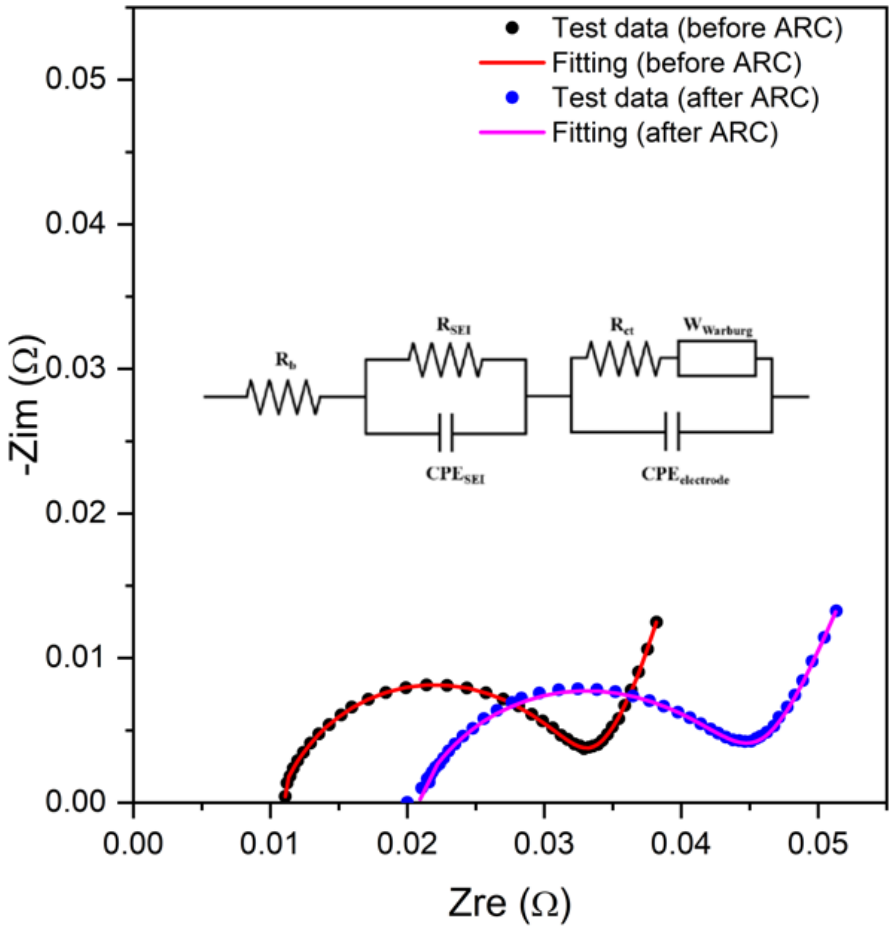

Figure 86. Nyquist plot of the JGNE Batt 4 before and after thermal runaway suspension experiment.

Table 29. Resistance comparison before and after thermal runaway suspension experiment.

JGNE LFP Battery (18650)	R_b (Ω)	R_{ct} (Ω)
Before	0.01055	0.02213
After	0.02047	0.02425

The cycling performance of JGNE Batt 4 saved from thermal runaway suspension is measured under four different C rates from 0.5 C to 5 C are shown in Figure 87 and compared with its performance before the thermal runaway test. The results show that the maximum voltage of this battery remains the same after thermal runaway suspension. The capacity of the battery however decreases by 20 %. Re-evaluation of the cycling performance of JGNE Batt 5 yields similar results.

During the thermal runaway suspension experiment, there are no signs of venting events and the mass change of the battery is negligible. However, the battery temperature does reach as high as 130 ℃, which is high enough to cause substantial vaporization of the electrolyte and to trigger reactions among battery components. The vaporization and condensation of the electrolyte is likely to change the local cell structure and increase the interfacial contact resistance among different cell components, and eventually increases the internal ohmic resistance and reduces cell capacity.

4. Conclusion

For the first time, this work reports experimental investigation on battery thermal runaway suppression with battery functionality retention. By revisiting the evolution of temperature and voltage signal during LFP 18650 battery thermal runaway triggered by step heating, we have observed a sudden voltage drop between the onsets of exothermicity and thermal runaway. Two criteria have been chosen accordingly to suspend thermal runaway and meanwhile reserve the functionality of the battery, when either voltage drop rate is beyond 0.02 V/min or the temperature reaches 130 ℃. Liquid N_2 cooling and room

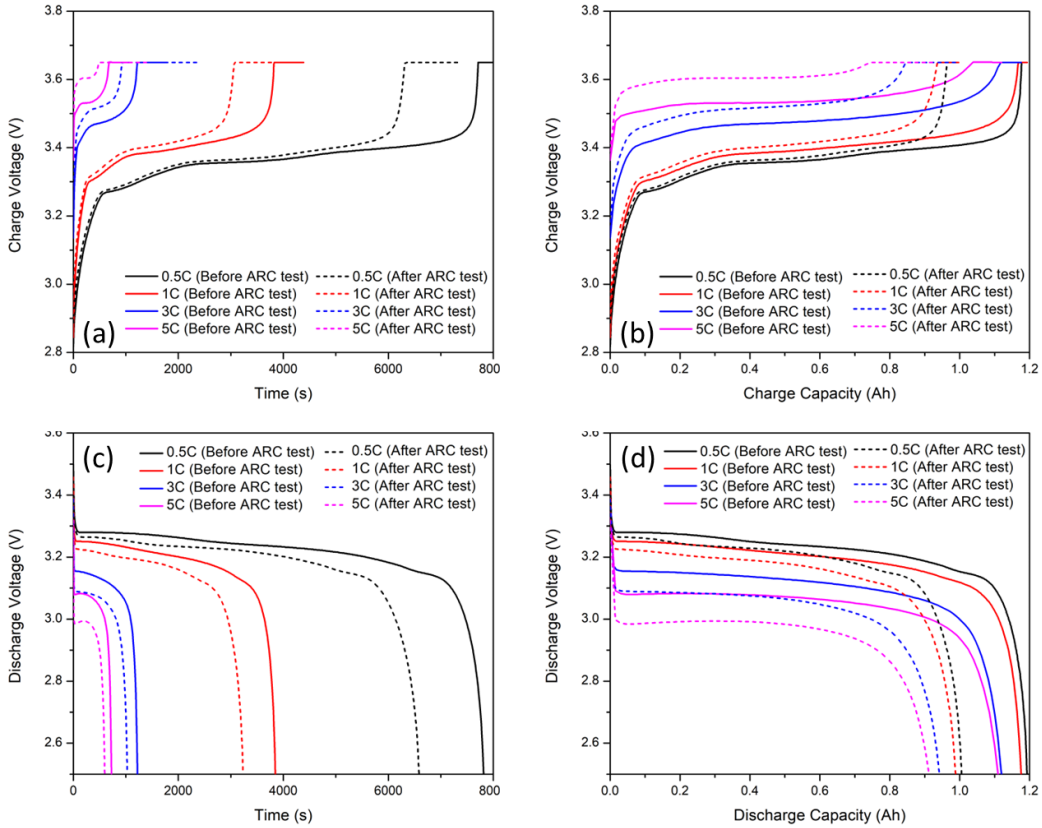

Figure 87. Cycling performance of JGNE Batt 4 before and after thermal runaway suspension experiment (a) voltage vs. time during charging; (b) voltage vs. time during discharging; (c) voltage vs. capacity during charging; (d) voltage vs. capacity during discharging.

temperature N_2 cooling, representing fast and slow cooling strategies, are applied to intervene battery thermal runaway test when either warning signal is received.

The results based on two types of LFP 18650 cells have shown that thermal runaway can be successfully prevented regardless of cooling strategy and warning signal, however, the extent of internal damage and functionality of the batteries are different. When the critical voltage drop rate of 0.02 V/min is chosen as the warning signal, it is observed that either the voltage drops so fast that even liquid N_2 cooling cannot save the battery, or the cooling rate is too slow that the voltage of the battery keeps dropping. Therefore, the voltage drop is not a reliable signal to retain the functionality of the battery. When adopting temperature of 130 ℃ as the warning signal, it is observed that the voltage level of the battery remains, and the battery is still functional regardless of cooling rate. Hence, temperature criterion is more useful to retain the functionality of the battery.

The cycling performance and impedance spectrum of the battery retained from thermal runaway are re-evaluated and compared to the condition before the thermal runaway test. Results show that the bulk ohmic resistance of the cells is nearly doubled, while there is little change in the polarization resistance of charge transfer. This is likely induced by the increased gap between different cell components in the battery and the increased interfacial contact resistance.

This research provides useful insights into fatal warning signs of battery health, thermal runaway suspension and battery functionality retention. It should be noted that the identification of a reliable temperature threshold is critical for the purpose of the current research, while the involvement of liquid N_2 cooling is found to be completely unnecessary.

The method can be easily extended to cells with other chemistry and practical configurations.

CONCLUSION AND FUTURE WORK

This dissertation comprehensively understands thermal runaway characteristics of batteries through a combination of experiments and numerical simulation, gaining insights into the complex details of Li-ion battery thermal runaway. It provides valuable information for enhancing battery safety and mitigating potential hazards. The main achievements are concluded below by summarizing the content of each chapter:

In Chapter One, this dissertation presents a detailed computational investigation into safety regime of LIBs TR, focusing on identifying critical heat source intensity and duration time that determine the boundary between thermal runaway and safe operational zones. It also evaluates key kinetic features, and the effects of heat source size and electrode material properties on TR. Through comparative analysis, it highlights that heat release from the negative electrode - electrolyte reactions directly correlate to thermal runaway. Sensitivity analysis reveals key parameters affecting delay time, emphasizing the role of positive electrode-electrolyte reaction. Additionally, it studies the heat release rate during an internal short circuit (ISC) event and combines thermal-electrochemical and thermal runaway models, validating the effectiveness of the model in linking electrochemical dynamic with thermal runaway behavior. This computational identification aims to understand the threshold conditions that lead to TR, offering valuable insights into battery design and safety protocols. Future work should aim to expand the safety regime diagram to a wider range of battery type and operational conditions, and further refine electrochemical-thermal runaway models to enhance predictive capabilities for practical applications.

In Chapter Two, the study provides significant insights into the complex dynamics of radiation-induced thermal runaway in Li-ion battery packs. We develop a theoretical model based on view factor theory to explore the effects of radiative heat transfer on thermal runaway propagation (TRP) between cylindrical Li-ion cells. It demonstrates that radiative heat transfer plays a key role in thermal runaway propagation, characterized by non-monotonic and nonlinear behaviors. These findings highlight the importance of considering radiative heat transfer in battery safety designs, especially in dense battery pack configurations. The work also emphasizes the need for more comprehensive studies to understand the interactions between radiative heat transfer and chemical kinetics in different geometric configurations of battery packs. This research provides a foundation for future investigations aimed at enhancing the safety of Li-ion battery packs, which is crucial for their widespread adoption in energy storage and electric vehicles.

In Chapter Three, this study has significantly advanced the understanding of cell-to-cell variability in Li-ion batteries, particularly focusing on the thermal runaway characteristics of 18650 LCO cells. The comprehensive approach, integrating experimental testing, statistical analysis, and kinetic modeling, has revealed substantial variations in thermal responses even among fresh cells with similar initial conditions. Key findings include the identification of significant differences in self-heating onset temperatures, thermal runaway delay times, and maximum temperatures, emphasizing the impact of manufacturing inconsistencies. Our results highlight the critical need for incorporating statistical analysis and uncertainty quantification in battery safety evaluations. This approach allows for a more rigorous and consistent assessment of safety risks, accounting

for the inherent variability in battery cells. Furthermore, the study suggests that reliance on single-cell testing may not be sufficient for safety evaluations and that a broader range of cells should be considered to accurately assess the risks associated with thermal runaway. The findings of this research have significant implications for the design, manufacturing, and safety evaluation of Li-ion batteries. They emphasize the importance of considering cell-to-cell variability in safety models and standards. Future research should focus on exploring the underlying causes of this variability and developing strategies to mitigate the associated risks. Moreover, further studies are needed to examine the variability in cells with different chemistries and degrees of degradation. In summary, this study provides valuable insights into the cell-to-cell variability of thermal runaway in Li-ion batteries, offering a foundation for more effective safety strategies and contributing to the advancement of safer battery technology.

In Chapter Four, thermal runaway behavior of commercial 18650 NMC Li-ion batteries with varying aging histories has been investigated, employing EIS and ARC. Our findings reveal significant differences in thermal runaway characteristics based on aging conditions, highlighting the role of lithium dendrites / plating in accelerating short circuits, particularly in cells subjected to low-temperature cycling. The study highlights the complexity of aging effects on Li-ion battery thermal behavior and emphasizes the necessity for customized safety strategies based on specific aging conditions. Our results provide valuable insights for advancing the safety and reliability of Li-ion batteries in real-world applications, emphasizing the importance of understanding aging mechanisms to

mitigate potential risks associated with these energy storage systems. Future work will focus on detailed analysis of the relationship between lithium plating and thermal runaway.

In Chapter Five, this dissertation explores the impact of lithium plating and dendrite formation on the thermal runaway behavior in 18650 LFP Li-ion batteries, focusing on the effects of low temperature cycling. The results indicate that LFP batteries exhibit an earlier onset of thermal runaway when subjected to low temperature cycling aging, primarily due to lithium plating and dendrite formation. This study also introduces a simplified model to understand the effect of local hot spots caused by lithium dendrite on thermal runaway, suggesting that the local hot spot can accelerate the process. This research provides critical insights into factors affecting the safety and stability of Li-ion batteries, emphasizing the dangers of aging and the role of internal hot spots in triggering thermal runaway.

In Chapter Six, this dissertation presents a comprehensive analysis of aerosol emissions during Li-ion battery thermal runaway, utilizing EEPS and APS to capture the dynamics of particle size distribution, peak diameter, and temporal evolution. Our findings reveal significant insights into the aerosol characteristics emitted from different types of Li-ion batteries under thermal runaway conditions. Future studies should aim to refine aerosol sampling techniques and extend the investigation to a broader range of battery chemistries and configurations to further advance our understanding of aerosol emissions and their implications for battery safety.

In Chapter Seven, we have successfully demonstrated a novel approach for suspending thermal runaway in Li-ion batteries, a critical issue in battery safety, without significantly compromising their health and performance. Our experimental setup,

involving monitoring of temperature and voltage signals, allowed for precise identification of the occurrence of thermal runaway. The results from our experiments are promising, indicating that it is feasible to suspend thermal runaway under controlled conditions while largely maintaining the structural integrity and capacity of the battery. This finding is significant as it opens up new possibilities for enhancing the safety of Li-ion batteries in practical applications, such as electric vehicles and large-scale energy storage systems, without severely impacting their performance or lifespan. In summary, the methods and insights derived from this research represent a substantial step forward in battery safety technology. Future research should focus on integrating these thermal runaway suspension techniques into standard battery designs and exploring their applicability in various types of Li-ion batteries. This could lead to the development of safer, more reliable energy storage solutions, crucial for the ongoing transition to sustainable energy sources.

In summary, this dissertation comprehensively addresses various aspects of Li-ion battery safety and performance. The study identifies the safety regime of Li-ion batteries, explores the role of radiative heat transfer in thermal runaway propagation, highlights the importance of considering cell variability and aging in battery safety protocols, analyze vent gas and aerosol emission among different battery chemistries and manufacturers during thermal runaway, and demonstrates a method to suspend thermal runaway without compromising battery health. These findings are crucial for advancing battery safety, informing future research, and enhancing Li-ion battery applications in sustainable energy sources and electric vehicles. This work represents a significant contribution to the field of battery technology and safety.

LIST OF REFERENCES

[1] D. Bradley, Building better batteries, Education in Chemistry 47 (2010) 124–125.

[2] S. Chu, A. Majumdar, Opportunities and challenges for a sustainable energy future, Nature 488 (2012) 294–303. https://doi.org/10.1038/nature11475.

[3] B. Dunn, H. Kamath, J.M. Tarascon, Electrical energy storage for the grid: A battery of choices, Science (1979) 334 (2011) 928–935. https://doi.org/10.1126/science.1212741.

[4] D. Yan, L. Lu, Z. Li, X. Feng, M. Ouyang, F. Jiang, Durability comparison of four different types of high-power batteries in HEV and their degradation mechanism analysis, Appl Energy 179 (2016) 1123–1130. https://doi.org/10.1016/j.apenergy.2016.07.054.

[5] B. Scrosati, J. Garche, Lithium batteries: Status, prospects and future, J Power Sources 195 (2010) 2419–2430. https://doi.org/10.1016/j.jpowsour.2009.11.048.

[6] M. Armand, P. Axmann, D. Bresser, M. Copley, K. Edström, C. Ekberg, D. Guyomard, B. Lestriez, P. Novák, M. Petranikova, W. Porcher, S. Trabesinger, M. Wohlfahrt-Mehrens, H. Zhang, Lithium-ion batteries – Current state of the art and anticipated developments, J Power Sources 479 (2020). https://doi.org/10.1016/j.jpowsour.2020.228708.

[7] Y. Yang, E.G. Okonkwo, G. Huang, S. Xu, W. Sun, Y. He, On the sustainability of lithium ion battery industry – A review and perspective, Energy Storage Mater 36 (2021) 186–212. https://doi.org/10.1016/j.ensm.2020.12.019.

[8] M. Killer, M. Farrokhseresht, N.G. Paterakis, Implementation of large-scale Li-ion battery energy storage systems within the EMEA region, Appl Energy 260 (2020) 114166. https://doi.org/10.1016/j.apenergy.2019.114166.

[9] J. Wen, D. Zhao, C. Zhang, An overview of electricity powered vehicles: Lithium-ion battery energy storage density and energy conversion efficiency, Renew Energy 162 (2020) 1629–1648. https://doi.org/10.1016/j.renene.2020.09.055.

[10] S. Koohi-Fayegh, M.A. Rosen, A review of energy storage types, applications and recent developments, J Energy Storage 27 (2020) 101047. https://doi.org/10.1016/j.est.2019.101047.

[11] P.G. Pereirinha, M. González, I. Carrilero, D. Anseán, J. Alonso, J.C. Viera, Main Trends and Challenges in Road Transportation Electrification, Transportation Research Procedia 33 (2018) 235–242. https://doi.org/10.1016/j.trpro.2018.10.096.

[12] M.M. Thackeray, C. Wolverton, E.D. Isaacs, Electrical energy storage for transportation - Approaching the limits of, and going beyond, lithium-ion batteries, Energy Environ Sci 5 (2012) 7854–7863. https://doi.org/10.1039/c2ee21892e.

[13] A.G. Boulanger, A.C. Chu, S. Maxx, D.L. Waltz, Vehicle electrification: Status and issues, Proceedings of the IEEE 99 (2011) 1116–1138. https://doi.org/10.1109/JPROC.2011.2112750.

[14] A. Masias, J. Marcicki, W.A. Paxton, Opportunities and Challenges of Lithium Ion Batteries in Automotive Applications, ACS Energy Lett 6 (2021) 621–630. https://doi.org/10.1021/acsenergylett.0c02584.

[15] X. Han, L. Lu, Y. Zheng, X. Feng, Z. Li, J. Li, M. Ouyang, A review on the key issues of the lithium ion battery degradation among the whole life cycle, ETransportation 1 (2019) 100005. https://doi.org/10.1016/j.etran.2019.100005.

[16] J.S. Edge, S. O'Kane, R. Prosser, N.D. Kirkaldy, A.N. Patel, A. Hales, A. Ghosh, W. Ai, J. Chen, J. Yang, S. Li, M.C. Pang, L. Bravo Diaz, A. Tomaszewska, M.W. Marzook, K.N. Radhakrishnan, H. Wang, Y. Patel, B. Wu, G.J. Offer, Lithium ion battery degradation: what you need to know, Physical Chemistry Chemical Physics 23 (2021) 8200–8221. https://doi.org/10.1039/d1cp00359c.

[17] K. Uddin, S. Perera, W.D. Widanage, L. Somerville, J. Marco, Characterising lithium-ion battery degradation through the identification and tracking of electrochemical battery model parameters, Batteries 2 (2016). https://doi.org/10.3390/batteries2020013.

[18] K.A. Severson, P.M. Attia, N. Jin, N. Perkins, B. Jiang, Z. Yang, M.H. Chen, M. Aykol, P.K. Herring, D. Fraggedakis, M.Z. Bazant, S.J. Harris, W.C. Chueh, R.D. Braatz, Data-driven prediction of battery cycle life before capacity degradation, Nat Energy 4 (2019) 383–391. https://doi.org/10.1038/s41560-019-0356-8.

[19] S.H. Park, J. Park, M.H. Ryou, Y.M. Lee, Sensitivity of power of lithium-ion batteries to temperature: A case study using cylindrical- and pouch-type cells, J Power Sources 465 (2020) 228238. https://doi.org/10.1016/j.jpowsour.2020.228238.

[20] M. Lagnoni, C. Nicolella, A. Bertei, Survey and sensitivity analysis of critical parameters in lithium-ion battery thermo-electrochemical modeling, Electrochim Acta 394 (2021) 139098. https://doi.org/10.1016/j.electacta.2021.139098.

[21] M. Song, S.Y. Choe, Parameter sensitivity analysis of a reduced-order electrochemical-thermal model for heat generation rate of lithium-ion batteries, Appl Energy 305 (2022) 117920. https://doi.org/10.1016/j.apenergy.2021.117920.

[22] X. Yu, W. Li, V. Gupta, H. Gao, D. Tran, S. Sarwar, Z. Chen, Current Challenges in Efficient Lithium-Ion Batteries' Recycling: A Perspective, Global Challenges 6 (2022). https://doi.org/10.1002/gch2.202200099.

[23] C.M. Costa, J.C. Barbosa, R. Gonçalves, H. Castro, F.J.D. Campo, S. Lanceros-Méndez, Recycling and environmental issues of lithium-ion batteries: Advances, challenges and opportunities, Energy Storage Mater 37 (2021) 433–465. https://doi.org/10.1016/j.ensm.2021.02.032.

[24] X. Wu, J. Ma, J. Wang, X. Zhang, G. Zhou, Z. Liang, Progress, Key Issues, and Future Prospects for Li-Ion Battery Recycling, Global Challenges 6 (2022). https://doi.org/10.1002/gch2.202200067.

[25] L. Gaines, K. Richa, J. Spangenberger, Key issues for Li-ion battery recycling, MRS Energy and Sustainability 5 (2018) 1–14. https://doi.org/10.1557/mre.2018.13.

[26] L. Lu, X. Han, J. Li, J. Hua, M. Ouyang, A review on the key issues for lithium-ion battery management in electric vehicles, J Power Sources 226 (2013) 272–288. https://doi.org/10.1016/j.jpowsour.2012.10.060.

[27] C. jie Wang, Y. li Zhu, X. kun Fan, C. Qi, F. Gao, Mathematical model for thermal behavior of lithium-ion battery pack under overheating, Appl Therm Eng 191 (2021) 116894. https://doi.org/10.1016/j.applthermaleng.2021.116894.

[28] D. Lisbona, T. Snee, A review of hazards associated with primary lithium and lithium-ion batteries, Process Safety and Environmental Protection 89 (2011) 434–442. https://doi.org/10.1016/j.psep.2011.06.022.

[29] Q. Wang, P. Ping, X. Zhao, G. Chu, J. Sun, C. Chen, Thermal runaway caused fire and explosion of lithium ion battery, J Power Sources 208 (2012) 210–224. https://doi.org/10.1016/j.jpowsour.2012.02.038.

[30] X. Feng, M. Ouyang, X. Liu, L. Lu, Y. Xia, X. He, Thermal runaway mechanism of lithium ion battery for electric vehicles: A review, Energy Storage Mater 10 (2018) 246–267. https://doi.org/10.1016/j.ensm.2017.05.013.

[31] B. Liu, Y. Jia, C. Yuan, L. Wang, X. Gao, S. Yin, J. Xu, Safety issues and mechanisms of lithium-ion battery cell upon mechanical abusive loading: A review, Energy Storage Mater 24 (2020) 85–112. https://doi.org/10.1016/j.ensm.2019.06.036.

[32] D. Ren, X. Feng, L. Liu, H. Hsu, L. Lu, L. Wang, X. He, M. Ouyang, Investigating the relationship between internal short circuit and thermal runaway of lithium-ion batteries under thermal abuse condition, Energy Storage Mater 34 (2021) 563–573. https://doi.org/10.1016/j.ensm.2020.10.020.

[33] H. Li, D. Zhou, M. Zhang, B. Liu, C. Zhang, Multi-field interpretation of internal short circuit and thermal runaway behavior for lithium-ion batteries under

mechanical abuse, Energy 263 (2023) 126027. https://doi.org/10.1016/j.energy.2022.126027.

[34] J. Hong, Z. Wang, C. Qu, Y. Zhou, T. Shan, J. Zhang, Y. Hou, Investigation on overcharge-caused thermal runaway of lithium-ion batteries in real-world electric vehicles, Appl Energy 321 (2022) 119229. https://doi.org/10.1016/j.apenergy.2022.119229.

[35] T. Ohsaki, T. Kishi, T. Kuboki, N. Takami, N. Shimura, Y. Sato, M. Sekino, A. Satoh, Overcharge reaction of lithium-ion batteries, J Power Sources 146 (2005) 97–100. https://doi.org/10.1016/j.jpowsour.2005.03.105.

[36] J. Liu, Z. Huang, J. Sun, Q. Wang, Heat generation and thermal runaway of lithium-ion battery induced by slight overcharging cycling, J Power Sources 526 (2022) 231136. https://doi.org/10.1016/j.jpowsour.2022.231136.

[37] J. Liu, Z. Wang, J. Bai, T. Gao, N. Mao, Heat generation and thermal runaway mechanisms induced by overcharging of aged lithium-ion battery, Appl Therm Eng 212 (2022) 118565. https://doi.org/10.1016/j.applthermaleng.2022.118565.

[38] D. Ren, X. Feng, L. Lu, M. Ouyang, S. Zheng, J. Li, X. He, An electrochemical-thermal coupled overcharge-to-thermal-runaway model for lithium ion battery, J Power Sources 364 (2017) 328–340. https://doi.org/10.1016/j.jpowsour.2017.08.035.

[39] H. Wang, E. Lara-Curzio, E.T. Rule, C.S. Winchester, Mechanical abuse simulation and thermal runaway risks of large-format Li-ion batteries, J Power Sources 342 (2017) 913–920. https://doi.org/10.1016/j.jpowsour.2016.12.111.

[40] H. Chen, E. Kalamaras, A. Abaza, Y. Tripathy, J. Page, A. Barai, Comprehensive analysis of thermal runaway and rupture of lithium-ion batteries under mechanical abuse conditions, Appl Energy 349 (2023) 121610. https://doi.org/10.1016/j.apenergy.2023.121610.

[41] Y. Xiao, F. Yang, Z. Gao, M. Liu, J. Wang, Z. Kou, Y. Lin, Y. Li, L. Gao, Y. Chen, S. Ren, X. Li, Review of mechanical abuse related thermal runaway models of lithium-ion batteries at different scales, J Energy Storage 64 (2023) 107145. https://doi.org/10.1016/j.est.2023.107145.

[42] L. Yiding, W. Wenwei, L. Cheng, Y. Xiaoguang, Z. Fenghao, Multi-physics safety model based on structure damage for lithium-ion battery under mechanical abuse, J Clean Prod 277 (2020) 124094. https://doi.org/10.1016/j.jclepro.2020.124094.

[43] J. Lamb, C.J. Orendorff, Evaluation of mechanical abuse techniques in lithium ion batteries, J Power Sources 247 (2014) 189–196. https://doi.org/10.1016/j.jpowsour.2013.08.066.

[44] P. Liu, C. Liu, K. Yang, M. Zhang, F. Gao, B. Mao, H. Li, Q. Duan, Q. Wang, Thermal runaway and fire behaviors of lithium iron phosphate battery induced by over heating, J Energy Storage 31 (2020) 101714. https://doi.org/10.1016/j.est.2020.101714.

[45] P.J. Bugryniec, J.N. Davidson, S.F. Brown, Assessment of thermal runaway in commercial lithium iron phosphate cells due to overheating in an oven test, Energy Procedia 151 (2018) 74–78. https://doi.org/10.1016/j.egypro.2018.09.030.

[46] H. Wang, W. Shi, F. Hu, Y. Wang, X. Hu, H. Li, Over-heating triggered thermal runaway behavior for lithium-ion battery with high nickel content in positive electrode, Energy 224 (2021) 120072. https://doi.org/10.1016/j.energy.2021.120072.

[47] M.S. Islam, C.A.J. Fisher, Lithium and sodium battery cathode materials: Computational insights into voltage, diffusion and nanostructural properties, Chem Soc Rev 43 (2014) 185–204. https://doi.org/10.1039/c3cs60199d.

[48] P. Arora, R.E. White, M. Doyle, Capacity Fade Mechanisms and Side Reactions in Lithium-Ion Batteries, J Electrochem Soc 145 (1998) 3647–3667. https://doi.org/10.1149/1.1838857.

[49] S. Baazouzi, N. Feistel, J. Wanner, I. Landwehr, A. Fill, K.P. Birke, Design, Properties, and Manufacturing of Cylindrical Li-Ion Battery Cells—A Generic Overview, Batteries 9 (2023). https://doi.org/10.3390/batteries9060309.

[50] Y. Inui, Y. Kobayashi, Y. Watanabe, Y. Watase, Y. Kitamura, Simulation of temperature distribution in cylindrical and prismatic lithium ion secondary batteries, Energy Convers Manag 48 (2007) 2103–2109. https://doi.org/10.1016/j.enconman.2006.12.012.

[51] Y. Chen, Y. Kang, Y. Zhao, L. Wang, J. Liu, Y. Li, Z. Liang, X. He, X. Li, N. Tavajohi, B. Li, A review of lithium-ion battery safety concerns: The issues, strategies, and testing standards, Journal of Energy Chemistry 59 (2021) 83–99. https://doi.org/10.1016/j.jechem.2020.10.017.

[52] P. Huang, C. Yao, B. Mao, Q. Wang, J. Sun, Z. Bai, The critical characteristics and transition process of lithium-ion battery thermal runaway, Energy 213 (2020) 119082. https://doi.org/10.1016/j.energy.2020.119082.

[53] L. Song, Y. Zheng, Z. Xiao, C. Wang, T. Long, Review on Thermal Runaway of Lithium-Ion Batteries for Electric Vehicles, J Electron Mater 51 (2022) 30–46. https://doi.org/10.1007/s11664-021-09281-0.

[54] S. Mallick, D. Gayen, Thermal behaviour and thermal runaway propagation in lithium-ion battery systems – A critical review, J Energy Storage 62 (2023) 106894. https://doi.org/10.1016/j.est.2023.106894.

[55] G. Xu, L. Huang, C. Lu, X. Zhou, G. Cui, Revealing the multilevel thermal safety of lithium batteries, Energy Storage Mater 31 (2020) 72–86. https://doi.org/10.1016/j.ensm.2020.06.004.

[56] Q. Wang, L. Jiang, Y. Yu, J. Sun, Progress of enhancing the safety of lithium ion battery from the electrolyte aspect, Nano Energy 55 (2019) 93–114. https://doi.org/10.1016/j.nanoen.2018.10.035.

[57] D. Kong, H. Lv, P. Ping, G. Wang, A review of early warning methods of thermal runaway of lithium ion batteries, J Energy Storage 64 (2023) 107073. https://doi.org/10.1016/j.est.2023.107073.

[58] C. Mikolajczak, P. Michael Kahn, K. White, R. Thomas Long, Lithium-Ion Batteries Hazard and Use Assessment Final Report, 2011.

[59] U.S. Energy Information Administration, Annual Energy Outlook 2019 Case Descriptions, Outlook 0383 (2019) 221. https://www.eia.gov/outlooks/aeo/case_descriptions.php.

[60] G.E. Blomgren, The Development and Future of Lithium Ion Batteries, J Electrochem Soc 164 (2017) A5019–A5025. https://doi.org/10.1149/2.0251701jes.

[61] T. Placke, R. Kloepsch, S. Dühnen, M. Winter, Lithium ion, lithium metal, and alternative rechargeable battery technologies: the odyssey for high energy density, Journal of Solid State Electrochemistry 21 (2017) 1939–1964. https://doi.org/10.1007/s10008-017-3610-7.

[62] M. Broussely, P. Biensan, F. Bonhomme, P. Blanchard, S. Herreyre, K. Nechev, R.J. Staniewicz, Main aging mechanisms in Li ion batteries, J Power Sources 146 (2005) 90–96. https://doi.org/10.1016/j.jpowsour.2005.03.172.

[63] K. Zhao, M. Pharr, J.J. Vlassak, Z. Suo, Fracture of electrodes in lithium-ion batteries caused by fast charging, J Appl Phys 108 (2010). https://doi.org/10.1063/1.3492617.

[64] C.T. Love, O.A. Baturina, K.E. Swider-Lyons, Observation of lithium dendrites at ambient temperature and below, ECS Electrochemistry Letters 4 (2014) A24–A27. https://doi.org/10.1149/2.0041502eel.

[65] Z. Xu, P. Zhao, M. Xu, X. Wang, Conductive heating of Li-ion batteries at low temperatures, ASME International Mechanical Engineering Congress and Exposition, Proceedings (IMECE) 6B-2018 (2018) 1–12. https://doi.org/10.1115/IMECE2018-88235.

[66] B. Liu, Y. Jia, J. Li, S. Yin, C. Yuan, Z. Hu, L. Wang, Y. Li, J. Xu, Safety issues caused by internal short circuits in lithium-ion batteries, J Mater Chem A Mater 6 (2018) 21475–21484. https://doi.org/10.1039/C8TA08997C.

[67] A. Simeone, D. Lv, X.Y. Liu, J. Zhang, Collision damage assessment in lithium-ion battery cells via sensor monitoring and ensemble learning, Procedia CIRP 78 (2018) 273–278. https://doi.org/10.1016/j.procir.2018.09.073.

[68] F. Larsson, P. Andersson, P. Blomqvist, A. Lorén, B.E. Mellander, Characteristics of lithium-ion batteries during fire tests, J Power Sources 271 (2014) 414–420. https://doi.org/10.1016/j.jpowsour.2014.08.027.

[69] Q.F. Yuan, F. Zhao, W. Wang, Y. Zhao, Z. Liang, D. Yan, Overcharge failure investigation of lithium-ion batteries, Electrochim Acta 178 (2015) 682–688. https://doi.org/10.1016/j.electacta.2015.07.147.

[70] D. Ren, X. Liu, X. Feng, L. Lu, M. Ouyang, J. Li, X. He, Model-based thermal runaway prediction of lithium-ion batteries from kinetics analysis of cell components, Appl Energy 228 (2018) 633–644. https://doi.org/10.1016/j.apenergy.2018.06.126.

[71] X. Feng, S. Zheng, D. Ren, X. He, L. Wang, H. Cui, X. Liu, C. Jin, F. Zhang, C. Xu, H. Hsu, S. Gao, T. Chen, Y. Li, T. Wang, H. Wang, M. Li, M. Ouyang, Investigating the thermal runaway mechanisms of lithium-ion batteries based on thermal analysis database, Appl Energy 246 (2019) 53–64. https://doi.org/10.1016/j.apenergy.2019.04.009.

[72] X. Feng, X. He, M. Ouyang, L. Wang, L. Lu, D. Ren, S. Santhanagopalan, A Coupled Electrochemical-Thermal Failure Model for Predicting the Thermal Runaway Behavior of Lithium-Ion Batteries, J Electrochem Soc 165 (2018) A3748–A3765. https://doi.org/10.1149/2.0311816jes.

[73] T.D. Hatchard, D.D. MacNeil, A. Basu, J.R. Dahn, Thermal Model of Cylindrical and Prismatic Lithium-Ion Cells, J Electrochem Soc 148 (2001) A755. https://doi.org/10.1149/1.1377592.

[74] R. Spotnitz, J. Franklin, Abuse behavior of high-power, lithium-ion cells, J Power Sources 113 (2003) 81–100. https://doi.org/10.1016/S0378-7753(02)00488-3.

[75] G.H. Kim, A. Pesaran, R. Spotnitz, A three-dimensional thermal abuse model for lithium-ion cells, J Power Sources 170 (2007) 476–489. https://doi.org/10.1016/j.jpowsour.2007.04.018.

[76] J. Li, D. Sun, X. Jin, W. Shi, C. Sun, Lithium-ion battery overcharging thermal characteristics analysis and an impedance-based electro-thermal coupled model simulation, Appl Energy 254 (2019) 113574. https://doi.org/10.1016/j.apenergy.2019.113574.

[77] P. Peng, F. Jiang, Thermal safety of lithium-ion batteries with various cathode materials: A numerical study, Int J Heat Mass Transf 103 (2016) 1008–1016. https://doi.org/10.1016/j.ijheatmasstransfer.2016.07.088.

[78] J. Xu, C. Lan, Y. Qiao, Y. Ma, Prevent thermal runaway of lithium-ion batteries with minichannel cooling, Appl Therm Eng 110 (2017) 883–890. https://doi.org/10.1016/j.applthermaleng.2016.08.151.

[79] C.F. Lopez, J.A. Jeevarajan, P.P. Mukherjee, Characterization of Lithium-Ion Battery Thermal Abuse Behavior Using Experimental and Computational Analysis, J Electrochem Soc 162 (2015) A2163–A2173. https://doi.org/10.1149/2.0751510jes.

[80] X. Feng, X. He, M. Ouyang, L. Lu, P. Wu, C. Kulp, S. Prasser, Thermal runaway propagation model for designing a safer battery pack with 25Ah LiNixCoyMnzO2 large format lithium ion battery, Appl Energy 154 (2015) 74–91. https://doi.org/10.1016/j.apenergy.2015.04.118.

[81] S. Santhanagopalan, P. Ramadass, J. (Zhengming) Zhang, Analysis of internal short-circuit in a lithium ion cell, J Power Sources 194 (2009) 550–557. https://doi.org/10.1016/j.jpowsour.2009.05.002.

[82] K.C. Chiu, C.H. Lin, S.F. Yeh, Y.H. Lin, K.C. Chen, An electrochemical modeling of lithium-ion battery nail penetration, J Power Sources 251 (2014) 254–263. https://doi.org/10.1016/j.jpowsour.2013.11.069.

[83] P. Peng, Y. Sun, F. Jiang, Thermal analyses of LiCoO2 lithium-ion battery during oven tests, Heat and Mass Transfer/Waerme- Und Stoffuebertragung 50 (2014) 1405–1416. https://doi.org/10.1007/s00231-014-1353-x.

[84] G. Liang, Y. Zhang, Q. Han, Z. Liu, Z. Jiang, S. Tian, A novel 3D-layered electrochemical-thermal coupled model strategy for the nail-penetration process simulation, J Power Sources 342 (2017) 836–845. https://doi.org/10.1016/j.jpowsour.2017.01.005.

[85] S. Abada, M. Petit, A. Lecocq, G. Marlair, V. Sauvant-Moynot, F. Huet, Combined experimental and modeling approaches of the thermal runaway of fresh and aged lithium-ion batteries, J Power Sources 399 (2018) 264–273. https://doi.org/10.1016/j.jpowsour.2018.07.094.

[86] K. Smith, C.Y. Wang, Power and thermal characterization of a lithium-ion battery pack for hybrid-electric vehicles, J Power Sources 160 (2006) 662–673. https://doi.org/10.1016/j.jpowsour.2006.01.038.

[87] Y. Ye, Y. Shi, N. Cai, J. Lee, X. He, Electro-thermal modeling and experimental validation for lithium ion battery, J Power Sources 199 (2012) 227–238. https://doi.org/10.1016/j.jpowsour.2011.10.027.

[88] B. Wu, V. Yufit, M. Marinescu, G.J. Offer, R.F. Martinez-Botas, N.P. Brandon, Coupled thermal-electrochemical modelling of uneven heat generation in lithium-ion battery packs, J Power Sources 243 (2013) 544–554. https://doi.org/10.1016/j.jpowsour.2013.05.164.

[89] W. Fang, P. Ramadass, Z. Zhang, Study of internal short in a Li-ion cell-II. Numerical investigation using a 3D electrochemical-thermal model, J Power Sources 248 (2014) 1090–1098. https://doi.org/10.1016/j.jpowsour.2013.10.004.

[90] T.G. Zavalis, M. Behm, G. Lindbergh, Investigation of Short-Circuit Scenarios in a Lithium-Ion Battery Cell, J Electrochem Soc 159 (2012) A848–A859. https://doi.org/10.1149/2.096206jes.

[91] M. Xu, R. Wang, B. Reichman, X. Wang, Modeling the effect of two-stage fast charging protocol on thermal behavior and charging energy efficiency of lithium-

ion batteries, J Energy Storage 20 (2018) 298–309. https://doi.org/10.1016/j.est.2018.09.004.

[92] Z.G. Qu, W.Q. Li, W.Q. Tao, Numerical model of the passive thermal management system for high-power lithium ion battery by using porous metal foam saturated with phase change material, Int J Hydrogen Energy 39 (2014) 3904–3913. https://doi.org/10.1016/j.ijhydene.2013.12.136.

[93] M. Xu, Z. Zhang, X. Wang, L. Jia, L. Yang, Two-dimensional electrochemical-thermal coupled modeling of cylindrical LiFePO4 batteries, J Power Sources 256 (2014) 233–243. https://doi.org/10.1016/j.jpowsour.2014.01.070.

[94] X. Li, S.Y. Choe, W.T. Joe, A reduced order electrochemical and thermal model for a pouch type lithium ion polymer battery with LiNixMnyCo1-x-yO2/LiFePO4 blended cathode, J Power Sources 294 (2015) 545–555. https://doi.org/10.1016/j.jpowsour.2015.06.090.

[95] C.D. Rahn, C.Y. Wang, Battery Systems Engineering, Battery Systems Engineering (2013). https://doi.org/10.1002/9781118517048.

[96] M. Doyle, J. Newman, A.S. Gozdz, C.N. Schmutz, J. Tarascon, Comparison of Modeling Predictions with Experimental Data from Plastic Lithium Ion Cells, J Electrochem Soc 143 (1996) 1890–1903. https://doi.org/10.1149/1.1836921.

[97] W. Mei, H. Chen, J. Sun, Q. Wang, Numerical study on tab dimension optimization of lithium-ion battery from the thermal safety perspective, Appl Therm Eng 142 (2018) 148–165. https://doi.org/10.1016/j.applthermaleng.2018.06.075.

[98] J. Li, Y. Cheng, L. Ai, M. Jia, S. Du, B. Yin, S. Woo, H. Zhang, 3D simulation on the internal distributed properties of lithium-ion battery with planar tabbed configuration, J Power Sources 293 (2015) 993–1005. https://doi.org/10.1016/j.jpowsour.2015.06.034.

[99] W.B. Gu, C.Y. Wang, Thermal and Electrochemical Coupled Modeling of a Lithium-Ion Cell, in Lithium Batteries, ECS Proceedings 99–25 (2000) 748–762.

[100] W. Mei, H. Chen, J. Sun, Q. Wang, The effect of electrode design parameters on battery performance and optimization of electrode thickness based on the electrochemical-thermal coupling model, Sustain Energy Fuels 3 (2019) 148–165. https://doi.org/10.1039/c8se00503f.

[101] M. Guo, G. Sikha, R.E. White, Single-Particle Model for a Lithium-Ion Cell: Thermal Behavior, J Electrochem Soc 158 (2011) A122. https://doi.org/10.1149/1.3521314.

[102] P. Zhao, S.H. Lam, Toward computational singular perturbation (CSP) without eigen-decomposition, Combust Flame 209 (2019) 63–73. https://doi.org/10.1016/j.combustflame.2019.07.028.

[103] D.H. Jeon, S.M. Baek, Thermal modeling of cylindrical lithium ion battery during discharge cycle, Energy Convers Manag 52 (2011) 2973–2981. https://doi.org/10.1016/j.enconman.2011.04.013.

[104] M. Xu, Z. Zhang, X. Wang, L. Jia, L. Yang, A pseudo three-dimensional electrochemical-thermal model of a prismatic LiFePO4 battery during discharge process, Energy 80 (2015) 303–317. https://doi.org/10.1016/j.energy.2014.11.073.

[105] Z. Chen, M.P. Burke, Y. Ju, On the critical flame radius and minimum ignition energy for spherical flame initiation, Proceedings of the Combustion Institute 33 (2011) 1219–1226. https://doi.org/10.1016/j.proci.2010.05.005.

[106] P. Zhao, Detailed Kinetics in Combustion Simulation: Manifestation, Model Reduction, and Computational Diagnostics, Energy, Environment, and Sustainability (2018) 45–71. https://doi.org/10.1007/978-981-10-7410-3_2.

[107] J. Vetter, P. Novák, M.R. Wagner, C. Veit, K.C. Möller, J.O. Besenhard, M. Winter, M. Wohlfahrt-Mehrens, C. Vogler, A. Hammouche, Ageing mechanisms in lithium-ion batteries, J Power Sources 147 (2005) 269–281. https://doi.org/10.1016/j.jpowsour.2005.01.006.

[108] A. Wang, S. Kadam, H. Li, S. Shi, Y. Qi, Review on modeling of the anode solid electrolyte interphase (SEI) for lithium-ion batteries, NPJ Comput Mater 4 (2018). https://doi.org/10.1038/s41524-018-0064-0.

[109] S.C. Chen, C.C. Wan, Y.Y. Wang, Thermal analysis of lithium-ion batteries, J Power Sources 140 (2005) 111–124. https://doi.org/10.1016/j.jpowsour.2004.05.064.

[110] X. Feng, L. Lu, M. Ouyang, J. Li, X. He, A 3D thermal runaway propagation model for a large format lithium ion battery module, Energy 115 (2016) 194–208. https://doi.org/10.1016/j.energy.2016.08.094.

[111] H. Maleki, S. Al Hallaj, J.R. Selman, R.B. Dinwiddie, H. Wang, Thermal Properties of Lithium-Ion Battery and Components, J Electrochem Soc 146 (1999) 947–954. https://doi.org/10.1149/1.1391704.

[112] V.R. Subramanian, V. Boovaragavan, V. Ramadesigan, M. Arabandi, Mathematical Model Reformulation for Lithium-Ion Battery Simulations: Galvanostatic Boundary Conditions, J Electrochem Soc 156 (2009) A260. https://doi.org/10.1149/1.3065083.

[113] D.H. Jeon, Numerical modeling of lithium ion battery for predicting thermal behavior in a cylindrical cell, Current Applied Physics 14 (2014) 196–205. https://doi.org/10.1016/j.cap.2013.11.006.

[114] K. Kumaresan, G. Sikha, R.E. White, Thermal Model for a Li-Ion Cell, J Electrochem Soc 155 (2008) A164. https://doi.org/10.1149/1.2817888.

[115] W. Fang, O.J. Kwon, C.-Y. Wang, Electrochemical–thermal modeling of automotive Li-ion batteries and experimental validation using a three-electrode cell, Int J Energy Res 34 (2010) 107–115. https://doi.org/10.1002/er.

[116] FCAB, National Blueprint for Runway Safety, Federal Consortium for Advanced Batteries (2021) 1–38. https://www.google.com/url?sa=t&rct=j&q=&esrc=s&source=web&cd=&cad=rja&uact=8&ved=2ahUKEwiS1LGvssPsAhXZe30KHUvrCUwQFjACegQIARAC&url=https%3A%2F%2Frosap.ntl.bts.gov%2Fview%2Fdot%2F15473%2Fdot_15473_DS1.pdf%3F&usg=AOvVaw31F0kuqTETXYv98O0CuBp_.

[117] Z. Huang, J. Liu, H. Zhai, Q. Wang, Experimental investigation on the characteristics of thermal runaway and its propagation of large-format lithium ion batteries under overcharging and overheating conditions, Energy 233 (2021) 121103. https://doi.org/10.1016/j.energy.2021.121103.

[118] Y.S. Duh, J.H. Theng, C.C. Chen, C.S. Kao, Comparative study on thermal runaway of commercial 14500, 18650 and 26650 LiFePO4 batteries used in electric vehicles, J Energy Storage 31 (2020) 101580. https://doi.org/10.1016/j.est.2020.101580.

[119] L. Liu, X. Feng, M. Zhang, L. Lu, X. Han, X. He, M. Ouyang, Comparative study on substitute triggering approaches for internal short circuit in lithium-ion batteries, Appl Energy 259 (2020) 114143. https://doi.org/10.1016/j.apenergy.2019.114143.

[120] Z. Huang, H. Li, W. Mei, C. Zhao, J. Sun, Q. Wang, Thermal Runaway Behavior of Lithium Iron Phosphate Battery During Penetration, Fire Technol 56 (2020) 2405–2426. https://doi.org/10.1007/s10694-020-00967-1.

[121] J. Xu, W. Mei, C. Zhao, Y. Liu, L. Zhang, Q. Wang, Study on thermal runaway mechanism of 1000 mAh lithium ion pouch cell during nail penetration, J Therm Anal Calorim 144 (2021) 273–284. https://doi.org/10.1007/s10973-020-10149-4.

[122] J. Gong, Q. Wang, J. Sun, Thermal analysis of nickel cobalt lithium manganese with varying nickel content used for lithium ion batteries, Thermochim Acta 655 (2017) 176–180. https://doi.org/10.1016/j.tca.2017.06.022.

[123] B. Lei, W. Zhao, C. Ziebert, N. Uhlmann, M. Rohde, H.J. Seifert, Experimental analysis of thermal runaway in 18650 cylindrical Li-Ion cells using an accelerating rate calorimeter, Batteries 3 (2017) 1–14. https://doi.org/10.3390/batteries3020014.

[124] C. Zhao, T. Wang, Z. Huang, J. Wu, H. Zhou, M. Ma, J. Xu, Z. Wang, H. Li, J. Sun, Q. Wang, Experimental study on thermal runaway of fully charged and

overcharged lithium-ion batteries under adiabatic and side-heating test, J Energy Storage 38 (2021) 102519. https://doi.org/10.1016/j.est.2021.102519.

[125] Y. Wang, D. Ren, X. Feng, L. Wang, M. Ouyang, Thermal kinetics comparison of delithiated Li[NixCoyMn1-x-y]O2 cathodes, J Power Sources 514 (2021) 230582. https://doi.org/10.1016/j.jpowsour.2021.230582.

[126] G. Offer, Y. Patel, A. Hales, L. Bravo Diaz, M. Marzook, Cool metric for lithium-ion batteries could spur progress, Nature 582 (2020) 485–487. https://doi.org/10.1038/d41586-020-01813-8.

[127] W. Yan, Z. Wang, D. Ouyang, S. Chen, Analysis and prediction of thermal runaway propagation interval in confined space based on response surface methodology and artificial neural network, J Energy Storage 55 (2022) 105822. https://doi.org/10.1016/j.est.2022.105822.

[128] Y. Zhu, Z. Wang, H. Bian, J. Wang, W. Bai, T. Gao, J. Bai, Y. Zhou, Critical conditions for the thermal runaway propagation of lithium-ion batteries in air and argon environments, J Therm Anal Calorim 147 (2022) 13699–13710. https://doi.org/10.1007/s10973-022-11575-2.

[129] Z. Wang, K. Wang, J. Wang, Y. Yang, Y. Zhu, W. Bai, Inhibition effect of liquid nitrogen on thermal runaway propagation of lithium ion batteries in confined space, J Loss Prev Process Ind 79 (2022) 104853. https://doi.org/10.1016/j.jlp.2022.104853.

[130] P. Zhao, A. García, T. Burton, Initiation and propagation of curved reaction front in solids: Insights into solid combustion and battery thermal runaway, Combust Flame 238 (2022) 111951. https://doi.org/10.1016/j.combustflame.2021.111951.

[131] Z. Jia, P. Qin, Z. Li, Z. Wei, K. Jin, L. Jiang, Q. Wang, Analysis of gas release during the process of thermal runaway of lithium-ion batteries with three different cathode materials, J Energy Storage 50 (2022) 104302. https://doi.org/10.1016/j.est.2022.104302.

[132] D. Mishra, K. Shah, A. Jain, Investigation of the Impact of Flow of Vented Gas on Propagation of Thermal Runaway in a Li-Ion Battery Pack, J Electrochem Soc 168 (2021) 060555. https://doi.org/10.1149/1945-7111/ac0a20.

[133] Q. Wang, P. Huang, P. Ping, Y. Du, K. Li, J. Sun, Combustion behavior of lithium iron phosphate battery induced by external heat radiation, J Loss Prev Process Ind 49 (2017) 961–969. https://doi.org/10.1016/j.jlp.2016.12.002.

[134] Z. Wang, T. He, H. Bian, F. Jiang, Y. Yang, Characteristics of and factors influencing thermal runaway propagation in lithium-ion battery packs, J Energy Storage 41 (2021) 102956. https://doi.org/10.1016/j.est.2021.102956.

[135] T.D. Hatchard, D.D. MacNeil, D.A. Stevens, L. Christensen, J.R. Dahn, Importance of heat transfer by radiation in Li-ion batteries during thermal abuse, Electrochemical and Solid-State Letters 3 (2000) 305–308. https://doi.org/10.1149/1.1391131.

[136] J. Fang, J. Cai, X. He, Experimental study on the vertical thermal runaway propagation in cylindrical Lithium-ion batteries: Effects of spacing and state of

charge, Appl Therm Eng 197 (2021) 117399. https://doi.org/10.1016/j.applthermaleng.2021.117399.

[137] Z. Tang, A. Song, S. Wang, J. Cheng, C. Tao, Numerical analysis of heat transfer mechanism of thermal runaway propagation for cylindrical lithium-ion cells in battery module, Energies (Basel) 13 (2020). https://doi.org/10.3390/en13041010.

[138] W. Yan, Z. Wang, S. Chen, Quantitative analysis on the heat transfer modes in the process of thermal runaway propagation in lithium-ion battery pack under confined and semi-confined space, Int J Heat Mass Transf 176 (2021) 121483. https://doi.org/10.1016/j.ijheatmasstransfer.2021.121483.

[139] W. Allafi, C. Zhang, K. Uddin, D. Worwood, T.Q. Dinh, P.A. Ormeno, K. Li, J. Marco, A lumped thermal model of lithium-ion battery cells considering radiative heat transfer, Appl Therm Eng 143 (2018) 472–481. https://doi.org/10.1016/j.applthermaleng.2018.07.105.

[140] C.F. Lopez, J.A. Jeevarajan, P.P. Mukherjee, Experimental Analysis of Thermal Runaway and Propagation in Lithium-Ion Battery Modules, J Electrochem Soc 162 (2015) A1905–A1915. https://doi.org/10.1149/2.0921509jes.

[141] D. Mishra, A. Jain, Multi-Mode Heat Transfer Simulations of the Onset and Propagation of Thermal Runaway in a Pack of Cylindrical Li-Ion Cells, J Electrochem Soc 168 (2021) 020504. https://doi.org/10.1149/1945-7111/abdc7b.

[142] D. Mishra, K. Shah, A. Jain, Investigation of the Impact of Radiative Shielding by Internal Partitions Walls on Propagation of Thermal Runaway in a Matrix of

Cylindrical Li-Ion Cells, J Electrochem Soc 168 (2021) 120507. https://doi.org/10.1149/1945-7111/ac3715.

[143] L. Zhang, S. Yang, L. Liu, P. Zhao, Cell-to-cell variability in Li-ion battery thermal runaway: Experimental testing, statistical analysis, and kinetic modeling, J Energy Storage 56 (2022). https://doi.org/10.1016/j.est.2022.106024.

[144] L. Zhang, P. Zhao, M. Xu, X. Wang, Computational identification of the safety regime of Li-ion battery thermal runaway, Appl Energy 261 (2020) 114440. https://doi.org/10.1016/j.apenergy.2019.114440.

[145] P. Zhao, L. Liu, L. Zhang, Y. Chen, Mitigating battery thermal runaway through mild combustion, Chemical Engineering Journal Advances 9 (2022) 100208. https://doi.org/10.1016/j.ceja.2021.100208.

[146] F.P. INCROPERA, D.P. DEWITT, T.L. BERGMAN, A.S. LAVINE, Fundamentals of Heat and Mass Transfer, 2011. https://doi.org/10.1007/978-3-031-28920-0_19.

[147] L. Fan, J.M. Khodadadi, A.A. Pesaran, A parametric study on thermal management of an air-cooled lithium-ion battery module for plug-in hybrid electric vehicles, J Power Sources 238 (2013) 301–312. https://doi.org/10.1016/j.jpowsour.2013.03.050.

[148] B. Coleman, J. Ostanek, J. Heinzel, Reducing cell-to-cell spacing for large-format lithium ion battery modules with aluminum or PCM heat sinks under failure conditions, Appl Energy 180 (2016) 14–26. https://doi.org/10.1016/j.apenergy.2016.07.094.

[149] Y. Jia, M. Uddin, Y. Li, J. Xu, Thermal runaway propagation behavior within 18,650 lithium-ion battery packs: A modeling study, J Energy Storage 31 (2020) 101668. https://doi.org/10.1016/j.est.2020.101668.

[150] M. Shahjalal, P.K. Roy, T. Shams, A. Fly, J.I. Chowdhury, M.R. Ahmed, K. Liu, A review on second-life of Li-ion batteries: prospects, challenges, and issues, Energy 241 (2022) 122881. https://doi.org/10.1016/j.energy.2021.122881.

[151] C.-H. Yim, S. Niketic, N. Salem, O. Naboka, Y. Abu-Lebdeh, Towards Improving the Practical Energy Density of Li-Ion Batteries: Optimization and Evaluation of Silicon:Graphite Composites in Full Cells, J Electrochem Soc 164 (2017) A6294–A6302. https://doi.org/10.1149/2.0481701jes.

[152] M.K. Hasan, M. Mahmud, A.K.M. Ahasan Habib, S.M.A. Motakabber, S. Islam, Review of electric vehicle energy storage and management system: Standards, issues, and challenges, J Energy Storage 41 (2021) 102940. https://doi.org/10.1016/j.est.2021.102940.

[153] J. Hou, L. Lu, L. Wang, A. Ohma, D. Ren, X. Feng, Y. Li, Y. Li, I. Ootani, X. Han, W. Ren, X. He, Y. Nitta, M. Ouyang, Thermal runaway of Lithium-ion batteries employing LiN(SO2F)2-based concentrated electrolytes, Nat Commun 11 (2020) 1–11. https://doi.org/10.1038/s41467-020-18868-w.

[154] R. Chen, A.M. Nolan, J. Lu, J. Wang, X. Yu, Y. Mo, L. Chen, X. Huang, H. Li, The Thermal Stability of Lithium Solid Electrolytes with Metallic Lithium, Joule 4 (2020) 812–821. https://doi.org/10.1016/j.joule.2020.03.012.

[155] M.E. Division, for Lithium-ion Rechargeable Cell, (2011).

[156] D.I. Townsend, J.C. Tou, Thermal hazard evaluation by an accelerating rate calorimeter, Thermochim Acta 37 (1980) 1–30. https://doi.org/10.1016/0040-6031(80)85001-5.

[157] M. Sheng, D. Valco, C. Tucker, Heat Loss in Accelerating Rate Calorimetry Analysis and Thermal Lag for High Self-Heat Rates, Org Process Res Dev 25 (2021) 108–119. https://doi.org/10.1021/acs.oprd.0c00459.

[158] X. He, C. Zhao, Z. Hu, F. Restuccia, F. Richter, Q. Wang, G. Rein, Heat transfer effects on accelerating rate calorimetry of the thermal runaway of Lithium-ion batteries, Process Safety and Environmental Protection 162 (2022) 684–693. https://doi.org/10.1016/j.psep.2022.04.028.

[159] C.Y. Jhu, Y.W. Wang, C.M. Shu, J.C. Chang, H.C. Wu, Thermal explosion hazards on 18650 lithium ion batteries with a VSP2 adiabatic calorimeter, J Hazard Mater 192 (2011) 99–107. https://doi.org/10.1016/j.jhazmat.2011.04.097.

[160] C.Y. Jhu, Y.W. Wang, C.Y. Wen, C.M. Shu, Thermal runaway potential of LiCoO2 and Li(Ni1/3Co1/3Mn1/3)O2 batteries determined with adiabatic calorimetry methodology, Appl Energy 100 (2012) 127–131. https://doi.org/10.1016/j.apenergy.2012.05.064.

[161] J. Jacques, C. Lavergne, N. Devictor, Sensitivity analysis in presence of model uncertainty and correlated inputs, Reliab Eng Syst Saf 91 (2006) 1126–1134. https://doi.org/10.1016/j.ress.2005.11.047.

[162] S. Katoch, S.S. Chauhan, V. Kumar, A review on genetic algorithm: past, present, and future, Multimedia Tools and Applications, 2021. https://doi.org/10.1007/s11042-020-10139-6.

[163] C. Zhao, J. Sun, Q. Wang, Thermal runaway hazards investigation on 18650 lithium-ion battery using extended volume accelerating rate calorimeter, J Energy Storage 28 (2020) 101232. https://doi.org/10.1016/j.est.2020.101232.

[164] J. Zhao, S. Lu, Y. Fu, W. Ma, Y. Cheng, H. Zhang, Experimental study on thermal runaway behaviors of 18650 li-ion battery under enclosed and ventilated conditions, Fire Saf J 125 (2021) 103417. https://doi.org/10.1016/j.firesaf.2021.103417.

[165] Z. Wang, N. Mao, F. Jiang, Study on the effect of spacing on thermal runaway propagation for lithium-ion batteries, J Therm Anal Calorim 140 (2020) 2849–2863. https://doi.org/10.1007/s10973-019-09026-6.

[166] W.Q. Walker, J.J. Darst, D.P. Finegan, G.A. Bayles, K.L. Johnson, E.C. Darcy, S.L. Rickman, Decoupling of heat generated from ejected and non-ejected contents of 18650-format lithium-ion cells using statistical methods, J Power Sources 415 (2019) 207–218. https://doi.org/10.1016/j.jpowsour.2018.10.099.

[167] D. Zeng, L. Gagnon, Y. Wang, Cell-level hazard evaluation of 18650 form-factor Lithium-ion battery with different cathode materials, Proceedings of the Combustion Institute 39 (2023) 3823–3831. https://doi.org/10.1016/j.proci.2022.07.185.

[168] Q. Zhang, T. Liu, Q. Wang, Experimental study on the influence of different heating methods on thermal runaway of lithium-ion battery, J Energy Storage 42 (2021). https://doi.org/10.1016/j.est.2021.103063.

[169] D. Ouyang, J. Weng, M. Chen, J. Wang, Z. Wang, Electrochemical and thermal characteristics of aging lithium-ion cells after long-term cycling at abusive-temperature environments, Process Safety and Environmental Protection 159 (2022) 1215–1223. https://doi.org/10.1016/j.psep.2022.01.055.

[170] J. Belt, A. Sorensen, Thermal and Electrochemical Analysis of Thermal Runaway Propagation of Samsung Cylindrical Cells in Lithium-ion Battery Modules, J Electrochem Soc 170 (2023) 010515. https://doi.org/10.1149/1945-7111/aca939.

[171] S. Shahid, M. Agelin-Chaab, A review of thermal runaway prevention and mitigation strategies for lithium-ion batteries, Energy Conversion and Management: X 16 (2022) 100310. https://doi.org/10.1016/j.ecmx.2022.100310.

[172] K. Zou, S. Lu, X. Chen, E. Gao, Y. Cao, Y. Bi, Thermal and gas characteristics of large-format LiNi0.8Co0.1Mn0.1O2 pouch power cell during thermal runaway, J Energy Storage 39 (2021) 102609. https://doi.org/10.1016/j.est.2021.102609.

[173] Q. Zhang, J. Niu, Z. Zhao, Q. Wang, Research on the effect of thermal runaway gas components and explosion limits of lithium-ion batteries under different charge states, J Energy Storage 45 (2022) 103759. https://doi.org/10.1016/j.est.2021.103759.

[174] Z. Zhong, L. Chen, C. Zhu, W. Ren, L. Kong, Y. Wan, Nano LiFePO4 coated Ni rich composite as cathode for lithium ion batteries with high thermal ability and

excellent cycling performance, J Power Sources 464 (2020) 228235. https://doi.org/10.1016/j.jpowsour.2020.228235.

[175] A.O. Said, C. Lee, S.I. Stoliarov, Experimental investigation of cascading failure in 18650 lithium ion cell arrays: Impact of cathode chemistry, J Power Sources 446 (2020) 227347. https://doi.org/10.1016/j.jpowsour.2019.227347.

[176] K.O.A. Amano, S.K. Hahn, R. Tschirschwitz, T. Rappsilber, U. Krause, An Experimental Investigation of Thermal Runaway and Gas Release of NMC Lithium-Ion Pouch Batteries Depending on the State of Charge Level, Batteries 8 (2022) 41. https://doi.org/10.3390/batteries8050041.

[177] A.W. Golubkov, S. Scheikl, R. Planteu, G. Voitic, H. Wiltsche, C. Stangl, G. Fauler, A. Thaler, V. Hacker, Thermal runaway of commercial 18650 Li-ion batteries with LFP and NCA cathodes - Impact of state of charge and overcharge, RSC Adv 5 (2015) 57171–57186. https://doi.org/10.1039/c5ra05897j.

[178] T. He, T. Zhang, S. Gadkari, Z. Wang, N. Mao, Q. Cai, An investigation on thermal runaway behaviour of a cylindrical lithium-ion battery under different states of charge based on thermal tests and a three-dimensional thermal runaway model, J Clean Prod 388 (2023) 135980. https://doi.org/10.1016/j.jclepro.2023.135980.

[179] M. Fleischhammer, T. Waldmann, G. Bisle, B.I. Hogg, M. Wohlfahrt-Mehrens, Interaction of cyclic ageing at high-rate and low temperatures and safety in lithium-ion batteries, J Power Sources 274 (2015) 432–439. https://doi.org/10.1016/j.jpowsour.2014.08.135.

[180] M. Petzl, M. Kasper, M.A. Danzer, Lithium plating in a commercial lithium-ion battery - A low-temperature aging study, J Power Sources 275 (2015) 799–807. https://doi.org/10.1016/j.jpowsour.2014.11.065.

[181] S. Wilke, B. Schweitzer, S. Khateeb, S. Al-Hallaj, Preventing thermal runaway propagation in lithium ion battery packs using a phase change composite material: An experimental study, J Power Sources 340 (2017) 51–59. https://doi.org/10.1016/j.jpowsour.2016.11.018.

[182] D. Becher, M. Bauer, H. Döring, O. Böse, B. Friess, M.A. Danzer, Preventing thermal propagation in battery packs using enthalpy supported thermal barriers, J Energy Storage 42 (2021) 103057. https://doi.org/10.1016/j.est.2021.103057.

[183] F. Chen, R. Huang, C. Wang, X. Yu, H. Liu, Q. Wu, K. Qian, R. Bhagat, Air and PCM cooling for battery thermal management considering battery cycle life, Appl Therm Eng 173 (2020) 115154. https://doi.org/10.1016/j.applthermaleng.2020.115154.

[184] T. Gao, J. Bai, D. Ouyang, Z. Wang, W. Bai, N. Mao, Y. Zhu, Effect of aging temperature on thermal stability of lithium-ion batteries: Part A – High-temperature aging, Renew Energy 203 (2023) 592–600. https://doi.org/10.1016/j.renene.2022.12.092.

[185] M. Börner, A. Friesen, M. Grützke, Y.P. Stenzel, G. Brunklaus, J. Haetge, S. Nowak, F.M. Schappacher, M. Winter, Correlation of aging and thermal stability of commercial 18650-type lithium ion batteries, J Power Sources 342 (2017) 382–392. https://doi.org/10.1016/j.jpowsour.2016.12.041.

[186] P. Kuntz, O. Raccurt, P. Azaïs, K. Richter, T. Waldmann, M. Wohlfahrt-Mehrens, M. Bardet, A. Buzlukov, S. Genies, Identification of degradation mechanisms by post-mortem analysis for high power and high energy commercial li-ion cells after electric vehicle aging, Batteries 7 (2021). https://doi.org/10.3390/batteries7030048.

[187] B. Ng, P.T. Coman, E. Faegh, X. Peng, S.G. Karakalos, X. Jin, W.E. Mustain, R.E. White, Low-Temperature Lithium Plating/Corrosion Hazard in Lithium-Ion Batteries: Electrode Rippling, Variable States of Charge, and Thermal and Nonthermal Runaway, ACS Appl Energy Mater 3 (2020) 3653–3664. https://doi.org/10.1021/acsaem.0c00130.

[188] J.V. Pastor, A. García, J. Monsalve-Serrano, D. Golke, Analysis of the aging effects on the thermal runaway characteristics of Lithium-Ion cells through stepwise reactions, Appl Therm Eng 230 (2023). https://doi.org/10.1016/j.applthermaleng.2023.120685.

[189] W. Wu, W. Wu, X. Qiu, S. Wang, Low-temperature reversible capacity loss and aging mechanism in lithium-ion batteries for different discharge profiles, Int J Energy Res 43 (2019) 243–253. https://doi.org/10.1002/er.4257.

[190] J. Zhu, M. Knapp, D.R. Sørensen, M. Heere, M.S.D. Darma, M. Müller, L. Mereacre, H. Dai, A. Senyshyn, X. Wei, H. Ehrenberg, Investigation of capacity fade for 18650-type lithium-ion batteries cycled in different state of charge (SoC) ranges, J Power Sources 489 (2021). https://doi.org/10.1016/j.jpowsour.2020.229422.

[191] D. Ren, H. Hsu, R. Li, X. Feng, D. Guo, X. Han, L. Lu, X. He, S. Gao, J. Hou, Y. Li, Y. Wang, M. Ouyang, A comparative investigation of aging effects on thermal runaway behavior of lithium-ion batteries, ETransportation 2 (2019) 100034. https://doi.org/10.1016/j.etran.2019.100034.

[192] D. Kong, H. Zhao, P. Ping, Y. Zhang, G. Wang, Effect of low temperature on thermal runaway and fire behaviors of 18650 lithium-ion battery: A comprehensive experimental study, Process Safety and Environmental Protection 174 (2023) 448–459. https://doi.org/10.1016/j.psep.2023.04.017.

[193] X. Feng, D. Ren, S. Zhang, X. He, L. Wang, M. Ouyang, Influence of aging paths on the thermal runaway features of lithium-ion batteries in accelerating rate calorimetry tests, Int J Electrochem Sci 14 (2019) 44–58. https://doi.org/10.20964/2019.01.14.

[194] R. Xiong, Y. Pan, W. Shen, H. Li, F. Sun, Lithium-ion battery aging mechanisms and diagnosis method for automotive applications: Recent advances and perspectives, Renewable and Sustainable Energy Reviews 131 (2020). https://doi.org/10.1016/j.rser.2020.110048.

[195] W. Choi, H.C. Shin, J.M. Kim, J.Y. Choi, W.S. Yoon, Modeling and applications of electrochemical impedance spectroscopy (EIS) for lithium-ion batteries, Journal of Electrochemical Science and Technology 11 (2020) 1–13. https://doi.org/10.33961/jecst.2019.00528.

[196] J. Wen, D. Zhao, C. Zhang, An overview of electricity powered vehicles: Lithium-ion battery energy storage density and energy conversion efficiency, Renew Energy 162 (2020) 1629–1648. https://doi.org/10.1016/j.renene.2020.09.055.

[197] B. Xu, J. Lee, D. Kwon, L. Kong, M. Pecht, Mitigation strategies for Li-ion battery thermal runaway: A review, Renewable and Sustainable Energy Reviews 150 (2021) 111437. https://doi.org/10.1016/j.rser.2021.111437.

[198] K. Liu, Y. Liu, D. Lin, A. Pei, Y. Cui, Materials for lithium-ion battery safety, (2018).

[199] P. Münster, M. Diehl, J.E. Frerichs, M. Börner, M.R. Hansen, M. Winter, P. Niehoff, Effect of Li plating during formation of lithium ion batteries on their cycling performance and thermal safety, J Power Sources 484 (2021) 0–7. https://doi.org/10.1016/j.jpowsour.2020.229306.

[200] S. Wu, C. Wang, W. Luan, Y. Zhang, Y. Chen, H. Chen, Thermal runaway behaviors of Li-ion batteries after low temperature aging: Experimental study and predictive modeling, J Energy Storage 66 (2023) 107451. https://doi.org/10.1016/j.est.2023.107451.

[201] S. Chavan, B. Venkateswarlu, R. Prabakaran, M. Salman, S.W. Joo, G.S. Choi, S.C. Kim, Thermal runaway and mitigation strategies for electric vehicle lithium-ion batteries using battery cooling approach: A review of the current status and challenges, J Energy Storage 72 (2023) 108569. https://doi.org/10.1016/j.est.2023.108569.

[202] S. Mallick, D. Gayen, Thermal behaviour and thermal runaway propagation in lithium-ion battery systems – A critical review, J Energy Storage 62 (2023) 106894. https://doi.org/10.1016/j.est.2023.106894.

[203] Y. Zheng, Z. Shi, D. Ren, J. Chen, X. Liu, X. Feng, L. Wang, X. Han, L. Lu, X. He, M. Ouyang, In-depth investigation of the exothermic reactions between lithiated graphite and electrolyte in lithium-ion battery, Journal of Energy Chemistry 69 (2022) 593–600. https://doi.org/10.1016/j.jechem.2022.01.027.

[204] S. El Moutchou, H. Aziam, M. Mansori, I. Saadoune, Thermal stability of Lithium-ion batteries: Case study of NMC811 and LFP cathode materials, Mater Today Proc 51 (2021) A1–A7. https://doi.org/10.1016/j.matpr.2022.02.324.

[205] D. Lu, S. Lin, S. Hu, W. Cui, T. Fang, A. Iqbal, Z. Zhang, W. Peng, Thermal behavior and failure mechanism of large format lithium-ion battery, Journal of Solid State Electrochemistry 25 (2021) 315–325. https://doi.org/10.1007/s10008-020-04810-z.

[206] Y. Zhang, S. Cheng, W. Mei, L. Jiang, Z. Jia, Z. Cheng, J. Sun, Q. Wang, Understanding of thermal runaway mechanism of LiFePO4 battery in-depth by three-level analysis, Appl Energy 336 (2023) 120695. https://doi.org/10.1016/j.apenergy.2023.120695.

[207] D. Ren, X. Feng, L. Liu, H. Hsu, L. Lu, L. Wang, X. He, M. Ouyang, Investigating the relationship between internal short circuit and thermal runaway of lithium-ion batteries under thermal abuse condition, Energy Storage Mater 34 (2021) 563–573. https://doi.org/10.1016/j.ensm.2020.10.020.

[208] H. Wang, H. Xu, Z. Zhao, Q. Wang, C. Jin, Y. Li, J. Sheng, K. Li, Z. Du, C. Xu, X. Feng, An experimental analysis on thermal runaway and its propagation in Cell-to-Pack lithium-ion batteries, Appl Therm Eng 211 (2022) 118418. https://doi.org/10.1016/j.applthermaleng.2022.118418.

[209] C.F. Lopez, J.A. Jeevarajan, P.P. Mukherjee, Experimental Analysis of Thermal Runaway and Propagation in Lithium-Ion Battery Modules, J Electrochem Soc 162 (2015) A1905–A1915. https://doi.org/10.1149/2.0921509jes.

[210] L. Yuan, T. Dubaniewicz, I. Zlochower, R. Thomas, N. Rayyan, Experimental study on thermal runaway and vented gases of lithium-ion cells, Process Safety and Environmental Protection 144 (2020) 186–192. https://doi.org/10.1016/j.psep.2020.07.028.

[211] L. Zhang, L. Liu, A. Terekhov, D. Warnberg, P. Zhao, Thermal runaway of Li-ion battery with different aging histories, Process Safety and Environmental Protection 185 (2024) 910–917. https://doi.org/10.1016/j.psep.2024.03.077.

[212] D. Ren, X. Liu, X. Feng, L. Lu, M. Ouyang, J. Li, X. He, Model-based thermal runaway prediction of lithium-ion batteries from kinetics analysis of cell components, Appl Energy 228 (2018) 633–644. https://doi.org/10.1016/j.apenergy.2018.06.126.

[213] S. Abada, M. Petit, A. Lecocq, G. Marlair, V. Sauvant-Moynot, F. Huet, Combined experimental and modeling approaches of the thermal runaway of fresh and aged lithium-ion batteries, J Power Sources 399 (2018) 264–273. https://doi.org/10.1016/j.jpowsour.2018.07.094.

[214] Z. An, K. Shah, L. Jia, Y. Ma, Modeling and analysis of thermal runaway in Li-ion cell, Appl Therm Eng 160 (2019). https://doi.org/10.1016/j.applthermaleng.2019.113960.

[215] S. Bilyaz, K.C. Marr, O.A. Ezekoye, Modeling of Thermal Runaway Propagation in a Pouch Cell Stack, Fire Technol 56 (2020) 2441–2466. https://doi.org/10.1007/s10694-020-00970-6.

[216] C.X. He, Q.L. Yue, Q. Chen, T.S. Zhao, Modeling thermal runaway of lithium-ion batteries with a venting process, Appl Energy 327 (2022). https://doi.org/10.1016/j.apenergy.2022.120110.

[217] A. Kriston, A. Podias, I. Adanouj, A. Pfrang, Analysis of the Effect of Thermal Runaway Initiation Conditions on the Severity of Thermal Runaway—Numerical Simulation and Machine Learning Study, J Electrochem Soc 167 (2020) 090555. https://doi.org/10.1149/1945-7111/ab9b0b.

[218] Y. Zhang, W. Mei, P. Qin, Q. Duan, Q. Wang, Numerical modeling on thermal runaway triggered by local overheating for lithium iron phosphate battery, Appl Therm Eng 192 (2021) 116928. https://doi.org/10.1016/j.applthermaleng.2021.116928.

[219] P. Zhao, L. Liu, Y. Chen, H. Ge, Theoretical and numerical analysis for thermal runaway propagation within a single cell, Int J Heat Mass Transf 181 (2021) 121901. https://doi.org/10.1016/j.ijheatmasstransfer.2021.121901.

[220] M. Parhizi, A. Jain, G. Kilaz, J.K. Ostanek, Accelerating the numerical solution of thermal runaway in Li-ion batteries, J Power Sources 538 (2022) 231531. https://doi.org/10.1016/j.jpowsour.2022.231531.

[221] W. Li, H. Wang, M. Ouyang, C. Xu, L. Lu, X. Feng, Theoretical and experimental analysis of the lithium-ion battery thermal runaway process based on the internal combustion engine combustion theory, Energy Convers Manag 185 (2019) 211–222. https://doi.org/10.1016/j.enconman.2019.02.008.

[222] X. Feng, F. Zhang, J. Feng, C. Jin, H. Wang, C. Xu, M. Ouyang, Propagation dynamics of the thermal runaway front in large-scale lithium-ion batteries: Theoretical and experiment validation, Int J Heat Mass Transf 225 (2024) 125393. https://doi.org/10.1016/j.ijheatmasstransfer.2024.125393.

[223] P. Zhao, A. García, T. Burton, Initiation and propagation of curved reaction front in solids: Insights into solid combustion and battery thermal runaway, Combust Flame 238 (2022) 111951. https://doi.org/10.1016/j.combustflame.2021.111951.

[224] P. Zhao, L. Liu, L. Zhang, Y. Chen, Mitigating battery thermal runaway through mild combustion, Chemical Engineering Journal Advances 9 (2022) 100208. https://doi.org/10.1016/j.ceja.2021.100208.

[225] O. Mathieu, C.M. Grégoire, M.A. Turner, D.J. Mohr, S.A. Alturaifi, J.C. Thomas, E.L. Petersen, Experimental Investigation of the Combustion Properties of an Average Thermal Runaway Gas Mixture from Li-Ion Batteries, Energy and Fuels 36 (2022) 3247–3258. https://doi.org/10.1021/acs.energyfuels.1c04057.

[226] D. Mishra, P. Zhao, A. Jain, Thermal Runaway Propagation in Li-ion Battery Packs Due to Combustion of Vent Gases, J Electrochem Soc 169 (2022) 100520. https://doi.org/10.1149/1945-7111/ac91a7.

[227] Z. Liu, X. Guo, N. Meng, Z. Yu, H. Yang, Study of thermal runaway and the combustion behavior of lithium-ion batteries overcharged with high current rates, Thermochim Acta 715 (2022) 179276. https://doi.org/10.1016/j.tca.2022.179276.

[228] J.S. Edge, S. O'Kane, R. Prosser, N.D. Kirkaldy, A.N. Patel, A. Hales, A. Ghosh, W. Ai, J. Chen, J. Yang, S. Li, M.C. Pang, L. Bravo Diaz, A. Tomaszewska, M.W. Marzook, K.N. Radhakrishnan, H. Wang, Y. Patel, B. Wu, G.J. Offer, Lithium ion battery degradation: what you need to know, Physical Chemistry Chemical Physics 23 (2021) 8200–8221. https://doi.org/10.1039/d1cp00359c.

[229] Y. Preger, H.M. Barkholtz, A. Fresquez, D.L. Campbell, B.W. Juba, J. Romàn-Kustas, S.R. Ferreira, B. Chalamala, Degradation of Commercial Lithium-Ion Cells as a Function of Chemistry and Cycling Conditions, J Electrochem Soc 167 (2020) 120532. https://doi.org/10.1149/1945-7111/abae37.

[230] R. Xiong, Y. Pan, W. Shen, H. Li, F. Sun, Lithium-ion battery aging mechanisms and diagnosis method for automotive applications: Recent advances and perspectives, Renewable and Sustainable Energy Reviews 131 (2020) 110048. https://doi.org/10.1016/j.rser.2020.110048.

[231] D.I. Stroe, M. Swierczynski, S.K. Kær, R. Teodorescu, Degradation Behavior of Lithium-Ion Batteries During Calendar Ageing - The Case of the Internal

Resistance Increase, IEEE Trans Ind Appl 54 (2018) 517–525. https://doi.org/10.1109/TIA.2017.2756026.

[232] S. Atalay, M. Sheikh, A. Mariani, Y. Merla, E. Bower, W.D. Widanage, Theory of battery ageing in a lithium-ion battery: Capacity fade, nonlinear ageing and lifetime prediction, J Power Sources 478 (2020) 229026. https://doi.org/10.1016/j.jpowsour.2020.229026.

[233] J. Zhu, M.S. Dewi Darma, M. Knapp, D.R. Sørensen, M. Heere, Q. Fang, X. Wang, H. Dai, L. Mereacre, A. Senyshyn, X. Wei, H. Ehrenberg, Investigation of lithium-ion battery degradation mechanisms by combining differential voltage analysis and alternating current impedance, J Power Sources 448 (2020) 28–30. https://doi.org/10.1016/j.jpowsour.2019.227575.

[234] Y. Gao, K. Liu, C. Zhu, X. Zhang, D. Zhang, Co-Estimation of State-of-Charge and State-of- Health for Lithium-Ion Batteries Using an Enhanced Electrochemical Model, IEEE Transactions on Industrial Electronics 69 (2022) 2684–2696. https://doi.org/10.1109/TIE.2021.3066946.

[235] A. Sarkar, I.C. Nlebedim, P. Shrotriya, Performance degradation due to anodic failure mechanisms in lithium-ion batteries, J Power Sources 502 (2021) 229145. https://doi.org/10.1016/j.jpowsour.2020.229145.

[236] J. Li, R.G. Landers, J. Park, A comprehensive single-particle-degradation model for battery state-of-health prediction, J Power Sources 456 (2020). https://doi.org/10.1016/j.jpowsour.2020.227950.

[237] F. Zhou, C. Bao, Analysis of the lithium-ion battery capacity degradation behavior with a comprehensive mathematical model, J Power Sources 515 (2021) 230630. https://doi.org/10.1016/j.jpowsour.2021.230630.

[238] G. Dong, J. Wei, A physics-based aging model for lithium-ion battery with coupled chemical/mechanical degradation mechanisms, Electrochim Acta 395 (2021) 139133. https://doi.org/10.1016/j.electacta.2021.139133.

[239] G. Zhang, X. Wei, S. Chen, G. Han, J. Zhu, H. Dai, Investigation the Degradation Mechanisms of Lithium-Ion Batteries under Low-Temperature High-Rate Cycling, ACS Appl Energy Mater (2022). https://doi.org/10.1021/acsaem.2c00957.

[240] S. Sahu, J.M. Foster, A continuum model for lithium plating and dendrite formation in lithium-ion batteries: Formulation and validation against experiment, J Energy Storage 60 (2023) 106516. https://doi.org/10.1016/j.est.2022.106516.

[241] H. Xu, C. Han, W. Li, H. Li, X. Qiu, Quantification of lithium dendrite and solid electrolyte interphase (SEI) in lithium-ion batteries, J Power Sources 529 (2022) 231219. https://doi.org/10.1016/j.jpowsour.2022.231219.

[242] X. Lin, K. Khosravinia, X. Hu, J. Li, W. Lu, Lithium Plating Mechanism, Detection, and Mitigation in Lithium-Ion Batteries, Prog Energy Combust Sci 87 (2021). https://doi.org/10.1016/j.pecs.2021.100953.

[243] T.M.M. Heenan, A. Wade, C. Tan, J.E. Parker, D. Matras, A.S. Leach, J.B. Robinson, A. Llewellyn, A. Dimitrijevic, R. Jervis, P.D. Quinn, D.J.L. Brett, P.R. Shearing, Identifying the Origins of Microstructural Defects Such as Cracking

within Ni-Rich NMC811 Cathode Particles for Lithium-Ion Batteries, Adv Energy Mater 10 (2020). https://doi.org/10.1002/aenm.202002655.

[244] M. Shahjalal, P.K. Roy, T. Shams, A. Fly, J.I. Chowdhury, M.R. Ahmed, K. Liu, A review on second-life of Li-ion batteries: prospects, challenges, and issues, Energy 241 (2022) 122881. https://doi.org/10.1016/j.energy.2021.122881.

[245] Y. Tao, C.D. Rahn, L.A. Archer, F. You, Second life and recycling: Energy and environmental sustainability perspectives for high-performance lithium-ion batteries, Sci Adv 7 (2021) 1–16. https://doi.org/10.1126/sciadv.abi7633.

[246] W. Ai, B. Wu, E. Martínez-Pañeda, A coupled phase field formulation for modelling fatigue cracking in lithium-ion battery electrode particles, J Power Sources 544 (2022) 231805. https://doi.org/10.1016/j.jpowsour.2022.231805.

[247] S. Lee, W. Li, A. Dolocan, H. Celio, H. Park, J.H. Warner, A. Manthiram, In-Depth Analysis of the Degradation Mechanisms of High-Nickel, Low/No-Cobalt Layered Oxide Cathodes for Lithium-Ion Batteries, Adv Energy Mater 11 (2021) 1–14. https://doi.org/10.1002/aenm.202100858.

[248] J. Zhu, I. Mathews, D. Ren, W. Li, D. Cogswell, B. Xing, T. Sedlatschek, S.N.R. Kantareddy, M. Yi, T. Gao, Y. Xia, Q. Zhou, T. Wierzbicki, M.Z. Bazant, End-of-life or second-life options for retired electric vehicle batteries, Cell Rep Phys Sci 2 (2021) 100537. https://doi.org/10.1016/j.xcrp.2021.100537.

[249] Y. Zhao, O. Pohl, A.I. Bhatt, G.E. Collis, P.J. Mahon, T. Rüther, A.F. Hollenkamp, A Review on Battery Market Trends, Second-Life Reuse, and Recycling,

Sustainable Chemistry 2 (2021) 167–205. https://doi.org/10.3390/suschem2010011.

[250] J.V. Pastor, A. García, J. Monsalve-Serrano, D. Golke, Analysis of the aging effects on the thermal runaway characteristics of Lithium-Ion cells through stepwise reactions, Appl Therm Eng 230 (2023). https://doi.org/10.1016/j.applthermaleng.2023.120685.

[251] T. Gao, J. Bai, D. Ouyang, Z. Wang, W. Bai, N. Mao, Y. Zhu, Effect of aging temperature on thermal stability of lithium-ion batteries: Part A – High-temperature aging, Renew Energy 203 (2023) 592–600. https://doi.org/10.1016/j.renene.2022.12.092.

[252] M. Yang, Y. Ye, A. Yang, Z. Jiang, X. Wang, H. Yuan, M. Rong, Comparative study on aging and thermal runaway of commercial LiFePO4/graphite battery undergoing slight overcharge cycling, J Energy Storage 50 (2022) 104691. https://doi.org/10.1016/j.est.2022.104691.

[253] C. jie Wang, Y. li Zhu, F. Gao, C. Qi, P. long Zhao, Q. fen Meng, J. yong Wang, Q. bing Wu, Thermal runaway behavior and features of LiFePO4/graphite aged batteries under overcharge, Int J Energy Res 44 (2020) 5477–5487. https://doi.org/10.1002/er.5298.

[254] W. Yuan, D. Liang, Y. Chu, Q. Wang, Aging effect delays overcharge-induced thermal runaway of lithium-ion batteries, J Loss Prev Process Ind 79 (2022) 104830. https://doi.org/10.1016/j.jlp.2022.104830.

[255] D. Ren, K. Smith, D. Guo, X. Han, X. Feng, L. Lu, M. Ouyang, J. Li, Investigation of Lithium Plating-Stripping Process in Li-Ion Batteries at Low Temperature Using an Electrochemical Model, J Electrochem Soc 165 (2018) A2167–A2178. https://doi.org/10.1149/2.0661810jes.

[256] T. Waldmann, M. Wohlfahrt-Mehrens, Effects of rest time after Li plating on safety behavior—ARC tests with commercial high-energy 18650 Li-ion cells, Electrochim Acta 230 (2017) 454–460. https://doi.org/10.1016/j.electacta.2017.02.036.

[257] S. Wang, K. Rafiz, J. Liu, Y. Jin, J.Y.S. Lin, Effects of lithium dendrites on thermal runaway and gassing of LiFePO4batteries, Sustain Energy Fuels 4 (2020) 2342–2351. https://doi.org/10.1039/d0se00027b.

[258] B. Ng, P.T. Coman, E. Faegh, X. Peng, S.G. Karakalos, X. Jin, W.E. Mustain, R.E. White, Low-Temperature Lithium Plating/Corrosion Hazard in Lithium-Ion Batteries: Electrode Rippling, Variable States of Charge, and Thermal and Nonthermal Runaway, ACS Appl Energy Mater 3 (2020) 3653–3664. https://doi.org/10.1021/acsaem.0c00130.

[259] P. Xu, J. Li, N. Lei, F. Zhou, C. Sun, An experimental study on the mechanical characteristics of Li-ion battery during overcharge-induced thermal runaway, Int J Energy Res 45 (2021) 19985–20000. https://doi.org/10.1002/er.7072.

[260] L. Zhao, M. Zheng, J. Zhang, H. Liu, W. Li, M. Chen, Numerical modeling of thermal runaway for low temperature cycling lithium-ion batteries, J Energy Storage 63 (2023) 107053. https://doi.org/10.1016/j.est.2023.107053.

[261] S. Wu, C. Wang, W. Luan, Y. Zhang, Y. Chen, H. Chen, Thermal runaway behaviors of Li-ion batteries after low temperature aging: Experimental study and predictive modeling, J Energy Storage 66 (2023) 107451. https://doi.org/10.1016/j.est.2023.107451.

[262] D. Kong, H. Zhao, P. Ping, Y. Zhang, G. Wang, Effect of low temperature on thermal runaway and fire behaviors of 18650 lithium-ion battery: A comprehensive experimental study, Process Safety and Environmental Protection 174 (2023) 448–459. https://doi.org/10.1016/j.psep.2023.04.017.

[263] H. Zhou, C. Fear, R.E. Carter, C.T. Love, P.P. Mukherjee, Correlating lithium plating quantification with thermal safety characteristics of lithium-ion batteries, Energy Storage Mater 66 (2024) 103214. https://doi.org/10.1016/j.ensm.2024.103214.

[264] E. Kwak, J. hyeong Kim, S.H. Hong, K.Y. Oh, Detailed modeling investigation of thermal runaway pathways of a lithium iron phosphate battery, Int J Energy Res 46 (2022) 1146–1167. https://doi.org/10.1002/er.7235.

[265] T. He, T. Zhang, S. Gadkari, Z. Wang, N. Mao, Q. Cai, An investigation on thermal runaway behaviour of a cylindrical lithium-ion battery under different states of charge based on thermal tests and a three-dimensional thermal runaway model, J Clean Prod 388 (2023) 135980. https://doi.org/10.1016/j.jclepro.2023.135980.

[266] W. Huang, X. Feng, Y. Pan, C. Jin, J. Sun, J. Yao, H. Wang, C. Xu, F. Jiang, M. Ouyang, Early warning of battery failure based on venting signal, J Energy Storage 59 (2023) 106536. https://doi.org/10.1016/j.est.2022.106536.

[267] M.K. Tran, A. Mevawalla, A. Aziz, S. Panchal, Y. Xie, M. Fowler, A Review of Lithium-Ion Battery Thermal Runaway Modeling and Diagnosis Approaches, Processes 10 (2022). https://doi.org/10.3390/pr10061192.

[268] M.M. Torabian, M. Jafari, A. Bazargan, Discharge of lithium-ion batteries in salt solutions for safer storage, transport, and resource recovery, Waste Management and Research 40 (2022) 402–409. https://doi.org/10.1177/0734242X211022658.

[269] C.M.R. Vendra, A. V. Shelke, J.E.H. Buston, J. Gill, D. Howard, E. Read, A. Abaza, B. Cooper, J.X. Wen, Numerical and experimental characterisation of high energy density 21700 lithium-ion battery fires, Process Safety and Environmental Protection 160 (2022) 153–165. https://doi.org/10.1016/j.psep.2022.02.014.

[270] L. Yuan, T. Dubaniewicz, I. Zlochower, R. Thomas, N. Rayyan, Experimental study on thermal runaway and vented gases of lithium-ion cells, Process Safety and Environmental Protection 144 (2020) 186–192. https://doi.org/10.1016/j.psep.2020.07.028.

[271] Q. Sun, H. Liu, M. Zhi, X. Chen, P. Lv, Y. He, Thermal characteristics of thermal runaway for pouch lithium-ion battery with different state of charges under various ambient pressures, J Power Sources 527 (2022) 231175. https://doi.org/10.1016/j.jpowsour.2022.231175.

[272] A. Kvasha, C. Gutiérrez, U. Osa, I. de Meatza, J.A. Blazquez, H. Macicior, I. Urdampilleta, A comparative study of thermal runaway of commercial lithium ion cells, Energy 159 (2018) 547–557. https://doi.org/10.1016/j.energy.2018.06.173.

[273] H. Wang, H. Xu, Z. Zhang, Q. Wang, C. Jin, C. Wu, C. Xu, J. Hao, L. Sun, Z. Du, Y. Li, J. Sun, X. Feng, Fire and explosion characteristics of vent gas from lithium-ion batteries after thermal runaway: A comparative study, ETransportation 13 (2022) 100190. https://doi.org/10.1016/j.etran.2022.100190.

[274] S. Chen, Z. Wang, W. Yan, Identification and characteristic analysis of powder ejected from a lithium ion battery during thermal runaway at elevated temperatures, J Hazard Mater 400 (2020) 123169. https://doi.org/10.1016/j.jhazmat.2020.123169.

[275] Y. Zhang, H. Wang, W. Li, C. Li, Quantitative identification of emissions from abused prismatic Ni-rich lithium-ion batteries, ETransportation 2 (2019) 100031. https://doi.org/10.1016/j.etran.2019.100031.

[276] V. Premnath, Y. Wang, N. Wright, I. Khalek, S. Uribe, Detailed characterization of particle emissions from battery fires, Aerosol Science and Technology 56 (2022) 337–354. https://doi.org/10.1080/02786826.2021.2018399.

[277] Y. Wang, H. Wang, Y. Zhang, L. Cheng, Y. Wu, X. Feng, L. Lu, M. Ouyang, Thermal oxidation characteristics for smoke particles from an abused prismatic Li(Ni0.6Co0.2Mn0.2)O2 battery, J Energy Storage 39 (2021). https://doi.org/10.1016/j.est.2021.102639.

[278] D. Sturk, L. Rosell, P. Blomqvist, A.A. Tidblad, Analysis of li-ion battery gases vented in an inert atmosphere thermal test chamber, Batteries 5 (2019) 1–17. https://doi.org/10.3390/batteries5030061.

[279] Y. Zhang, H. Wang, W. Li, C. Li, M. Ouyang, Size distribution and elemental composition of vent particles from abused prismatic Ni-rich automotive lithium-ion batteries, J Energy Storage 26 (2019) 100991. https://doi.org/10.1016/j.est.2019.100991.

[280] TSI, 3090_Engine-Exhaust-Particle-Sizer, (n.d.).

[281] TSI, 3321_Aerodynamic-Particle-Sizer, (n.d.) 2–4.

[282] TSI Incorporated, TSI Applicatin note PR-001 - Aerosol statistics, lognormal distributions and dN / dlogD p, (2012) 1–6.

[283] M.P. Macdonald, S. Chandrasekaran, S. Garimella, T.F. Fuller, Thermal runaway in a prismatic lithium ion cell triggered by a short circuit, J Energy Storage 40 (2021) 102737. https://doi.org/10.1016/j.est.2021.102737.

[284] J. Hu, T. Liu, X. Wang, Z. Wang, L. Wu, Investigation on thermal runaway of 18,650 lithium ion battery under thermal abuse coupled with charging, J Energy Storage 51 (2022) 104482. https://doi.org/10.1016/j.est.2022.104482.

[285] C. Jin, Y. Sun, H. Wang, X. Lai, S. Wang, S. Chen, X. Rui, Y. Zheng, X. Feng, H. Wang, M. Ouyang, Model and experiments to investigate thermal runaway characterization of lithium-ion batteries induced by external heating method, J Power Sources 504 (2021) 230065. https://doi.org/10.1016/j.jpowsour.2021.230065.

[286] Z. Jia, P. Qin, Z. Li, Z. Wei, K. Jin, L. Jiang, Q. Wang, Analysis of gas release during the process of thermal runaway of lithium-ion batteries with three different

cathode materials, J Energy Storage 50 (2022) 104302. https://doi.org/10.1016/j.est.2022.104302.

[287] K. Zou, S. Lu, X. Chen, E. Gao, Y. Cao, Y. Bi, Thermal and gas characteristics of large-format LiNi0.8Co0.1Mn0.1O2 pouch power cell during thermal runaway, J Energy Storage 39 (2021) 102609. https://doi.org/10.1016/j.est.2021.102609.

[288] A. Bordes, G. Marlair, A. Zantman, S. Herreyre, A. Papin, P. Desprez, A. Lecocq, New insight on the risk profile pertaining to lithium-ion batteries under thermal runaway as affected by system modularity and subsequent oxidation regime, J Energy Storage 52 (2022) 1–12. https://doi.org/10.1016/j.est.2022.104790.

[289] Y.S. Duh, M.T. Tsai, C.S. Kao, Characterization on the thermal runaway of commercial 18650 lithium-ion batteries used in electric vehicle, J Therm Anal Calorim 127 (2017) 983–993. https://doi.org/10.1007/s10973-016-5767-1.

[290] Z. Zhong, L. Chen, C. Zhu, W. Ren, L. Kong, Y. Wan, Nano LiFePO4 coated Ni rich composite as cathode for lithium ion batteries with high thermal ability and excellent cycling performance, J Power Sources 464 (2020) 228235. https://doi.org/10.1016/j.jpowsour.2020.228235.

[291] O.S. Mendoza-Hernandez, H. Ishikawa, Y. Nishikawa, Y. Maruyama, M. Umeda, Cathode material comparison of thermal runaway behavior of Li-ion cells at different state of charges including over charge, J Power Sources 280 (2015) 499–504. https://doi.org/10.1016/j.jpowsour.2015.01.143.

[292] B. Mao, P. Huang, H. Chen, Q. Wang, J. Sun, Self-heating reaction and thermal runaway criticality of the lithium ion battery, Int J Heat Mass Transf 149 (2020) 119178. https://doi.org/10.1016/j.ijheatmasstransfer.2019.119178.

[293] C. Lee, A.O. Said, S.I. Stoliarov, Impact of State of Charge and Cell Arrangement on Thermal Runaway Propagation in Lithium Ion Battery Cell Arrays, Transp Res Rec 2673 (2019) 408–417. https://doi.org/10.1177/0361198119845654.

[294] J. Liu, Q. Duan, M. Ma, C. Zhao, J. Sun, Q. Wang, Aging mechanisms and thermal stability of aged commercial 18650 lithium ion battery induced by slight overcharging cycling, J Power Sources 445 (2020) 227263. https://doi.org/10.1016/j.jpowsour.2019.227263.

[295] Y. Chen, Y. Kang, Y. Zhao, L. Wang, J. Liu, Y. Li, Z. Liang, X. He, X. Li, N. Tavajohi, B. Li, A review of lithium-ion battery safety concerns: The issues, strategies, and testing standards, Journal of Energy Chemistry 59 (2021) 83–99. https://doi.org/10.1016/j.jechem.2020.10.017.

[296] A. Friesen, F. Horsthemke, X. Mönnighoff, G. Brunklaus, R. Krafft, M. Börner, T. Risthaus, M. Winter, F.M. Schappacher, Impact of cycling at low temperatures on the safety behavior of 18650-type lithium ion cells: Combined study of mechanical and thermal abuse testing accompanied by post-mortem analysis, J Power Sources 334 (2016) 1–11. https://doi.org/10.1016/j.jpowsour.2016.09.120.

[297] S. Wilke, B. Schweitzer, S. Khateeb, S. Al-Hallaj, Preventing thermal runaway propagation in lithium ion battery packs using a phase change composite material:

An experimental study, J Power Sources 340 (2017) 51–59. https://doi.org/10.1016/j.jpowsour.2016.11.018.

[298] K.S. Kshetrimayum, Y.G. Yoon, H.R. Gye, C.J. Lee, Preventing heat propagation and thermal runaway in electric vehicle battery modules using integrated PCM and micro-channel plate cooling system, Appl Therm Eng 159 (2019) 113797. https://doi.org/10.1016/j.applthermaleng.2019.113797.

[299] T.D. Hatchard, D.D. MacNeil, A. Basu, J.R. Dahn, Thermal Model of Cylindrical and Prismatic Lithium-Ion Cells, J Electrochem Soc 148 (2001) A755. https://doi.org/10.1149/1.1377592.

[300] J. Liu, Z. Wang, J. Gong, K. Liu, H. Wang, L. Guo, Experimental study of thermal runaway process of 18650 lithium-ion battery, Materials 10 (2017). https://doi.org/10.3390/ma10030230.

[301] P. Liu, Y. Li, B. Mao, M. Chen, Z. Huang, Q. Wang, Experimental study on thermal runaway and fire behaviors of large format lithium iron phosphate battery, Appl Therm Eng 192 (2021) 116949. https://doi.org/10.1016/j.applthermaleng.2021.116949.

[302] L. Li, X. Ju, X. Zhou, Y. Peng, Z. Zhou, B. Cao, L. Yang, Experimental study on thermal runaway process of 18650 lithium-ion battery under different discharge currents, Materials 14 (2021). https://doi.org/10.3390/ma14164740.

[303] B. Mao, C. Zhao, H. Chen, Q. Wang, J. Sun, Experimental and modeling analysis of jet flow and fire dynamics of 18650-type lithium-ion battery, Appl Energy 281 (2021) 116054. https://doi.org/10.1016/j.apenergy.2020.116054.

[304] P.J. Bugryniec, J.N. Davidson, S.F. Brown, Assessment of thermal runaway in commercial lithium iron phosphate cells due to overheating in an oven test, Energy Procedia 151 (2018) 74–78. https://doi.org/10.1016/j.egypro.2018.09.030.

[305] P.J. Bugryniec, J.N. Davidson, D.J. Cumming, S.F. Brown, Pursuing safer batteries: Thermal abuse of LiFePO4 cells, J Power Sources 414 (2019) 557–568. https://doi.org/10.1016/j.jpowsour.2019.01.013.

[306] W. Zhao, M. Rohde, I.U. Mohsin, C. Ziebert, Y. Du, H.J. Seifert, Combined Thermal Runaway Investigation of Coin Cells with an Accelerating Rate Calorimeter and a Tian-Calvet Calorimeter, Batteries 8 (2022). https://doi.org/10.3390/batteries8020015.

[307] D.P. Finegan, M. Scheel, J.B. Robinson, B. Tjaden, M. Di Michiel, G. Hinds, D.J.L. Brett, P.R. Shearing, Investigating lithium-ion battery materials during overcharge-induced thermal runaway: An operando and multi-scale X-ray CT study, Physical Chemistry Chemical Physics 18 (2016) 30912–30919. https://doi.org/10.1039/c6cp04251a.

[308] D.P. Finegan, M. Scheel, J.B. Robinson, B. Tjaden, I. Hunt, T.J. Mason, J. Millichamp, M. Di Michiel, G.J. Offer, G. Hinds, D.J.L. Brett, P.R. Shearing, In-operando high-speed tomography of lithium-ion batteries during thermal runaway, Nat Commun 6 (2015) 1–10. https://doi.org/10.1038/ncomms7924.

[309] D. Ren, X. Liu, X. Feng, L. Lu, M. Ouyang, J. Li, X. He, Model-based thermal runaway prediction of lithium-ion batteries from kinetics analysis of cell

components, Appl Energy 228 (2018) 633–644. https://doi.org/10.1016/j.apenergy.2018.06.126.

[310] P. Huang, H. Chen, A. Verma, Q. Wang, P. Mukherjee, J. Sun, Non-dimensional analysis of the criticality of Li-ion battery thermal runaway behavior, J Hazard Mater 369 (2019) 268–278. https://doi.org/10.1016/j.jhazmat.2019.01.049.

[311] K. Shah, D. Chalise, A. Jain, Experimental and theoretical analysis of a method to predict thermal runaway in Li-ion cells, J Power Sources 330 (2016) 167–174. https://doi.org/10.1016/j.jpowsour.2016.08.133.

[312] H. Wu, S. Chen, J. Chen, C. Jin, C. Xu, X. Rui, H. Hsu, Y. Zheng, X. Feng, Dimensionless normalized concentration based thermal-electric regression model for the thermal runaway of lithium-ion batteries, J Power Sources 521 (2022) 230958. https://doi.org/10.1016/j.jpowsour.2021.230958.

[313] P. Zhao, L. Liu, Y. Chen, H. Ge, Theoretical and numerical analysis for thermal runaway propagation within a single cell, Int J Heat Mass Transf 181 (2021) 121901. https://doi.org/10.1016/j.ijheatmasstransfer.2021.121901.

[314] P. Zhao, A. García, T. Burton, Initiation and propagation of curved reaction front in solids: Insights into solid combustion and battery thermal runaway, Combust Flame 238 (2022) 111951. https://doi.org/10.1016/j.combustflame.2021.111951.

[315] X. Liu, D. Ren, H. Hsu, X. Feng, G.L. Xu, M. Zhuang, H. Gao, L. Lu, X. Han, Z. Chu, J. Li, X. He, K. Amine, M. Ouyang, Thermal Runaway of Lithium-Ion Batteries without Internal Short Circuit, Joule 2 (2018) 2047–2064. https://doi.org/10.1016/j.joule.2018.06.015.

[316] B. Xu, J. Lee, D. Kwon, L. Kong, M. Pecht, Mitigation strategies for Li-ion battery thermal runaway: A review, Renewable and Sustainable Energy Reviews 150 (2021) 111437. https://doi.org/10.1016/j.rser.2021.111437.

[317] X. Cui, T. Hu, Robust predictive thermal management strategy for lithium-ion battery based on thermoelectric cooler, Appl Therm Eng 221 (2023) 119833. https://doi.org/10.1016/j.applthermaleng.2022.119833.

[318] E. Yousefi, H. Najafi Khaboshan, F. Jaliliantabar, A. Adam Abdullah, The effect of different enclosure materials and NePCMs on performance of battery thermal management system, Mater Today Proc 75 (2022) 1–9. https://doi.org/10.1016/j.matpr.2022.09.261.

[319] F. Jaliliantabar, R. Mamat, S. Kumarasamy, Prediction of lithium-ion battery temperature in different operating conditions equipped with passive battery thermal management system by artificial neural networks, Mater Today Proc 48 (2021) 1796–1804. https://doi.org/10.1016/j.matpr.2021.09.026.

[320] T.R.B. Grandjean, J. Groenewald, J. Marco, The experimental evaluation of lithium ion batteries after flash cryogenic freezing, J Energy Storage 21 (2019) 202–215. https://doi.org/10.1016/j.est.2018.11.027.

[321] Z. Huang, P. Liu, Q. Duan, C. Zhao, Q. Wang, Experimental investigation on the cooling and suppression effects of liquid nitrogen on the thermal runaway of lithium ion battery, J Power Sources 495 (2021) 229795. https://doi.org/10.1016/j.jpowsour.2021.229795.

[322] C.J. Orendorff, The role of separators in lithium-ion cell safety, Electrochemical Society Interface 21 (2012) 61–65. https://doi.org/10.1149/2.F07122if.

[323] L. Bodenes, R. Naturel, H. Martinez, R. Dedryvère, M. Menetrier, L. Croguennec, J.P. Pérès, C. Tessier, F. Fischer, Lithium secondary batteries working at very high temperature: Capacity fade and understanding of aging mechanisms, J Power Sources 236 (2013) 265–275. https://doi.org/10.1016/j.jpowsour.2013.02.067.

[324] X. Feng, M. Ouyang, X. Liu, L. Lu, Y. Xia, X. He, Thermal runaway mechanism of lithium ion battery for electric vehicles: A review, Energy Storage Mater 10 (2018) 246–267. https://doi.org/10.1016/j.ensm.2017.05.013.

[325] B. Gaulupeau, B. Delobel, S. Cahen, S. Fontana, C. Hérold, Real-time mass spectroscopy analysis of Li-ion battery electrolyte degradation under abusive thermal conditions, J Power Sources 342 (2017) 808–815. https://doi.org/10.1016/j.jpowsour.2016.12.078.

LIST OF PUBLICATIONS

1. L. Zhang, L. Liu, A. Terekhov, D. Warnberg, P. Zhao, Thermal runaway of Li-ion battery with different aging histories, *Process Safety and Environmental Protection* 185 (2024) 910–917.

2. L. Zhang, L. Liu, S. Yang, Z. Xie, F. Zhang, P. Zhao, Experimental investigation on thermal runaway suspension with battery health retention, *Applied Thermal Engineering* 225 (2023): 120239.

3. L. Zhang, Y. Chen, H. Ge, A. Jain, P. Zhao, Radiation induced thermal runaway propagation in a cylindrical Li-ion battery pack: Non-monotonicity, chemical kinetics, and geometric considerations, *Applied Sciences* 13.14 (2023): 8229

4. L. Zhang, S. Yang, L. Liu, P. Zhao, Cell-to-cell variability in Li-ion battery thermal runaway: Experimental testing, statistical analysis, and kinetic modeling, *Journal of Energy Storage* 56 (2022): 106024.

5. P. Zhao, L. Liu, L. Zhang, Y. Chen, Mitigating battery thermal runaway through mild combustion, *Chemical Engineering Journal Advances* 9 (2022): 100208.

6. M. Xu, X. Wang, L. Zhang, P. Zhao, Comparison of the effect of linear and two-step fast charging protocols on degradation of lithium ion batteries, *Energy* 227 (2021): 120417.

7. L. Zhang, P. Zhao, M. Xu, X. Wang, Computational identification of the safety regime of Li-ion battery thermal runaway, *Applied Energy* 261 (2020): 114440

8. L. Zhang, P. Zhao, M. Xu, X. Wang, A computational study on the critical ignition energy and chemical kinetic feature for Li-ion battery thermal runaway, *SAE Technical Paper* (2018) No. 2018-01-0437

VITA

Liwen Zhang, a Ph.D. student in Mechanical Engineering under the supervision of Dr. Peng Zhao at the University of Tennessee, Knoxville (UTK), specializes in Li-ion battery experiments and modeling, particularly focusing on the safety regime, degradation and thermal runaway of Li-ion batteries. She was born in Rushan, Shandong, P. R. China and her journey in academia began with a B.S. in Optical Information Science and Technology from Beijing Information Science and Technology University (BISTU), followed by a M.S. in Mechanical Engineering from Oakland University (OU).